

**DEVELOPMENT AND CHARACTERIZATION OF NOVEL PROBES TO
ELUCIDATE THE ROLE OF UBIQUITIN C-TERMINAL HYDROLASE
L1 IN CANCER BIOLOGY**

by

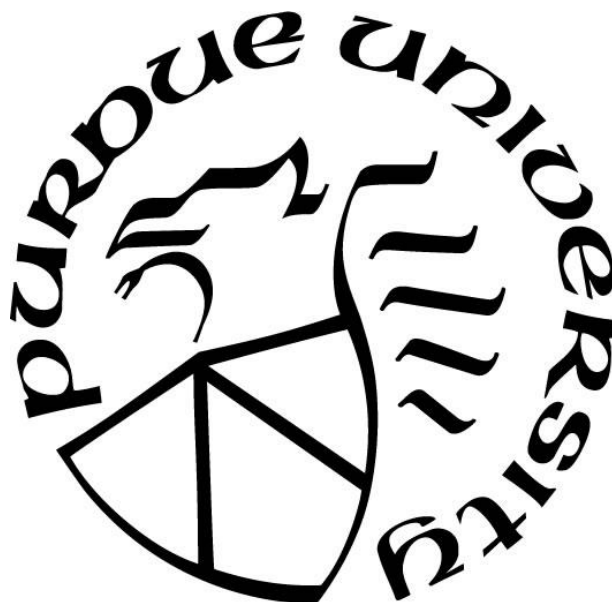
Aaron D. Krabill

A Dissertation

Submitted to the Faculty of Purdue University

In Partial Fulfillment of the Requirements for the degree of

Doctor of Philosophy



Department of Medicinal Chemistry and Molecular Pharmacology

West Lafayette, Indiana

December 2020

THE PURDUE UNIVERSITY GRADUATE SCHOOL
STATEMENT OF COMMITTEE APPROVAL

Dr. Daniel P. Flaherty, Chair

Department of Medicinal Chemistry and Molecular Pharmacology

Dr. Michael K. Wendt

Department of Medicinal Chemistry and Molecular Pharmacology

Dr. Zhong-Yin Zhang

Department of Medicinal Chemistry and Molecular Pharmacology

Dr. Chittaranjan Das

Department of Chemistry

Approved by:

Dr. Andy Hudmon

To my family and friends – thank you all.

To Brook and Olivia – This would not have been possible without you.

ACKNOWLEDGMENTS

First, I would like to thank Dr. Daniel Flaherty for his support and guidance through my doctoral studies. I appreciate the opportunities I have received, and his willingness to allow me to pursue my passions during my research. I would also like to thank my advisory committee for their guidance: Dr. Chittaranjan Das, Dr. Michael Wendt, and Dr. Zhong-Yin Zhang.

I would like to thank the current and past members of the Flaherty lab, particularly Lisha Ha, for lending an ear and always offering kind words. I would also like to thank the current members of the Flaherty lab: Chad Hewitt, Jason Scott, Ryan Imhoff, Molly Youse, Weiwei An, and Xufeng Cao for their helpful discussions and assistance. I wish you all the best in your continued efforts.

I would also like to thank my collaborators in the Das and Wendt lab. With their assistance, collaboration was effortless and fruitful.

I would like to express my deep appreciation for Barbara Mullenberg and Rozlyn Batta for all they do for the MCMP students, both in and out of the lab.

Finally, I would like to thank my family and friends. I wish I could mention you all by name, but instead I will focus on one person. Thank you Brook Krabill for your endless support and love. Thank you for motivating me to do my best by providing an example of what that looks like every day.

Financial support for my graduate work was provided by Purdue University and the Purdue Research Foundation.

TABLE OF CONTENTS

LIST OF FIGURES	7
LIST OF TABLES	10
LIST OF SCHEMES.....	11
ABBREVIATIONS	12
ABSTRACT.....	17
CHAPTER 1. INTRODUCTION	18
1.1 Ubiquitin C-Terminal Hydrolase L1 in Disease States	19
1.1.1 Ubiquitin C-Terminal Hydrolase L1 in Oncology	19
1.1.2 Ubiquitin C-Terminal Hydrolase L1 in Neurodegenerative Disease	23
1.1.3 Ubiquitin C-Terminal Hydrolases in other Disease States.....	24
1.2 Structure and Function of Ubiquitin C-Terminal Hydrolase L1	25
1.3 Efforts Towards the Development of Ubiquitin C-Terminal Hydrolase L1 Inhibitors.....	27
1.4 Project Summary	30
CHAPTER 2. BIOCHEMICAL AND CELLULAR CHARACTERIZATION OF A COVALENT CYANOPYRROLIDINE-BASED UCHL1 INHIBITOR.....	32
2.1 Introduction	32
2.2 Results and Discussion	35
2.2.1 Chemistry	35
2.2.2 Biochemical Characterization of Cyanopyrrolidine Inhibition	35
2.2.3 Structural Characterization and Molecular Modelling of Cyanopyrrolidine Inhibition	39
2.2.4 Cellular Characterization.....	42
2.3 Conclusion.....	51
2.4 Experimental.....	52
2.4.1 Chemical Synthesis	53
2.4.2 Biochemical and Cellular Assays.....	56
CHAPTER 3. OPTIMIZATION AND CHARACTERIZATION OF A COVALENT PEPTIDE- BASED UBIQUITIN C-TERMINAL HYDROLASE L1 INHIBITOR	63
3.1 Introduction	63

3.2	Results and Discussion	65
3.2.1	Chemical Synthesis of VAEFMK and Analogs	65
3.2.2	Structure-Activity Relationship for VAEFMK (1)	68
3.2.3	Binding Characterization and Kinetic Evaluation of Fluoromethylketone Analogs..	77
3.2.4	Cellular Characterization of Fluoromethylketone Analogs.....	80
3.3	Conclusion.....	90
3.4	Experimental.....	91
3.4.1	Chemical Synthesis	91
3.4.2	Biochemical and Cellular Assays.....	109
CHAPTER 4. A MECHANISTIC UNDERSTANDING OF A NOVEL MACROMOLECULAR UCHL1 INHIBITOR		116
4.1	Introduction	116
4.2	Results and Discussion	118
4.2.1	Computational Prediction and Biochemical Testing of UCHL1-Selective UbVs ...	118
4.2.2	Modeling and Molecular Dynamics Simulations of the Ub ^{T9F} mutant with UCHL1 and UCHL3	122
4.3	Conclusion.....	131
4.4	Experimental.....	132
4.4.1	Biochemical Assays	132
4.4.2	Computational Modeling and Analysis.....	138
CHAPTER 5. FUTURE DIRECTIONS		140
5.1	Further Optimization of VAEFMK	140
5.2	Covalent Fragments as UCHL1 Inhibitors	143
5.3	A Novel Caged-Luciferin Ubiquitin Variant for Tracking UCH Activity in Cells.....	145
5.4	Conclusion.....	145
REFERENCES		147
VITA.....		162
PUBLICATIONS.....		163

LIST OF FIGURES

Figure 1.1 Role of UCHL1 in blood cancers.	20
Figure 1.2 Role of UCHL1 in TNBC.....	22
Figure 1.3 Single point mutations of UCHL1 associated with neurodegenerative diseases.	23
Figure 1.4 The misaligned active site of UCHL1.	25
Figure 1.5 The binding of ubiquitin brings the active site of UCHL1 into a productive conformation.	26
Figure 1.6 Small molecule inhibitors of UCHL1.....	27
Figure 1.7 Binding of VAEFMK to UCHL1.....	29
Figure 2.1 Reported UCHL1 inhibitors.	33
Figure 2.2 Proposed mechanism for inhibition of UCHL1 by 1	34
Figure 2.3 Biochemical inhibition of UCHL1 by 1	36
Figure 2.4 Compound 1 is a slowly reversible inhibitor.....	38
Figure 2.5 Engagement of UCHL1 in cell lysate by 1	38
Figure 2.6 NMR spectra of UCHL1 with 1	40
Figure 2.7 Binding site of 1	40
Figure 2.8 Predicted binding pose of compound 1 (magenta) with UCHL1 (grey), supported by 3D intermolecular-NOE NMR experiments.	42
Figure 2.9 Cellular inhibition of UCHL1 by 1	43
Figure 2.10 Cell proliferation data for 1 versus KMS11 and KMS12 cells.	43
Figure 2.11 Compound 2 dose-response inhibition assay.	44
Figure 2.12 Representative bioconjugation reactions for compound 2	45
Figure 2.13 Dose-dependent labelling of recombinant UCHL1 by 2	46
Figure 2.14 Specific labelling of UCHL1s catalytic cysteine by 2	46
Figure 2.15 Labelling of proteins in intact cells by 2 . KMS11.....	47
Figure 2.16 Engagement of UCHL1 in KMS11 and SW1271 cells.....	48
Figure 2.17 Cellular engagement of UCHL1 by compound 2 by chemoprecipitation.....	50
Figure 3.1 LDN-57444 and covalent inhibitors of UCHL1.....	65
Figure 3.2 Time-dependent inhibition of His-UCHL1 by 1	68

Figure 3.3 Chemical structures and 3-hour IC ₅₀ values for 1 and 16 .	69
Figure 3.4 Warhead half-life analysis.	70
Figure 3.5 Intermolecular interaction between 1 and UCHL1.	71
Figure 3.6 Chemical structures and 3-hour IC ₅₀ values for 1 and 17 .	72
Figure 3.7 Potential structure of the pH dependent cyclization of glutamic acid fluoromethylketone.	72
Figure 3.8 Overlay of the UCHL1: 1 complex and UCHL3.	77
Figure 3.9 Inactivation kinetics for FMK analogs.	79
Figure 3.10 1 is a competitive inhibitor.	80
Figure 3.11 Compound 1 reduces KMS11 cell proliferation.	81
Figure 3.12 Immunoblots from KMS11 cells treated with 1 .	82
Figure 3.13 Compound 1 and 38 do not reduce SW1271 cell viability.	83
Figure 3.14 Compound 38 engages UCHL1 in SW1271 cell lysate.	84
Figure 3.15 Compound 38 selectively inhibits UCHL1 in intact SW1271 cells.	85
Figure 3.16 Recombinantly expressed His-UCHL1 is labelled in a dose-dependent manner by 38 .	86
Figure 3.17 Specific labelling of UCHL1s catalytic cysteine by 38 .	87
Figure 3.18 Selective labeling of UCHL1 in intact SW1271 cells by 38 .	87
Figure 3.19 Selective labeling of UCHL1 in intact SW1271 cells by 38 .	89
Figure 3.20 Selective inhibition of UCHL1 by 1 or 38 reduces SW1271 cell migration.	90
Figure 4.1 UCHL1 bound to ubiquitin.	119
Figure 4.2 UbV ^{T9FT66K} -ABP inhibits UCHs in a time-dependent manner.	120
Figure 4.3 UbV ^{T9FT66K} -ABP inhibits the UCH family selectively.	121
Figure 4.4 β 1– β 2 loop dynamics and predicted interactions with UCHL1.	123
Figure 4.5 Molecular dynamics simulation of β 1– β 2 loop of UbV ^{T9F} upon binding to UCHL3.	125
Figure 4.6 F214 activation cascade by the Ub β 1– β 2 loop.	126
Figure 4.7 Molecular dynamics of Phe214 of apo-UCHL1 crystal structure (PDB: 2ETL) with no Ub present.	127
Figure 4.8 Molecular dynamics of Phe214 from Ub-bound UCHL1 crystal structure (PDB: 3KW5).	128

Figure 4.9 Molecular dynamics of Phe214 of apo-UCHL1 crystal structure (PDB: 2ETL) with Ub present.	129
Figure 4.10 Dynamics of Phe214 upon binding of UbV ^{T9F}	130
Figure 5.1 Chemical structures of caspase-1 inhibitors.	141
Figure 5.2 Molecular modeling of VAEFMK analogs with UCHL1.	141
Figure 5.3 Predicted pose and interactions between VPGCMK and UCHL1.	142
Figure 5.4 Biochemical and cellular engagement of UCHL1 by fragment 1 and 2	144

LIST OF TABLES

Table 2.1 Compound 1 covalently modifies UCHL1.	37
Table 2.2 Identification of putative off-targets by tandem mass spectrometry analysis.	51
Table 3.1 Structure-activity relationship for substituents at R ₃	73
Table 3.2 Structure-activity relationship for substituents at R ₄	74
Table 3.3 Structure-activity relationship for substituents at R ₅	76
Table 3.4 $k_{\text{inact}}/K_{\text{I}}$ values for 1 , 38 , and 40 versus UCHL1.	79
Table 4.1 IC ₅₀ and K _d values for UbVs with His-UCHL1 and His-UCHL3	119
Table 4.2 $k_{\text{inact}}/K_{\text{I}}$ values for ABPs with UCHL1 and UCHL3.	121

LIST OF SCHEMES

Scheme 2.1 Preparation of 1 . Reagents and Conditions:	35
Scheme 2.2 Preparation of 2 . Reagents and Conditions:	44
Scheme 3.1 Synthesis of Boc-Glu(OR)-FMK 8 - 9	66
Scheme 3.2 Synthesis of Boc-Glu(OMe)-CMK 10	66
Scheme 3.3 Synthesis of Cbz-protected dipeptide acid 12a - t	67
Scheme 3.4 Synthesis of p-ethynyl-Cbz-protected dipeptide acid 14a - d	67
Scheme 3.5 Synthesis of carbamate-protected dipeptide acid 1, 16 - 44	68

ABBREVIATIONS

ABP –	Activity based probe
ACN –	Acetonitrile
AD –	Alzheimer’s disease
APCI –	Atmospheric pressure chemical ionization
ASAP –	As soon as possible
ATCC –	American type culture collection
ATP –	Adenosine triphosphate
BAP1 –	BRCA 1 associated protein
BCA –	Bicinchoninic acid
BLI –	Biolayer interferometry
BMRB –	Biomolecular Magnetic Resonance Bank
BOC –	Tert-Butoxycarbonyl
C90A –	Cysteine 90 to alanine mutation
Cbz –	Carboxybenzyl
CC ₅₀ –	Half-maximal cytotoxic concentration
CDCl –	Deuterated chloroform
CHCl ₃ –	Chloroform
CI –	Confidence interval
CMK –	Chloromethylketone
CSF –	Cerebrospinal fluid
CuAAC –	Copper-catalyzed Azide Alkyne Cycloaddition
Cy5-N ₃ –	Sulfo-Cyanine5
DCM –	Dichloromethane
DIPEA –	N, N-Diisopropylethylamine
DMEM –	Dulbecco’s Modified Eagle Medium
DMF –	Dimethylformamide
DMSO –	Dimethyl sulfoxide
DTT –	Dithiothreitol
DUB –	Deubiquitinase

E.coli –	Escherchia coli
EDTA –	Ethylenediaminetetraacetic acid
Equiv –	Equivalent
ESI –	Electrospray Ionization
EtOAc –	Ethyl Acetate
FBS –	Fetal bovine serum
FDA –	Food and Drug Administration
FMK –	Fluoromethylketone
Fmoc –	Fluorenylmethyloxycarbonyl
GSH –	Glutathione
H ₂ O –	Water
HA –	Hemagglutinin
HA-Ub-VME –	Hemagglutinin-tagged ubiquitin vinylmethylester
HATU –	Hexafluorophosphate Azabenzotriazole Tetramethyl Uronium
Hg –	Mercury
HIF –	Hypoxia-inducible factor
HPLC –	High-performance liquid chromatography
HSQC –	Heteronuclear single quantum coherence
IC ₅₀ –	Half-maximal inhibition concentration
IPrMgCl –	Isopropyl magnesium chloride
IPTG –	Isopropyl β-d-1-thiogalactopyranoside
JAMM –	Jab1/Mov34/Mpr1 Pad1 N-terminal+
K ₂ CO ₃ –	Potassium Carbonate
KCl –	Potassium Chloride
K _d –	Dissociation constant
K _I –	Inhibition constant
k _{inact} –	Rate of inactivation at saturation
k _{obs} –	Observed rated of inactivation
LC/MS –	Liquid chromatography mass spectrometry
LiOH –	Lithium hydroxide
m/z –	Mass to charge ratio

MD –	Molecular Dynamics
MeOH –	Methanol
MESNa –	2-ethanesulfonic acid sodium salt
mg –	Milligram
MgCl ₂ –	Magnesium Chloride
MINDY –	motif interacting with Ub-containing novel DUB family
MJD –	Machado-Josephin domain
mM	Millimolar
MM-GBSA –	Molecular mechanics - generalized Born and surface area
mmol –	Millimoles
mTOR –	Mammalian target of Rapamycin
MW –	Molecular weight
Na ₂ SO ₄ –	Sodium sulfate
NaCl –	Sodium Chloride
NaHCO ₃ –	Sodium Bicarbonate
NaOH –	Sodium hydroxide
Ni-NTA –	Nickel nitriloacetic acid
nM –	Nanomolar
NMR –	Nuclear Magnetic Resonance
NOE –	Nuclear Overhauser Effect
NP-40 –	Nonidet P-40
NSCLC –	Non-small cell lung cancer
OMe –	Methylester
OTU –	Ovarian Tumor Protease
PBS –	Phosphate buffered saline
PD –	Parkinson's disease
Pd(dppf)Cl ₂ –	1,1'-Bis(diphenylphosphino)ferrocene]palladium(II) dichloride
PDB –	Protein Data Bank
ppm –	Parts per million
PRG –	Propargylamine
qRT-PCR –	Real-time polymerase chain reaction

R _g –	Radius of Gyration
SAR –	Structure-activity relationship
SBDD –	Structure-based drug design
SCLC –	Small cell lung cancer
SDS –	Sodium dodecyl sulfate
SDS-PAGE –	Sodium dodecyl sulfate – gel electrophoresis
shRNA –	Short hairpin ribonucleic acid
T2D –	Type 2 diabetes
TBI –	Traumatic brain injury
TBS –	Tris buffered saline
tBuOH –	Tert-butyl alcohol
TCEP –	Tris(2-carboxyethyl)phosphine
TEA –	Triethylamine
TFA –	Trifluoroacetic acid
TGF –	Transforming growth factor
THF –	Tetrahydrofuran
THPTA –	Tris-hydroxypropyltriazolylmethylamine
TIPS –	Triisopropylsilane
TMS –	Tetramethylsilane
TNBC –	Triple negative breast cancer
TRIS –	Tris(hydroxymethyl)aminomethane
Trt –	Triphenylmethyl
Ub –	Ubiquitin
Ub-AMC –	Ubiquitin aminomethyl coumarin
Ub-Rho –	Ubiquitin Rhodamine 110G
Ub-VME –	Ubiquitin Vinylmethylester
UbV –	Ubiquitin variant
UCH –	Ubiquitin C-terminal Hydrolase
UCHL1 –	Ubiquitin C-terminal Hydrolase L1
UCHL3 –	Ubiquitin C-terminal Hydrolase L3
UCHL5 –	Ubiquitin C-terminal Hydrolase L5

UPS –	Ubiquitin Proteasome System
USP –	Ubiquitin specific protease
UV –	Ultraviolet
VAEFMK –	Benzyloxycarbonyl-Val-Ala-Glu(gamma-methoxy)-fluoromethylketone
VME –	Vinylmethylester
WT –	Wild type
ZUFSP –	Zinc finger containing ubiquitin peptidase 1
μM –	Micromolar

ABSTRACT

Ubiquitin C-terminal hydrolase L1 (UCHL1) is a deubiquitinating enzyme (DUB) that is expressed in the central nervous system under normal physiological conditions, comprising 1-5% of the total soluble tissue in the brain. Ectopic expression of UCHL1 is observed in a number of aggressive forms cancers, where increased protein levels correlate with an increased invasive phenotype, supporting UCHL1 as an oncogene. Despite this, there is a significant lack of useful probes to validate targeting UCHL1 *in vivo*. In this work, both small molecule inhibitors and macromolecular inhibitors of UCHL1 were designed and characterized in an effort to alleviate this issue.

Few small molecule inhibitors of UCHL1 are available, with the current gold standard LDN-57444 suffering for poor chemical stability as well as an inability to engage UCHL1 in cells. Two previously published inhibitors, MT-19 and VAEFMK, represent viable alternatives to LDN-57444. However, it was imperative to characterize these molecules in detail to confirm their utility. Using a number of approaches, it was determined that while MT-19 is a potent inhibitor of UCHL1, it suffers from non-specific toxicity and engages other proteins in the cell, making it unsuitable for use as a probe. On the other hand, a similar approach validates VAEFMK as a UCHL1-selective probe, though it suffers from low potency and requires high concentrations in cells to fully engage UCHL1.

Alternatively, the high intrinsic affinity of UCHL1 for ubiquitin (Ub) provides a starting point for macromolecular inhibitor design. However, Ub interacts with many proteins, including the nearly 100 DUBs expressed in the human genome. Using the co-crystal structures of UCHL1 and UCHL3 with Ub, a number of Ub variants (UbVs) were designed *in silico* to leverage the difference in the Ub-interfaces of UCHL1 and UCHL3. Biochemical testing shows that selectivity towards UCHL1 was achieved, though this selectivity was lost upon conversion of the UbV into an activity-based probe (ABP). Molecular dynamics (MD) simulations provide data to rationalize why this occurs.

Although much work remains to identify an inhibitor that displays suitable potency and selectivity towards UCHL1 in cells, this work sheds light the mechanistic rationale for a variety of inhibitors and will serve as a useful reference for the design of future UCHL1-selective probes.

CHAPTER 1. INTRODUCTION

The post-translational modification of proteins with ubiquitin (Ub) is a key mechanism for regulating homeostasis.¹ Addition of Ub to substrates is carried out by the cascading E1 (Ub-activating enzyme) – E2 (Ub-conjugating) – and E3 (Ub-ligating) enzymes, resulting in the conjugated protein-Ub complex through a covalent bond between the ϵ -amino group of a lysine and the carboxylate of the terminal Gly76 residue of Ub.^{2–4} Repetition of this cascade results in the formation of a poly-Ub chain, where the subsequent Ub monomers are covalently linked to the first Ub through an isopeptide bond between one of the seven lysines of the first Ub or the Met1 amino group and the Gly76 carboxylate of the later Ub monomers. Eight types of linkages are therefore possible, adding layers of complexity with potential for various branched architectures.^{5,6} The Ub-Ub chain linkages and branching provide the basis for the complex Ub-signaling pathways that are observed in eukaryotes.⁷

Ub can be removed from proteins (or from other groups in the poly-Ub chain) via hydrolysis of the isopeptide bond by a group of proteases known as deubiquitinases (DUBs).⁸ Humans express approximately 100 DUBs separated into 7 families.⁹ The majority of DUBs are cysteine proteases comprised of six different families including: ubiquitin-specific proteases (USP), ubiquitin c-terminal hydrolases (UCH), Machado-Josephin domain (MJD) proteases, ovarian-tumor proteases (OTU), as well as the most recently discovered MINDY and ZUFSP type proteases.^{9–11} A separate class within the DUB family is the JAB1/MPN/MOV34 metalloenzyme (JAMM) proteases, which require a zinc cofactor for their catalytic activity.¹² As key players in the maintenance of cellular protein homeostasis, DUBs have emerged as potential therapeutic targets for a number of disease states including cancer,¹³ autoimmune,^{14–16} and neurodegenerative diseases.^{17–19}

The UCH family is comprised of four members: BRCA1 associated protein-1 (BAP1), ubiquitin c-terminal hydrolase L1 (UCHL1), ubiquitin c-terminal hydrolase L3 (UCHL3), and ubiquitin c-terminal hydrolase L5 (UCHL5). UCHL1 was one of the first DUBs discovered, yet much about its physiological role under normal conditions remains unclear. UCHL1 is expressed predominantly in neuroendocrine tissue and is estimated to comprise 1-2% of total soluble brain proteins.²⁰ Overexpression of UCHL1 in peripheral tissues is observed in a number of cancers including pancreatic cancer, non-small cell lung cancer, and breast cancer among others.^{21–25} Furthermore, there is a strong correlation between the size and invasiveness of tumors and UCHL1

expression levels.^{24,26–28} Taken together, these data underscore the significance of UCHL1 as a therapeutic target.

While small molecule inhibitors for UCHL1 have been discovered,^{29–33} the vast majority of research supporting the roles of UCHL1 in disease state pathogenesis has been performed using genetic manipulation. Until recently there has been only a single UCHL1 inhibitor used in scientific studies. However, this molecule has significant liabilities and has never been shown to directly engage UCHL1 in cells. This highlights the importance of efforts to discover novel, quality small molecule inhibitors to probe the functions of UCHL1 in complex model systems. Herein, I present the roles of UCHL1 in disease state pathogenesis, the existing field of inhibitors, and my contributions to the understanding and development of novel small molecule inhibitors of UCHL1.

1.1 Ubiquitin C-Terminal Hydrolase L1 in Disease States

Ectopic expression of UCHL1 has been implicated in a number of cancers including blood cancers,^{28,34–36} lung cancer,^{37–40}, and others.^{41–43}

1.1.1 Ubiquitin C-Terminal Hydrolase L1 in Oncology

Lymphoma

Lymphoma is perhaps the most well validated UCHL1-associated disease state, with much of the data generated by Dr. Paul Galardy's lab at the Mayo Clinic. UCHL1 expression is observed in patient-derived B-cell lymphoma samples, providing clinical relevance to this target.⁴⁴ Furthermore, patient survival is diminished when UCHL1 expression levels are high, independent of other oncogenes.²⁸ Using a transgenic mouse model that overexpresses UCHL1 ubiquitously, it was confirmed for the first time that UCHL1 acts as an oncogene in *in vivo*. Not only were these mice prone to the development of lymphoma and lung adenoma, the presence of UCHL1 also accelerated the rate of lymphomagenesis.⁴⁵

Elevated levels of UCHL1 has also been observed in myeloma as well. Using UCHL1 positive (KMS11) and negative (KMS12) myeloma cell lines, it was demonstrated that UCHL1 is required for the growth of malignant B-cells. Knockdown of UCHL1 using short-hairpin RNA (shRNA) decreased cell viability specifically in KMS11, but not KMS12, cells. Furthermore, this shRNA induced cell death was rescued by the reincorporation of catalytically active UCHL1, but

not by an inactive C90A mutant, suggesting that the oncogenic role of UCHL1 is dependent on its catalytic activity.³⁴ Knockdown of endogenous UCHL1 in a similar myeloma cell line (KMS28) resulted in reduced AKT phosphorylation, suggesting that UCHL1's role in myeloma may be upstream of AKT.³⁴

As a key regulator of metabolism, proliferation, and survival in cells mTOR complex 2 (C2) is responsible for phosphorylating and fully activating AKT.⁴⁶ Transfecting HeLa cells with UCHL1 decreased the phosphorylation of various proteins downstream of mTORC2, but increased the phosphorylation of AKT, consistent with mTORC1 inhibition and mTORC2 activation. Catalytically inactive UCHL1 was not able to produce the same effects. Immunoprecipitation experiments suggested that UCHL1 was destabilizing mTORC1 by disrupting the damage specific DNA binding protein 1 (DDB1) – Raptor complex that is essential for maintaining the stability of mTORC1. This increased levels of free mTOR, shifting the balance towards mTORC2 without altering overall levels of mTOR. However, this did not explain UCHL1's ability to drive the development of cancer, as mTORC1 is responsible for maintaining levels of protein biosynthesis, a necessity for cell growth.⁴⁶ It was later determined that UCHL1 was able to bypass the need for mTORC1 by directly promoting the assembly of the eIF4F transcription initiation complex, a downstream target of mTORC1 (Figure 1.1), preserving protein biosynthesis and promoting tumorigenesis.⁴⁷

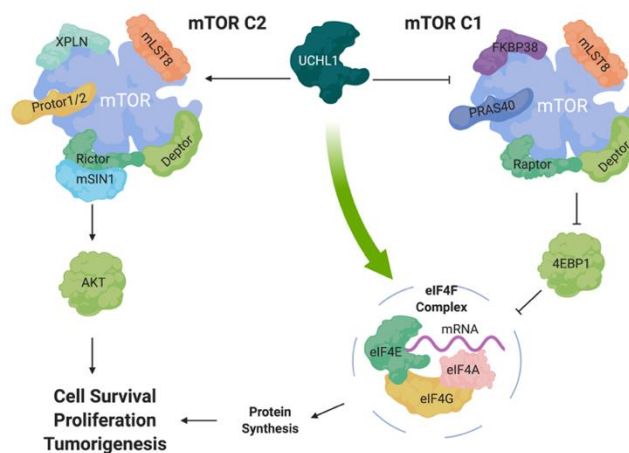


Figure 1.1 Role of UCHL1 in blood cancers. UCHL1 disrupts the mTORC1 complex without altering total levels of mTOR, allowing more mTORC2 to form and increasing cell survival, proliferation, and tumorigenesis. Simultaneously, UCHL1 bypasses the need for mTORC1 by promoting formation of the eIF4F complex which is responsible for protein biosynthesis. Figure adapted from Bedekovics et al. 2019

Lung Cancer

UCHL1 is also implicated as an oncogene in lung cancer. Expression of UCHL1 is observed in small cell (SCLC) and non-small cell lung cancers (NSCLC), where increased levels of UCHL1 corresponds to decreased disease-free survival rates.⁴⁸

Using a number of cell lines with varying invasive capabilities, it was determined that the UCHL1 protein levels had a positive correlation to the invasiveness of cancer cells.³⁸ Additionally, exogenous expression of UCHL1 in cells resulted in an increased invasive behavior compared to non-UCHL1 transfected controls, which was shown to be dependent on both the level of protein expression and the catalytic activity of UCHL1.³⁸ Corroborating these observations, silencing endogenous UCHL1 in a highly invasive cell line reduced metastatic capabilities. Though the mechanistic understanding of UCHL1's role in this cell line was not fully elucidated, increased levels of phosphorylated AKT suggested that UCHL1 may be playing a role in this pathway, consistent with the putative role for UCHL1 in other cancers.³⁸

Another explanation for UCHL1's role in lung cancer lies in the hypoxia-inducible factor 1 (HIF-1) pathway. Exogenous expression of UCHL1 induced HIF-1 activity regardless of oxygen levels, whereas knockdown of endogenous UCHL1 resulted in the opposite effect.²⁴

Under normoxic conditions, HIF-1 α (a component of HIF-1) is ubiquitinated by a von Hippel-Lindau E3 Ub ligase, resulting in proteasomal degradation.⁴⁹ In the presence of UCHL1, the stability of HIF-1 α is increased regardless of oxygen levels, activating HIF-1 and promoting tumor metastasis. Transfecting cancer cells with catalytically inactive UCHL1^{C90S} abrogated UCHL1's ability to stabilize HIF-1 α . Knockdown of endogenous UCHL1 increased levels of ubiquitinated HIF-1 α , whereas overexpression of UCHL1 decreased HIF-1 α ubiquitination, suggesting that HIF-1 α is a substrate of UCHL1. The end result of HIF-1 α stabilization by UCHL1 is an increased propensity for the formation of metastatic colonies in the lungs in a HIF-1 dependent manner, without altering cellular proliferation.⁵⁰

Breast Cancer

High UCHL1 protein expression levels are observed in breast cancer cell lines and are correlated with the recurrence of invasive breast cancer in patients.^{51,52} To determine the function of UCHL1 in triple-negative breast cancer (TNBC), the global activity of DUBs was surveyed in 52

different human breast cancer cell lines and patient tumor tissues using a DUB activity-based probe (ABP).⁵² Both gel fluorescence and liquid-chromatography mass spectroscopy (LC/MS) experiments identified UCHL1 as an activated protein in highly aggressive breast cancer cells.⁵² UCHL1 expression correlated with increased invasiveness, though proliferation was not effected in a zebrafish xenograft model.⁵² Knockdown of UCHL1 in the xenograft model drastically reduced the number of invasive cells. These results were also validated in a mouse model, where UCHL1 promoted invasion and metastasis in breast cancer. In this context, UCHL1 deubiquitinates TGF β receptor 1 (TGFR1) and SMAD2/3, stabilizing these proteins and facilitating TGF β induced migration in TNBC (Figure 1.2).⁵² Of further interest in this study was the observation that UCHL1 was also exported in exosomes, and that these exosomes could promote migration in recipient cells.⁵² Thus, UCHL1 could be considered both a biomarker and therapeutic target in TNBC.

Taken together, these studies suggest that UCHL1 is a target worthy of further pharmacological validation in a number of cancer models and the pursuit of small-molecule inhibitors should be considered a high priority.

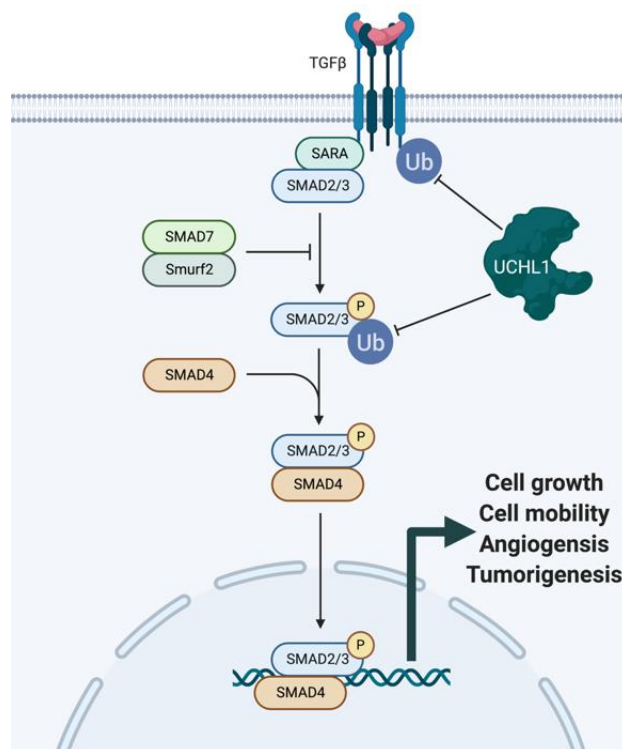


Figure 1.2 Role of UCHL1 in TNBC. UCHL1 deubiquitinates and stabilizes TGF β R1 and SMAD2/3 to promote the expression of target genes that ultimately result in cell growth, cell mobility, angiogenesis, and tumorigenesis.

1.1.2 Ubiquitin C-Terminal Hydrolase L1 in Neurodegenerative Disease

UCHL1 is one of the most abundant soluble proteins in brain tissue and is a major component of the Lewy bodies that are associated with both Parkinson's disease (PD) and Alzheimer's disease (AD).⁵³ Genetic links between UCHL1 and neurodegenerative diseases have been observed, many of which are ascribed to various single-point mutations including S18Y, E7A, R178Q, and I93M (Figure 1.3).^{53–58} The most prominent of these mutations is attributed to the *PARK5* gene. Individuals that harbor this gene suffer from a familial form of PD and carry an I93M (UCHL1^{I93M}) mutation that results in early-onset PD. Compared to wild-type UCHL1, UCHL1^{I93M} displays no discernable structural changes that could be detected by NMR or X-ray crystallography, though the I93M mutant does have a slightly reduced α -helical content as observed by circular dichroism.⁵⁹ This mutation significantly affects the proteins activity, stability, and solubility resulting in aberrant interactions with other proteins.^{54,56} Although the understanding of UCHL1^{I93M}'s contribution to PD pathogenesis is not fully understood, it is believed that it may alter the regulation of the chaperone-mediated autophagy of alpha synuclein aggregates.^{60,61} Whether the effect of UCHL1 on neurodegenerative diseases is due to a loss-of-function or a toxic gain-of-function is not well understood, and research in this field would benefit greatly from the development of high-quality UCHL1 selective probes.

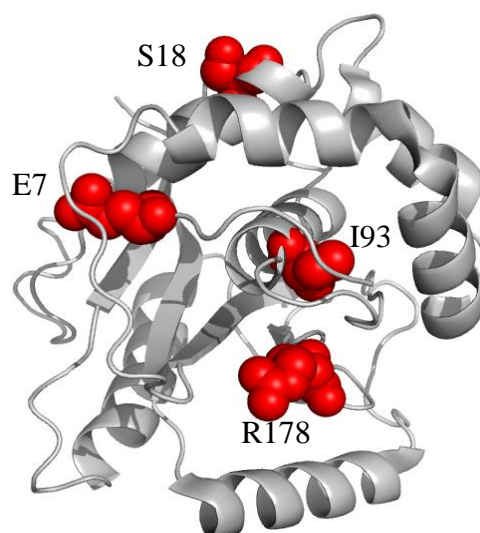


Figure 1.3 Single point mutations of UCHL1 associated with neurodegenerative diseases. UCHL1 (gray) with amino acids (red spheres) that are often mutated in neurodegenerative diseases.

1.1.3 Ubiquitin C-Terminal Hydrolases in other Disease States

In addition to cancer and neurodegeneration, UCHL1 plays a role in a variety of other disease states including diabetes,^{62–64} traumatic brain injury,^{65,66} and fibrosis among others.^{67–69} While the pathological role of UCHL1 is less understood in these illnesses, studies are being published rapidly, denoting the importance of this protein in diseases other than cancer and neurodegeneration.

Diabetes

Genetic analysis of non-diabetic and type 2 diabetic (T2D) islets by microarray, with a focus on the components of the ubiquitin-proteasome system (UPS), revealed over one-thousand genes that differed in expression level.⁶³ Quantitative reverse-transcriptase polymerase chain-reaction (qRT-PCR) showed that a number of genes associated with the UPS were down-regulated specifically in T2D islets over non-diabetic islets, including various DUBs and the proteasome.⁶³ Among the DUBs with reduced levels of expression was UCHL1, particularly in β -cells. Reduction in UCHL1 levels is accompanied by an increase in poly-ubiquitinated proteins⁶³, resulting in high levels of amyloid formation and increased cell toxicity.⁶⁴ Reduced expression of UCHL1 in amyloid expressing β -cells accelerates the onset of diabetes, resulting in decreased β -cell viability by inducing endoplasmic reticulum stress, culminating in apoptosis.⁶²

Brain Injury

UCHL1 has been identified as a protein whose levels are increased in both brain tissue and cerebrospinal fluid (CSF) shortly after traumatic brain injury (TBI).⁶⁵ Patients suffering from aneurismal subarachnoid hemorrhage displayed increased amounts of UCHL1 in the CSF two weeks after suffering from an aneurism, even after other biomarkers were reduced to normal levels. Individuals with particularly high UCHL1 levels had poorer outcomes than others.⁷⁰ Taken together, these data suggest that UCHL1 should be considered as a biomarker for TBI and that UCHL1 expression levels correspond to the severity of TBI.⁶⁶

Fibrosis

UCHL1 had previously been observed in fibrotic tissue of the heart, lungs, liver, and lung, but little was known about the role that it plays in fibrosis.^{69,71} Increased UCHL1 is observed in

fibrotic tissue compared to non-fibrotic tissue,⁶⁹ and knockdown of UCHL1 in hepatic stellate cells resulted in reduced proliferation in response to proliferation-inducing cytokines, suggesting that UCHL1 may represent a therapeutic target for fibrotic diseases.⁶⁸ Indeed, pharmacological inhibition of UCHL1 has been shown to be effective in cellular models for both lung and liver fibrosis through mechanisms associated with the transforming growth factor (TGF) pathway.^{67,72} This conforms to previous observations in breast cancer models where UCHL1 protects TGF- β type 1 receptor and the downstream target SMAD2 from ubiquitination in lung cancer, providing a potential mechanistic rationale behind the therapeutic value of UCHL1 inhibitors in fibrotic diseases.⁵²

1.2 Structure and Function of Ubiquitin C-Terminal Hydrolase L1

The structure of UCHL1 was determined via X-ray crystallography by Das *et al* in 2006.⁷³ Using the homologous protein UCHL3, molecular replacement was performed yielding a successful model. After refinement, R_{work} and R_{free} scores of 22.2% and 27.5% respectively suggested a quality structure had been solved to a resolution of 2.4 Å. The protein was completely solved excluding the N-terminal GST-tag residues left after proteolytic cleavage during protein expression. Although the crystal structure was deposited as a dimer, there was no evidence that this dimer was biologically relevant. Of particular interest from this structure was the observation that UCHL1's catalytic triad (cysteine 90, histidine 161, and aspartate 176) of the apo-form, non-ubiquitin bound, was not in a productive orientation, with histidine 161 positioned 8.2 Å away from the catalytic cysteine (Figure 1.4). At this distance, histidine is not capable of deprotonating the active site cysteine, which may explain the low *in vitro* activity compared to its homolog UCHL3.⁷⁴

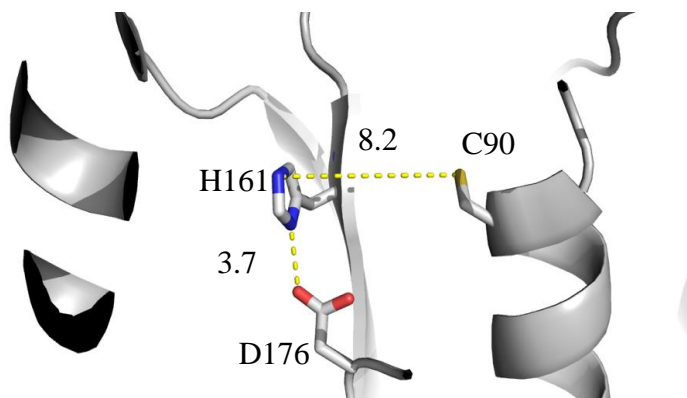


Figure 1.4 The misaligned active site of UCHL1. In its apo form (PDB ID 2ETL), aspartate 176 stabilizes histidine 161 8.2 Å away from catalytic cysteine 90, resulting in an unproductive conformation.

A future study shed light onto the nature of UCHL1's activity through the crystal structures of UCHL1^{WT}, UCHL1^{I93M}, and UCHL1^{S18Y} bound to Ub vinyl methyl ester (Ub-VME),⁷⁵ an ABP of Ub, where the C-terminal glycine is replaced by a glycine vinyl methyl ester (VME). This places a Michael acceptor at the scissile bond of Ub, resulting in the formation of a thioester between the β -carbon of the Michael acceptor and the sulfur of the active site cysteine of UCHL1.

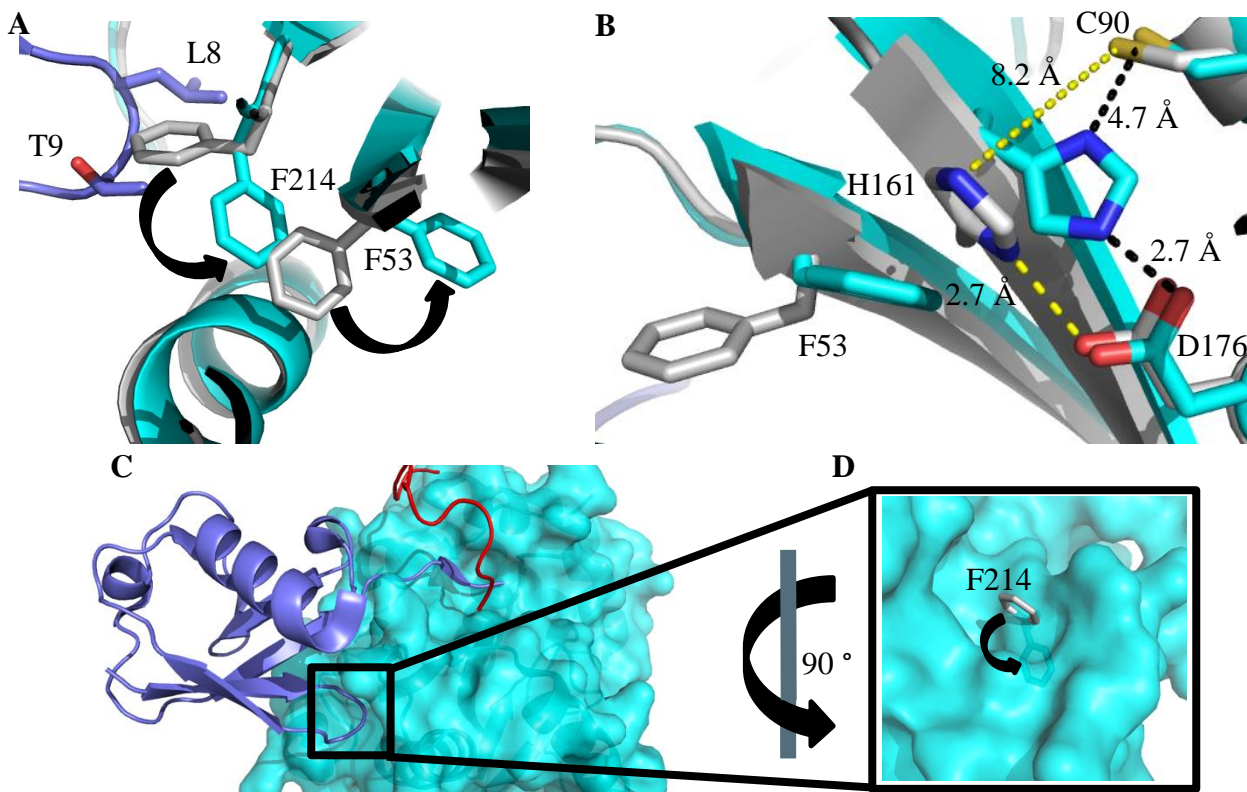


Figure 1.5 The binding of ubiquitin brings the active site of UCHL1 into a productive conformation. **A)** Conformational changes of two side chains of UCHL1 induced by the binding of ubiquitin. Overlay of apo-UCHL1 (PDB ID 2ETL) (gray) and ubiquitin bound UCHL1 (PDB ID 3KW5) (cyan) showing the conformational crosstalk of F214 and F53 induced by L8 and T9 of ubiquitin (slate). **B)** Superposition of apo UCHL1 (gray) and ubiquitin bound UCHL1 (cyan) showing the active site alignment of UCHL1 in the presence of ubiquitin. **C)** The ubiquitin-UCHL1 interface that induces conformational change occurs distally from the active site (crossover loop shown as red cartoon for clarity). **D)** Apo-UCHL1 F214 (gray) swivels towards the interior of UCHL1 when bound to ubiquitin (cyan).

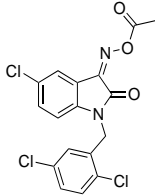
In contrast to the apo structure, the active site of the Ub-bound crystal structure is in an active conformation. A conformational crosstalk beginning with the Ub L8-T9 and the UCHL1 F214 interface causes F214 to rotate towards the interior of UCHL1, ultimately moving 7.1 Å, causing the nearby F53 ring to pivot 7.8 Å from its original position in the apo structure (Figure 1.5A). This

further propagates movement of H161, part of the catalytic triad, bringing it into a productive conformation with the basic amino acid within 4 Å of C90 (Figure 1.5B). Furthermore, the observation that the F214-F53-H161 crosstalk is relevant was corroborated by a biochemical activity assay using a UCHL1^{F214A} mutant. This single mutation, which is distal from the active site (Figure 1.5C and 1.5D), abrogates UCHL1's enzymatic activity in a ubiquitin aminomethyl coumarin (Ub-AMC) hydrolysis assay. The Ub-dependent activation of UCHL1 is unique within the UCH sub-family of DUBs. The catalytic triad of the closely related UCHL3, for example, is properly aligned in the apo-state and results in an increased catalytic activity.^{74,76}

1.3 Efforts Towards the Development of Ubiquitin C-Terminal Hydrolase L1 Inhibitors

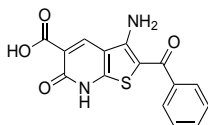
Though UCHL1 has been the topic of many scientific studies in an assortment of therapeutic contexts, it wasn't until fifteen years after its discovery that a UCHL1 specific inhibitor was developed.²⁹ A fluorescence intensity high-throughput screen using the fluorogenic Ub-AMC substrate identified a series of isatins with single digit micromolar activity against UCHL1. Optimization led to the development of LDN-57444 (Figure 1.6), an inhibitor with IC₅₀ and K_i values of 0.88 µM and 0.40 µM respectively and 28-fold selectivity for UCHL1 over UCHL3. Further characterization led the authors to conclude that this inhibitor is a competitive inhibitor and binds to the active site of UCHL1.

LDN-57444

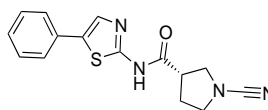


Second-generation cyanopyrrolidine inhibitor

LDN-91946



First-generation cyanopyrrolidine inhibitor



VAEFMK

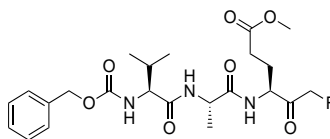
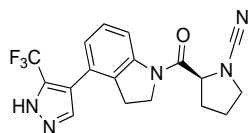


Figure 1.6 Small molecule inhibitors of UCHL1.

Additional studies using this molecule have cast doubt upon its reliability. In our hands, as well as the hands of other researchers, LDN-57444 has proven to be an ineffective inhibitor of

UCHL1.⁷² Not only is LDN-75444 unable to engage and inhibit UCHL1 in a variety of biochemical assays,⁷² it also degrades in cell treatment conditions within 30 minutes of addition to cell culture media (data not shown). Taken together, it is apparent that this inhibitor is not suitable to probe the role of UCHL1 in disease states. Despite this, publications continue to be released using this molecule to pharmacologically probe UCHL1's role in a number of diseases.^{67,77,78} Any experimental results determined using this molecule should undergo rigorous validation using a more appropriate UCHL1 probe.

Identified from the same high-throughput screen, LDN-91946 (Figure 1.6) was published four years later.³⁰ With a K_i of 2.8 μM and only 7-fold selectivity for UCHL1, LDN-91946 is not as effective of an inhibitor as LDN-57444. However, it is still of interest as kinetic characterization suggested a novel class of inhibition. Determining V_{max} and K_m values at various fixed concentrations of LDN-91946 suggested that these values were not affected by the concentration of the inhibitor. As hydrolases undergo an initial binding step with their substrates (formation of the Michaelis complex), followed by the formation of a covalent thioester bond (acyl-enzyme) before releasing product, it was necessary to determine which enzyme state the LDN-91946 bound to and inhibited. Transient steady state kinetic experiments with LDN-91946 showed that the acyl-enzyme did not accumulate when steady state kinetics were reached and that the formation of the acyl-enzyme was the rate-limiting step. This suggests that LDN-91946 binds not to the acyl-enzyme but rather the Michaelis complex, a novel mode of inhibition for UCHL1.

The development of reversible inhibitors has proven to be a successful strategy other DUBs such as USP7, which binds Ub weakly ($\text{Ub } K_d = 200 \mu\text{M}$).^{79,80} In stark contrast, the binding constant for the Ub-UCHL1 complex is among the tightest of all DUBs ($\text{Ub } K_d = 140 \text{ nM}$),⁸¹ requiring a very high-affinity small molecule to out-compete Ub and effectively inhibit UCHL1. Thus, an attractive alternative for UCHL1 inhibitor development is the covalent modification of UCHL1's active site cysteine.

Five years after the discovery of LDN-91946, and nine years after LDN-57444, the first co-crystal structure of UCHL1 with an inhibitor was published, exemplifying covalent modification of UCHL1's active site cysteine.³³ The tripeptide inhibitor Z-VAE(OMe)-fluoromethyl ketone (VAEFMK) (Figures 1.6 and 1.7) was initially discovered as a UCHL1 inhibitor during a counter screen for hits against herpes simplex viral protease UL36. In both cell lysate and intact cells, VAEFMK was able to inhibit UCHL1 at 100 μ M with no effect on UCHL3 or UCHL5. A possible rationale for the selectivity of this inhibitor was elucidated through the crystal structure where it was revealed that VAEFMK covalently bound to the active site cysteine and approached the active site from the opposite side of the crossover loop as the Ub-binding site (Figure 1.7). The selectivity towards UCHL1, absence of non-specific cysteine modification, and presence of ligand-bound structural data combine to make VAEFMK an attractive starting point for optimization, though further research is necessary to determine the utility of this molecule.

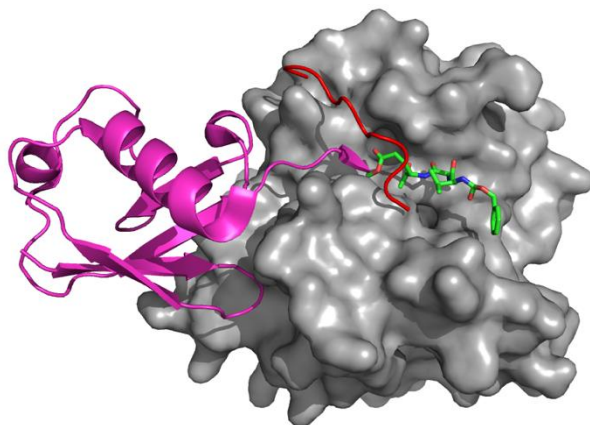


Figure 1.7 Binding of VAEFMK to UCHL1. VAEFMK (green) binds to UCHL1 (gray) on the opposite side of the active site as Ub (magenta). The UCHL1 cross-over loop (red) is shown as a cartoon for clarity.

A final class of covalent cyanopyrrolidine-based UCHL1 inhibitors were recently reported.^{52,72,82,83} These molecules were originally described in a series of patents by Mission Therapeutics,^{31,32} but lacked any quantifiable inhibition data in biochemical and cellular assays. Due to this lack of characterization, representative molecules from the first- and second-generation patents (Figure 1.6) were synthesized and characterized by our lab⁸² and others,^{52,72} and the resulting data revealed that the molecules were potent and selective inhibitors of UCHL1. The full

biochemical, kinetic and cellular results from our studies will be presented in a later chapter. While the exact molecule synthesized by our lab displayed off-target interactions and non-specific toxicity towards UCHL1 non-expressing cells (Figure 1.6 – Second-generation cyanopyrrolidine inhibitor), analogs tested by other groups appear to be more selective for UCHL1, suggesting increased potential as a probe.⁷² However, no cell toxicity assays were performed to determine off-target toxicity. Regardless, groups using these inhibitors did observe efficacy in animal models for various UCHL1-dependent disease states including fibrosis and breast cancer.^{52,72} While this represents the biggest step forward towards pharmacological inhibition of UCHL1 since the publication of LDN-57444, much work remains to optimize the selectivity and tune the reactivity of these probes in order to reduce off-target toxicity.

1.4 Project Summary

A growing body of literature points to UCHL1 as a potential therapeutic or diagnostic target for a number of disease states, yet little has been done to advance our understanding of both UCHL1 inhibitor design and the pool of available small molecule probes. My project focuses on elucidating mechanisms of inhibition for existing UCHL1 inhibitors, as well as the design and characterization of novel small molecule and macromolecular UCHL1 inhibitors.

Chapter 2 will focus on the characterization and utility of a novel cyanopyrrolidine scaffold of UCHL1 inhibitors introduced above. This inhibitor is characterized using a combination of biochemical assays and experiments and introduces the utility of covalent inhibitors as activity-based probes using bioconjugation. Chapter 3 will characterize the selectivity and utility of a previously published covalent inhibitor of UCHL1, VAEFMK, as well as structure-activity relationship studies. Chapter 4 explores the dynamics and mechanism of action for a new set of macromolecular Ub-based inhibitors supported by biochemical and molecular dynamics simulations. Chapter 5 will introduce future directions for the identification and development of novel covalent UCHL1 inhibitors.

Taken together, these chapters describe in detail the design of new covalent inhibitors as well as the biochemistry and kinetics of UCHL1 inhibition with various electrophilic warheads. The results will be relevant for optimization and design of future UCHL1 covalent inhibitors and improve their potential as selective probes that should replace LDN-57444 and be used to elucidate UCHL1's

role in disease state pathogenesis. Finally, these studies will confirm the validity of covalent inhibition as the leading approach to target UCHL1.

CHAPTER 2. BIOCHEMICAL AND CELLULAR CHARACTERIZATION OF A COVALENT CYANOPYRROLIDINE-BASED UCHL1 INHIBITOR

The following chapter is reproduced and modified with permission from Aaron D. Krabill, Hao Chen, Chad Hewitt, Sajjad Hussain, Chao Feng, Ammara Abdullah, Chittaranjan Das, Uma K. Aryal, Carol Beth Post, Michael K. Wendt, Paul J. Galaray, and Daniel P. Flaherty. *ChemBioChem* **2020**, *21*, 712 – 722. © Wiley-VCH Verlag GmbH & Co. KGaA, Weinheim.

The deubiquitinase (DUB) Ubiquitin C-terminal Hydrolase L1 (UCHL1) is expressed primarily in the central nervous system under normal physiological conditions. However, UCHL1 is overexpressed in various aggressive forms of cancer with strong evidence supporting UCHL1 as an oncogene in lung, glioma, and blood cancers. In particular, the level of UCHL1 expression in these cancers correlates with increased invasiveness and metastatic behavior, as well as poor patient prognosis. Although UCHL1 is considered an oncogene with potential as a therapeutic target, there remains a significant lack of useful small-molecule probes to pharmacologically validate in vivo targeting of the enzyme. Herein, we describe the characterization of a new covalent cyanopyrrolidine-based UCHL1 inhibitory scaffold in biochemical and cellular studies to better understand the utility of this inhibitor in elucidating the role of UCHL1 in cancer biology.

2.1 Introduction

The addition of ubiquitin (Ub) to proteins is a post-translational modification important for regulating many aspects of eukaryotic biology.⁷ Ubiquitin is added to Lys residues of target proteins through a covalent bond between the ϵ -amino group of the Lys residue and the last carboxylate group of the terminal Gly76 of Ub through an isopeptide bond. This covalent addition is catalyzed by the sequential action of three enzymes known as the E1 Ub activating enzyme,² E2 Ub conjugating enzyme,³ and E3 Ub ligases in an ATP-driven process.⁴ This usually results in attachment of several Ub groups as a polyubiquitin-chain modification of the target proteins; wherein, successive Ub groups are added to the first Ub via one of seven Lys residues on Ub or its Met1 group in isopeptide (or peptide) links that connect Ub monomers in the polyubiquitin chain. Eight distinct types of polyubiquitin chains resulting from linkage through each distinct amino group of Ub, along with branched architectures, can result in complex biological signals that form the basis

of the Ub signaling system in eukaryotes.^{5,6} Ub can be released from proteins (and other Ub groups in polyubiquitin chains) through hydrolysis by means of one of several enzymes that are collectively known as deubiquitinases (DUBs).⁸ Humans have close to 100 DUBs, most of which are cysteine proteases, with one separate enzymatic class being the so-called JAMM proteases, which require Zn dependent catalysis.¹² The cysteine protease DUBs are grouped into six types: the Ubiquitin Specific Proteases (USP), Ubiquitin C-terminal Hydrolase (UCH), Machado-Josephin Domain, Ovarian Tumor Proteases, and the more recently discovered Mindy and ZUFSP groups.^{10,12,84,85} Regulation of the ubiquitination and deubiquitination processes has implications on various disease states including neurodegenerative diseases and cancer.^{13,21,23,29,42,86–91} Many cellular processes are subject to precise regulation through a balance of ubiquitination and its removal by DUBs; accordingly, DUBs have emerged as key players in cellular homeostasis and, when deregulated have impact on various disease states. Thus, DUBs are novel targets for therapeutic intervention in cancer, autoimmune, and neurodegenerative diseases.¹³

The DUB known as Ubiquitin C-terminal Hydrolase L1 (UCHL1), is a 25 kDa protein that is expressed almost exclusively in the central and peripheral nervous system under normal physiological conditions.²⁰ While UCHL1 has been studied for nearly 20 years, its biological role under normal and pathophysiological conditions has yet to be elucidated. As one of the most abundant soluble proteins in the brain, it has been linked to the progression of Alzheimer's and Parkinson's disease.^{59,87,92–96} There is also strong evidence supporting UCHL1 as an oncogene in various cancers including glioblastoma, small-cell lung cancer, and blood cancers, among others.^{97–99} In particular, increased UCHL1 levels in these cancers correlates with increased invasiveness and metastatic behavior as well as poor patient prognosis.^{24,26,27,100} In many cases reducing UCHL1 activity either by performing genetic depletion experiments or expression of catalytically inactive mutants results in a significant reduction in the metastatic behavior of certain cancer cell lines.^{24,38,51}

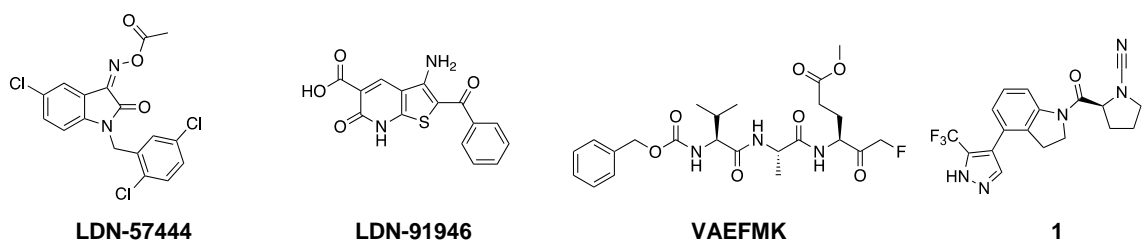


Figure 2.1 Reported UCHL1 inhibitors.

Although UCHL1 is considered an oncogene with potential as a therapeutic target, there is a significant lack of small-molecule inhibitor development in the field. LDN-57444²⁹ and LDN-91946³⁰ (Figure 2.1) were identified in the early 2000's. LDN-57444, the more potent of the two (IC₅₀ value of $0.88 \pm 0.14 \mu\text{M}$), serves as the de facto chemical probe for UCHL1 (Figure 1). However, this molecule has liabilities including off-target toxicity and chemical instability.¹⁰⁰ A peptide-based covalent inhibitor VAEFMK (Figure 2.1) has been identified and characterized structurally with UCHL1, though no cellular or inhibitory data have been reported.³³ Recently, a new series of cyanopyrrolidine-based inhibitors have been identified in patent literature (Figure 1, compound **1**),^{31,101} however, there was little inhibitory information and no on-target cellular validation has been reported. Given the relative paucity of UCHL1 inhibitors in the literature, we set out to characterize this new class of inhibitor in biochemical and cellular assays, as well as determine its mechanism of action. Successfully determining the mechanism of action and validating on-target cellular activity could provide new insights into future UCHL1 inhibitor design.

Cyanopyrrolidines have been previously utilized as cysteine reactive electrophilic warheads to target cathepsins^{102,103} where the active site cysteine undergoes nucleophilic attack on the electrophilic center at the carbon of the nitrile moiety. Given that UCHL1 is also a cysteine protease, we hypothesized that this molecule may be acting via covalent modification of the active site cysteine (Figure 2.2). We selected a potent analog from the patent report to carry out the characterization. The results of these studies and cellular on-target validation as well as toxicity assays are presented herein.

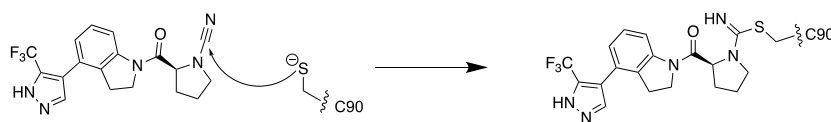
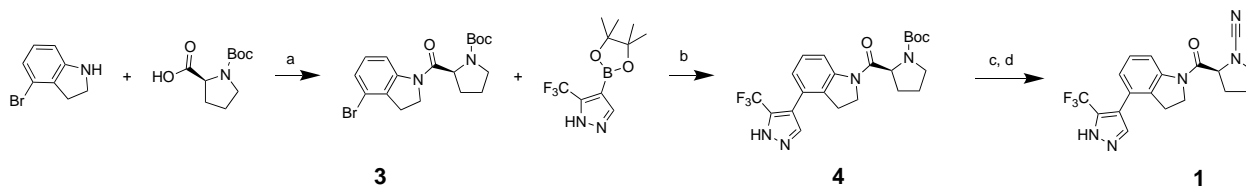


Figure 2.2 Proposed mechanism for inhibition of UCHL1 by **1**.

2.2 Results and Discussion

2.2.1 Chemistry

Compound **1** was synthesized according to a modified procedure from the original report (Scheme 2.1).¹⁰¹ In brief, Boc-L-proline was reacted with 4-bromoindoline via amide bond coupling using HATU to form intermediate **3**. Intermediate **3** was converted to **4** using a microwave assisted Suzuki-Miyaura reaction. This was followed by Boc-deprotection and subsequent cyanamide formation using cyanogen bromide to provide the final compound **1**.



Scheme 2.1 Preparation of **1**. Reagents and Conditions: a) HBTU (1.25 eq), DIPEA (1.5 eq), THF, 25 °C, 16 hr; b) NaCO₃H (2 eq), Pd(dppf)Cl₂ (0.1 eq), 9:1 DMF:H₂O, 110 °C, 1.5 hr; c) TFA (20 eq), DCM, 25 °C, 2 hr; d) K₂CO₃ (2.2 eq), BrCN (1.0 eq), THF, 0 °C, 30 minutes.

2.2.2 Biochemical Characterization of Cyanopyrrolidine Inhibition

The *in vitro* inhibition of UCHL1, and the closely related UCHL3, by **1** was determined by monitoring cleavage of rhodamine110 from ubiquitin substrate (Ub-Rho).¹⁰⁴ Both UCHL1 and UCHL3 were pre-incubated with compound **1** for 30 minutes before the addition of Ub-Rho. Compound **1** inhibited both UCHL1 (Figure 2.3A, black line) and UCHL3 (Figure 2.3A, red line) with IC₅₀ ± standard error values of 0.67 ± 1.0 μM and 6.4 ± 1.1 μM, respectively when pre-incubated for 30 minutes. While this represents a slight improvement in potency compared to the current best-in-class UCHL1 inhibitor (Figure 2.1, LDN-57444, IC₅₀ value of 0.88 ± 0.14 μM), it also has decreased selectivity for UCHL1 over UCHL3 compared to LDN-57444.

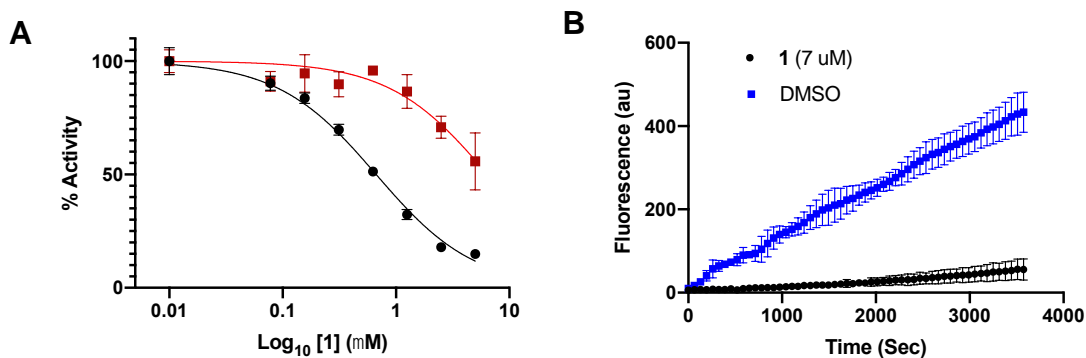


Figure 2.3 Biochemical inhibition of UCHL1 by **1**. A) IC₅₀ curves for compound **1** against UCHL1 (black) and UCHL3 (red) after 30 minutes of preincubation. B) Progress curves for UCHL1 treated with DMSO (blue) or compound **1** (black) following dilution into substrate.

Nitrile electrophiles are common warheads for other proteases, forming an isothioureia as the result of the nucleophilic attack by the cysteine (Figure 2.2).¹⁰² The reactive free energies of various nitriles have been calculated computationally, and the reaction energy of a cyanamide such as in molecule **1** is higher than a typical nitrile, though such an electrophile is known to be reversible.¹⁰⁵ To confirm that compound **1** is indeed a covalent modifier of UCHL1 and assess the rate of reversibility, we performed a jump-dilution experiment¹⁰⁶ in which UCHL1 was pre-incubated with **1** at 7 μ M, approximately 10-fold the IC₅₀ value, for 30 minutes. The enzyme-inhibitor complex was then rapidly diluted 100-fold into a solution containing Ub-Rho. Upon dilution into a substrate-containing solution, enzymes treated with non-covalent or quickly reversible covalent inhibitors are expected to regain activity and display progress curves similar to DMSO treated controls. Very slowly reversible or irreversible covalent inhibitors will not regain activity and their progress curves are expected to look similar to fully inhibited enzyme in a non-jump-dilution experiment. The resulting progress curve for compound **1** matched that of a very slowly reversible or irreversible inhibitor (Figure 2.3B).¹⁰⁷ Additionally, His-tagged UCHL1 Wild-type (WT) and catalytically inactive mutant His-UCHL1^{C90A} were incubated with either compound **1** or DMSO for 30 minutes and subjected to analysis by electrospray ionization-mass spectrometry. Detected mass-to-charge ratios were deconvoluted using the analysis software (DataExpress version 6.0.11.3, Advion). The sample of His-UCHL1^{WT} treated with compound **1** displayed an average mass shift of molecular weight approximately 372, which corresponds to the addition of one molecule of **1** (molecular weight 375 g/mol), while the DMSO treated sample of His-UCHL1^{WT} matched the mass of apo

UCHL1. His-UCHL1^{C90A} did not display a change in mass corresponding to the addition of **1** (Table 2.1).

Table 2.1 Compound **1** covalently modifies UCHL1. A) His-UCHL1^{WT} treated with DMSO, average deconvoluted mass \pm S.D. shown below table; B) His-UCHL1^{WT} treated with compound **1** average deconvoluted mass \pm S.D. shown below table. C) His-UCHL1^{C90A} treated with DMSO, average deconvoluted mass \pm S.D. shown below table; D) His-UCHL1^{C90A} treated with compound **1** average deconvoluted mass \pm S.D. shown below table. E) Molecular weight of compound **1** and detected mass shift from difference in samples treated with **1** and DMSO control.

His-UCHL1 ^{WT} + DMSO			His-UCHL1 ^{WT} + Compound 1		
m/z	Charge	Predicted Mass	m/z	Charge	Predicted Mass
1034	26	26859.2	1009.8	27	27237.6
1075.3	25	26858.4	1048.5	26	27236.2
1120.9	24	26878.8	1090.8	25	27245.2
1171.2	23	26915.3	1136.1	24	27243
1222.4	22	26869.9	1137.7	24	27281.6
Average Mass = 26,873.4 \pm 17.2			Average Mass = 27,245.1 \pm 12.7		
His-UCHL1 ^{C90A} + DMSO			His-UCHL1 ^{C90A} + Compound 1		
m/z	Charge	Predicted Mass	m/z	Charge	Predicted Mass
928.7	29	26902.7	1073.9	25	26822
994.7	27	26830.5	1118.6	24	26822.6
1037.5	26	26948.7	1119.2	24	26835.9
1075.6	25	26864.3	1168.2	23	26845.2
1124.3	24	26958.6	1228.9	22	27012.8
1167.5	23	26829.1	1284.3	21	26949.7
1169	23	26865	Average Mass = 26,881.2 \pm 76.6		
1220.4	22	26827.2			
1278.8	21	26833.2			
1343.1	20	26842.6			
Average Mass = 26,874.5 \pm 48.1					
Compound 1 MW		Change in Detected Mass (His-UCHL1 ^{WT})	Change in Detected Mass (His-UCHL1 ^{C90A})		
375.13		371.7	6.7		

The rate of reversibility was then determined by observing the change in enzymatic activity over time when preincubated with **1**. Compound **1** was most potent within 30 minutes, with a steady decrease in potency as time progressed out to 24 hours (Figure 2.4). Irreversible inhibitors display a steady increase in potency until all of the molecule has formed a covalent bond with the target protein and should result in a linear change in IC_{50} .¹⁰⁸ The slow recovery of enzymatic activity over time confirmed the very slow reversibility of the inhibitor, likely into a non-reactive product.

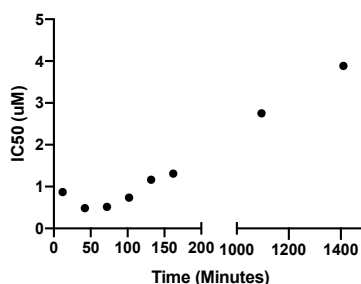


Figure 2.4 Compound **1** is a slowly reversible inhibitor. UCHL1 incubated with **1** regains activity over time.

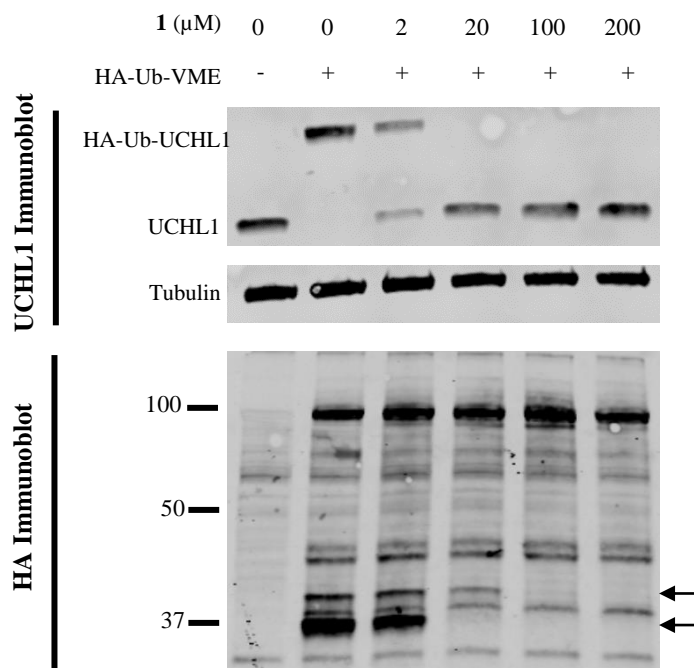


Figure 2.5 Engagement of UCHL1 in cell lysate by **1**. HEK293T cell lysate was incubated with **1** for 10 minutes at room temperature before addition of HA-Ub-VME. This was incubated for 10 additional minutes then quenched by the addition of 4x Laemlli buffer and heated at 90 °C for 5 minutes. UCHL1 immunoblot shows a reduction of HA-Ub-UCHL1 formation with increased concentration of **1**. HA immunoblot shows two bands decrease as the concentration of **1** is increased, denoted by black arrows.

To confirm that the molecule engages UCHL1 in lysates a ubiquitin activity-based probe gel shift assay was employed.¹⁰⁹ Using hemagglutinin-tagged Ub-vinylmethylester (HA-Ub-VME) compound **1** activity in HEK293T cell lysate was assessed. Blotting for UCHL1 showed the expected molecular weight shift of the newly formed HA-Ub-UCHL1 adduct (Figure 2.5, top panel) compared to UCHL1 alone. Compound **1** inhibited UCHL1 activity in these lysates in a dose-dependent manner as evidenced by the decreased intensity of the band corresponding to HA-Ub-UCHL1 with increasing dose of molecule. Subsequently blotting for the HA-tag showed compound **1** exhibited dose-dependent inhibition of another DUB in these lysates along with UCHL1. The identity of this off-target DUB remains to be determined (Figure 2.5, bottom panel).

2.2.3 Structural Characterization and Molecular Modelling of Cyanopyrrolidine Inhibition

While multiple crystal structures of UCHL1 have been deposited into the Protein Data Bank (PDB), only one is bound to a small-molecule inhibitor (PDB ID 4DM9). To better understand the ligand binding mode with UCHL1 for this new class of inhibitor we turned to high-resolution nuclear magnetic resonance (NMR) experiments. ¹⁵N-heteronuclear single quantum coherence (HSQC) chemical shift assignments known for the unligated UCHL1 were kindly provided by Shang-Te Hsu (National Taiwan University – Taipei), and side chain ¹³C and ¹H resonance assignments were from the Biological Magnetic Resonance bank (BMRB) (ID 17260).

Information about the site of interaction between **1** and UCHL1 was obtained from ligand-induced changes in the ¹⁵N-HSQC spectrum of UCHL1. Upon addition of **1**, a number of peaks shifted in frequency (Figure 2.6). The difference in chemical shift in the absence and presence of **1** was quantified for well-resolved resonances, and the residues with the changes in chemical shift >0.15 ppm were mapped to the structure in Figure 2.7A (blue). Most of the mapped residues are localized to a region near the cross-over loop (residues 149-160) and Cys 90, which indicates **1** binds near the active site pocket.

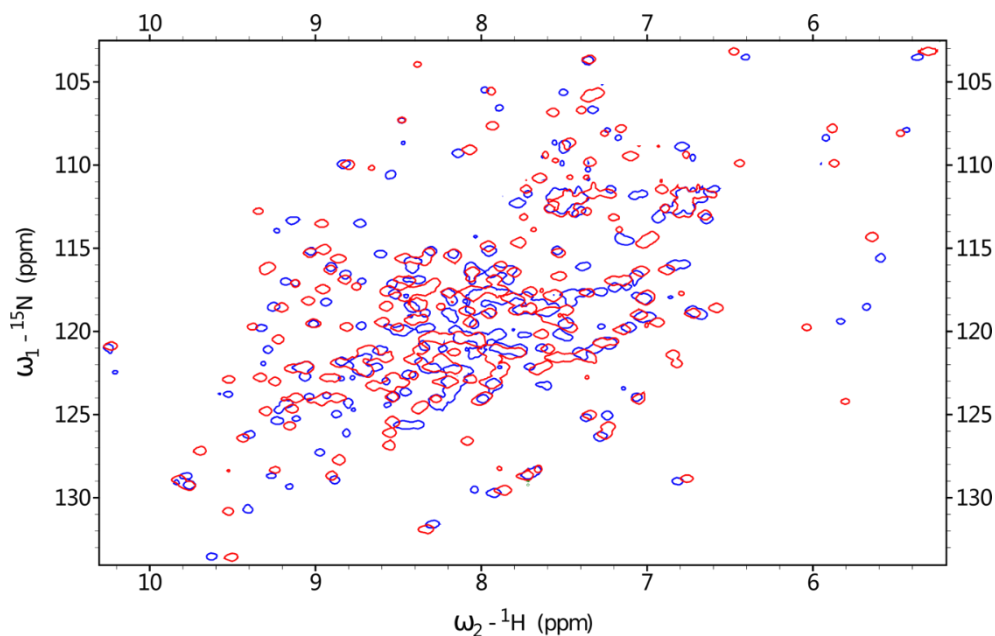


Figure 2.6 NMR spectra of UCHL1 with **1**. The overlaid ^{15}N -HSQC spectra for unligated (red) and UCHL1 bound (blue) with **1**.

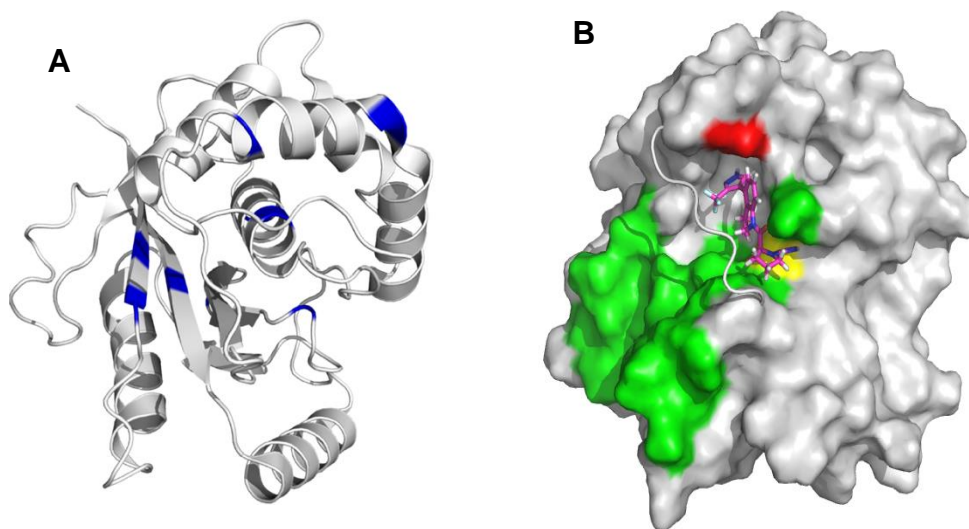


Figure 2.7 Binding site of **1**. **A**) Chemical shift changes ($\sqrt{((\Delta\delta_{\text{HN}})^2 + (0.154\Delta\delta_{\text{N}})^2)/2}$) greater than 0.15 ppm are mapped to the structure of UCHL1 (PDB ID: 2ETL). The difference in ^{15}N -HSQC chemical shifts between unligated UCHL1 and after addition of **1** were measured at a molar ratio [1:1]. The orientation of UCHL1 is approximately the same as Figure 7B. **B**) Predicted binding pose of compound **1** (magenta sticks) with UCHL1 (grey), supported by 3D NOE NMR experiments. The crossover loop of UCHL1 is shown as a cartoon for clarity. Compound **1** binds to UCHL1 on the same side of the crossover loop as the ubiquitin binding interface of UCHL1 (green surface). Compound **1** forms a covalent bond with cysteine 90 (yellow surface) and has an experimentally determined NOE with alanine 147 (red surface).

Intermolecular Nuclear Overhauser Effects (NOE's) were measured^{110–113} with ¹⁵N-¹³C labeled UCHL1 to further define the interaction with **1**. A number of isotope-filtered NOE crosspeaks were observed between ligand protons and protein protons bonded to ¹³C-labeled carbons. The intermolecular distance information from the NOE crosspeaks was used in an interactive, self-consistent approach involving potential crosspeak assignments and computationally modeling the complex with NOE-distance restraints.

For the modeling studies we used the crystal structure of UCHL1 (PDB ID 2ETL)⁷³ and prepared the protein coordinates for computational studies using Maestro (Schrödinger, LLC). Using CovDock (Schrödinger, LLC) a docking site was defined around the active site of UCHL1 as indicated by the chemical shift changes (Figure 2.7A), a NOE constraint of 1 to 6 angstroms was set as a requirement between aromatic indoline proton 3 of the ligand and C^βH₃ side chain of Ala147 (Figure 2.7B, red surface and Figure 2.8), and Cys90 (Figure 2.7B, yellow surface and Figure 2.8) was set as the nucleophilic residue.

In the crystal structure, the first nine *N*-terminal residues (Met1 – Asn9) lie below the cross-over loop in a groove between the two amino acids used as constraints, Ala147 and Cys90. Given the experimental NOE observed between the ligand and Ala147 and the inherent flexibility of terminal residues, it was hypothesized that the *N*-terminal portion of UCHL1 may adopt an alternative position upon ligand binding. To account for this possibility, docking was performed both with the full-length crystallographic structure and with the *N*-terminal residues removed. The pose accepted from iterative docking with Cys90 as the nucleophilic residue and iterative NOE-derived distance restraints is shown in Figure 2.7 and Figure 2.8. This pose predicts the molecule threads into a cavity under the cross-over loop of UCHL1 and that the isothioureia resulting from the nucleophilic attack of Cys90 on the cyanamide carbon of **1** interacts with the putative oxyanion hole stabilizing residues Gln84 and Asn88,⁷³ consistent with previous observations between other cyanamide inhibitors and their corresponding cysteine protease targets.¹⁰² The inhibitor is also stabilized by an interaction between the amide carbonyl of **1** and the sidechain of Asn88. While further studies are necessary to validate this binding pose it is consistent with an experimentally observed intermolecular NOE assignment to Ala147 H^β and ligand H3, and the cyanamide electrophile reacting with Cys90.

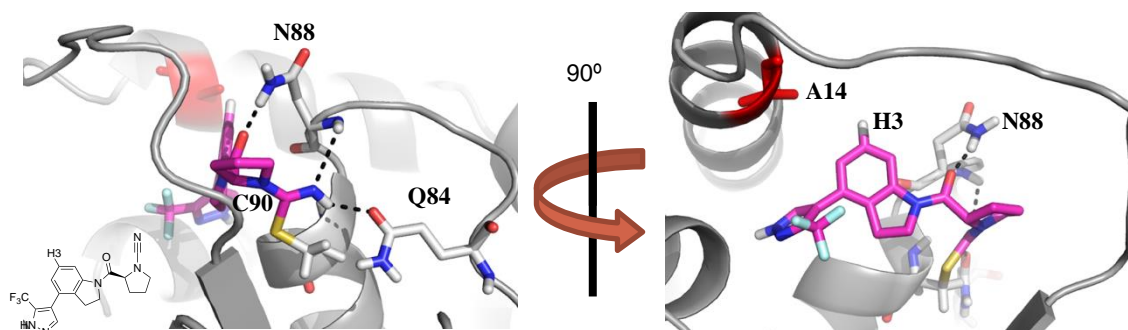


Figure 2.8 Predicted binding pose of compound **1** (magenta) with UCHL1 (grey), supported by 3D intermolecular-NOE NMR experiments. Constraints provided when docking included formation of a covalent bond with cysteine 90 (yellow), and a distance between 1 and 6 angstroms between ligand proton 3 (H3) and alanine 147 (red sticks). The resulting pose shows hydrogen bonds (black dashed lines) between compound **1** and the oxyanion hole (Q84 and N88) of UCHL1.

2.2.4 Cellular Characterization

UCHL1 levels of expression and enzymatic activity are correlated with increased metastatic behavior in various cancers, including small-cell lung cancer, myeloma, and lymphoma.^{21,36,39,97–100} Three cell lines were selected to evaluate the efficacy of compound **1** based on their sensitivity to genetic depletion of UCHL1: SW1271 (small-cell lung cancer line), KMS11, and KMS12 (myeloma cell lines). SW1271 and KMS11 cells have high levels of UCHL1 expression and are sensitive to shRNA depletion of UCHL1, as determined by the project Achilles score.^{97,114} In contrast, KMS12 cells have low levels of UCHL1 and are not dependent on the DUB for proliferation (Figure 2.9A).⁹⁷ Thus, we sought to evaluate differential cell growth in these cell lines upon pharmacological inhibition of UCHL1. As predicted, treatment of SW1271 cells with compound **1** displayed a dose-dependent response with a $CC_{50} = 139$ nM as monitored using a CellTiter-Glo[®] assay (Figure 2.9B). Compound **1** activity was also assessed in KMS11 and KMS12 cells by tracking percent proliferation over time at various concentrations of **1**. Consistent with their differential expression of UCHL1, compound **1** resulted in cell toxicity in the KMS11 cells while only reducing proliferation in the KMS12 cells upon treatment with the same concentration compound (Figure 2.9C). The enhanced inhibition of proliferation in the KMS11 cells was observed at several concentrations of compound **1** (Figure 2.10). Taken together, these data suggest on target inhibition of UCHL1, but the observed growth inhibition induced by **1** in the KMS12 cells is likely due to off-target interactions.

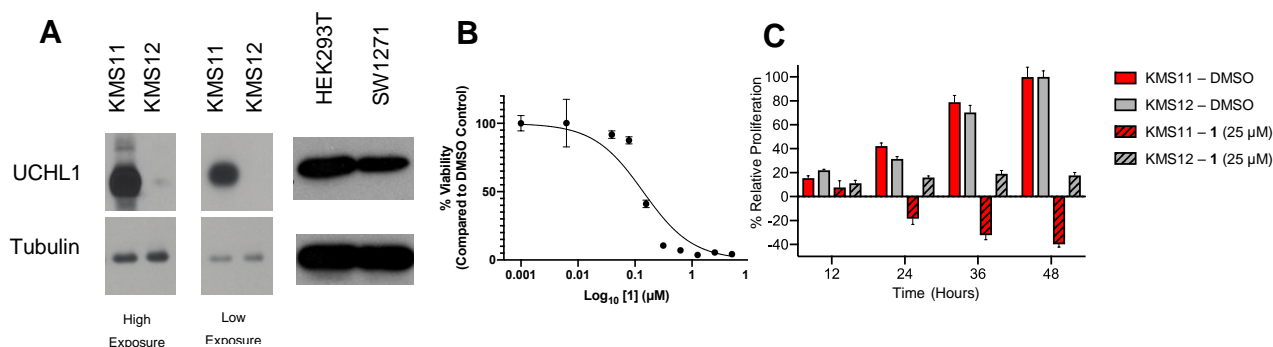


Figure 2.9 Cellular inhibition of UCHL1 by **1**. **A**) Immunoblots of KMS11, KMS12, HEK293, and SW1271 showing UCHL1 expression. **B**) Compound **1** displays a dose-dependent effect on the viability of SW1271 cells ($CC_{50} = 138.9$ nM). **C**) Compound **1** decreases the rate of proliferation for both KMS11 and KMS12 cells at 25 μM.

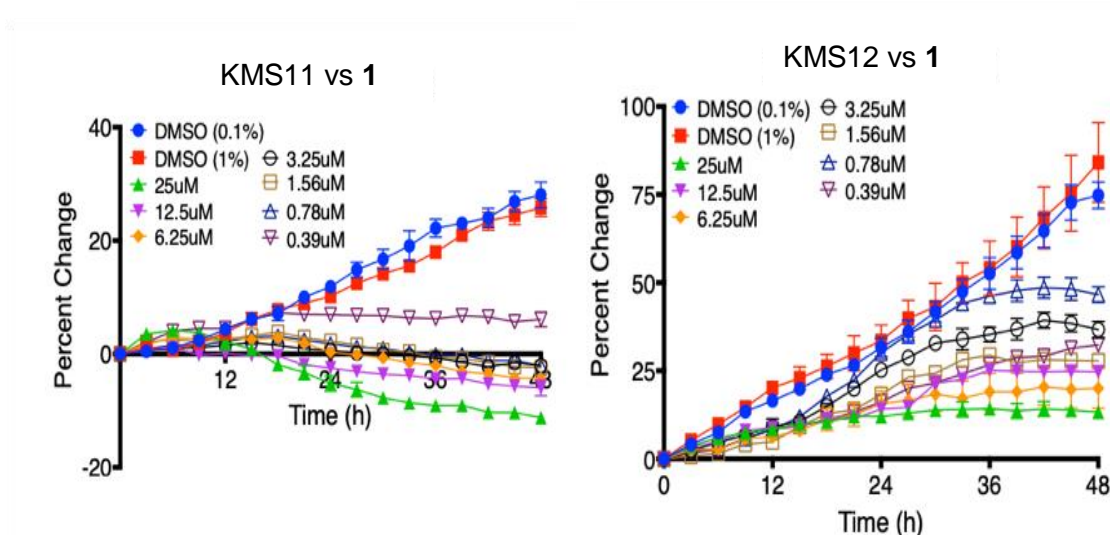
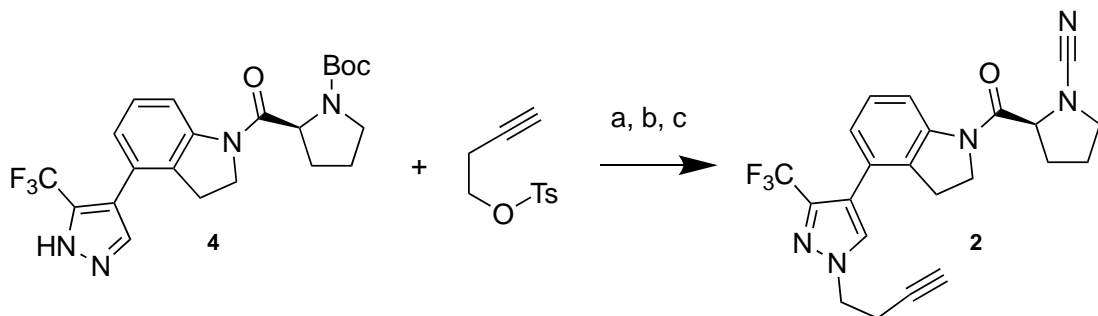


Figure 2.10 Cell proliferation data for **1** versus KMS11 and KMS12 cells. KMS11 and KMS12 cells incubated with various concentrations of **1** display a dose-dependent change in proliferation.

To further investigate if the inhibitor engages UCHL1 in intact cells and to identify potential off-targets for compound **1** an alkyne containing analog was synthesized. Intermediate **4** was *N*-alkylated to append an alkyne moiety on the pyrazole ring (Scheme 2.2). Subsequent deprotection of the Boc group using TFA and addition of the cyanamide via cyanogen bromide provided final compound **2**. Compound **2** retained UCHL1 activity albeit with a 10-fold reduction in potency (IC_{50}

value of $6.4 \pm 1.2 \mu\text{M}$, Figure 2.11). This loss of activity is consistent with the predicted binding pose as the alkylated nitrogen of the pyrazole points towards the protein surface, likely perturbing the binding of the inhibitor. The IC_{50} for UCHL3 did not significantly change ($5.5 \pm 1.1 \mu\text{M}$) effectively making **2** equipotent against each enzyme.



Scheme 2.2 Preparation of **2**. Reagents and Conditions: a) K₂CO₃ (2 eq), ACN, 110 °C, 1.5 hr; b) TFA (20 eq), DCM, 25 °C, 2 hr; c) K₂CO₃ (2.2 eq), BrCN (1.0 eq), THF, 0 °C, 30 minutes.

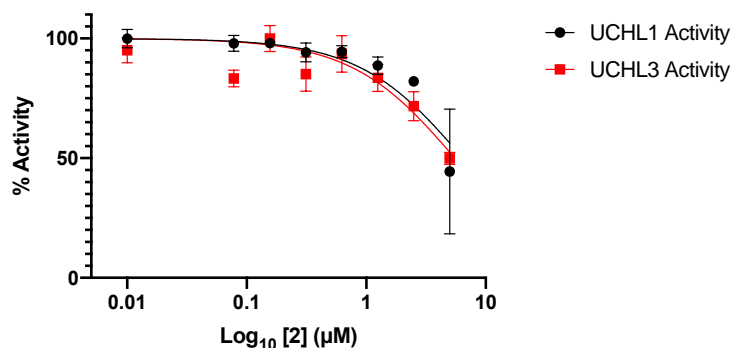


Figure 2.11 Compound **2** dose-response inhibition assay. IC₅₀ curves for compound **2** against UCHL1 (black) and UCHL3 (red) after 30 minutes of preincubation.

To determine the off-target interactions between **1** and proteins other than UCHL1, we utilized copper catalyzed azide-alkyne cycloaddition (CuAAC) to ligate either biotin or a sulfo-Cyanine5 (Cy5-Azide) fluorophore to the protein-ligand complex (Figure 2.12).^{115–118} First it was confirmed that the CuACC ligation could proceed while **2** was bound to recombinant UCHL1. UCHL1 was treated with **2** in a dose-dependent manner, followed by CuAAC ligation with Cy5-Azide. This sample was then subjected to gel electrophoresis and imaged. The results confirmed successful CuACC addition of the fluorophore to compound **2** while bound to UCHL1 as evidenced by increased fluorescence band intensity as the concentration of **2** increased (Figure 2.13). UCHL1

contains five surface exposed cysteines in addition to the catalytic Cys90. It is possible that the fluorescent labeling of UCHL1 with **2** could be due to a covalent adduct formed with any one of the surface exposed cysteines. To rule this possibility out the same experiment was performed by treating both wild-type UCHL1 and a catalytically inactive Cys90Ala UCHL1 mutant (UCHL1^{C90A}) in parallel. Samples were subjected to gel electrophoresis, which revealed that WT-UCHL1 was fluorescently labeled while UCHL1^{C90A} exhibited no detectable fluorescence confirming the probe covalently targets the active site cysteine (Figure 2.14). This data, combined with the ESI-MS data described above confirms the molecule preferentially modifies the Cys90.

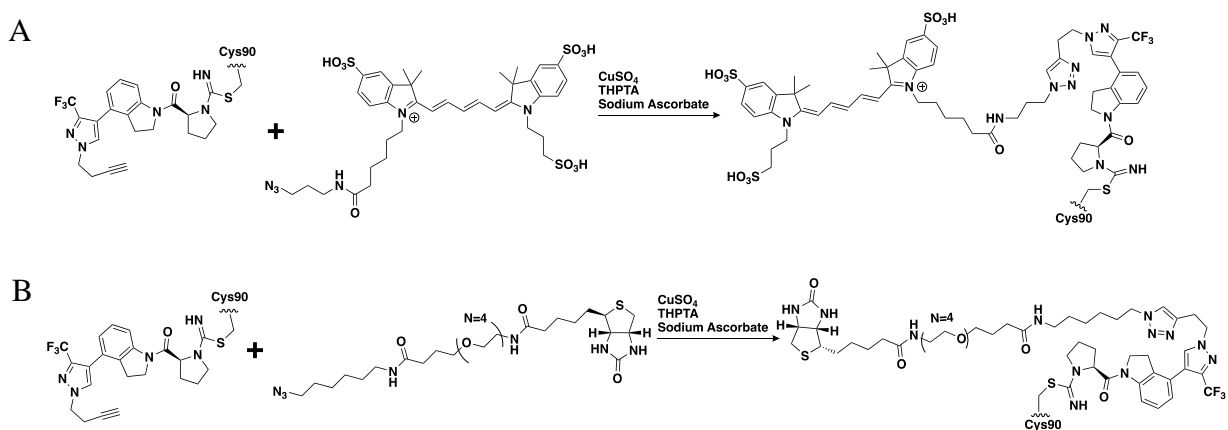


Figure 2.12 Representative bioconjugation reactions for compound **2**. CuAAC reaction of UCHL1 treated with **2**. General reaction scheme for the formation of UCHL1-Compound **2** complex, followed by the CuAAC ligation of (A) sulfo-Cyanine5 azide or (B) Biotin azide.

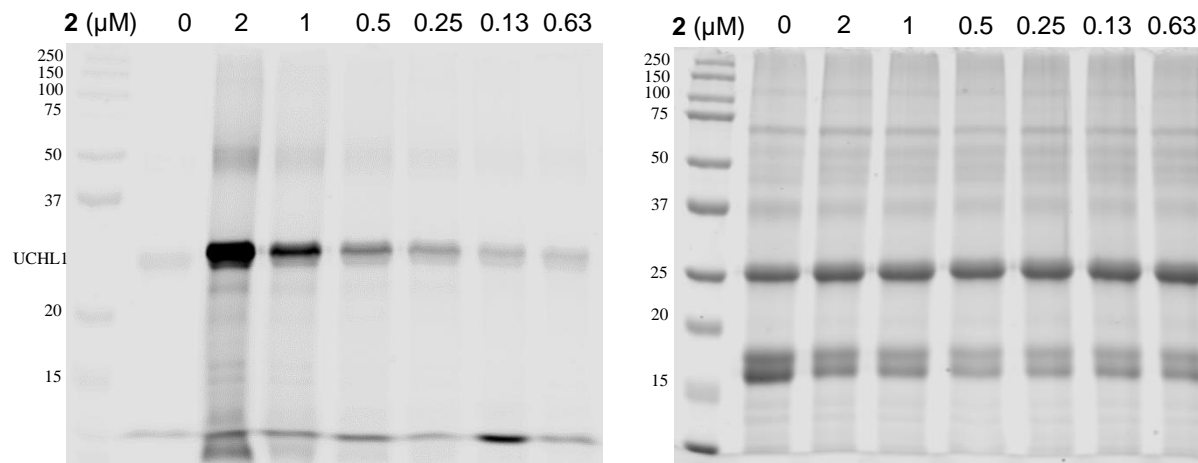


Figure 2.13 Dose-dependent labelling of recombinant UCHL1 by **2**. Recombinantly expressed UCHL1^{WT} treated with decreasing concentrations of **2** results in a corresponding decrease in fluorescent band intensity (left). Coomassie stained gel (right) indicates equal loading of UCHL1.

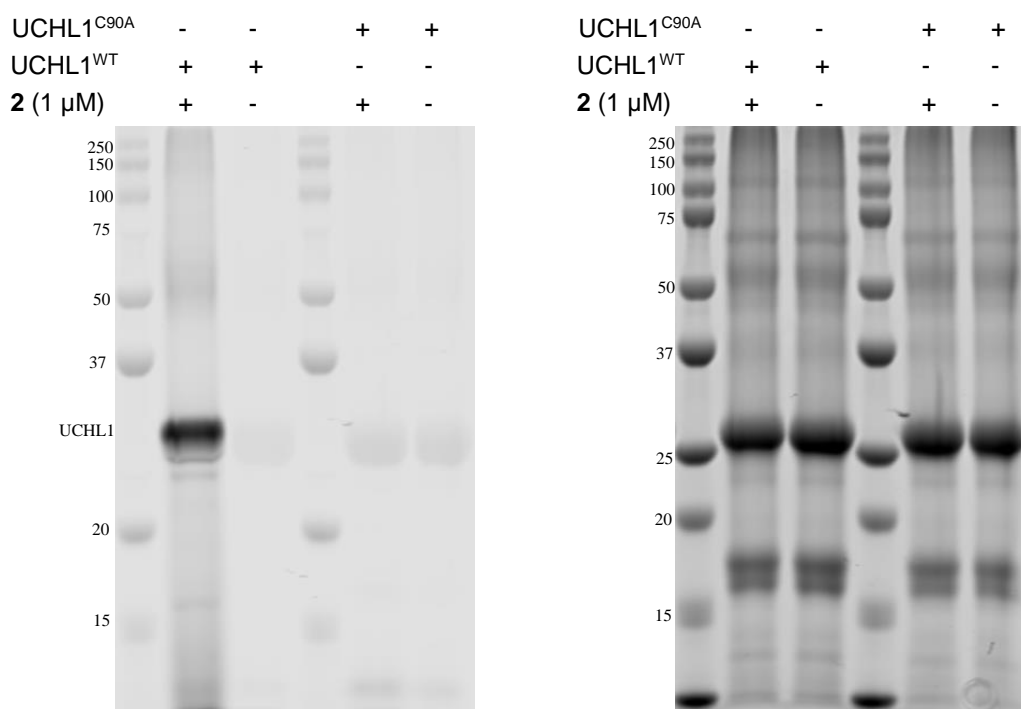


Figure 2.14 Specific labelling of UCHL1s catalytic cysteine by **2**. Recombinantly expressed UCHL1^{WT} or catalytically inactive mutant UCHL1^{C90A} treated with 1 μM **2** results in selective labelling of UCHL1^{WT} at the catalytic cysteine (residue 90) as visualized by fluorescent bands (left). Coomassie stained gel (right) indicates equal loading of all proteins.

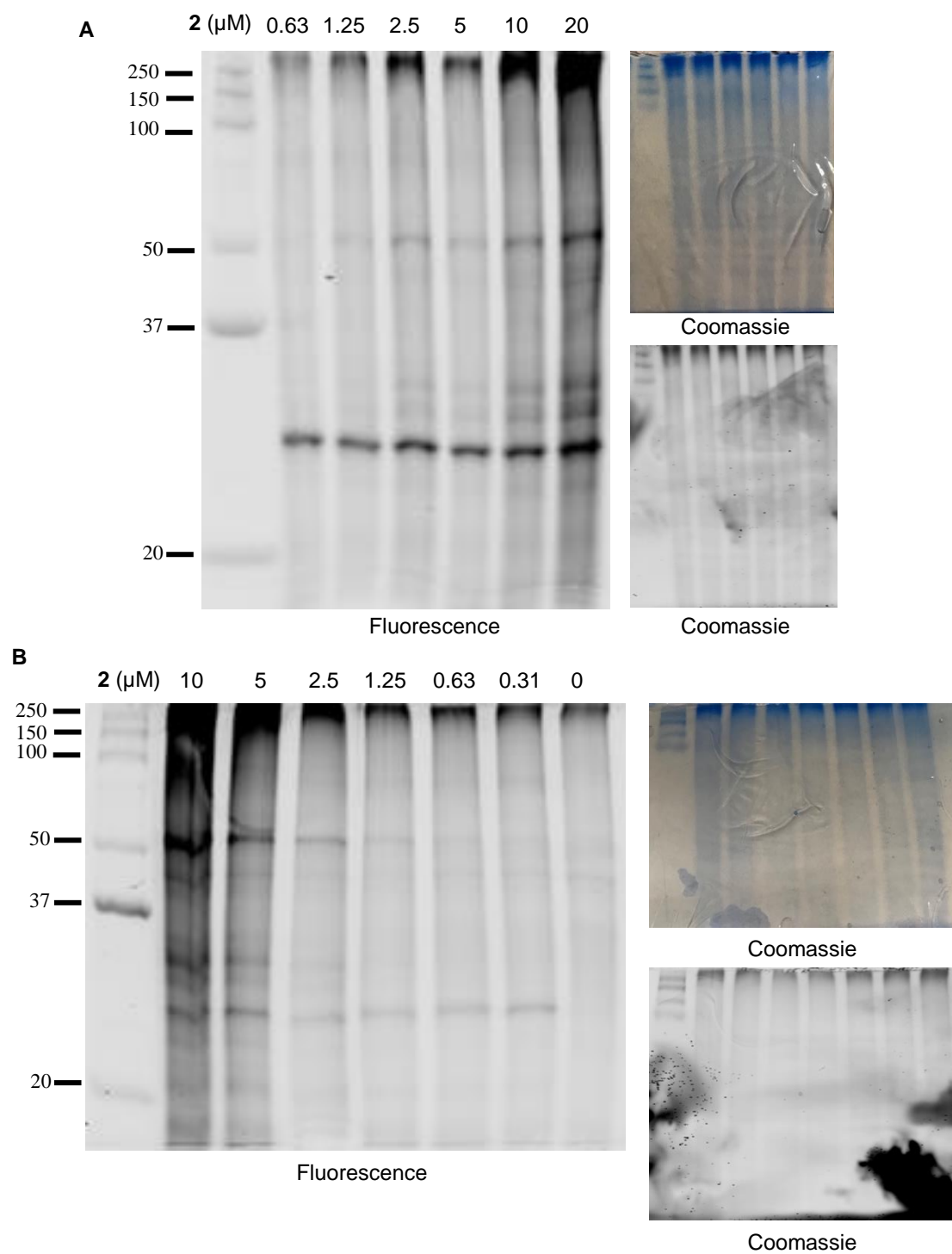


Figure 2.15 Labelling of proteins in intact cells by **2**. KMS11 **A**) and SW1271 **B**) cells treated with various **2** results in a dose-dependent change in fluorescent band intensity. Bands were undetectable by Coomassie staining.

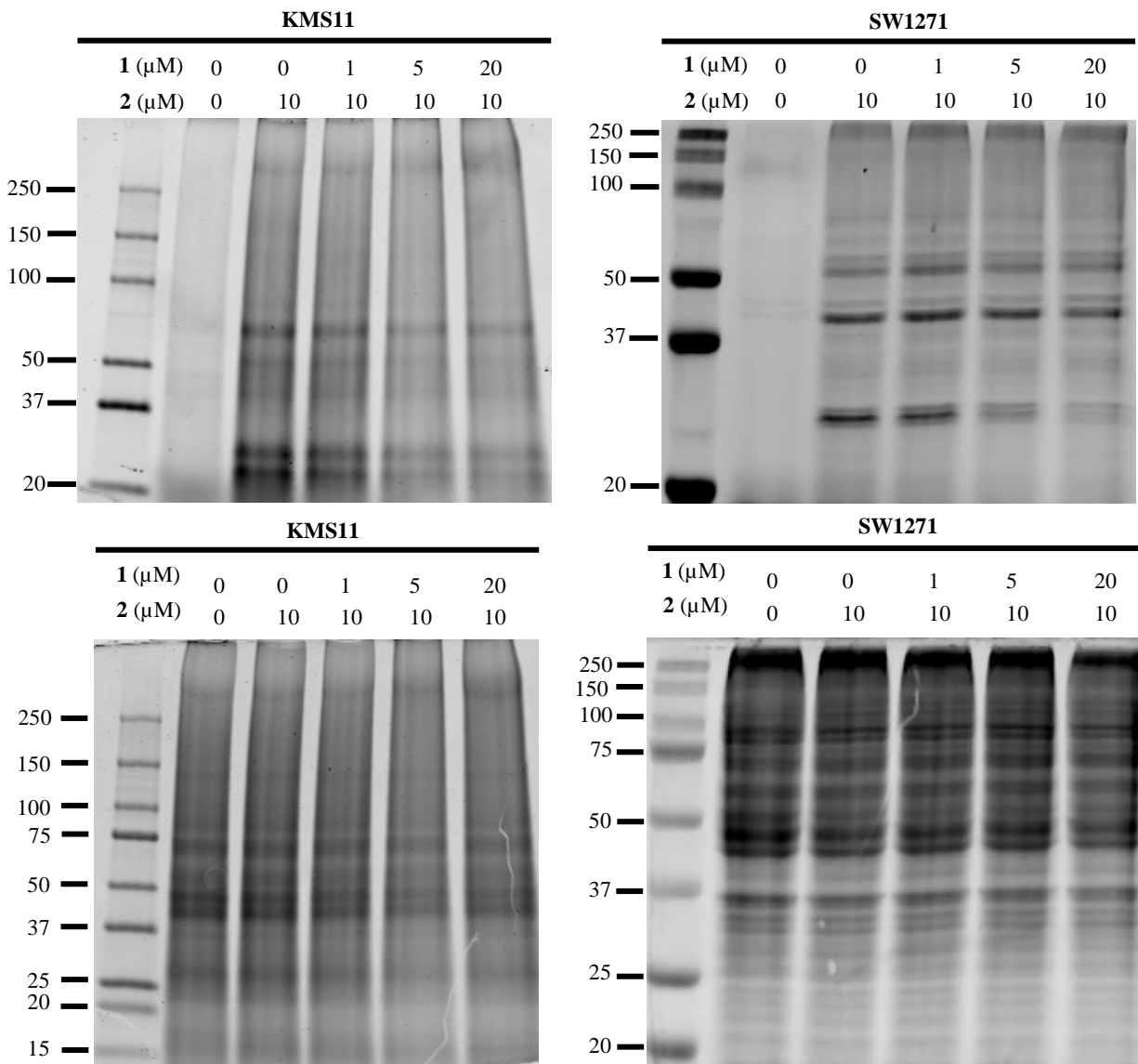


Figure 2.16 Engagement of UCHL1 in KMS11 and SW1271 cells. Fluorescence imaged gels (top) from KMS11 and SW1271 cells treated simultaneously with 10 μ M of compound **2** and increasing concentrations of compound **1** for 4 hours then subjected to CuAAC labeling with Cy5 dye show a dose-dependent decrease in intensity for a band near 25 kDa. Loading control of fluorescence gels (bottom) in KMS11 and SW1271 cells treated simultaneously with a 10 μ M of compound **2** and increasing concentrations of compound **1** show equal loading in each lane as visualized by Coomassie stain.

We next utilized the alkyne probe to assess off-targets in both KMS11 and SW1271 cells. These cells were incubated with **2** in dose-response for 4 hours before being washed 3 times with PBS, collected, and lysed. The normalized cell lysate was then subjected to CuAAC reaction with

Cy5-azide to label all proteins with which **2** was able to interact. In both cell lines, a dose-dependent labelling of proteins was observed (Figure 2.15). Additionally, to confirm that **2** was specifically labelling UCHL1 in a dose-dependent manner, an out-competition experiment was performed by treating cells simultaneously with **2** (10 μ M) in the presence of increasing concentrations of **1** (0 – 20 μ M). Here, it was observed that **1** was able to out-compete **2** for UCHL1 in both SW1271 and KMS11 cell lines in a dose-dependent manner (Figure 2.16). However, the alkyne probe maintained binding to higher molecular weight proteins and the dose-dependent decrease in fluorophore intensity was not as robust as with UCHL1. Given the loss of UCHL1 selectivity resulting from the addition of the alkyne moiety, the apparent non-specific interactions observed here could feasibly be a result of the reduced selectivity from the alkyne addition. However, we believe there is some degree of off-target binding as the bands at approximately 37 kDa and 50 kDa have slight reduction of the fluorescence signal from the alkyne probe **2** at the highest concentration of the non-alkyne containing competitor **1**.

In an attempt to identify these non-specific binding and off-targets for **2**, a biotin-streptavidin pull-down experiment was performed. UCHL1 expressing KMS11 cells were treated with either **1** or **2** for 4 hours before being washed, collected, and lysed. A CuAAC reaction was performed using biotin-azide, biotinylating all proteins with which **2** interacted in the cells. This sample was subjected to pulldown using streptavidin-bound magnetic beads. The beads, washed of all non-specific proteins, were eluted and analyzed by gel electrophoresis and immunoblotting for UCHL1 (Figure 2.17). Tryptic digestion followed by mass spectrometry confirmed the presence of UCHL1 in the streptavidin-enriched sample, matching a peptide sequence from recombinantly expressed UCHL1 (Figure 2.18). However, no other DUBs were present in a sufficient quantity at the level of our detection compared to DMSO control to be considered off-target interactors. Therefore, even though it is observed that **2** does covalently modify proteins other than UCHL1 in intact cells using the fluorophore-linked **2**, we were not able to definitively identify these proteins in this round of pull-down/mass spectrometry experiments. A tabular list of the highest confidence putative off-target interactions is provided in the supplemental information (Table 2.2) and will be validated in future work

25

2

1

FT W1 W2 W3 E1 E2 E3 FT W1 W2 W3 E1 E2 E3

A

LICH1616865-17259 RT: 31.66-32.11 AV/34 NL: 9.87E8
T: FTMS + p NSI Full ms [400,000-1600,000]

B

LICH1616790 RT: 31.56 AV/1 NL: 7.94E5
T: FTMS + c NSI Full ms2 [170,361.60] [100,000-1470,000]

C

Peptide View

MS/MS Fragmentation of LGGFDGSLVK
Found in: AENLJ7.p Uniprot; Human; HSAENLJ7.HUMAN Ubiquitin carboxyl-terminal hydrolase O6-Homo sapiens GN=LICHE1 PE=2 SV=1
Match to Query 241: 1063.55583 Score/332.784972.2v / intensity(1124689.6250) scans(12794) stanoesdcon(1765.02)
Title: (consensusType=0) controlNumber(s)=17695
Data file: nucleus.msn.pandora.edu/hedrick/Desktop/Krabill_gel_1_A.raw

? 20.08 to 1062.48

.label all possible matches • Label matches only for scoring *

monoisotopic mass of neutral peptide M(calc.): 1063.5556
[used modifications]: Carbamidomethyl(C); (C) apply to specified residues or termini only
ions score: 59 Expect: 0.00011
atches: 11/78 Fragment Ions using 22 most intense peaks ([help](#))

#	b	b ⁺⁺	b ⁰	b ⁺⁺	Seq.	y	y ⁺⁺	y ⁺	y ⁺⁺	y ⁰	y ⁺⁺	#
1	114.0913	57.5493			L							10
2	171.1128	86.0600			G	951.4782	476.2427	934.4516	467.7295	933.4616	467.2374	9
3	318.1812	159.5942			F	894.4567	447.7320	877.4302	439.2187	876.4462	438.7267	8
4	447.2238	224.1155	429.2132	215.1103	E	747.3883	374.1978	730.3618	365.6845	729.3777	365.1923	7
5	562.2508	281.6290	544.2402	272.6237	D	618.3457	309.6763	601.3192	301.1632	600.3352	300.6172	6
6	619.2722	310.1397	601.2617	301.1345	G	503.3188	252.1630	486.2922	243.6498	485.3082	243.1577	5
7	706.3424	353.6538	688.2937	344.6505	S	446.2973	223.6523	429.2708	215.1390	428.2867	214.6470	4
8	805.3727	403.1900	787.3621	394.1847	V	299.2632	180.1363	342.2387	171.6230			3
9	918.4567	459.7320	900.4462	450.7267	L	260.1969	130.6021	243.1703	122.0888			2
10					K	117.1128	74.0600	130.0863	65.5468			1

50

Table 2.2 Identification of putative off-targets by tandem mass spectrometry analysis. Putative off-target interactions of compound **2** were identified using Mascot Daemon. Proteins were filtered and accepted if signal (LFQ Intensity) was present in only the probe-treated samples, and if the MS/MS count was greater than 2 in at least two of three samples tested.

Protein Name	Gene Name	Molecular Weight (kDa)	LFQ Intensity DMSO	LFQ Intensity Compound 1	MS/MS Count DMSO	MS/MS Count Compound 1
Forkhead box protein N4	FOXN4	55.277	0	95486000	0	2
40S ribosomal protein S14	RPS14	16.273	0	44447000	0	2
Retina-specific copper amine oxidase	AOC2	83.672	0	9107700	0	3
Protein-glutamine gamma-glutamyltransferase K	TGM1	82.355	0	25026000	0	3
Membrane-spanning 4-domains subfamily A member 10	MS4A10	29.747	0	74649000	0	5
Alpha-amylase	AMY1A	56.21	0	4854700	0	5
Catalase	CAT	59.755	0	46581000	0	5
Cystatin-SN	CST1	16.387	0	13196000	0	6
Transcription factor HES-1	HES1	14.429	0	113100000	0	6
Fibronectin	FN1	246.7	0	178110000	0	31

2.3 Conclusion

In summary, we have presented the characterization of a new class of UCHL1 inhibitor. The cyanopyrrolidine scaffold was confirmed to bind to UCHL1 via covalent modification of the active site Cys90 with very slow reversibility. The molecule was shown to inhibit UCHL1, along with at least one other DUB, in HEK293 cell lysate by using the HA-Ub-VME activity-based probe. NMR

and docking studies suggest that the inhibitor lies in a region overlapping the ubiquitin contact surface of the UCHL1 active site groove directly underneath the active site cross-over loop (Figure 2.8), a feature of UCHL1 believed to play a key role in size-based selection of ubiquitinated substrates.⁷³ In addition to the isothioureia linkage produced from the covalent attack of the catalytic cysteine, the molecule may engage in some prominent interactions with the active site pocket, specifically with the oxyanion hole via hydrogen bonding with Gln84 and an adjacent residue Asn88. The molecule exhibits efficacy at sub-micromolar concentrations against cancer cell lines KMS11 and SW1271 that are known to be sensitive UCHL1 knockdown while also displaying moderate growth inhibition against KMS12 myeloma cells that are not sensitive to UCHL1 depletion. These data suggest potential off-target interactions may contribute to the inhibition of cell growth. Using an alkyne-tagged probe analog the molecule was confirmed to inhibit UCHL1 in cells while also binding to other proteins in a dose-dependent manner; however, further work is necessary to definitively identify these proteins and define the nature of their interaction with the probe molecule. While the cyanopyrrolidine scaffold of compound **1** was likely developed for therapeutic purposes to target UCHL1 it may not serve as a suitable chemical probe due to the lack of selectivity and off-target toxicity. However, the compound may prove useful for validating on target engagement of future UCHL1 inhibitors in intact cells and provide insight into effective inhibitory strategies for the UCHL1.

2.4 Experimental

General: ¹H and ¹³C NMR spectra were recorded on Bruker DRX500 spectrometer (operating at 500 and 126 MHz) in DMSO-d₆ or CDCl₃ with or without the internal standard of TMS at 0.05% v/v. The chemical shifts (δ) reported as parts per million (ppm) and the coupling constants are reported as s = singlet, bs = broad singlet, d = doublet, t = triplet, q = quartet, dd = doublet of doublet, m = multiplet. The purity of all final compounds was >95 % purity as assessed by HPLC according to current American Chemical Society guidelines for publication. Final compounds were analyzed on an Agilent 1200 series chromatograph. The chromatographic method utilized as ThermoScientific Hypersil GOLD C-18 or silica column. UV detection wavelength = 220/254 nm; flow-rate = 1.0 mL/min; solvent = acetonitrile/water for reverse phase. Both organic and aqueous mobile phases contain 0.1% v/v formic acid. The mass spectrometer used is an Advion CMS-L Compact Mass Spectrometer with an ESI or an APCI source. Samples are submitted for analysis using the

atmospheric solids analysis probe (ASAP). Compounds were prepared according to following protocols and are detailed below.

2.4.1 Chemical Synthesis

tert-butyl (S)-2-(4-bromoindoline-1-carbonyl)pyrrolidine-1-carboxylate (3)

To a solution of boc-L-proline (1.2 g, 4.9 mmol, 1.2 eq) in THF was added HATU (2.3 g, 6.1 mmol, 1.5 eq) and DIPEA (1.4 mL, 8.1 mmol, 2.0 eq) at 25 °C. The reaction mixture was stirred for 1 hour. 4-Bromoindoline (0.8 mg, 4.0 mmol, 1.0 eq) was added to the reaction mixture. The reaction mixture was stirred at 25 °C for 15 hours. The resulting mixture was poured into saturated NaHCO₃ (10 mL). The organic phase was collected, dried over Na₂SO₄, filtered, and concentrated under reduced pressure. The resulting residue was purified by column chromatography (5-50% Ethyl Acetate in Hexanes). The material was washed with hexanes and dried yielding *tert-butyl (S)-2-(4-bromoindoline-1-carbonyl)pyrrolidine-1-carboxylate (3)* (1.4 g, 86%). ¹H NMR (300 MHz, DMSO-d₆) δ 8.16 – 7.93 (m, 1H), 7.30 – 7.03 (m, 2H), 4.64 – 4.42 (m, 1H), 4.33 – 4.05 (m, 2H), 3.56 – 3.35 (m, 2H), 3.15 (t, J = 9.0 Hz, 2H), 2.36 – 2.12 (m, 1H), 1.95 – 1.75 (m, 3H), 1.43 – 1.12 (m, 9H). MS APCI+: 295.0 [M-Boc+H].

tert-butyl (S)-2-(4-(5-(trifluoromethyl)-1H-pyrazol-4-yl)indoline-1-carbonyl)pyrrolidine-1-carboxylate (4)

To a solution of intermediate **3** (856 mg, 2.2 mmol, 1.0 eq) in DMF:Water (9:1, 1.5 mL) was added 4-(4,4,5,5-tetramethyl-1,3,2-dioxaborolan-2-yl)-5-(trifluoromethyl-1H-pyrazol-4-yl)indoline-1-carboxylate (567 mg, 2.2 mmol, 1 eq) and NaHCO₃ (364 mg, 4.30 mmol, 2.0 eq). The reaction mixture was stirred at 25 °C in a microwave tube and degassed for 15 minutes. Pd(dppf)Cl₂ (158 mg, 0.22 mmol, 0.1 eq) was added and the reaction tube was sealed and heated at 110 °C for 1.5 hours in a microwave. The reaction mixture was poured into water (20 mL) and extracted with Ethyl Acetate (3 x 50 mL). The combined organic phase was washed with brine (20 mL), dried over Na₂SO₄, filtered, and concentrated under reduced pressure. The resulting residue was purified by column chromatography (5% Methanol in DCM). The material obtained from chromatographic purification was azeotropically distilled with a mixture of hexane:diethyl ether (1:1, 50 mL) yielding *tert-butyl (S)-2-(4-(5-(trifluoromethyl)-1H-pyrazol-4-yl)indoline-1-carbonyl)pyrrolidine-1-carboxylate (4)*

(636.4 mg, 65.2%). ¹H NMR (300 MHz, DMSO-d₆) δ 13.81 (s, 1H), 8.23 – 8.01 (m, 2H), 7.31 – 7.12 (m, 1H), 6.93 (d, J = 7.6 Hz, 1H), 4.61 – 4.43 (m, 1H), 4.34 – 3.98 (m, 2H), 3.50 – 3.36 (m, 2H), 3.06 (t, J = 8.6 Hz, 2H), 2.37 – 2.12 (m, 1H), 2.07 – 1.64 (m, 3H), 1.42 – 1.18 (m, 9H). APCI-MS: m/z 351.2 [M-Boc+H]⁺.

(S)-2-(4-(5-(trifluoromethyl)-1H-pyrazol-4-yl)indoline-1-carbonyl)pyrrolidine-1-carbonitrile (1)

Step 1. To a solution of intermediate **4** (100 mg, 0.22 mmol, 1 eq) in DCM was added TFA (0.5 mL) at 25 °C. The reaction mixture was stirred for 2 hours, and then concentrated under reduced pressure. The obtained residue was triturated with diethyl ether (1 mL) yielding (S)-1-propyl-5-(5-carbonyl)pyrrolidine-1-carboxylate TFA salt (70.9 mg, 68.8% yield). APCI-MS: m/z 351.2 [M + H]⁺. This material was used directly for the next step without further purification.

Step 2. To a solution of (S)-1-propyl-5-(5-carbonyl)pyrrolidine-1-carboxylate TFA salt (25.0 mg, 54 μM, 1 eq) in THF was added K₂CO₃ (17.0 mg, 120 μM, 2.2 eq) at 0 °C. Cyanogen bromide (6.0 mg, 54 μM, 1.0 eq) was added to the reaction mixture at 0 °C. The reaction mixture was stirred at 25 °C for 30 minutes and then poured onto water (50 mL). The resulting mixture was extracted with Ethyl Acetate (3 x 50 mL), combined, washed with brine, dried over Na₂SO₄, filtered, and concentrated under reduced pressure. The resulting residue was purified by column chromatography (5% Methanol in Ethyl Acetate) yielding title compound **S)-2-(4-(5-(trifluoromethyl)-1H-pyrazol-4-yl)indoline-1-carbonyl)pyrrolidine-1-carbonitrile (1)** (14 mg, 69%). ¹H NMR (500 MHz, Chloroform-d) δ 8.27 (d, J = 8.1 Hz, 1H), 7.67 (s, 1H), 7.24 (d, J = 8.0 Hz, 1H), 7.03 (d, J = 7.7 Hz, 1H), 4.63 – 4.42 (m, 1H), 4.21 (d, J = 9.7 Hz, 1H), 4.04 (d, 1H), 3.65 (m, 2H), 3.29 – 2.95 (m, 2H), 2.40 – 2.21 (m, 1H), 2.20 – 2.07 (m, 2H), 2.07 – 1.92 (m, 2H). ¹³C NMR (126 MHz, CDCl₃) δ 167.8, 142.5, 130.4, 129.6, 127.8, 127.1, 126.3, 120.4, 118.5, 117.1, 116., 62.3, 51.5, 47.6, 30.0, 29.6, 27.7, 24.3. APCI-MS: m/z 376.1 [M + H]⁺. HPLC retention time: 11.251 min. HPLC Purity: 98.17%.

(S)-2-(4-(1-(but-3-yn-1-yl)-3-(trifluoromethyl)-1H-pyrazol-4-yl)indoline-1-carbonyl)pyrrolidine-1-carbonitrile (2)

Step 1. To a solution of tert-butyl (2S)-2-(4-(5-(trifluoromethyl)-1H-pyrazol-4-yl)-2,3-dihydro-1H-indene-1-carbonyl)pyrrolidine-1-carboxylate (50 mg, 1 eq, 0.11 mmol) in acetonitrile.

K₂CO₃ (31 mg, 2 eq, 0.22 mmol) was added, followed by but-3-yn-1-yl 4-methylbenzenesulfonate (75 mg, 3.3 eq, 0.33 mmol) was added to the reaction mixture. The reaction was heated to 110 °C in a microwave for 1 hour. The resulting reaction mixture was quenched with water (50 mL) and brine (50 mL), extracted with ethyl acetate (3x50 mL), rinsed with saturated NaHCO₃ (50 mL), and rinsed with brine (50 mL). The organic layer was dried over Na₂SO₄, filtered, and concentrated under reduced pressure. The resulting oil was purified using flash chromatography (0->50% EtOAc over 10 min, hold 5 min, 50->80% EtOAc over 10 min, hold 5 min.). The resulting residue was azeotroped with dichloromethane and dried using under reduced pressure yielding tert-butyl (S)-2-(4-(1-(but-3-yn-1-yl)-3-(trifluoromethyl)-1H-pyrazol-4-yl)indoline-1-carbonyl)pyrrolidine-1-carboxylate. ¹H NMR (300 MHz, Chloroform-d) δ 8.26 (t, J = 8.6 Hz, 1H), 7.53 (d, J = 8.6, 1.1 Hz, 1H), 7.24 – 7.13 (m, 1H), 7.03 – 6.91 (m, 1H), 4.64 – 4.42 (m, 1H), 4.33 (td, 2H), 4.24 – 3.96 (m, 2H), 3.78 – 3.39 (m, 2H), 3.04 (q, J = 7.2, 6.5 Hz, 2H), 2.80 (tt, J = 6.6, 2.6 Hz, 2H), 2.33 – 2.09 (m, 2H), 2.07 (t, J = 2.7 Hz, 1H), 2.01 – 1.79 (m, 2H), 1.49 – 1.27 (m, 9H). APCI-MS: m/z 403.1 [M-Boc+H]⁺.

Step 2. To a solution of tert-butyl (S)-2-(4-(1-(but-3-yn-1-yl)-3-(trifluoromethyl)-1H-pyrazol-4-yl)indoline-1-carbonyl)pyrrolidine-1-carboxylate (38.9 mg, 0.077 mmol, 1 eq) in DCM was added TFA (0.5 mL) at 25 °C. The reaction mixture was stirred for 2 hours, and then concentrated under reduced pressure. The obtained residue was triturated with diethyl ether (1 mL) yielding (S)-4-(1-(but-3-yn-1-yl)-3-(trifluoromethyl)-1H-pyrazol-4-yl)-1-prolylindoline, 2,2,2-trifluoroacetate salt. MS APCI+: 403.2 [M+H]. This material was used directly for the next step.

Step 3. To a solution of (S)-4-(1-(but-3-yn-1-yl)-3-(trifluoromethyl)-1H-pyrazol-4-yl)-1-prolylindoline, 2,2,2-trifluoroacetate salt (40 mg, 0.08 mmol, 1 eq) in THF was added K₂CO₃ (24 mg, 0.17 mmol, 2.2 eq) at 0 °C. Cyanogen bromide (9.53 mg, 0.09 mmol, 1.2 eq) was added to the reaction mixture at 0 °C. The reaction mixture was stirred at 25 °C for 30 minutes and then poured onto water (50 mL). The resulting mixture was extracted with Ethyl Acetate (3 x 50 mL), combined, washed with brine, dried over Na₂SO₄, filtered, and concentrated under reduced pressure. The resulting residue was purified by column chromatography (5% Methanol in Ethyl Acetate) yielding title compound (S)-2-(4-(1-(but-3-yn-1-yl)-3-(trifluoromethyl)-1H-pyrazol-4-yl)indoline-1-carbonyl)pyrrolidine-1-carbonitrile (2) (24 mg, 72%). ¹H NMR (300 MHz, Chloroform-d) δ 8.25 (d, J = 8.1 Hz, 1H), 7.55 (s, 1H), 7.22 (d, J = 8.0 Hz, 1H), 7.01 (d, J = 7.7 Hz, 1H), 4.47 (dd, J = 8.1, 3.4

Hz, 1H), 4.34 (t, J = 6.5 Hz, 2H), 4.27 – 4.14 (m, 1H), 4.08 – 3.94 (m, 1H), 3.82 – 3.44 (m, 2H), 3.20 – 2.95 (m, 2H), 2.80 (td, J = 6.5, 2.6 Hz, 2H), 2.38 – 2.21 (m, 1H), 2.19 – 2.09 (m, 2H), 2.07 (t, J = 2.6 Hz, 2H), 2.04 – 1.89 (m, 1H). ^{13}C NMR (75 MHz, CDCl_3) δ 167.9, 142.6, 131.6, 131.0, 130.5, 127.9, 127.3, 126.3, 123.1, 119.5, 118.8, 117.2, 116.3, 79.8, 71.8, 71.0, 62.4, 62.1, 51.5, 30.1, 27.8, 24.4, 20.5. APCI-MS: m/z 428.2 $[\text{M}+\text{H}]^+$. HPLC retention time: 12.453 min. HPLC Purity: 99.0%.

2.4.2 Biochemical and Cellular Assays

Protein Expression and Purification

UCHL1 for NMR experiments (Plasmid provided by Chittaranjan Das – Purdue University) was grown in M9 minimal media supplemented with 2 g/L ^{13}C Glucose and 1g/L $^{15}\text{NH}_4\text{Cl}$ (Cambridge Isotopes) as the sole carbon and nitrogen sources. Bacterial cultures were grown at 37 °C to an optical density of 0.6-0.8. After 0.1 mM IPTG induction at 17 °C for 18 hours, the bacteria were lysed and pelleted at 15,000 x g, and clarified lysate was purified via glutathione-Sepharose (GE Life Sciences) column according to manufacturer's instructions. The protein was purified further by size exclusion chromatography on a Superdex S75 column (Amersham Pharmacia).

UCHL1, UCHL1^{C90A}, and UCHL3 (Expressed in pET15b by GenScript) for biochemical assays were grown in LB growth medium at 37 °C to an optical density of 0.6-0.8. After 0.1 mM IPTG induction at 17 °C for 18 hours the bacteria were lysed and pelleted at 15,000 x g, and clarified lysate was purified via HisPur Ni-NTA resin (Thermo Scientific) according to manufacturer's instructions.

ESI-MS for Intact UCHL1 and UCHL1 - Compound 1 Complex

Recombinantly expressed His-UCHL1^{WT} or His-UCHL1^{C90A} were diluted into assay buffer (50 mM Tris pH 7.6, 0.5 mM EDTA, 1 mM DTT) to a concentration of 5 mg/mL in the presence of DMSO (1% v/v) or compound **1** (200 μM) and incubated at room temperature for 30 minutes. This was then diluted 8-fold into mass spectrometry buffer (75% acetonitrile, 25% water, 0.1% formic acid, 0.1% ammonium formate). 40 μL of a buffer-containing blank, a DMSO treated samples, or compound **1** treated samples were injected into an Advion CMS-L Compact Mass Spectrometer outfitted with an ESI ionization source. After subtracting the blank from each sample, the data was manually deconvoluted and analyzed using DataExpress (Advion, version 6.0.11.3).

Fluorescence-based Deubiquitinase Activity Assay

Reactions were performed in black 384 well plates (Fisher 12566624) in a final volume of 50 μ L. DUBs were diluted in reaction buffer (50 mM Tris pH 7.6, 0.5 mM EDTA, 5 mM DTT, 0.1% (w/v) BSA) to a concentration of 2.5 nM or 0.25 nM for UCHL1 and UCHL3 respectively (Final concentration in well 1 nM or 0.1 nM for UCHL1 and UCHL3 respectively). To each well was added 20 μ L of DUB containing solution and 10 μ L of 5X inhibitor dissolved in reaction buffer (final concentration 5, 2.5, 1.5, 0.625, 0.3125, 0.15625, 0.078125, 0 μ M) and this was allowed to incubate for 30 minutes at room temperature. Reactions were initiated by the addition of 20 μ L 450 nM Ub-Rho (Boston Biochem U-555, Final concentration 180 nM). Reactions were incubated at room temperature and read immediately (Excitation = 485 nm, Emission = 535 nm) for 20 minutes. Readings were performed on a Synergy Neo2. Biochemical IC₅₀ were calculated using GraphPad Prism 8 (GraphPad Software, San Diego, California USA, www.graphpad.com) and the standard deviation was determined over three independent experiments.

Jump-Dilution Experiment

Reactions were performed in black 384 well plates (Fisher 12566624) in a final volume of 50 μ L. UCHL1 was diluted in reaction buffer (50 mM Tris pH 7.6, 0.5 mM EDTA, 5 mM DTT, 0.1% (w/v) BSA) to a concentration of 100 nM (Final concentration in well 1 nM). To this was added 7 μ M compound **1** or DMSO, and the mixture was incubated for 30 minutes at room temperature. This was then diluted 100-fold into Ub-Rho containing buffer (stock concentration 181.2 nM, final concentration 180 nM in well). Reactions were incubated at room temperature and read immediately (Excitation = 485 nm, Emission = 535 nm) for 20 minutes. Readings were performed on a Synergy Neo2.

Time-Dependent Activity Assay

Reactions were performed in black 384 well plates (Fisher 12566624) in a final volume of 50 μ L. UCHL1 was diluted in reaction buffer (50 mM Tris pH 7.6, 0.5 mM EDTA, 5 mM DTT, 0.1% (w/v) BSA) to a concentration of 2.5 nM (Final concentration in well 1 nM). To each well was added 20 μ L of DUB containing solution and 10 μ L of 5X inhibitor dissolved in reaction buffer (final concentration 5, 2.5, 1.5, 0.63, 0.31, 0.16, 0.078, 0 μ M) and this was allowed to incubate for 12, 42,

72, 102, 132, 162, 1095, and 1410 minutes at room temperature. Reactions were initiated by the addition of 20 μ L 450 nM Ub-Rho (Boston Biochem U-555, Final concentration 180 nM). Reactions were incubated at room temperature and read immediately (Excitation = 485 nm, Emission = 535 nm) for 20 minutes. Readings were performed on a Synergy Neo2. Biochemical IC₅₀ were calculated using GraphPad Prism 8 (GraphPad Software, San Diego, California USA, www.graphpad.com).

Probe Labelling Assays

HEK293T cells (2.8×10^6 cell/mL * 8 mL) were lysed in 400 μ L of lysis buffer (50 mM Tris pH 7.4, 150 mM NaCl, 5 mM MgCl₂, 0.5 mM EDTA, 5 mM DTT, 2 mM ATP, 0.5% NP-40, 10% glycerol) and incubated on ice for 30 min. Cells were lysed on ice using sonication, and centrifuged at 17,000 x g for 10 min to remove cell debris. Concentration of cell lysate was measured using a Bradford assay. To microcentrifuge tubes was added 245 μ g cell lysate and 10 μ L of DMSO or **2**, and the mixture was allowed to incubate at room temperature for 10 minutes. HA-Ub-VME was added to a final concentration of 0.49 μ M, and the mixture was incubated at room temperature for 10 minutes. The reaction was quenched using 4x laemlli buffer and heated to 90 °C for 5 minutes before being analyzed by immunoblot.

Cell Proliferation Assay

The proliferation of KMS11 and KMS12 cells was monitored using an IncuCyte device (Sartorius; www.essenbioscience.com). Cells (3×10^4 per well; 200 μ l) were seeded in triplicate in 96 well plates the night prior to the addition of compounds. The IncuCyte was set to collect images from five fields per well at four hour intervals using the nuclear dye Nuclight Red (Sartorius; www.essenbioscience.com). At each timepoint, the number of cells per well was determined by taking the mean of the five locations in each well. The relative proliferation at each timepoint was normalized, with 100% set as the number of cells observed for incubated with DMSO (0.1%) controls at 72 hours.

Cell Toxicity Assay

SW1271 cells were purchased from the ATCC and cultured in DMEM containing 10% FBS and 1% Penicillin/Streptomycin. For growth inhibition assays, five thousand cells were planted per

well in a 96-well white wall plate in the presence of the indicated doses of compound **1**. Cells were grown for a period of 144 hours at which point cell viability was quantified using the Cell Titer Glo Assay (Promega #G7572). Changes in luminescence units were normalized to vehicle control wells and plotted using a log(inhibitor) vs. response curve fit analysis.

CuAAC Ligation and in-gel Fluorescence – Dose-Response with Recombinant Protein

1 mg/mL UCHL1 (49 μ L) was incubated with **2** (2, 1, 0.5, 0.25, 0.125, 0.0625 μ M) in PBS blocking buffer (ThermoScientific # 37538) for 30 minutes at room temperature. To each reaction sample is added: 90 μ L of 1X PBS, 20 μ L of 2.5 mM Cy5 Azide (Click Chemistry Tools #AZ118), 10 μ L of 100 mM THPTA pre-mixed with 10 μ L 20 mM CuSO₄, and 10 μ L of 300 mM Sodium Ascorbate. This mixture mixed by gently vortexing and allowed to incubate for 2 hours protected from light at room temperature. Protein was precipitated by sequential addition of MeOH (600 μ L), CHCl₃ (150 μ L) and water (400 μ L). Protein was pelleted by centrifugation at 17,000 \times g for 5 min and then further washed in methanol (450 μ L x 2) and re-pelleted. Pellets were air dried protected from light for one hour and stored at -20 °C until ready for use. Samples were resuspended in 1x PBS with 2% w/v SDS before adding 4x laemlli buffer and heated to 95 °C for 5 minutes prior to SDS page. Samples were separated by SDS page and the gels were scanned using a Licor Odyssey. Gels were subsequently Coomassie stained to determine loading.

CuAAC Ligation and in-gel Fluorescence – UCHL1^{WT} and UCHL1^{C90A}

1 mg/mL His-UCHL1^{WT} or His-UCHL1^{C90A} was incubated with 1 μ M **2** (2% v/v DMSO final) for 30 minutes at room temperature. To each reaction sample is added: μ L of 1X PBS, 20 μ L of 2.5 mM Cy5 Azide (Click Chemistry Tools #AZ118), 10 μ L of 100 mM THPTA pre-mixed with 10 μ L 20 mM CuSO₄, and 10 μ L of 300 mM Sodium Ascorbate. This mixture mixed by gently vortexing and allowed to incubate for 2 hours protected from light at room temperature. Protein was precipitated by sequential addition of MeOH (600 μ L), CHCl₃ (150 μ L) and Water (400 μ L). Protein was pelleted by centrifugation at 17,000 \times g for 5 min and then further washed in methanol (450 μ L x 2) and re-pelleted. Pellets were air dried protected from light for one hour and stored at -20 °C until ready for use. Samples were resuspended in 1x PBS with 2% w/v SDS before adding 4x laemlli buffer and heated to 95 °C for 5 minutes prior to SDS page. Samples were separated by SDS page

and the gels were scanned using a Licor Odyssey. Gels were subsequently Coomassie stained to determine loading.

CuAAC Ligation and in-gel Fluorescence – Treated Cells

Cells were treated with 0, 1, 5, or 20 μM 1 with concurrently with 10 μM 2 for 4 hours before being washed, scraped, and collected. Cells were lysed in 200 μL lysis buffer (1x PBS, 0.1% w/v SDS, 1% v/v Triton X-100, 1X HALT protease inhibitor) on ice for 30 minutes with vigorous vortexing every 10 minutes. Cells were centrifuged at 17,000 x g for 10 minutes, and the supernatant was collected. The concentration was measured by BCA, and cell lysate was normalized to 2 mg/mL and used immediately. The remainder of the lysate was stored at -80°C until use. 50 μL of each sample (at 2 mg/mL) was added to a new tube. To each tube was added 6 μL of a freshly prepared click cocktail: 3 μL 1.7 mM THPTA in 1:4 DMSO:tBuOH (100 μM final concentration), 1 μL 50 mM CuSO_4 in water (1 mM final concentration), 1 μL 1.25 mM Cy5-N3 (25 μM final concentration), 1 μL 50 mM TCEP (1 mM final concentration – prepared directly before use). The samples were vortexed briefly and let to react for 2 hours at room temperature, protected from light. The reactions were quenched by the addition of 17 μL 4x laemlli buffer. 15 μL was added per lane, and bands were separated by SDS-PAGE. Gels were scanned using a Licor Odyssey and were subsequently Coomassie stained to determine loading.

Sample Preparation for Proteomic Analysis

Cells were lysed in 100 μL lysis buffer (1x PBS, 0.1% w/v SDS, 1% v/v Triton X-100, 1X HALT protease inhibitor) on ice for 30 minutes with vigorous vortexing every 10 minutes. Cells were centrifuged at 17,000 x g for 10 minutes, and the supernatant was collected. The concentration was measured by BCA, and cell lysate was normalized to 6 mg/mL and stored at -80°C until use. 50 μL of each sample (at 6 mg/mL) was added to a new tube. To each tube was added: 90 μL 1X PBS, 20 μL of 2.5 mM Biotin-PEG3-Azide (Click Chemistry Tools Product # AZ104-25), 20 μL of pre-mixed (100 mM THPTA - 10 μL and 20 mM CuSO_4 – 10 μL), and 10 μL of 300 mM Sodium Ascorbate. The mixture was gently vortexed with each addition, and then allowed to react at room temperature for 2 hours protected from light. Samples were precipitated by adding 600 μL MeOH, 150 μL Chloroform, and 400 μL MilliQ water to each tube and vortexing. Samples were centrifuged

at 17,000 x g for 5 minutes, and the aqueous layer removed. The precipitate was washed with 450 μ L MeOH centrifuged at 17,000 g, and decanted (2X) before being air dried for 1 hour while protected from light. Samples were then stored at -20 °C overnight. To each sample was added 300 μ L Binding Buffer (1X TBS pH 7.6, 0.1% Tween-20). Samples were vortexed, sonicated, gently heated, and centrifuged at 17,000 x g for 5 minutes. This sample was added to 100 μ L of pre-washed Pierce Streptavidin Magnetic Beads (Product # 88816). Samples were incubated at room temperature on a rocker for 1.5 hours before separating liquid from beads using a magnetic stand. Beads were washed with 300 μ L of Wash Buffer (1X TBS pH 7.6 + 2M Urea) (3X). Beads were eluted sequentially using 100 μ L of: 1) 1X TBS + 5 mM Biotin, 2) 1X TBS + 2% w/v SDS and, 3) 4X Laemlli Buffer (Biorad Product #1610747). 5 μ L of 4X Laemlli Buffer was added to 15 μ L of each sample, and 10 μ L of this was loaded onto a 12% SDS PAGE gel before analysis by immunoblot.

NMR Experiments

All NMR data were collected at 300 K on a Bruker Avance-III-800 spectrometer equipped with a QCI cryoprobe. Samples of ^{15}N , ^{13}C labelled UCHL1 (0.6-0.8 mM in 50 mM d-Tris, pH 7.4, 50 mM NaCl, 1 mM DTT) alone or in complex with un-labelled **1** (molar ratio 1:1) were prepared as aforementioned.

2D ^{15}N -HSQC experiments (pulse program HSQCETFGPSI2) were performed with 1024 and 128 complex points, spectral width 14 and 32 ppm, and carrier frequency on water and 118.5 ppm for the proton and nitrogen dimension, respectively. 2D ^{13}C -HSQC experiments (pulse program HSQCETGPSISP2.2) were performed with 1024 and 256 complex points, spectral width 16 and 72 ppm, and carrier frequency on water and 36 ppm for the proton and carbon dimension, respectively. Intermolecular NOEs were measured by a 3D filtered NOE experiment (pulse program NOESYHSQCGPWGX13D) with 1024, 64, and 32 complex points and spectral width 14, 70, and 12 ppm in the protein proton, aliphatic carbon, and ligand proton dimension, respectively. The carrier frequencies were set on water for proton dimensions and 34.5 ppm for carbon dimension. Spectra were collected with 150 ms mixing time.

The chemical shift perturbation analysis for the apo and bound UCHL1 is described in a previous publication.¹¹⁹ Details for analysing the Intermolecular NOE data are described in Supporting Information.

3D NOE Determination

Intermolecular NOE crosspeaks were detected for 26 intermolecular contacts. Preliminary assignments were made for the NOE crosspeaks that matched in frequency with reported resonance assignments for aliphatic sidechains of UCHL1 (BMRB entry 17260). The BMRB assigned chemical shifts were first aligned with our measured spectra by minimizing the difference in ppm values between the BMRB entries and the peak positions in a ^{13}C -HSQC spectrum for unligated UCHL1. Eight intermolecular NOE crosspeaks overlaid peaks in both the unligated and bound ^{13}C -HSQC spectra and were given ambiguous assignments based on close matches in ppm values with the BMRB assignment list. This list of ambiguous assignments was inspected for residues near the active site pocket and these were selected for use as distance restraints in docking with CovDock (Schrödinger, LLC). Many of the docking computations failed to reach an acceptable complex structure. Docked poses were accepted for the case where distance-restrained docking was conducted with a single intermolecular NOE distance restraint between Ala 147 HB and H3 of **1**. Docking against the truncated form of UCHL1 without the N-terminal nine residues resulted in a pose with good interactions involving the oxyanion hole, and is the selected pose described in the main text.

Computational Docking

UCHL1 was prepared using Protein PrepWizard from PDB ID 2ETL using OPLS3 force fields within the Maestro suite version 2016-3 (Schrödinger LLC). Compound **1** was prepared within LigPrep generating possible states at $\text{pH } 7.0 \pm 2.0$, retaining specified chiralities using an OPLS3 forcefield. Docking of **1** within UCHL1's active site was performed using CovDock. The receptor was centered around cysteine 90, cysteine 90 was defined as the nucleophilic residue, and a nucleophilic addition to a triple bond was selected as the reaction type. A NOE constraint was defined, requiring the placement of ligand proton H3 to be between 1 and 6 angstroms from C β of alanine 147. No torsional constraints were defined. Resulting poses were analyzed using Pymol.

CHAPTER 3. OPTIMIZATION AND CHARACTERIZATION OF A COVALENT PEPTIDE-BASED UBIQUITIN C-TERMINAL HYDROLASE L1 INHIBITOR

Ubiquitin C-Terminal Hydrolase L1 (UCHL1) is a deubiquitinating enzyme (DUB) that is of great interest as a potential therapeutic target, yet few inhibitors are available to pharmacologically probe the enzyme. The most widely cited UCHL1 inhibitor, LDN-57444, suffers from chemical instability and is not effective in the hands of multiple researchers.

An alternative inhibitor identified during a counter screen for a viral protease, the tripeptide benzyloxycarbonyl-Val-Ala-Glu(γ -methoxy)-fluoromethylketone (VAEFMK), represents the only small molecule-bound co-crystal structure of UCHL1. With little biochemical or cellular data available for this inhibitor, we found it appropriate to pursue an in-depth characterization of this molecule and carry out medicinal chemistry optimization of the scaffold. Herein, we present the in-depth characterization of VAEFMK and derivatives in biochemical and cellular experiments, as well as describe the structure-activity relationship (SAR) for VAEFMK and analogs.

3.1 Introduction

Ubiquitination of substrate proteins plays a role in a number of cellular pathways including protein trafficking, DNA damage response, and proteasomal degradation.^{120–122} The formation of a covalent bond between the C-terminus carboxylic acid of ubiquitin (Ub) and a lysine side chain amine of substrate proteins results in an isopeptide bond. This bond formation is catalyzed by a series of cascading E1 (activating), E2 (conjugating), and E3 (ligating) enzymes, which often results in the addition of one or more Ub monomers in the form of a poly-ubiquitin chain.^{2–4} The complexity of this signaling event is increased by the number of lysine residues on Ub. Additional monomers can be attached to the initial Ub on the substrate-Ub complex through any of the seven lysine residues or even the N-terminal methionine residue, resulting in eight possible types of Ub-Ub linkages. In addition to this, both linear and branched architectures are possible.^{12,123,124} Together this forms the basis of the complex Ub-signaling pathway observed in eukaryotes.

The removal of ubiquitin is catalyzed by deubiquitinases (DUBs), of which there are approximately 100 in the human genome.⁸ The majority of these DUBs are cysteine proteases, although a family of DUBs, the JAMM proteases, do require a zinc cofactor for catalysis.¹² The

cysteine protease DUBs are categorized into six sub-families: ubiquitin specific proteases (USP), Machado-Josephin domain (MJD), Ovarian tumor proteases (OTU), Ubiquitin C-terminal hydrolases (UCH), and the more recently discovered MINDY and ZUFSP DUBs.^{10,11} Dysregulation of protein ubiquitination status is implicated in a number of disease states including cancer^{13,19,91} and neurodegeneration,^{18,90} and as such DUBs have emerged as potential therapeutic targets.^{94,125,126}

Ubiquitin C-terminal Hydrolase L1 (UCHL1) is a 25 kDa DUB whose ectopic expression is linked to a number of cancers.¹²⁷ Normally found in the central and peripheral nervous system, its physiological role under normal conditions is not well understood. It comprises 1-5% of the total soluble protein in the brain and is implicated in the progression of neurodegenerative diseases.¹²⁸ It is also considered an oncogene in a number of cancers including lymphoma,^{97,99,129} small-cell lung cancers,^{39,40,48} glioblastoma,⁴² and others.^{52,100,130} Additionally, expression of UCHL1 in these cancers often correlates with increased metastatic behavior, aggressiveness, and poor patient prognosis.^{25,27,48,86} Both genetic depletion of UCHL1 as well as transfection to introduce a catalytically inactive UCHL1 mutant reduced the ability of various cancer cell lines to metastasize.^{24,38} This suggests that pharmacological inhibition of UCHL1 is a potential therapeutic avenue for treatment of UCHL1-implicated cancers.

With a new set of reversible covalent inhibitors recently described, a new interest in UCHL1 probe development has occurred in the field.^{52,82,131} Covalent inhibition of UCHL1 represents a promising, novel approach to develop potent and selective inhibitors. However, these inhibitors currently suffer from non-selective toxicity in non-UCHL1 expressing cells, presumably due to the reactivity of the electrophilic cyanamide moiety that is responsible for covalently modifying UCHL1.⁸² To this end, we set out to characterize and perform SAR studies on a previously published inhibitor of UCHL1. The tripeptide benzyloxycarbonyl-Val-Ala-Glu(γ -methoxy)-fluoromethylketone (VAEFMK, **1**) (Figure 1) represents the only small molecule-bound co-crystal structure of UCHL1, though little biochemical and cellular information is reported.³³ Successfully characterizing this inhibitor and confirming on-target engagement in a cellular environment would serve to validate this molecular scaffold as a starting point for the development of a novel set of UCHL1 probes.

Covalent peptides have long been utilized as inhibitors for proteases, and a diverse set of electrophilic warheads have been used to varying degrees of success.¹³² Indeed, covalent peptide inhibitors that target the proteasome have been used as therapeutic agents in the treatment of multiple

myeloma, substantiating this class of molecules not only as promising starting points for optimization, but as endpoints in medicinal chemistry campaigns as well.^{133,134} Given the selectivity information of this compound,³³ we hypothesized that it would be a suitable starting point for optimization using structure and ligand-based drug design. To this end, we set out to characterize **1**, and analogs, in biochemical and cellular assays and study SAR around the scaffold with the goal to provide a more suitable pharmacologic probe for UCHL1 compared to LDN-57444,²⁹ as well as complement the recently reported cyanopyrrolidine-based probes 6RK73, MT-19, and IMP-1710 (Figure 3.1).^{52,82,131} Herein, we present the results of these studies, as well as validate on-target engagement in a cellular environment and toxicity data for **1** and analogs.

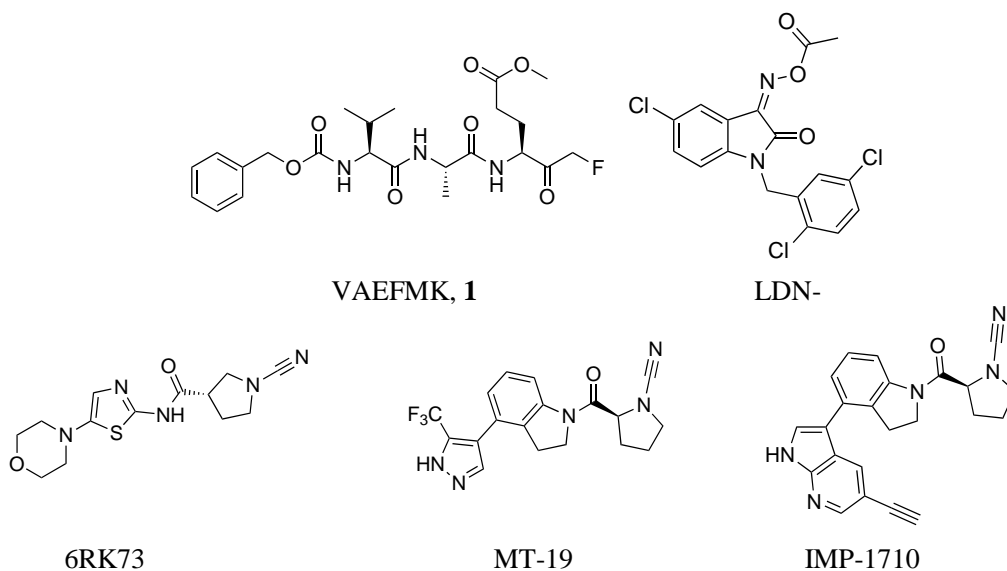


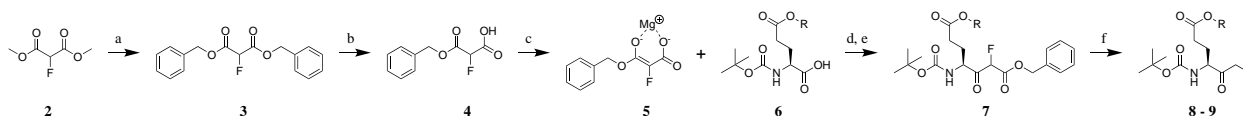
Figure 3.1 LDN-57444 and covalent inhibitors of UCHL1.

3.2 Results and Discussion

3.2.1 Chemical Synthesis of VAEFMK and Analogs

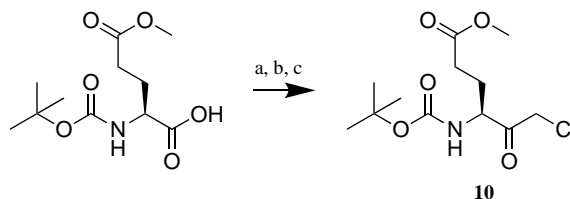
VAEFMK **1** and analogs were synthesized using variations to previously published protocols.^{135–138} In brief, to prepare the FMK containing intermediate (Scheme 3.1) the key fluorinating reagent was synthesized via transesterification of dimethyl fluoromalonate **2** with benzyl alcohol, resulting in dibenzyl fluoromalonate **3**. Hydrolysis of a single benzyl group yielded key reagent 3-(benzyloxy)-2-fluoro-3-oxopropanoic acid (MBF) **4**. The reagents could be converted to the magnesium enolate **5** and added to an activated ester of Boc-Glu(OMe)-OH or Boc-

Glu(OtBu)-OH **6**, forming intermediate **7**. This intermediate was isolated and immediately hydrogenated using H₂/PdC to yield the key building blocks Boc-Glu(OMe)-FMK **8** or Boc-Glu(OtBu)-FMK **9**.



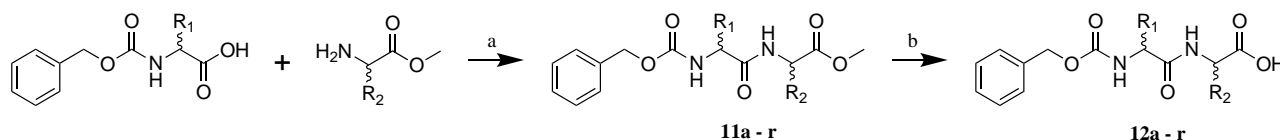
Scheme 3.1 Synthesis of Boc-Glu(OR)-FMK **8 - 9**. Reagents and conditions: a) benzyl alcohol (10 eq), TsOH (0.1 eq), toluene, 75 °C, 2 hr; b) NaOH (1.05 eq), *i*-PrOH, 45 °C, 70 min; c) isopropyl MgCl (2 eq), THF, 0 °C, 1 hr, crude to next step; d) CDI (1.1 eq), THF, 0 °C, 1 hr, crude to next step; e) **5** (2 eq), **6** (1 eq), THF, -20 °C - RT, 3.5 hr, crude to next step; f) H₂, Pd/C, toluene, RT, overnight. R = OMe, OtBu.

Boc-Glu(OMe)-CMK **10** was afforded by formation of an activated ester via CDI, followed by the nucleophilic addition of diazomethane, generated *in situ*, to form a diazoketone. Quenching the reaction with HCl in 1,4-dioxane provided the building block Boc-Glu(OMe)-CMK (Scheme 3.2).



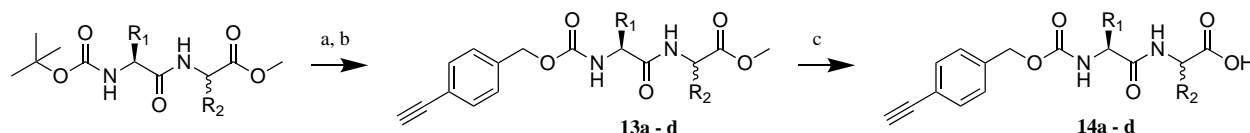
Scheme 3.2 Synthesis of Boc-Glu(OMe)-CMK **10**. Reagents and conditions: a) N-methylmorpholine (1.3 eq), Isobutyl Chloroformate (1.2 eq), THF, 0 °C, 45 minutes; b) Diazald (2.2 eq), Carbitor (1 mL), Ether (1 mL) 37% w/v KOH, 0 °C, 2 hr; c) 4 M HCl in 1,4-dioxane, until solution is not yellow, 0 °C, 30 minutes.

An amide bond was formed between the N-terminal Cbz-protected amino acid building blocks and C-terminal methylester protected building blocks to form **11a – r** (Scheme 3.3), followed by subsequent C-terminal deprotection using LiOH to form the desired Cbz-protected dipeptide acids **12a - r**.



Scheme 3.3 Synthesis of Cbz-protected dipeptide acid **12a - t**. Reagents and conditions: a) Carboxylic acid (1 eq), Amine (1 eq), N-methylmorpholine (4 eq), Isobutyl Chloroformate (1.5 eq), THF, 0 °C – RT, Overnight; b) LiOH (1.2 eq), 4:1 THF:H₂O, 0 °C, 3 hours.

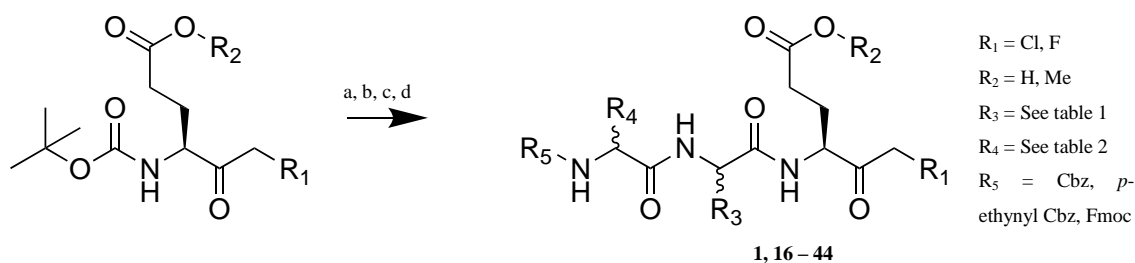
P-ethynyl-Cbz-protected dipeptide acids were generated in an analogous manner (Scheme 3.4). Here, a Boc-protected N-terminal dipeptide methylester was Boc-deprotected with HCl in 1,4-dioxane followed by the addition of *p*-ethynyl chloroformate to form intermediates **13a - d**. C-terminal deprotection using LiOH afforded the *p*-ethynyl-Cbz-protected dipeptide acids **14a - d**.



Scheme 3.4 Synthesis of *p*-ethynyl-Cbz-protected dipeptide acid **14a - d**. Reagents and conditions: a) 4 M HCl in 1,4-dioxane (11 eq), DCM, 30 minutes; b) *p*-ethynylchloroformate (1.01 eq), TEA (2.4 eq), THF, 0 °C – RT, Overnight; c) LiOH (1.2 eq), 0 °C, 4:1 THF:H₂O, 3 hours.

Fmoc-protected dipeptide acids were generated by treating the unprotected dipeptide with Fmoc-chloroformate, directly affording the desired intermediate **15**.

Deprotection of Boc-Glu(OR)-FMK provided the HCl salt of Glu(OMe)-FMK, Glu(OtBu)-FMK, or Glu(OMe)-CMK (Scheme 3.5) which could be coupled to an activated N-terminal-protected dipeptide (Cbz-XX, *p*-ethynyl-Cbz-XX, or Fmoc-XX) resulting in respective N-terminal protected tripeptide halomethylketones. Global deprotection of any side chain protecting group afforded the desired final products **1, 16 – 44**.



Scheme 3.5 Synthesis of carbamate-protected dipeptide acid **1**, **16 - 44**. Reagents and conditions: a) 4 M HCl in 1,4-dioxane (7.4 eq), 30 minutes, RT; b) carbamate-protected dipeptide acid (0.8 eq) (**12a – t**, **14a – d**, **15**), N-methylmorpholine (4 eq), Isobutyl Chloroformate (1.5 eq), THF, 0 °C, 45 minutes, then add product from step a, THF, 0 °C – RT, Overnight; d) 95:2.5:2.5 TFA:TIPS:H₂O, 1 hour, room temperature.

3.2.2 Structure-Activity Relationship for VAEFMK (**1**)

The *in vitro* inhibition of UCHL1 was determined by monitoring the cleavage of rhodamine 110 from substrate ubiquitin (Ub-Rho).¹⁰⁴ As a putative irreversible inhibitor of UCHL1, the potency of **1** did increase with increasing length of preincubation, confirming the irreversible nature of inhibition (Figure 3.2). After approximately 2 hours, the molecule had reached near maximum efficacy, with the half maximal inhibitory concentration (IC₅₀) value of 28.84 μM (95% confidence interval (CI) = 16.17 μM to 51.15 μM). Thus, a 3-hour preincubation period was selected for the structure-activity relationship (SAR) comparison of all analogs.

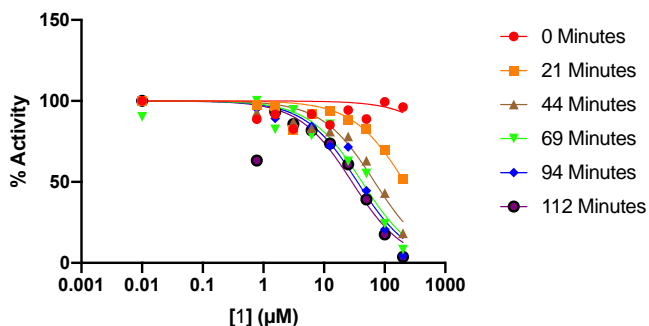


Figure 3.2 Time-dependent inhibition of His-UCHL1 by **1**. IC₅₀ curves for His-UCHL1 treated with **1** at various points in time shows increasing potency with increasing length of incubation.

The *in vitro* efficacy of covalent inhibitors can be broken down into the reversible interactions that contribute to binding affinity and the covalent reactivity of the electrophilic “warhead”. The fluoromethylketone of **1** is very slow to react with the active site cysteine, requiring approximately 2 hours to reach nearly full occupancy. Chloromethyl ketones are more reactive than fluoromethyl ketones, and have been shown to be 3-fold more effective in matched molecular pair analogs.¹³² Therefore, we rationalized that the efficacy of **1** could be improved simply by increasing the reactivity of the warhead. To test this hypothesis, the fluoromethylketone of **1** was substituted for a chloromethyl ketone, resulting in compound **16** (Figure 3.3). Surprisingly, subsequent testing revealed a complete loss of activity against UCHL1.

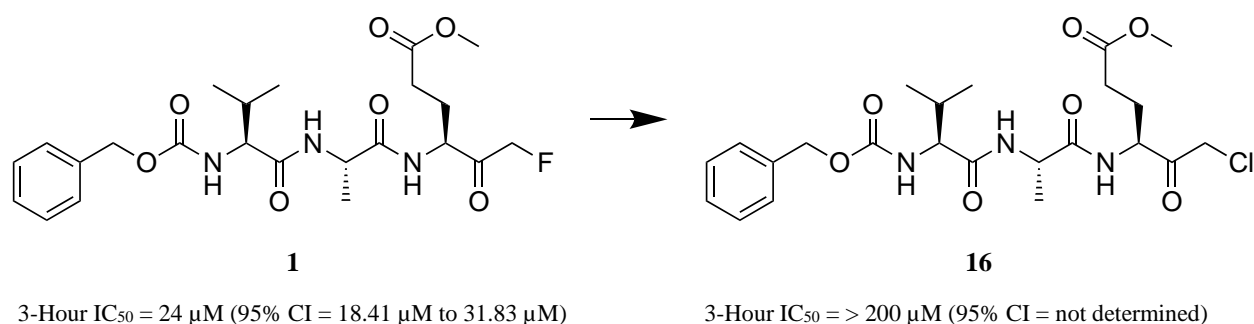


Figure 3.3 Chemical structures and 3-hour IC₅₀ values for **1** and **16**.

The Ub-Rho assay uses dithiothreitol (DTT) as a sulfur-based reducing agent to keep the active site cysteine in a reduced state for reactivity. We hypothesized that perhaps the chloromethylketone was too prone to nucleophilic attack by sulfur. To investigate this possibility a high-performance liquid chromatography (HPLC) assay was employed to assess stability of the molecule in the presence of sulfur, glutathione. The Cbz containing end group was not visible in the UV region necessary to monitor the molecule stability, thus, Fmoc-protected analogs in place of Cbz for **1** and **16** were synthesized resulting in the analogous fluoromethylketone **43** and chloromethylketone **44**, allowing for observation at 254 nm in an HPLC chromatogram (Figure 3.4). **43** and **44** were incubated at 37 °C with either the model binucleophile glutathione or DMSO control. Glutathione was chosen as the model sulfur-containing nucleophile because it would provide a shift in elution time on the HPLC chromatogram while DTT did not. Peak areas for **43** and **44** in the presence of glutathione could then be determined and normalized to samples incubated with DMSO to determine the percent of unmodified inhibitor remaining over time, confirming the chemical

reactivity of the chloromethylketone (Figure 3.4). As expected, the fluoromethylketone **43** (half-life = n.d.) was unreactive towards glutathione,¹³² while the chloromethylketone **44** (half-life = 14.23 minutes) reacted with glutathione more quickly than both **43** and cyanamide inhibitor MT-19 (half-life = 67.03 minutes). The loss of activity for **16** could be explained for a few reasons. With the short half-life of chloromethylketones in the presence of a thiol, it is possible that **16** reacts with the excess reducing agent DTT in the well plate before it is able to covalently modify UCHL1. However, analogous warheads containing chlorines are able to inhibit UCHL1 under the same assay conditions in our lab, suggesting that this is not a contributing factor to the loss of efficacy (data not shown). Alternatively, because chlorine atoms (0.99 Å) are 33% larger than fluorine atoms (0.64 Å), it is possible that **16** is occluded from the active site due to steric repulsion when considering the added bulk from the glutamic acid side chain. Although other warheads are possible to install to further tune the reactivity of the probe, we instead decided to focus on improving the reversible interactions by modifying the amino acid side chains of **1**.

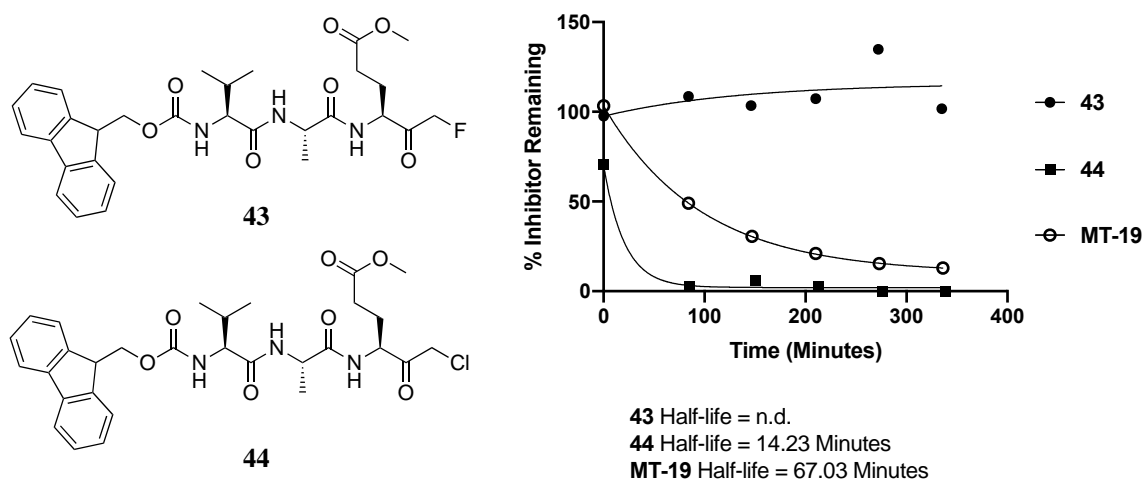


Figure 3.4 Warhead half-life analysis. Fluoromethylketone **43** is unreactive towards model bionucleophile glutathione, while chloromethylketone **44** and MT-19 have half-life values of 14.23 minutes and 67.03 minutes, respectively. n.d. = not determined.

Analysis of the UCHL1-**1** co-crystal structure shows few hydrogen bond interactions (Figure 3.5).³³ A hydrogen bond is observed between the carbonyl oxygen of the fluoromethylketone and the amide nitrogen of C90, as well as the ϵ^2 nitrogen of UCHL1's Q84 side chain. The amide carbonyl between the glutamic acid methylester and alanine of **1** forms a hydrogen bond with backbone amide

of N88. Finally, the ϵ^2 oxygen of the glutamic acid methyl ester of **1** forms a hydrogen bond with an R153 side chain guanidine proton. Thus, we hypothesized that removal of the glutamic acid methylester of matched molecular pair analog **19** (R_2) to provide the glutamate side chain (**17**) would replace the R153 hydrogen bond with a salt bridge interaction (Figure 3.6). Unexpectedly, this modification resulted in a complete abrogation of activity, even after 6 hours of incubation with the enzyme. One possible reason for the loss of efficacy is the potential for an intramolecular cyclization between the glutamate oxygen and the fluoromethylketone carbonyl, resulting in the formation of a six-membered lactone (Figure 3.7). A similar observation has been documented for the C-terminal aspartic acid fluoromethylketone, which undergoes a pH dependent cyclization as observed by NMR.¹³⁵ However, **1** is known to inhibit UCHL1 in cells, where the ester is likely cleaved by an esterase to provide the unmasked carboxylic acid,¹³⁹ bringing into question the biological significance of this structure.

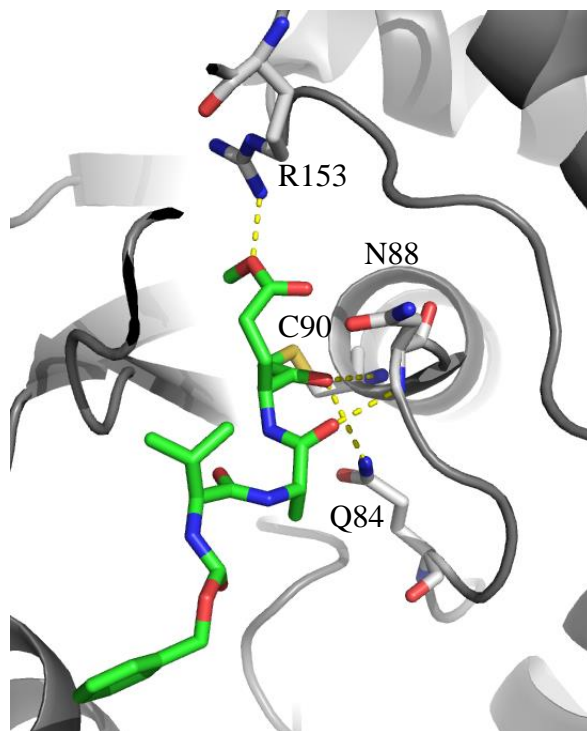


Figure 3.5 Intermolecular interaction between **1** and UCHL1. Hydrogen bond interactions (yellow dashed lines) between **1** (green sticks) and UCHL1 (grey cartoon and sticks).

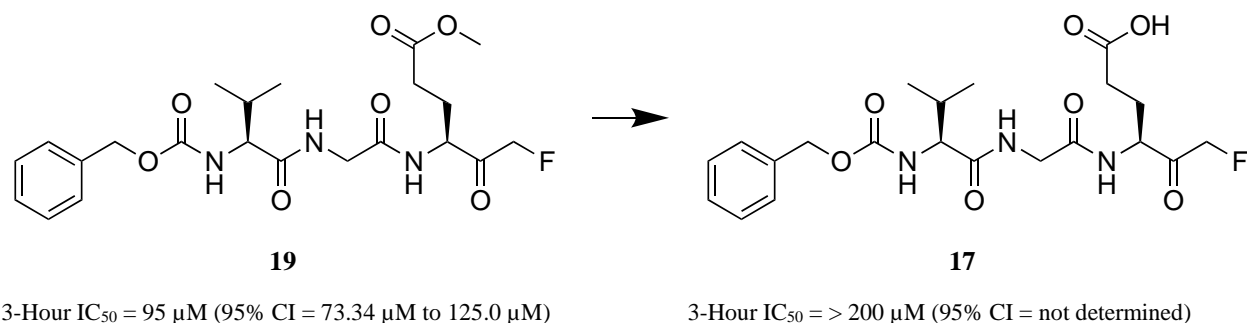


Figure 3.6 Chemical structures and 3-hour IC₅₀ values for **19** and **17**.

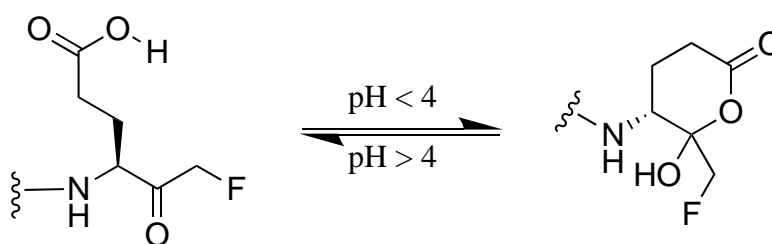


Figure 3.7 Potential structure of the pH dependent cyclization of glutamic acid fluoromethylketone.

Next, we turned to elucidating the SAR at positions R₃ and R₄. A set of amino acids were selected to investigate the contributions of stereochemistry, chain length, bulk, polarity, and charge at positions R₃ and R₄. The analog with glycine (**19**) at R₃ displayed an IC₅₀ value of 95 μM, representing a 4-fold loss in efficacy (Table 3.1). Whether this is due to a loss of non-polar interactions or an increased penalty in entropy upon binding due to the decreased rigidity of glycine is unclear and requires further investigation. Inverting the stereochemistry at R₃ by replacing *L*Ala with *D*Ala (**18**) resulted in a complete loss of activity (IC₅₀ = > 200 μM). While this modification does not improve the inhibitory efficacy against UCHL1, it does provide a structurally similar compound that may be used as a control in place of DMSO for future biochemical and cellular experiments. Further increasing bulk by installing a valine (**20**) in place of alanine (**1**) also resulted in a complete loss in activity, displaying an IC₅₀ value of > 200 μM. Serine (**23**) at R₃ is tolerated (IC₅₀ = 100 μM), though results in a 4-fold loss in efficacy. All analogs tested with side chains larger than a serine were inactive. In hindsight, this could be expected as the alanine side chain of **1** makes contact with the surface of UCHL1 in the ligand-bound crystal structure with little room for

increasing steric bulk. Due to the limited success for improving potency with modifications at this position, future efforts may benefit from rigidifying the inhibitor at this position,¹⁴⁰ while maintaining the nearby protein-ligand interactions observed in the co-crystal structure. Substituting the entire alanine “building block” for a proline or amide isostere such as an oxadiazole may serve to add drug-likeness while maintaining the key hydrogen bonds.¹⁴¹

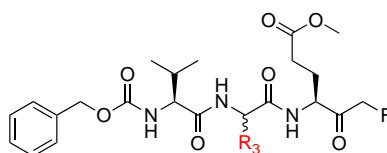


Table 3.1 Structure-activity relationship for substituents at R₃.

I.D.	R ₃	IC ₅₀ (μM)	95% CI (μM)
1	Ala	24	18.41 to 31.83
18	DAla	> 200	n.d.
19	Gly	95	73.34 to 125.0
20	Val	> 200	n.d.
21	Leu	> 200	n.d.
22	Phe	> 200	n.d.
23	Ser	100	76.89 to 131.5
24	Thr	> 200	n.d.
25	Asn	> 200	n.d.
26	Asp	> 200	n.d.
27	Glu	> 200	n.d.

Experiments were performed in technical triplicate and averages are reported. IC₅₀ values are from 3 hours of preincubation with UCHL1. Amino acids are L unless specified otherwise. n.d. = values could not be accurately determined. Errors reported as 95% confidence interval (95% CI).

SAR at R₄ displayed a more defined trend, with added hydrophobic bulk increasing the efficacy of the analogs (Table 3.2). Removal of the side chain entirely (**29**) results in a complete abrogation of activity against UCHL1. Simply extending the alkyl chain a single carbon out from the peptide backbone rescues activity (**30**), though the molecule is 3-fold less effective (IC₅₀ = 76 μM) than parent compound **1**. Increasing the chain length compared to **1** but keeping the bulk consistent results in compound **31** with leucine at R₄, which is equipotent to the parent compound

(IC₅₀ = 23 μM). It is not until a much bulkier substituent is installed, phenylalanine (**32**), that the efficacy is improved with an IC₅₀ value of 13 μM.

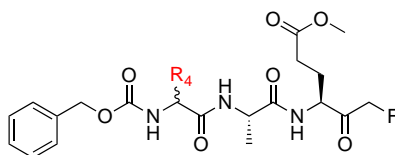


Table 3.2 Structure-activity relationship for substituents at R₄.

I.D.	R ₄	IC ₅₀ (μM)	95% CI (μM)
1	Val	24	18.41 to 31.83
28	DVal	> 200	n.d.
29	Gly	> 200	173.2 to 316.1
30	Ala	76	53.56 to 83.82
31	Leu	23	16.63 to 32.03
32	Phe	13	9.998 to 17.89
33	Ser	185	155.9 to 220.8
34	Thr	100	80.26 to 125.1
35	Asn	119	86.50 to 167.9
36	Asp	>200	n.d.

Experiments were performed in technical triplicate and averages are reported. IC₅₀ values are from 3 hours of preincubation with UCHL1. Amino acids are L unless specified otherwise. n.d. = values could not be accurately determined. Errors reported as 95% confidence interval (95% CI).

While larger hydrophobic functional groups are tolerated at R₄ favoring increased bulk, polar functional groups are not tolerated regardless of size. The analog containing a threonine (**34**) displayed an IC₅₀ value of 100 μM, which was a 4-fold reduction in activity over the parent valine (**1**) at the R₄ position. Given that threonine and valine are roughly the same size, the decrease in activity is likely attributable to the incorporation of a polar alcohol to the side chain in place of the lipophilic valine rather than any change in sterics. In a similar vein, it is apparent that negatively charged functional groups are disfavored, with aspartic acid (**36**) at R₄ resulting in an inactive compound while asparagine (**35**), though a less potent inhibitor, remains active (IC₅₀ = 119 μM). Finally, in agreement with the SAR at R₃, inversion of the stereocenter to DVal (**28**) also results in an inactive compound (IC₅₀ > 200 μM), though this again serves as an excellent control for

biochemical and cellular studies. Taken together, it is apparent that natural amino acids of increasing chain length and hydrophobic nature are preferred at this position.

An SAR pattern at R₅ showed the addition of an alkyne to the para-position on the Cbz protecting group improved the efficacy for three sets of matched molecular pairs of analogs (Table 3.3). For example, the efficacy of parent compound **1** was improved 3-fold by the addition of the alkyne (**38**), with this analog displaying an IC₅₀ value of 7.7 μM and 26-fold selectivity for UCHL1 over UCHL3. Though the increase in potency with the addition of the alkyne was not as drastic for the other matched molecular pair analogs (**19** → **37** and **32** → **40**), it was apparent that the addition of an alkyne to the Cbz group was beneficial to the efficacy of this scaffold. Additionally, both **37** and **40** maintained a high degree of selectivity towards UCHL1 over UCHL3 (Table 3.3). The alkyne moiety was initially added to the Cbz group based on observations from the ligand-bound crystal structure (PDB entry 4DM9). In this structure the Cbz group is largely solvent exposed and we rationalized that this would provide a facile location for the addition of an alkyne without drastically altering the efficacy of the inhibitor so that this molecule could be used for copper-catalyzed azide-alkyne cycloaddition (CuAAC) “click” chemistry experiments to test the validity of these compounds as intracellular probes.^{115,116,118} However, because the electron density of this group was weak in the ligand-bound crystal structure, it is difficult to determine how the alkyne may be facilitating new contributions to the binding of the analogs. The effect of the alkyne may be due to added non-polar interactions directly between the alkyne carbons and UCHL1, or potentially because of the altered electronic effects of the Cbz benzyl group. Future efforts may benefit from additional SAR at this position to explore the role of alkyl substitution and electron-withdrawing or donating groups on the benzyl ring.

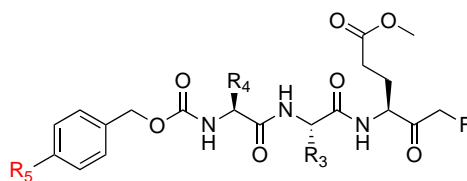


Table 3.3 Structure-activity relationship for substituents at R₅.

ID	R ₄	R ₃	R ₅	L1 IC ₅₀ (μM)	95% CI (μM)	L3 IC ₅₀ (μM)	95% CI (μM)
19	Val	Gly	H	95	73.34 to 125.0	N/A	N/A
37			CCH	62	48.49 to 79.56	N/A	N/A
1	Val	Ala	H	24	18.41 to 31.83	> 200	n.d.
38			CCH	7.7	6.108 to 9.746	> 200	n.d.
32	Phe	Ala	H	13	9.998 to 17.89	N/A	N/A
40			CCH	11	8.931 to 13.82	>200	n.d.

Experiments were performed in technical triplicate and averages are reported. IC₅₀ values are from 3 hours of preincubation with UCHL1 (L1) or UCHL3 (L3). Amino acids are L unless specified otherwise. n.d. = values could not be accurately determined. N/A = not applicable. Errors reported as 95% confidence interval (95% CI).

Optimization of **1** was difficult and few improvements to the molecule were made. Rather, the bulk of information gained about this molecular scaffold includes modifications that are not tolerated. However, this information remains important for future efforts. Outside of the four observed hydrogen bonds in the co-crystal structure, it appears that the side chains are important for recognition more-so than increasing the affinity of **1** for UCHL1. Future efforts may benefit from structure-based design, using computational tools to generate a pharmacophore-based on the SAR described in this section. Focusing on maintaining the observed interactions while searching for alternative molecular scaffolds may provide an opportunity to explore more drug-like space, in addition to tuning the reactivity of the electrophilic warhead to increase the efficacy of the inhibitor.

Finally, satisfying this pharmacophore may continue to confer a high degree of selectivity for UCHL1 over UCHL3. UCHL1 and UCHL3 share a high level of sequence homology and as such, the selectivity of the fluormethylketone analogs are impressive. Analysis of the UCHL1:**1** co-crystal structure (PDB entry 4DM9) overlaid with the UCHL3 crystal structure (PDB entry 1UCH) may provide a rationale behind the experimentally determined selectivity (Figure 3.8). The residues on UCHL1 that interact with **1** (Q84, N88, and C90), excluding R153 which is not modeled in 1UCH, are identical to the analogous residues on UCHL3 (Q89, N93, and C95). In fact, these residues in

both proteins are in a close enough proximity that it is feasible that **1** could maintain the same interactions upon binding to both proteins. However, the H3 helix of UCHL3 that corresponds to the $\alpha 3$ helix of UCHL1 extends an additional 2 amino acids, extending the length of the α -helix approximately 6 Å into the analogous binding site on UCHL3 (Figure 3.8). Because of this added helical structure, it is likely that the binding of **1** to UCHL3 would be precluded by unfavorable steric interactions with H3 and the requisite hydrogen bond interactions would not occur, conferring selectivity towards UCHL1.

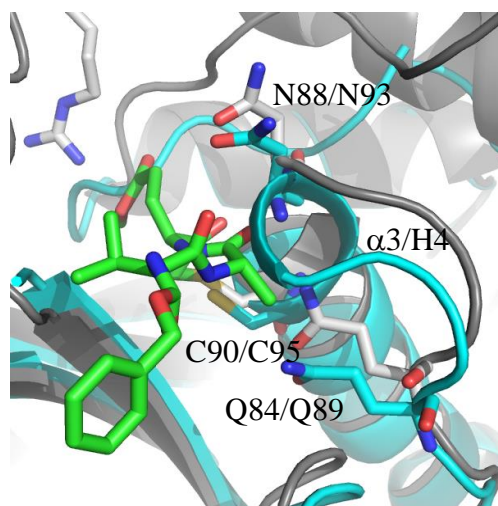


Figure 3.8 Overlay of the UCHL1:**1** complex and UCHL3. **1** (green sticks) binding to UCHL1 (grey) (PDB entry 4DM9) overlaid with the crystal structure of UCHL3 (cyan) (PDB entry 1UCH). Residues and helices are labeled as (UCHL1/UCHL3).

3.2.3 Binding Characterization and Kinetic Evaluation of Fluoromethylketone Analogs

Irreversible covalent inhibitors may be further characterized by determining the reversible binding constant (K_I) as well as the rate of the covalent bond formation under saturating conditions (k_{inact}).^{106,108,142} By determining the IC_{50} over the course of various timepoints, the first-order rate constant (k_{obs}) was calculated. Plotting the k_{obs} as a function of inhibitor concentration generated a curve that could be fit using the equation $Y = k_{\text{inact}} * X / (K_I + X)$ (Figure 3.9).¹⁴³ For parent compound **1**, these values were determined to be 60.04 μM and 0.0173 s^{-1} , resulting in a k_{inact}/K_I value of 288.05 $\text{M}^{-1}\text{s}^{-1}$ and an R^2 of 0.9623 (Table 3.4). In comparison, the k_{inact}/K_I values for the two more potent analogs from the SAR studies were 810.0 $\text{M}^{-1}\text{s}^{-1}$ and 208.4 $\text{M}^{-1}\text{s}^{-1}$ for **38** and **40**, respectively. This was unexpected for **40**, as **40** was more effective than **1** during the previous enzymatic activity assays

with a set preincubation of 3 hours. However, because covalent inhibitors become more potent over time,¹⁰⁸ it is possible that the discrepancy between IC₅₀ values and $k_{\text{inact}}/K_{\text{I}}$ values may be attributed to differences in the length of preincubation. This underscores the importance of determining the $k_{\text{inact}}/K_{\text{I}}$ value for key analogs to robustly determine inhibitor efficacy.

To further characterize **1**, it was necessary to determine whether the type of inhibition was competitive, uncompetitive, or non-competitive. The co-crystal structure of **1** with UCHL1 reveals that UCHL1 approaches the active site on the opposite face as Ub. **1** is able to bind to UCHL1 in the *in vitro* Ub-Rho enzyme activity assay, which is in the absence of substrate. This suggests that it is not behaving as an uncompetitive inhibitor. As **1** and Ub both compete for the same active site but bind to distinctly different surfaces of UCHL1, it seemed possible that **1** might be behaving as either a competitive or non-competitive inhibitor. This was investigated by preincubating 5 μM His-UCHL1 with an excess of **1** (2 mM) or DMSO overnight at room temperature. After removing the excess **1**, the ability of UCHL1 to bind to Ub was assessed by biolayer interferometry (BLI). The dissociation constant (K_{d}) of His-UCHL1 towards Ub in the presence of DMSO was similar to previously published affinities, while the presence of **1** completely abrogated the ability of UCHL1 to interact with Ub (Figure 3.12). Taken together, these data suggest that **1** is a competitive inhibitor, either by precluding the Ub-tail to feed into the catalytic active site of UCHL1 even though the rest of the inhibitor positions itself away from the canonical Ub-binding site or by repositioning the cross-over loop upon binding to the active site to sterically hinder Ub binding.

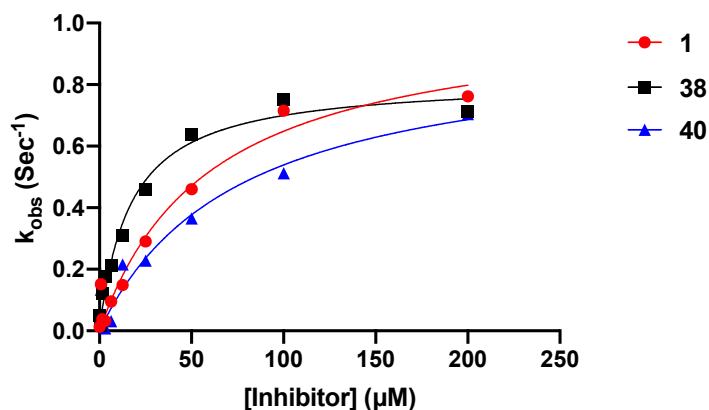


Figure 3.9 Inactivation kinetics for FMK analogs. k_{inact}/K_I plots for His-UCHL1 treated with **1**, **38**, and **40** (Values are 288.05 M⁻¹S⁻¹, 813.3 M⁻¹S⁻¹, and 209.9 M⁻¹S⁻¹ for **1**, **38**, and **40**, respectively).

Table 3.4 k_{inact}/K_I values for **1**, **38**, and **40** versus UCHL1.

I.D.	k_{inact} (s ⁻¹)	95% CI (s ⁻¹)	K_I (μM)	95% CI (μM)	k_{inact}/K_I (M ⁻¹ s ⁻¹)	R ²
1	0.0173	0.014 to 0.234	60.04	32.21 to 117.8	288.1	0.9623
38	0.0136	0.012 to 0.015	16.79	11.00 to 25.39	810.0	0.9779
40	0.0157	0.011 to 0.026	75.32	32.91 to 201.9	208.4	0.9478

Experiments were performed in technical triplicate and averages are reported. Errors reported as 95% confidence interval (95% CI).

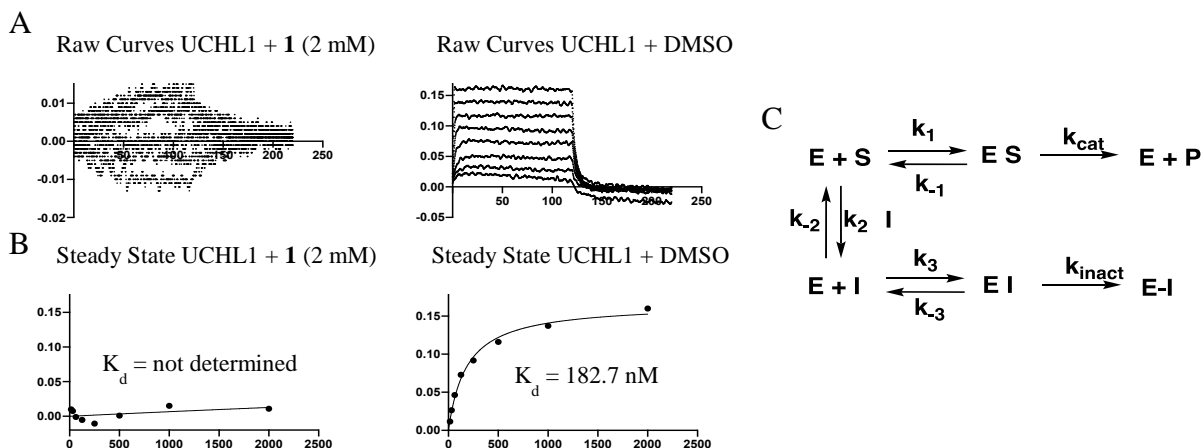


Figure 3.10 **1** is a competitive inhibitor. **A**) Biolayer interferometry association and dissociation curves, and **B**) steady state binding curves. **C**) Model of **1** as a competitive, covalent inhibitor of UCHL1.

3.2.4 Cellular Characterization of Fluoromethylketone Analogs

Fluoromethylketone Inhibitor Efficacy in Myeloma Cells

UCHL1 level of expression, as well as its enzymatic activity, is correlated with increased metastatic behavior and poor patient prognosis in a number of cancers including small-cell lung cancer,^{37,38} myeloma,¹⁰⁰ and lymphoma.^{28,44,97,99,129} To evaluate **1** and analogs in a cellular context, three previously validated cell lines were utilized based on their sensitivity to UCHL1 depletion: SW1271 (small-cell lung cancer), KMS11, and KMS12 (myeloma cell lines).⁸² KMS11 cells express UCHL1 and are sensitive to genetic depletion using shRNA, whereas KMS12 cells do not express UCHL1 and are not sensitive to genetic depletion using the same shRNA, providing a good control for evaluating off-target effects of UCHL1 inhibitors.⁸² Consistent with their reported sensitivity to UCHL1 depletion KMS11 cells dosed with 100 μ M **1** exhibited reduced proliferation compared to DMSO controls after 24, 48, 72 and 96 hour timepoints (Figure 3.11). Alternatively, KMS12 cells, which are not reported to be sensitive to UCHL1 genetic depletion, showed reduced growth at the 24 hour timepoint but regained proliferation ability at the 72 and 96 hour timepoints suggesting these cells are not sensitive to **1** (Figure 3.8). These results suggest that these analogs selectively inhibit UCHL1 in KMS11 cells. To confirm on-target engagement in KMS11 cells, a Ub activity-based probe (ABP) gel-shift assay was employed.¹⁴⁴ Using hemagglutinin-tagged Ub-vinylmethylester (HA-Ub-VME) to examine the activity of **1** in KMS11 cells, an immunoblot was performed. Blotting

for UCHL1 showed a dose-dependent decrease in HA-Ub-UCHL1 complex formation with increasing concentration of **1**, confirming on-target engagement of UCHL1 in cells (Figure 3.12 top). Blotting for HA revealed that **1** exhibited dose-dependent decrease primarily in HA-Ub-UCHL1 complex formation, although a higher exposure showed another DUB may also be inhibited at 250 μ M, corresponding to the molecular weights of one of the other UCH family members UCHL5 (Figure 3.12 bottom). However, no other DUBs in the KMS11 cell line showed any changes in complex formation upon treatment with **1** suggesting selectivity for UCHL1 within the DUBs expressed in this cell line and corroborating the observed UCHL1-dependent reduction in cell proliferation. However, further experiments are needed to confirm that **1** does not covalently modify any off-targets.

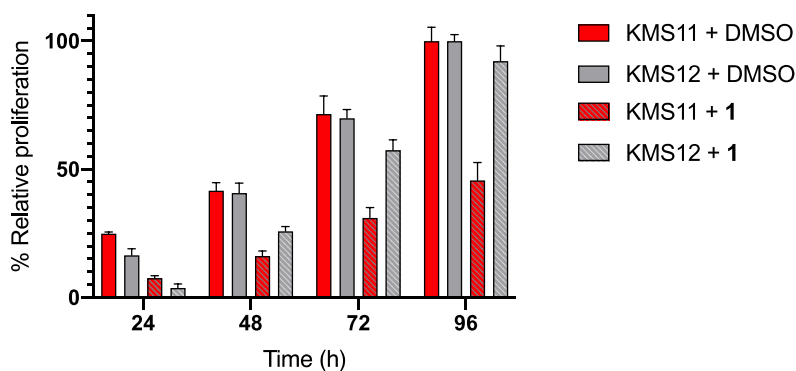


Figure 3.11 Compound **1** reduces KMS11 cell proliferation. KMS11 and KMS12 show differential abilities to proliferate in the presence of UCHL1-specific inhibitors **1** at 100 μ M.

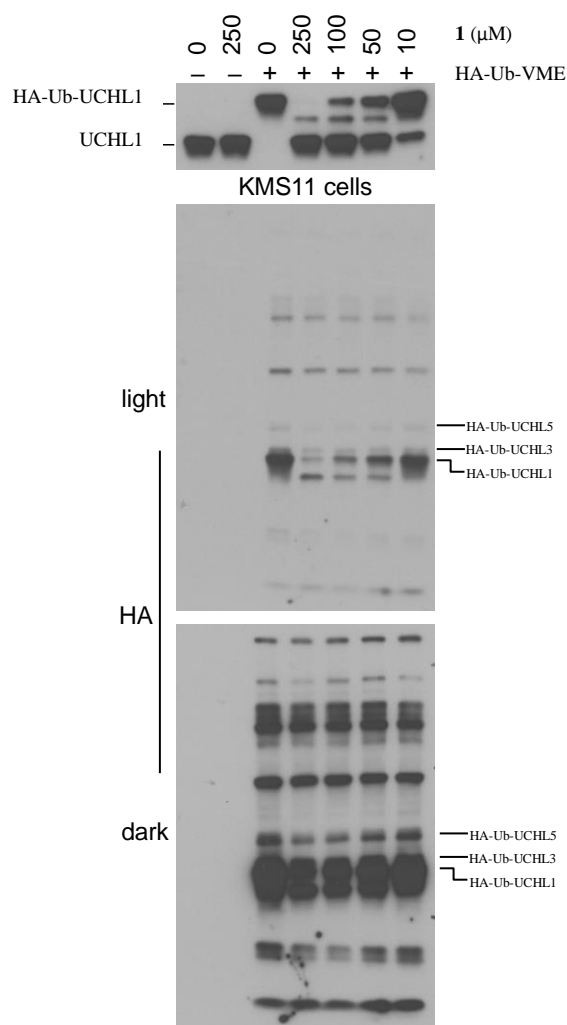


Figure 3.12 Immunoblots from KMS11 cells treated with **1**. (Top) Anti-UCHL1 blot showing UCHL1 and the covalent HA-Ub-UCHL1 adduct. Light (Middle) and dark (Bottom) exposure anti-HA blot to show all HA-Ub-DUB adducts. Inhibited DUBS will display a dose-dependent decrease in HA signal as is observed for UCHL1. Slight inhibition is observed for UCHL5 at 250 μM.

Fluoromethylketone Inhibitor Efficacy in Small Cell Lung Cancer Cells

SW1271 small-cell lung cancer cells are dependent on UCHL1 to promote cell migration and metastasis.⁸² Genetic depletion of UCHL1 via shRNA (3.13A) reduces the proliferation of SW1271 cells compared to pLKO vector controls, though complete depletion of UCHL1 does not fully kill cells (Figure 3.13B), suggesting that UCHL1 is not required for cell survival. Treatment of SW1271 cells with fluoromethylketones **1** and **38** (100 μ M) has no effect on the cell viability, whereas chloromethylketones **16** and **39** both kill the cells in a dose-dependent manner as monitored by a CellTiter-Glo assay (CC_{50} = 0.156 μ M and 0.176 μ M respectively) (Figure 3.13C). **16** and **39** are potently toxic towards SW1271 cells, killing them at a concentration of 10 μ M. Even complete depletion of UCHL1 by shRNA does not kill these cells, suggesting that chloromethylketones **16** and **38** engage off-targets resulting in non-specific toxicity towards SW1271 cells while the fluoromethylketone analogs appear to remain selective.

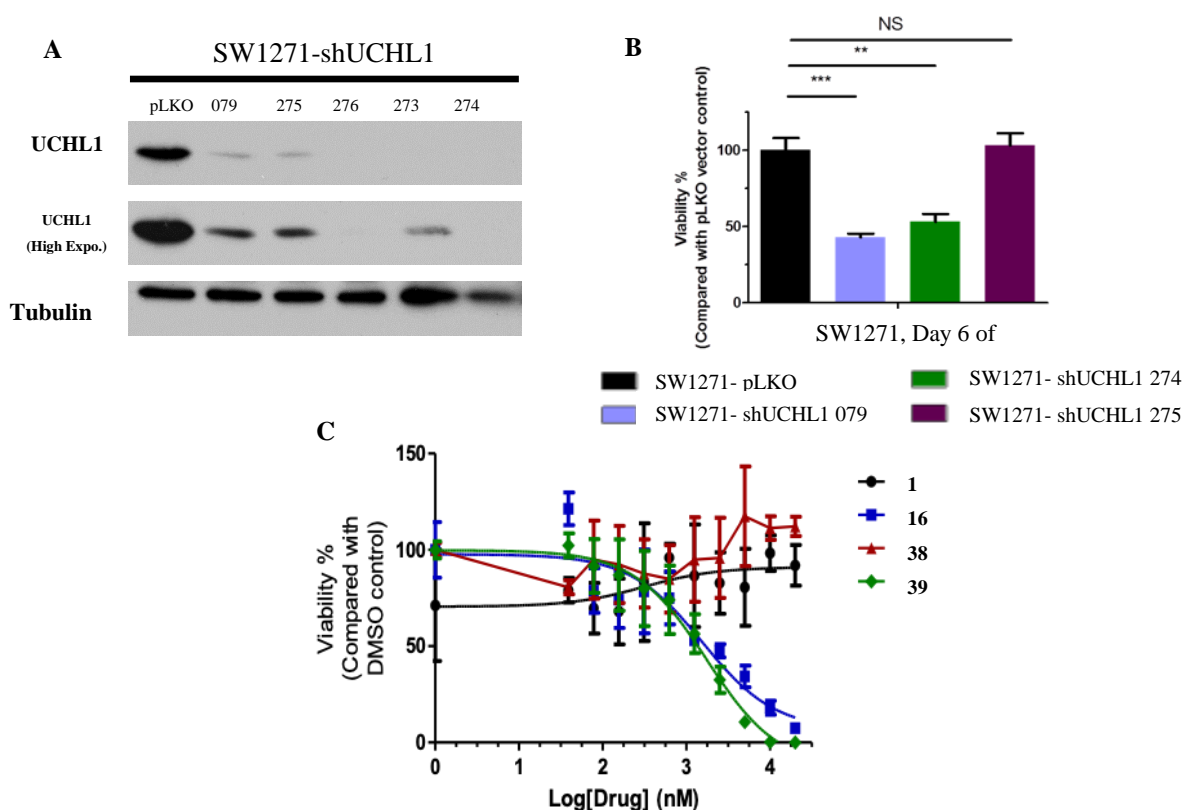


Figure 3.13 Compound **1** and **38** do not reduce SW1271 cell viability. **A**) Genetic depletion of UCHL1 by shRNA. **B**) Cell viability is reduced upon genetic depletion of UCHL1 (**: $P < 0.01$, ***: $P < 0.001$). **C**) SW1271 cell viability after treatment with fluoromethylketones **1** and **38** and chloromethylketones **16** (CC_{50} = 0.156 μ M) and **39** (CC_{50} = 0.176 μ M).

To confirm on-target engagement in SW1271 cells, a Ub activity-based probe (ABP) gel-shift assay was again employed.¹⁴⁴ Blotting for UCHL1 showed the expected shift in molecular weight upon reaction with HA-Ub-VME compared to UCHL1 alone. **38** inhibited UCHL1 in SW1271 cell lysate in a dose-dependent manner, evidenced by the corresponding decrease in the HA-Ub-UCHL1 complex formation with increasing concentration of **38** (Figure 3.14 top). Blotting for HA showed that the only visible HA-Ub-DUB complex with an altered band intensity corresponding to the amount of inhibitor added was in agreement with the molecular weight of HA-Ub-UCHL1 (Figure 3.14 bottom).

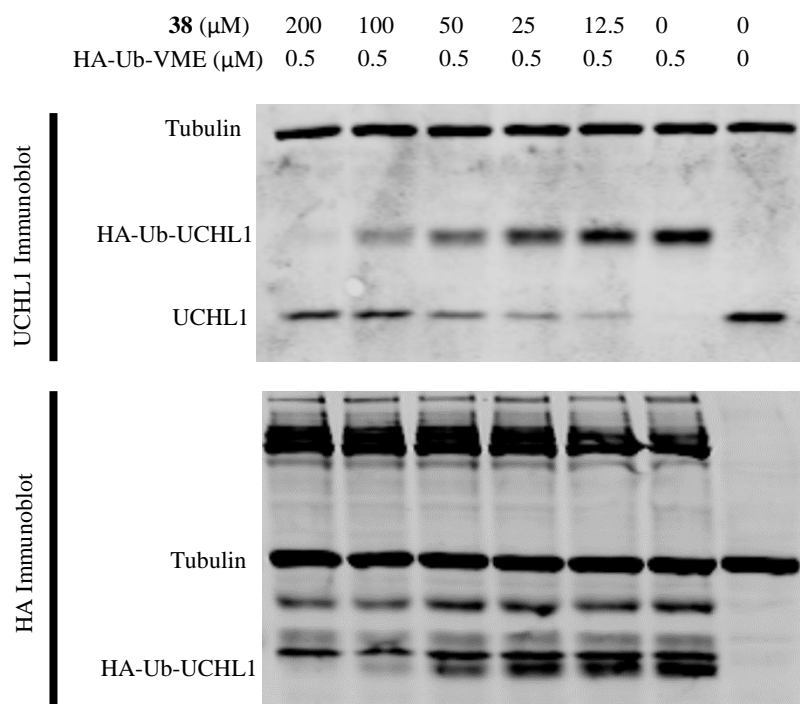


Figure 3.14 Compound **38** engages UCHL1 in SW1271 cell lysate. SW1271 cell lysate was incubated with **38** for 3 hours at room temperature before the addition of HA-Ub-VME. This was incubated for an additional 30 minutes before adding 4X Laemmli buffer and heat denaturing at 95 °C for 5 minutes. UCHL1 immunoblot shows a dose-dependent decrease in HA-Ub-UCHL1 formation with increasing concentrations of **38**. HA immunoblot shows only one band that decreases corresponding to the amount of **38**, which matches the molecular weight of HA-Ub-UCHL1.

Blotting for UCHL1 confirmed engagement of UCHL1 by **38** in intact cells, where a 100 μM treatment almost completely prevented the interaction between HA-Ub-VME and UCHL1 compared

to a DMSO treated control as evidenced HA-Ub-ABP gel shift assay (Figure 3.15A). Blotting for HA corroborated the results from the cell lysate treatment; only the band corresponding to HA-Ub-UCHL1 was reduced in the **38** treated sample compared to the DMSO treated control (Figure 3.15B). Taken together, this data suggests that **38** engages UCHL1 selectively in intact SW1271 cells. However, it is possible that inhibitor interacts non-specifically with enzymes that are not DUBs. Thus, a global profiling of target engagement is necessary to confirm the selectivity of the inhibitor.

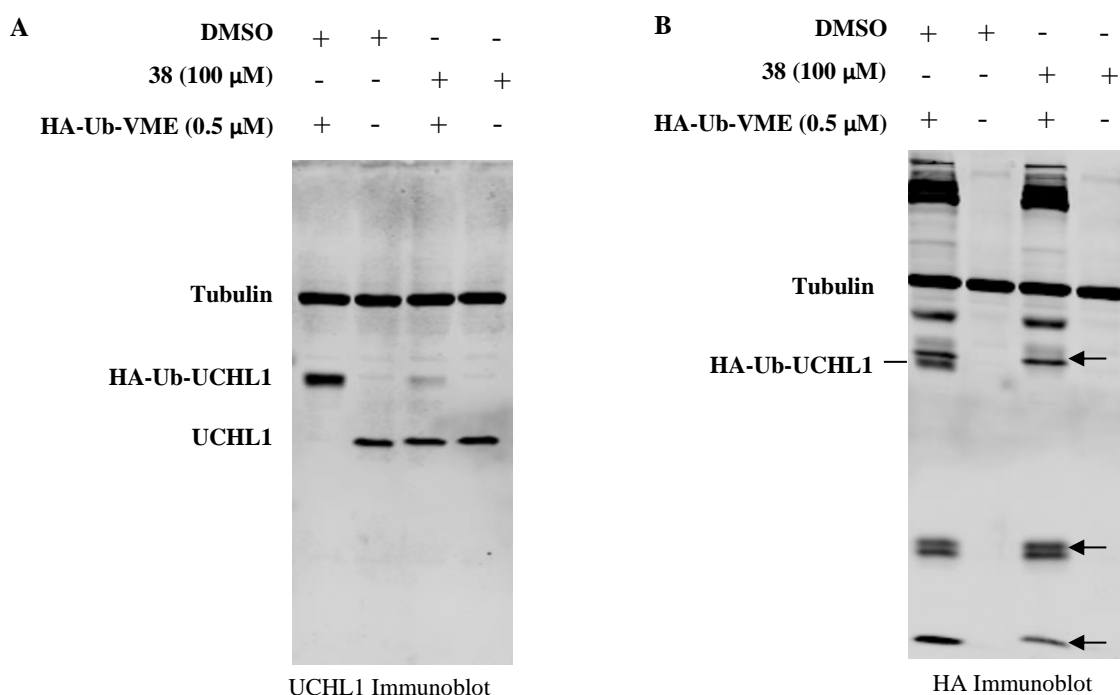


Figure 3.15 Compound **38** selectively inhibits UCHL1 in intact SW1271 cells. Intact SW1271 cells pretreated with DMSO or **38** were reacted with HA-Ub-VME. This was incubated for an additional 30 minutes before adding 4X Laemmli buffer and heat denaturing at 95 °C for 5 minutes. **A)** UCHL1 immunoblot shows complete inhibition of the HA-Ub-UCHL1 complex compared to the DMSO control. **B)** HA immunoblot shows that the only HA-DUB band that decreases in the cells treated with **38** compared to DMSO corresponds to HA-Ub-UCHL1. Bands from HA-Ub-VME denoted by black arrows.

To further confirm selective on-target engagement of UCHL1, an alkyne bearing analog was utilized. SW1271 Cells pre-treated with **38** could be conjugated to the fluorophore sulfo-cyanine5 azide (Cy5-N₃) to observe all proteins with which **38** interacts. First, it was confirmed that **38** labelled recombinantly expressed UCHL1 in a dose-dependent manner. Treatment of UCHL1 with

38 followed by CuAAC ligation to Cy5-N₃ and gel electrophoresis confirmed this, as the fluorescence intensity of bands corresponding to UCHL1 decreased with decreasing concentrations of **38** (Figure 3.16), though the amount of UCHL1 in each bioconjugation reaction remained constant.

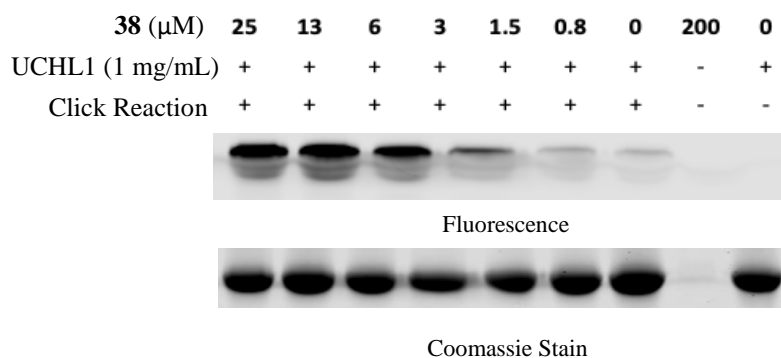


Figure 3.16 Recombinantly expressed His-UCHL1 is labelled in a dose-dependent manner by **38**.

While the co-crystal structure of UCHL1 and **1** suggests that **1** selectively alkylates the active site cysteine, UCHL1 has five solvent-accessible cysteines in addition to the catalytic cysteine 90, providing the possibility that multiple cysteines could be modified. To examine this, both catalytically active (WT) and inactive (C90A) UCHL1 were incubated with DMSO or **38**. After performing a click reaction with Cy5-N₃, samples were subjected to gel electrophoresis and fluorescence imaging, revealing that **38** labelled wild-type UCHL1 (UCHL1^{WT}) while UCHL1^{C90A} displayed no labelling (Figure 3.17). This data, combined with the single modification of cysteine 90 in the co-crystal structure, confirm that **38** selectively labels the active site cysteine of UCHL1.

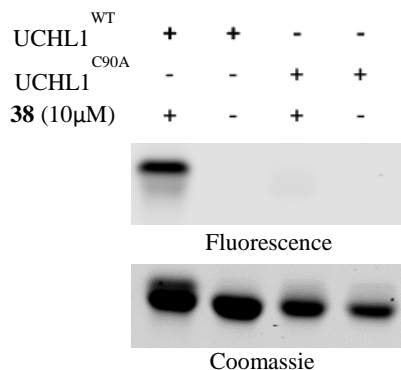


Figure 3.17 Specific labelling of UChL1s catalytic cysteine by **38**. Recombinantly expressed His-UChL1^{WT} or the catalytically inactive mutant His-UChL1^{C90A} treated with 10 μM **38** results in selective labeling of UChL1s catalytic cysteine, as visualized by fluorescent bands. Coomassie staining the same gel indicates the presence of UChL1 in all samples.

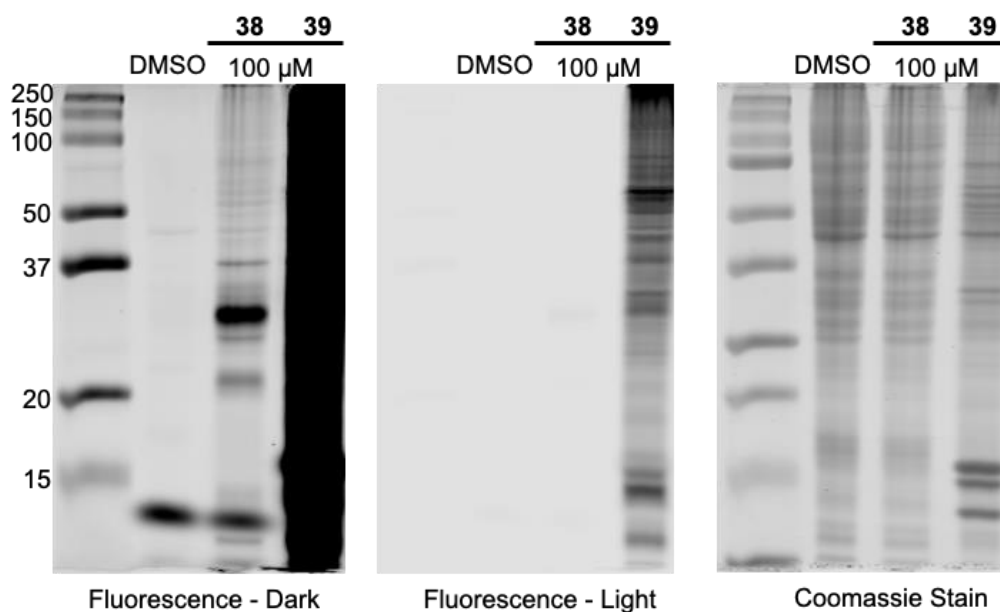


Figure 3.18 Selective labeling of UChL1 in intact SW1271 cells by **38**. SW1271 cells were genetically depleted of UChL1 to varying levels. Intact cells were treated with **38** or **39** (100 μM) followed by washing and pelleting. Clarified cell lysates were subjected to a CuAAC ligation reaction. Analysis by gel electrophoresis and fluorescent imaging shows labeling of a protein corresponding to the molecular weight of UChL1 by **38**. UChL1 is not labeled by **39**, which engages many other proteins.

We next used the alkyne probe to assess off-targets in intact SW1271 cells. Cells were treated with **38** or **39** for 4 hours prior to washing with phosphate buffered saline (PBS). Following lysis and clarification, the normalized supernatant was subjected to a CuAAC ligation of Cy5-N₃ to fluorescently label all proteins with which **38** and **39** were able to interact. Compared to the DMSO treated control, **38** labeled mainly one band, corresponding to the molecular weight of UCHL1 (Figure 3.18). **39** labeled a multitude of proteins, corroborating the off-target interactions hypothesized from the cell viability experiments (Figure 3.18).

To confirm the identity of the band labeled by **38**, UCHL1 was depleted from SW1271 cells with varying efficiencies using shRNA. Cells were treated with 100 μ M **38** followed by CuAAC ligation of Cy5-N₃ and analysis by gel electrophoresis. Fluorescent imaging of the gel indicated that the band with the greatest intensity in the pLKO + **38** treated SW1271 cells corresponds to the molecular weight of UCHL1, suggesting selective labelling of UCHL1 in intact cells. This was confirmed to be UCHL1, as this band intensity decreases with a corresponding decrease in intracellular UCHL1 (Figure 3.19). Although this data suggests that **38** selectively engages UCHL1 in SW1271 cells, there are minor bands present in the treated samples, regardless of intracellular UCHL1 levels, confirming selective engagement of UCHL1 in intact cancer cells. However, the identity of any off-targets should be determined and remains the topic of future work.

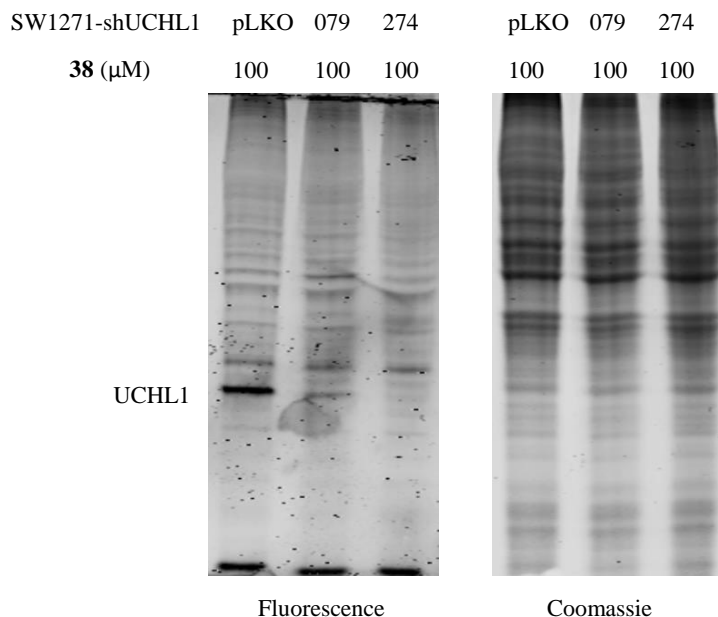


Figure 3.19 Selective labeling of UCHL1 in intact SW1271 cells by **38**. SW1271 cells were genetically depleted of UCHL1 to varying levels. Intact cells were treated with **38** (100 μ M) followed by washing and pelleting. Clarified cell lysates were subjected to a CuAAC ligation reaction. Analysis by gel electrophoresis and fluorescent imaging shows labeling of UCHL1 by **38**. Identity of UCHL1 is confirmed by the disappearance of the labeled band with decreasing intracellular UCHL1 (left). Coomassie staining shows equal loading of cell lysate into all lanes (right).

In addition to decreasing cell viability, genetic depletion of UCHL1 has been shown to reduce the migratory ability of lung cancer cells.³⁸ To simulate migration, a scratch wound healing assay was used. Complete genetic depletion of UCHL1 reduced the ability of SW1271 cells to migrate by approximately 20%, though it did not prevent migration entirely (Figure 3.20A). Consistent with this result, treatment of SW1271 cells with 100 μ M **1** or **38** also reduced the ability of the cells to migrate by 20%, and the inactive control compound **28** was similar to DMSO treatments (Figure 3.20B). Interestingly, MT-19, a potent cyanopyrrolidine inhibitor of UCHL1, almost completely abrogates the cells ability to migrate at a concentration of only 10 μ M. This compound has been previously reported by our group to kill SW1271 cells (CC_{50} = 139 nm)⁸², These results together suggest that MT-19 engages off-targets in this cell line, therefore, evaluating the anti-migratory phenotype for MT-19 is complicated by the cytotoxicity. Taken together, this data

confirms the selective engagement of UCHL1 in intact cancer cells, with pharmacological inhibition results matching those expected from genetic experiments.

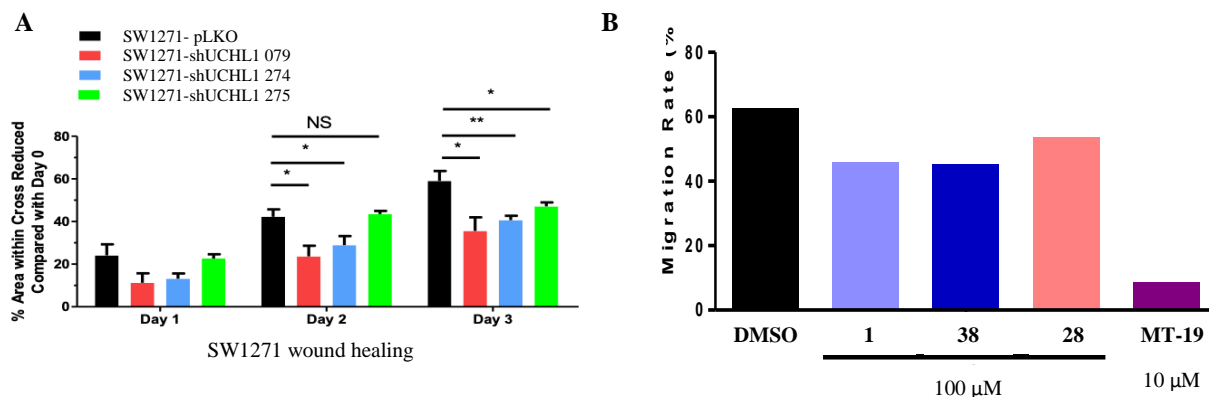


Figure 3.20 Selective inhibition of UCHL1 by **1** or **38** reduces SW1271 cell migration. **A**) Genetic depletion of UCHL1 via shRNA reduces the migration of SW1271 cells in a scratch wound healing migration assay (*:P<0.05, **:P<0.01, ***:P<0.001). Pharmacological inhibition of UCHL1 in SW1271 by **1** and **38** reduce migration to a similar degree as shRNA knockdown.

3.3 Conclusion

In summary, we have presented an SAR study and biochemical characterization of an understudied inhibitor of UCHL1. A pharmacophore was developed via SAR studies, and suggestions to improve this molecule have been described. Using this information, a structure-based pharmacophore screen may be performed to find novel scaffolds with covalent warheads that fulfil all important hydrogen bond interactions and explore more drug-like space. The covalent warhead can then be tuned to provide the correct balance of reactivity and selectivity. Parent compound **1** was confirmed to irreversibly alkylate the active site cysteine of UCHL1 selectively and was shown to be a competitive inhibitor of Ub. Furthermore, this scaffold was shown to inhibit the growth or migration of UCHL1 dependent cell lines (KMS11 and SW1271) to the same extent as genetic depletion via shRNA, while having no effect on non-UCHL1 expressing cell lines (KMS12). Comparatively, a previously published cyanopyrrolidine inhibitor of UCHL1 (MT-19) that was suggested to engage off-targets in both cell lines prevented the growth of SW1271 cells potently, suggesting that its efficacy may be due in part to non-specific toxicity. Dose-dependent target engagement of UCHL1 by this scaffold was confirmed in both KMS11 and SW1271 cells, both by HA-Ub-ABP assays as well as conversion of **1** into an ABP by the addition of an alkyne. Use of this

alkyne analog (**38**) for the bioconjugation of a fluorophore confirmed selective target engagement with minimal labeling of proteins other than UCHL1. However, further work is necessary to determine the identity of these off-targets. While this series lacks the potency required for use as a therapeutic, it serves as the most selective UCHL1 probe to date and provides a starting point for structure-based drug design to develop more potent UCHL1 inhibitors.

3.4 Experimental

General: ^1H , ^{13}C , and ^{19}F NMR spectra were recorded on Bruker DRX500 or ARX-800 spectrometers in $[\text{D}_6]\text{DMSO}$ or CDCl_3 with or without the internal standard of TMS at 0.05 or 0.1% v/v. The purity of all final compounds was > 95% purity as assessed by HPLC according to the current American Chemical Society guidelines for publication. Final compounds were analyzed on an Agilent 1200 series chromatograph. The chromatographic methods used either A) ThermoScientific Hypersil GOLD C18 column (3 μM particle size, 150 mm length, 4.6 mm ID) or B) ThermoScientific Hypersil GOLD C18 column (3 μM particle size, 250 mm length, 4.6 mm ID). UV detection wavelength = 254 nm; flow rate = 1.0 mL min $^{-1}$; solvent = acetonitrile/water. Both organic and aqueous mobile phase contain 0.1% v/v trifluoroacetic acid. The mass spectrometer used is an Advion CMS-L Compact Mass Spectrometer with an ESI or an APCI ionization source. Samples are submitted for analysis using either the atmospheric solids analysis probe (ASAP) or flow injection analysis (FIA). Compounds were prepared according to the following protocols and are detailed below.

3.4.1 Chemical Synthesis

Synthesis of dibenzyl fluoromalonate 3.

A mixture of dimethyl fluoromalonate (2.0 g, 13 mmol, 1.0 equiv), benzyl alcohol (7.0 g, 6.7 mL, 4.9 equiv, 65 mmol), p-toluenesulfonic acid monohydrate (150 mg, 0.80 mmol, 0.06 equiv) in Toluene (5.6 mL) in a round bottom flask outfitted with a Dean-Stark apparatus was heated with stirring to 75 °C *in vacuo* (27 mm of Hg) until all of the toluene had distilled, then (75 mm Hg, 112 °C) for an additional 5 hours. The mixture was cooled to 75 °C and isopropanol (15 mL) was added, then hexanes (30 mL). The mixture was placed in the freezer and allowed to crystallize overnight. The product was filtered, washed with hexanes (2 X 30 mL), and dried overnight *in vacuo*,

yielding dibenzyl fluoromalonate (**3**) (3.0 g, 76%) as a solid. ^1H NMR (500 MHz, Chloroform-*d*) δ 7.64 – 7.28 (m, 10H), 5.37 (d, J = 48.0 Hz, 1H), 5.25 (s, 4H); APCI-MS: m/z 301.1 $[\text{M-H}]^-$.

Synthesis of monobenzyl fluoromalonic acid 4.

Dibenzyl fluoromalonate **3** (2.0 g, 6.6 mmol, 1.0 equiv) was suspended in isopropanol (12 mL) and heated to 45 °C. 1 M aqueous NaOH (6.9 mL, 6.9 mmol, 1.1 equiv) was added dropwise over 1 hour. After an additional 10 minutes, the solution was concentrated to 5 mL and water (2.5 mL) was added. The pH was adjusted to 9 using saturated sodium bicarbonate and washed with DCM (5 X 5 mL) to remove benzyl alcohol. The pH of the solution was adjusted to 2.2 using 5 M HCl, and diisopropyl ether (5 mL) was used to extract. The pH of the aqueous layer was adjusted to 1.9 using 5 M HCl, and further extracted with diisopropyl ether (5 mL). The combined extracts were washed with brine (5 mL), dried over MgSO_4 , filtered, and concentrated *in vacuo* under 35 °C to give an oily residue. This was triturated with hexanes (7 mL) overnight with stirring to give a solid. The solid was filtered and dried under vacuum yielding monobenzyl fluoromalonic acid (**4**) (420 mg, 30%). ^1H NMR (500 MHz, Chloroform-*d*) δ 7.38 (d, J = 2.6 Hz, 5H), 5.40 (d, J = 47.9 Hz, 1H), 5.32 (d, J = 1.1 Hz, 2H). Mass not observed.

Synthesis of methyl (S)-4-((tert-butoxycarbonyl)amino)-6-fluoro-5-oxohexanoate 8.

To a vial was added 3-(benzyloxy)-2-fluoro-3-oxopropanoic acid (**4**) (1.3 g, 6.3 mmol, 1.2 equiv) and THF (2 mL/mmol). This was cooled to 0 °C before adding isopropylmagnesium chloride (1.29 g, 6.25 mL, 2.00 molar in THF, 12.5 mmol, 2.40 equiv). The white suspension was stirred for 1 hour at 0 °C and used for the next reaction.

To a different vial was added (S)-2-((tert-butoxycarbonyl)amino)-5-methoxy-5-oxopentanoic acid (1.4 g, 5.2 mmol, 1.0 equiv) and THF (25 mL). The solution was cooled to 0 °C before adding di(1H-imidazol-1-yl)methanone (850 mg, 5.2 mmol, 1.0 equiv). The reaction was stirred for 1 hour at 0 °C. The second vial was cooled to -20 °C before adding the contents of the first vial dropwise. The mixture was stirred for 45 min at -20 °C, and then allowed to react for 3.5 hour at 25 °C. The reaction was then poured onto 1M HCl, extracted with EtOAc, washed with saturated sodium bicarbonate, brine, dried over sodium sulfate, and concentrated under reduced pressure. The residue was dissolved in toluene and hydrogen gas was bubbled through the solution

for 10 minutes after adding palladium on carbon (100 mg, 0.94 mmol, 0.18 equiv). The reaction was allowed to react overnight at room temperature. The mixture was then filtered, concentrated, and purified via flash chromatography (5 → 60% EtOAc in Hexanes), yielding methyl (S)-4-((tert-butoxycarbonyl)amino)-6-fluoro-5-oxohexanoate (850 mg, 59%). ¹H NMR (500 MHz, Chloroform-d) δ 5.21 (s, 1H), 5.15 – 4.91 (m, 2H), 4.62 (s, 1H), 3.68 (s, 3H), 2.57 – 2.31 (m, 2H), 2.27 – 2.16 (m, 1H), 1.88 (dq, J = 14.8, 7.4 Hz, 1H), 1.44 (s, 9H). APCI-MS: *m/z* 278.0 [M+H]⁺.

Synthesis of tert-butyl (S)-4-((tert-butoxycarbonyl)amino)-6-fluoro-5-oxohexanoate 9.

To a vial was added 3-(benzyloxy)-2-fluoro-3-oxopropanoic acid (**4**) (1.3 g, 6.2 mmol, 1.3 equiv) and THF (2 mL/mmol). This was cooled to 0 °C before adding isopropylmagnesium chloride (1.3 g, 6.2 mL, 2.0 molar, 12 mmol, 2.5 equiv) (2M in THF). The white suspension was stirred for 1 hour at 0 °C and used for the next reaction.

To a different vial was added (S)-5-(tert-butoxy)-2-((tert-butoxycarbonyl)amino)-5-oxopentanoic acid (1.5 g, 4.9 mmol, 1.0 equiv) and THF (15 mL). The solution was cooled to 0 °C before adding CDI (840 mg, 5.2 mmol, 1.0 equiv). The reaction was stirred for 1 hour at 0 °C. The second vial was cooled to -20 °C before adding the contents of the first vial dropwise. The mixture was stirred for 45 min at -20 °C, and then allowed to react for 3.5 hour at 25 °C. The reaction was then poured onto 1 M HCl, extracted with EtOAc, washed with saturated sodium bicarbonate, brine, dried over sodium sulfate, and concentrated under reduced pressure. The residue was dissolved in toluene and hydrogen gas was bubbled through the solution for 10 minutes after adding palladium on carbon (53 mg, 490 μmol, 0.1 equiv). The reaction was allowed to react overnight at room temperature. The mixture was then filtered, concentrated, and purified via flash chromatography (5 → 60% EtOAc in Hexanes) yielding tert-butyl (S)-4-((tert-butoxycarbonyl)amino)-6-fluoro-5-oxohexanoate (1.1 g, 82 %). ¹H NMR (500 MHz, Chloroform-d) δ 5.23 (d, J = 8.0 Hz, 1H), 5.16 – 4.90 (m, 2H), 4.66 – 4.49 (m, 1H), 2.41 – 2.27 (m, 2H), 2.15 (dq, J = 12.2, 6.7 Hz, 1H), 1.86 (dt, J = 14.6, 7.4 Hz, 1H), 1.53 – 1.35 (m, 18H). APCI-MS: *m/z* 320.2 [M+H]⁺.

Synthesis of methyl (S)-4-((tert-butoxycarbonyl)amino)-6-chloro-5-oxohexanoate 10.

Using an Aldrich® diazomethane-generator with System 45™ compatible connection, to the outer tube of was added (S)-2-((tert-butoxycarbonyl)amino)-5-methoxy-5-oxopentanoic acid (280 mg, 1.1 mmol, 1.0 equiv) THF. To this stirring solution at 0 °C was added N-methylmorpholine (140 mg, 150 µL, 1.4 mmol, 1.3 equiv) and isobutyl chloroformate (170 mg, 160 µL, 1.3 mmol, 1.2 equiv). This was allowed to react for 45 minutes. To the inner tube was added N,4-dimethyl-N-nitrosobenzenesulfonamide (500 mg, 2.3 mmol, 2.2 equiv), carbitol (1.0 mL), and ether (1.0 mL). The system was closed, and 1.5 mL of 37% w/v KOH was added to initiate the reaction. After 2 hours, the reaction in the outer tube reaction had turned yellow and was transferred to a new vial where 4 M HCl in 1,4-dioxane was added dropwise until the yellow color disappeared. This was allowed to stir at 0 °C for 30 minutes before diluting with EtOAc and washing with sodium bicarbonate solution, water, and brine, then drying over sodium sulfate and concentrating. The resulting oil was purified by flash chromatography (10 → 75% EtOAc in Hexanes) yielding methyl (S)-4-((tert-butoxycarbonyl)amino)-6-chloro-5-oxohexanoate (0.20 g, 62 %). ¹H NMR (500 MHz, Chloroform-d) δ 5.21 (d, J = 8.1 Hz, 1H), 4.62 – 4.48 (m, 1H), 4.32 (s, 2H), 3.69 (s, 3H), 2.53 – 2.36 (m, 2H), 2.31 – 2.15 (m, 1H), 2.00 – 1.83 (m, 1H), 1.64 – 1.39 (m, 10H). APCI-MS: *m/z* 294.0 [M+H]⁺.

Synthesis of p-ethynylbenzyl carbonochloridate.

Triphosgene (1.1 g, 3.8 mmol, 0.5 equiv) was dissolved in DCM. A mixture of (4-ethynylphenyl)methanol (1.0 g, 7.6 mmol, 1.0 equiv) and DIPEA (0.98, 1.3 mL, 7.6 mmol, 1.0 equiv) in DCM was added dropwise to the stirring solution of triphosgene at 0 °C. After 30 minutes stirring at 0 °C the reaction mixture was evaporated to dryness and taken forward crude to the next reaction.

General procedure for peptide coupling: synthesis of Carbamate/methyl ester protected dipeptides 11a – r.

To a solution of N-terminal carbamate-protected amino acid (1.0 equiv) N-methylmorpholine (4 equiv) at 0 °C in anhydrous THF was added isobutyl chloroformate (1.5 equiv). The C-terminal methyl ester-protected amino acid was added, and the reaction was allowed to warm slowly to room temperature overnight. The reaction mixture was diluted with EtOAc (25 mL) and

washed with 1 M HCl (50 mL), 5% sodium carbonate solution (50 mL), brine (50 mL), then dried over sodium sulfate before filtering and concentrating *in vacuo*. The residue was recrystallized in a DCM:Hexanes solution and filtered, yielding the expected carbamate / methyl ester protected dipeptides.

Boc-L-Val-Gly methylester. ^1H NMR (500 MHz, Chloroform-*d*) δ 6.46 (s, 1H), 5.02 (d, $J = 8.5$ Hz, 1H), 4.14 – 3.89 (m, 3H), 3.76 (s, 3H), 2.29 – 2.07 (m, 1H), 1.45 (s, 9H), 0.95 (dd, $J = 26.7, 6.8$ Hz, 6H); APCI-MS: m/z 289.2 $[\text{M}+\text{H}]^+$. Yield: 0.30 g (90%).

Boc-L-Val-L-Ala methylester. ^1H NMR (500 MHz, Chloroform-*d*) δ 6.36 (s, 1H), 5.04 (s, 1H), 4.68 – 4.47 (m, 1H), 3.98 – 3.84 (m, 1H), 3.75 (s, 3H), 2.27 – 2.01 (m, 1H), 1.50 – 1.31 (m, 12H), 0.95 (dd, $J = 25.0, 6.8$ Hz, 6H); APCI-MS: m/z 303.2 $[\text{M}+\text{H}]^+$. Yield: 0.49 mg (35%).

Cbz-D-Val-L-Ala methylester 11a. ^1H NMR (500 MHz, DMSO-*d*₆) δ 8.31 (d, $J = 7.1$ Hz, 1H), 7.43 – 7.14 (m, 6H), 5.00 (d, $J = 1.4$ Hz, 2H), 4.23 (p, $J = 7.2$ Hz, 1H), 3.86 (dd, $J = 9.3, 6.9$ Hz, 1H), 3.58 (s, 3H), 1.99 – 1.76 (m, 1H), 1.22 (d, $J = 7.3$ Hz, 3H), 0.80 (t, $J = 7.0$ Hz, 6H); APCI-MS: m/z 337.2 $[\text{M}+\text{H}]^+$. Yield: 0.68 g (84%).

Cbz-Gly-L-Ala methylester 11b. ^1H NMR (500 MHz, DMSO-*d*₆) δ 8.28 (d, $J = 7.1$ Hz, 1H), 7.41 (t, $J = 6.2$ Hz, 1H), 7.38 – 7.18 (m, 5H), 4.99 (s, 2H), 4.35 – 4.15 (m, 1H), 3.73 – 3.50 (m, 5H), 1.23 (d, $J = 7.3$ Hz, 3H); APCI-MS: m/z 295.0 $[\text{M}+\text{H}]^+$. Yield: 0.37 g (52%).

Cbz-L-Ala-L-Ala methylester 11c. ^1H NMR (500 MHz, DMSO-*d*₆) δ 8.26 (d, $J = 7.1$ Hz, 1H), 7.40 (d, $J = 7.8$ Hz, 1H), 7.37 – 7.18 (m, 5H), 4.97 (d, $J = 4.0$ Hz, 2H), 4.31 – 4.11 (m, 1H), 4.10 – 3.93 (m, 1H), 3.57 (s, 3H), 1.24 (d, $J = 7.3$ Hz, 3H), 1.16 (d, $J = 7.2$ Hz, 3H); APCI-MS: m/z 309.0 $[\text{M}+\text{H}]^+$. Yield: 0.39 g (52%).

Cbz-L-Ser(OtBu)-L-Ala methylester 11d. ^1H NMR (500 MHz, DMSO-*d*₆) δ 8.29 (d, $J = 7.2$ Hz, 1H), 7.42 – 7.11 (m, 6H), 4.99 (d, $J = 5.2$ Hz, 2H), 4.33 – 4.18 (m, 1H), 4.18 – 3.97 (m, 1H), 3.57 (s, 3H), 3.52 – 3.42 (m, 1H), 1.24 (d, $J = 7.3$ Hz, 3H), 1.07 (s, 9H); APCI-MS: m/z 381.1 $[\text{M}+\text{H}]^+$. Yield: 0.61 g (67%).

Cbz-L-Asn(Trt)-L-Ala methylester 11e. ^1H NMR (500 MHz, Chloroform-*d*) δ 8.49 (s, 1H), 8.32 (d, $J = 6.9$ Hz, 1H), 7.52 (d, $J = 8.4$ Hz, 1H), 7.43 – 6.91 (m, 21H), 5.01 (d, $J = 3.2$ Hz, 2H), 4.38 – 4.25 (m, 1H), 4.25 – 4.12 (m, 1H), 3.56 (s, 3H), 2.70 – 2.53 (m, 1H), 1.00 (d, $J = 6.1$ Hz, 3H); APCI-MS: m/z not determined. Yield: 0.02 g (25%).

Cbz-L-Thr(OtBu)-L-Ala methylester 11f. ^1H NMR (500 MHz, Chloroform-*d*) δ 8.16 (d, $J = 6.9$ Hz, 1H), 7.40 – 7.24 (m, 5H), 6.80 (d, $J = 9.5$ Hz, 1H), 5.01 (d, $J = 2.6$ Hz, 2H), 4.24 (p, $J = 7.2$ Hz, 1H), 4.03 – 3.88 (m, 1H), 3.87 – 3.75 (m, 1H), 3.58 (s, 3H), 1.25 (d, $J = 7.3$ Hz, 3H), 1.09 – 0.96 (m, 13H); APCI-MS: m/z 395.1 $[\text{M}+\text{H}]^+$. Yield: 0.66 g (69%).

Cbz-L-Leu-L-Ala methylester 11g. ^1H NMR (500 MHz, DMSO-*d*₆) δ 8.32 (d, $J = 6.9$ Hz, 1H), 7.44 – 7.21 (m, 6H), 4.97 (s, 2H), 4.21 (p, $J = 7.1$ Hz, 1H), 4.10 – 3.94 (m, 1H), 3.56 (s, 3H), 1.69 – 1.53 (m, 1H), 1.50 – 1.31 (m, 2H), 1.24 (d, $J = 7.3$ Hz, 3H), 0.83 (dd, $J = 9.8, 6.6$ Hz, 6H); APCI-MS: m/z 351.2 $[\text{M}+\text{H}]^+$. Yield: 0.62 g (73%).

Cbz-L-Phe-L-Ala methylester 11h. ^1H NMR (500 MHz, DMSO-*d*₆) δ 8.49 (d, $J = 7.1$ Hz, 1H), 7.49 (d, $J = 8.8$ Hz, 1H), 7.37 – 7.02 (m, 10H), 4.88 (s, 2H), 4.39 – 4.10 (m, 2H), 3.58 (s, 3H), 2.96 (dd, $J = 13.9, 3.7$ Hz, 1H), 2.67 (dd, $J = 13.7, 11.0$ Hz, 1H), 1.28 (d, $J = 7.3$ Hz, 3H); APCI-MS: m/z 385.1 $[\text{M}+\text{H}]^+$. Yield: 0.61 g (66%).

Cbz-L-Asp(OtBu)-L-Ala methylester 11i. ^1H NMR (500 MHz, DMSO-*d*₆) δ 8.34 (d, $J = 7.1$ Hz, 1H), 7.52 (d, $J = 8.4$ Hz, 1H), 7.30 (q, $J = 12.4, 9.4$ Hz, 5H), 4.99 (q, $J = 12.6$ Hz, 2H), 4.45 – 4.27 (m, 1H), 4.20 (p, $J = 7.1$ Hz, 1H), 3.57 (s, 3H), 2.58 (dd, $J = 16.4, 4.4$ Hz, 1H), 2.42 – 2.33 (m, 2H), 1.48 – 1.05 (m, 12H); APCI-MS: m/z 409.1 $[\text{M}+\text{H}]^+$. Yield: 0.47 g (48%).

Cbz-L-Val-D-Ala methylester 11j. ^1H NMR (500 MHz, DMSO-*d*₆) δ 8.31 (d, $J = 7.1$ Hz, 1H), 7.41 – 7.16 (m, 6H), 5.00 (d, $J = 1.4$ Hz, 2H), 4.23 (p, $J = 7.2$ Hz, 1H), 3.87 (dd, $J = 9.2, 6.9$ Hz, 1H), 3.58 (s, 3H), 1.89 (h, $J = 6.8$ Hz, 1H), 1.22 (d, $J = 7.3$ Hz, 3H), 0.80 (t, $J = 6.9$ Hz, 6H); APCI-MS: m/z 337.2 $[\text{M}+\text{H}]^+$. Yield: 0.32 g (40%).

Cbz-L-Val-L-Val methylester 11k. ^1H NMR (500 MHz, DMSO- d_6) δ 8.09 (d, $J = 7.9$ Hz, 1H), 7.41 – 7.20 (m, 6H), 5.04 (s, 2H), 4.24 – 4.12 (m, 1H), 4.12 – 3.89 (m, 1H), 3.63 (s, 3H), 2.17 – 1.78 (m, 2H), 1.01 – 0.72 (m, 12H); APCI-MS: m/z 365.2 $[\text{M}+\text{H}]^+$. Yield: 0.61 g (70%).

Cbz-L-Val-L-Leu methylester 11l. ^1H NMR (500 MHz, DMSO- d_6) δ 8.25 (d, $J = 7.4$ Hz, 1H), 7.47 – 7.15 (m, 6H), 5.13 – 4.94 (m, 2H), 4.37 – 4.20 (m, 1H), 3.99 – 3.82 (m, 1H), 3.61 (s, 3H), 2.01 – 1.91 (m, 1H), 1.75 – 1.42 (m, 3H), 0.88 (dt, $J = 24.4, 6.5$ Hz, 12H); APCI-MS: m/z 379.2 $[\text{M}+\text{H}]^+$. Yield: 0.63 g (69%).

Cbz-L-Val-L-Phe methylester 11m. ^1H NMR (500 MHz, DMSO- d_6) δ 8.36 (d, $J = 7.4$ Hz, 1H), 7.58 – 7.05 (m, 11H), 5.04 (s, 2H), 4.49 (dt, $J = 8.9, 7.1$ Hz, 1H), 3.89 (dd, $J = 9.1, 7.1$ Hz, 1H), 3.57 (s, 3H), 3.10 – 2.82 (m, 2H), 1.92 (h, $J = 6.9$ Hz, 1H), 0.82 (t, $J = 6.8$ Hz, 6H); APCI-MS: m/z 413.2 $[\text{M}+\text{H}]^+$. Yield: 0.50 g (51%).

Cbz-L-Val-L-Ser(OtBu) methylester 11n. ^1H NMR (500 MHz, DMSO- d_6) δ 8.12 (d, $J = 7.7$ Hz, 1H), 7.43 – 7.25 (m, 6H), 5.05 (s, 2H), 4.45 (dt, $J = 7.6, 4.8$ Hz, 1H), 4.00 (dd, $J = 9.1, 6.8$ Hz, 1H), 3.63 (s, 3H), 3.52 (dd, $J = 9.3, 4.6$ Hz, 1H), 2.00 – 1.94 (m, 1H), 1.12 (s, 9H), 0.92 – 0.83 (m, 7H); APCI-MS: m/z 409.3 $[\text{M}+\text{H}]^+$. Yield: 0.83 g (85%).

Cbz-L-Val-L-Thr(OtBu) methylester 11o. ^1H NMR (500 MHz, DMSO- d_6) δ 7.73 (d, $J = 8.7$ Hz, 1H), 7.46 – 7.25 (m, 5H), 5.14 – 4.89 (m, 2H), 4.40 (dd, $J = 8.7, 2.8$ Hz, 1H), 4.19 – 4.12 (m, 1H), 4.12 – 3.97 (m, 1H), 3.63 (s, 3H), 2.07 – 1.91 (m, 1H), 1.17 – 1.01 (m, 12H), 0.92 – 0.79 (m, 7H); APCI-MS: m/z 423.3 $[\text{M}+\text{H}]^+$. Yield: 0.81 g (80%).

Cbz-L-Val-L-Asn(Trt) methylester 11p. ^1H NMR (500 MHz, DMSO- d_6) δ 8.74 (s, 1H), 8.33 (d, $J = 7.6$ Hz, 1H), 7.50 – 7.12 (m, 19H), 5.07 – 5.03 (m, 2H), 4.66 – 4.47 (m, 1H), 3.99 – 3.84 (m, 1H), 3.58 (s, 3H), 2.79 (dd, $J = 15.6, 6.2$ Hz, 1H), 2.74 – 2.60 (m, 1H), 0.98 – 0.76 (m, 9H); APCI-MS: m/z 622.3 $[\text{M}+\text{H}]^+$. Yield: 0.38 g (25%).

Cbz-L-Val-L-Asp(OtBu) methylester 11q. ^1H NMR (500 MHz, DMSO- d_6) δ 8.37 (d, $J = 7.8$ Hz, 1H), 7.47 – 7.19 (m, 6H), 5.04 (s, 2H), 4.63 (q, $J = 7.1$ Hz, 1H), 3.90 (dd, $J = 9.0, 6.9$ Hz, 1H), 3.62

(s, 3H), 2.72 (dd, $J = 16.2, 5.9$ Hz, 1H), 2.60 (dd, $J = 16.3, 7.5$ Hz, 1H), 2.06 – 1.85 (m, 1H), 1.39 (s, 9H), 0.87 (dd, $J = 15.2, 6.8$ Hz, 6H); APCI-MS: m/z 437.2 $[M+H]^+$. Yield: 0.52 g (49%).

Cbz-L-Val-L-Glu(OtBu) methylester 11r. ^1H NMR (500 MHz, DMSO- d_6) δ 8.30 (d, $J = 7.3$ Hz, 1H), 7.45 – 7.16 (m, 6H), 5.05 (s, 2H), 4.38 – 4.20 (m, 1H), 3.99 – 3.82 (m, 1H), 3.62 (s, 3H), 2.31 (t, $J = 7.5$ Hz, 2H), 2.05 – 1.85 (m, 2H), 1.85 – 1.73 (m, 1H), 1.40 (s, 9H), 0.88 (dd, $J = 17.9, 6.7$ Hz, 6H); APCI-MS: m/z 451.3 $[M+H]^+$. Yield: 0.36 g (33%).

Boc-L-Phe-L-Ala methylester. ^1H NMR (500 MHz, DMSO- d_6) δ 8.36 (d, $J = 7.1$ Hz, 1H), 7.29 – 7.11 (m, 5H), 6.87 (d, $J = 8.8$ Hz, 1H), 4.26 (p, $J = 7.2$ Hz, 1H), 4.19 – 4.09 (m, 1H), 3.58 (s, 3H), 2.93 (dd, $J = 13.9, 3.9$ Hz, 1H), 2.66 (dd, $J = 13.9, 10.7$ Hz, 1H), 1.30 – 1.20 (m, 11H); APCI-MS: m/z 351.3 $[M+H]^+$. Yield: 0.89 g (68%).

Boc-L-Phe-D-Ala methylester. ^1H NMR (500 MHz, DMSO- d_6) δ 8.31 (d, $J = 7.3$ Hz, 1H), 7.36 – 7.07 (m, 5H), 6.83 (d, $J = 8.8$ Hz, 1H), 4.30 – 4.11 (m, 2H), 3.59 (s, 3H), 2.87 (dd, $J = 13.6, 4.9$ Hz, 1H), 2.69 (dd, $J = 13.7, 10.0$ Hz, 1H), 1.35 – 1.10 (m, 12H); APCI-MS: m/z 351.3 $[M+H]^+$. Yield: 0.87 g (66%).

General procedure for the synthesis of *p*-ethynylbenzyl carbamate dipeptides (13a-d).

To a stirring solution of Boc-protected dipeptide methyl ester (1 Eq) in DCM was added HCl (11 equiv, 4.0 molar in 1,4-dioxane). This was allowed to stir at 25 °C for 30 minutes before concentrating *in vacuo* and triturating with ether to remove excess HCl. The residue dissolved in THF (4 mL) and TEA (2.4 equiv) was added. To this was added *p*-ethynylbenzyl carbonochloridate (1.01 equiv) dissolved in THF dropwise at 0 °C and allowed to run overnight at room temperature. The reaction mixture was then diluted with EtOAc (25 mL), and washed with water (50 mL), 1 N HCl (50 mL), saturated sodium bicarbonate, and brine before drying over sodium sulfate, filtering, concentrating *in vacuo*, and triturating with hexanes to yield the expected *p*-ethynyl-Cbz-dipeptide methylester (**13a-d**).

p-ethyny-Cbz-L-Val-L-Ala methylester 13a. ^1H NMR (500 MHz, Chloroform- d) δ 7.48 (d, $J = 8.1$ Hz, 2H), 7.31 (d, $J = 8.0$ Hz, 2H), 6.26 (d, $J = 7.4$ Hz, 1H), 5.36 (d, $J = 8.9$ Hz, 1H), 5.10 (s, 2H),

4.59 (q, $J = 7.1$ Hz, 1H), 4.10 – 3.91 (m, 1H), 3.76 (s, 3H), 3.08 (s, 1H), 2.12 (q, $J = 6.7$ Hz, 1H), 1.42 (d, $J = 7.2$ Hz, 3H), 0.96 (dd, $J = 21.5, 6.8$ Hz, 5H); APCI-MS: m/z 361.4 $[M+H]^+$. Yield: 0.09 g (24%).

p-ethyny-Cbz-L-Val-Gly methylester 13b. ^1H NMR (500 MHz, Chloroform- d) δ 7.55 – 7.40 (m, 2H), 7.31 (d, $J = 7.9$ Hz, 2H), 6.40 – 6.25 (m, 1H), 5.34 (d, $J = 8.3$ Hz, 1H), 5.10 (s, 2H), 4.18 – 3.97 (m, 3H), 3.76 (s, 3H), 3.08 (s, 1H), 2.25 – 2.07 (m, 1H), 0.97 (dd, $J = 21.6, 6.8$ Hz, 6H); APCI-MS: m/z 345.0 $[M-H]^-$. Yield: 0.01 g (8%).

p-ethyny-Cbz-L-Phe-L-Ala methylester 13c. ^1H NMR (500 MHz, DMSO- d_6) δ 8.49 (d, $J = 7.1$ Hz, 1H), 7.54 (d, $J = 8.8$ Hz, 1H), 7.46 – 7.04 (m, 9H), 4.90 (s, 2H), 4.34 – 4.19 (m, 2H), 4.16 (s, 1H), 3.58 (s, 3H), 2.96 (dd, $J = 13.9, 3.7$ Hz, 1H), 2.67 (dd, $J = 13.8, 11.0$ Hz, 1H), 1.28 (d, $J = 7.3$ Hz, 3H); APCI-MS: m/z 409.4 $[M+H]^+$. Yield: 0.16 g (23%).

p-ethynyl-Cbz-L-Phe-D-Ala methylester 13d. ^1H NMR (500 MHz, DMSO- d_6) δ 8.45 (d, $J = 7.3$ Hz, 1H), 7.53 (d, $J = 8.9$ Hz, 1H), 7.46 – 7.31 (m, 2H), 7.31 – 7.01 (m, 7H), 5.08 – 4.59 (m, 2H), 4.34 – 4.20 (m, 2H), 4.16 (s, 1H), 3.59 (s, 3H), 2.91 (dd, $J = 13.6, 4.5$ Hz, 1H), 2.70 (dd, $J = 13.5, 10.4$ Hz, 1H), 1.19 (d, $J = 7.2$ Hz, 3H); APCI-MS: m/z 409.4 $[M+H]^+$. Yield: 0.10 g (45%).

Synthesis of Fmoc-L-Val-L-Ala-OH 15.

To a stirring solution of L-valyl-L-alanine (100 mg, 0.53 mmol, 1.0 equiv) in THF (2 mL) and Na_2CO_3 (0.56 g, 2 mL, 0.53 mmol, 1.0 equiv) (10% w/v) at room temperature was added (9H-fluoren-9-yl)methyl carbonochloridate (140 mg, 0.53 mmol, 1.0 equiv). This was allowed to stir for 48 hours. The reaction was then partitioned between ether (3 X 10 mL) and water (30 mL). The aqueous layer was acidified to a pH of 1 and extracted with EtOAc (3 X 15 mL). The organic extracts were combined, washed with brine, dried over sodium sulfate, filtered, and concentrated *in vacuo* to yield (((9H-fluoren-9-yl)methoxy)carbonyl)-L-valyl-L-alanine (126 mg, 58 %). ^1H NMR (500 MHz, DMSO) δ 12.47 (s, 1H), 8.20 (d, $J = 7.1$ Hz, 1H), 7.86 (d, $J = 7.6$ Hz, 2H), 7.72 (t, $J = 7.1$ Hz, 2H), 7.48 – 7.34 (m, 3H), 7.34 – 7.22 (m, 2H), 4.32 – 4.10 (m, 4H), 3.85 (dd, $J = 9.1, 7.1$ Hz, 1H), 2.00 – 1.85 (m, 1H), 1.23 (d, $J = 7.3$ Hz, 3H), 0.84 (dd, $J = 17.7, 6.8$ Hz, 6H). APCI-MS: m/z 411.3 $[M+H]^+$. Yield: 0.13 g (58%).

General procedure for methylester deprotection 12a – r, 14a – d.

The dipeptide (1.0 equiv) was dissolved in THF:H₂O (4:1, 10 mL) and LiOH (1.2 equiv) was added at 0 °C. The mixture was stirred at 0 °C for 3 hours before acidifying with 1 M HCl (2 mL) to < pH 3. The aqueous phase was extracted with EtOAc (3 X 5 mL), dried over sodium sulfate, filtered, and concentrated to yield the Cbz-protected dipeptide acids, which were taken forward crude.

General procedure for peptide coupling: synthesis of carbamate protected tripeptide halomethylketone 16 – 44.

To a vial was added the corresponding boc-protected halomethylketone (1.0 equiv) and HCl (4.0 molar in 1,4-dioxane, 7.4 equiv). This was allowed to react for 30 minutes at room temperature and monitored for completion by TLC, which indicated the formation of a very polar product. Upon completion, the solvent was removed *in vacuo*, and the oil was triturated with ether for 10 minutes and carefully decanted. The resulting oil was diluted in THF and used directly in the next step.

In a separate vial, isobutyl chloroformate (1.5 equiv) and N-methylmorpholine (4.0 equiv) were added to a stirring solution of carbamate-protected dipeptide acid (0.8 equiv) in THF at 0 °C under argon. This was allowed to react while the first reaction was being run and worked up. After ~45 minutes, the molecule from step one (dissolved in THF) was added dropwise at 0 °C and allowed to stir for 15 minutes before warming to 25 °C and warming to room temperature slowly overnight. The reaction was diluted with EtOAc and washed with 1 N HCl, 5% sodium bicarbonate, and brine before drying over sodium sulfate, filtering, and concentrating *in vacuo* to yield the crude carbamate-protected tripeptide fluoromethylketones.

If no side chain protecting groups were present, the residue was then recrystallized in DCM:Hexanes overnight, filtered, and dried *in vacuo* to yield pure product.

In the presence of side chain protecting groups, the resulting residue was treated with a 4 mL solution of 95:2.5:2.5 TFA:Triisopropyl silane:water for 1 hour before evaporating the solvent and triturating with ether before purifying on HPLC (5 → 95 % ACN:H₂O over 30 minutes) to yield pure product.

Cbz-L-Val-L-Ala-L-Glu(OMe)-fluoromethylketone 1. ¹H NMR (800 MHz, DMSO-*d*₆) δ 8.33 (d, *J* = 7.4 Hz, 1H), 8.10 (d, *J* = 6.7 Hz, 1H), 7.40 – 7.26 (m, 6H), 5.15 (dq, *J* = 50.5, 46.7, 16.6 Hz, 2H),

5.02 (q, $J = 12.6$ Hz, 2H), 4.31 – 4.26 (m, 1H), 4.23 (p, $J = 7.0$ Hz, 1H), 3.87 (dd, $J = 8.6, 6.7$ Hz, 1H), 3.57 (s, 3H), 2.40 – 2.25 (m, 2H), 2.07 – 2.00 (m, 1H), 1.95 (h, $J = 6.8$ Hz, 1H), 1.78 – 1.69 (m, 1H), 1.22 (d, $J = 7.1$ Hz, 3H), 0.84 (dd, $J = 31.9, 6.8$ Hz, 6H). ^{13}C NMR (201 MHz, DMSO- d_6) δ 173.22, 173.11, 171.40, 156.59, 137.43, 128.71, 128.15, 128.03, 83.84, 65.77, 60.28, 54.65, 51.74, 48.53, 40.39, 40.28, 30.67, 29.66, 24.55, 19.52, 18.43, 18.01. ^{19}F NMR (470 MHz, CDCl_3) δ -233.89, -233.99, -234.09; ESI-MS: m/z 482.5 $[\text{M}+\text{H}]^+$; HPLC t_R = 11.434 min (Column B); HPLC purity: 96%. Yield: 45 mg (43%).

Cbz-L-Val-L-Ala-L-Glu(OMe)-chloromethylketone 16. ^1H NMR (800 MHz, DMSO- d_6) δ 8.41 (d, $J = 7.4$ Hz, 1H), 8.11 (d, $J = 6.7$ Hz, 1H), 7.44 – 7.21 (m, 6H), 5.02 (q, $J = 12.6$ Hz, 2H), 4.54 (s, 2H), 4.33 – 4.26 (m, 1H), 4.23 (p, $J = 7.0$ Hz, 1H), 3.87 (dd, $J = 8.6, 6.7$ Hz, 1H), 3.57 (s, 3H), 2.38 – 2.27 (m, 2H), 2.08 – 2.01 (m, 1H), 1.97 – 1.92 (m, 1H), 1.79 – 1.70 (m, 1H), 1.23 (d, $J = 7.1$ Hz, 3H), 0.84 (dd, $J = 30.4, 6.8$ Hz, 6H). ^{13}C NMR (201 MHz, DMSO) δ 200.65, 173.23, 173.11, 171.45, 156.58, 137.44, 128.71, 128.15, 128.03, 65.77, 60.26, 56.06, 51.75, 48.57, 47.99, 40.39, 40.28, 30.67, 29.77, 24.87, 19.51, 18.45, 17.96; ESI-MS: m/z 498.3 $[\text{M}+\text{H}]^+$; HPLC t_R = 11.704 min (Column B); HPLC Purity: 97.6%. Yield: 22 mg (26%).

Cbz-L-Val-Gly-L-Glu-fluoromethylketone 17 ^1H NMR (500 MHz, Chloroform- d) δ 7.64 (s, 1H), 7.52 (s, 1H), 7.37 – 7.27 (m, 5H), 5.86 (d, $J = 7.6$ Hz, 1H), 5.25 – 4.86 (m, 4H), 4.78 (s, 1H), 4.16 – 3.98 (m, 2H), 3.98 – 3.80 (m, 1H), 2.38 (s, 2H), 2.22 – 2.14 (m, 1H), 2.12 – 2.04 (m, 1H), 2.00 (s, 1H), 1.94 – 1.82 (m, 1H), 0.93 (dd, $J = 16.7, 6.7$ Hz, 6H). ^{13}C NMR (126 MHz, CDCl_3) δ 175.86, 173.02, 170.01, 157.4, 135.64, 128.47, 128.24, 127.91, 84.68, 83.18, 67.37, 60.82, 54.73, 42.82, 30.50, 29.44, 24.68, 22.54, 19.10, 17.77, 14.01, 1.79. ^{19}F NMR (470 MHz, Chloroform- d) -232.91 (t, $J = 46.9$ Hz); ESI-MS: m/z 454.2 $[\text{M}+\text{H}]^+$; HPLC t_R = 10.679 min (Column B); HPLC Purity: 98.9%. Yield: 13 mg (4.5%).

Cbz-L-Val-D-Ala-L-Glu(OMe)-fluoromethylketone 18. ^1H NMR (800 MHz, DMSO- d_6) δ 8.26 (d, $J = 7.0$ Hz, 1H), 8.18 (d, $J = 7.7$ Hz, 1H), 7.48 – 7.20 (m, 6H), 5.36 – 4.91 (m, 4H), 4.36 – 4.29 (m, 1H), 4.23 (p, $J = 7.1$ Hz, 1H), 3.82 (t, $J = 7.7$ Hz, 1H), 3.56 (s, 3H), 2.11 – 1.98 (m, 1H), 1.91 (h, $J = 6.9$ Hz, 1H), 1.84 – 1.69 (m, 1H), 1.22 (d, $J = 7.1$ Hz, 3H), 0.85 (t, $J = 7.3$ Hz, 7H). ^{13}C NMR (201 MHz, DMSO) δ 203.81, 203.74, 173.19, 173.02, 171.71, 156.71, 137.32, 128.72, 128.20, 128.08,

84.62, 83.74, 65.86, 60.84, 54.57, 51.75, 48.64, 30.42, 29.66, 24.65, 19.46, 18.88, 18.04. ^{19}F NMR (470 MHz, DMSO) δ -234.14, -234.24, -234.34; ESI-MS: m/z 482.1 $[\text{M}+\text{H}]^+$; HPLC t_{R} = 11.413 min (Column B); HPLC Purity: 97.9%. Yield: 28 mg (33%).

Cbz-L-Val-Gly-L-Glu(OMe)-fluoromethylketone 19. ^1H NMR (500 MHz, Chloroform-*d*) δ 7.37 – 7.29 (m, 5H), 6.95 – 6.73 (m, 1H), 5.47 (d, J = 7.4 Hz, 1H), 5.20 – 4.88 (m, 4H), 4.86 – 4.72 (m, 1H), 4.18 – 3.82 (m, 3H), 3.70 – 3.55 (m, 3H), 2.52 – 2.29 (m, 2H), 2.31 – 2.19 (m, 1H), 2.18 – 2.05 (m, 1H), 2.02 – 1.84 (m, 1H), 1.74 (s, 1H), 0.97 (dd, J = 14.7, 6.9 Hz, 6H). ^{13}C NMR (126 MHz, CDCl_3) δ 203.87, 203.72, 173.19, 171.95, 168.96, 156.67, 135.80, 128.47, 128.21, 128.10, 127.97, 84.68, 83.21, 67.20, 61.13, 60.97, 54.46, 51.83, 42.84, 30.37, 29.50, 25.09, 19.16, 17.93. ^{19}F NMR (470 MHz, Chloroform-*d*) δ -232.82 (t, J = 47.1 Hz), -232.99 (t, J = 47.1 Hz); ESI-MS: m/z 468.1 $[\text{M}+\text{H}]^+$; HPLC t_{R} = 11.382 min (Column B); HPLC Purity: 97.8%. Yield: 11 mg (21%).

Cbz-L-Val-L-Val-L-Glu(OMe)-fluoromethylketone 20. ^1H NMR (800 MHz, DMSO-*d*₆) δ 8.47 (d, J = 7.2 Hz, 1H), 7.84 (d, J = 8.4 Hz, 1H), 7.38 – 7.28 (m, 6H), 5.15 (d, J = 46.7 Hz, 2H), 5.03 (s, 2H), 4.34 – 4.29 (m, 1H), 4.12 (t, J = 7.9 Hz, 1H), 3.95 – 3.89 (m, 1H), 3.57 (s, 3H), 2.39 – 2.26 (m, 2H), 2.08 – 2.00 (m, 1H), 2.00 – 1.88 (m, 2H), 1.76 – 1.69 (m, 1H), 0.88 – 0.79 (m, 13H). ^{13}C NMR (201 MHz, DMSO) δ 203.45, 203.38, 173.05, 171.88, 171.65, 156.47, 137.47, 128.70, 128.13, 128.00, 84.79, 83.90, 65.72, 60.51, 58.07, 54.40, 51.75, 30.69, 30.60, 29.71, 24.60, 19.54, 19.50, 18.65, 18.54. ^{19}F NMR (470 MHz, DMSO) δ -233.28, -233.38, -233.48; ESI-MS: m/z 510.3 $[\text{M}+\text{H}]^+$; HPLC t_{R} = 7.577 min (Column A); HPLC Purity: 95.5%. Yield: 30 mg (32%).

Cbz-L-Val-L-Leu-L-Glu(OMe)-fluoromethylketone 21. ^1H NMR (800 MHz, DMSO-*d*₆) δ 8.38 (d, J = 7.4 Hz, 1H), 8.00 (d, J = 7.7 Hz, 1H), 7.38 – 7.27 (m, 6H), 5.21 – 4.97 (m, 4H), 4.35 – 4.23 (m, 2H), 3.90 – 3.82 (m, 1H), 3.57 (s, 3H), 2.39 – 2.27 (m, 2H), 2.07 – 2.00 (m, 1H), 1.95 (h, J = 6.8 Hz, 1H), 1.77 – 1.70 (m, 1H), 1.64 – 1.57 (m, 1H), 1.52 – 1.40 (m, 2H), 0.93 – 0.79 (m, 13H). ^{13}C NMR (201 MHz, DMSO) δ 203.52, 203.44, 173.10, 172.94, 171.57, 156.60, 137.42, 128.70, 128.62, 128.15, 128.03, 127.38, 84.68, 83.79, 65.78, 60.54, 54.58, 51.73, 51.29, 40.68, 30.62, 29.67, 24.56, 24.50, 23.25, 21.96, 19.50, 18.46. ^{19}F NMR (470 MHz, DMSO) δ -233.72, -233.82, -233.92; ESI-MS: m/z 524.3 $[\text{M}+\text{H}]^+$; HPLC t_{R} = 7.805 min (Column A); HPLC Purity: 96.1%. Yield: 26 mg (27%).

Cbz-L-Val-L-Phe-L-Glu(OMe)-fluoromethylketone 22. ¹H NMR (800 MHz, DMSO-*d*₆) δ 8.42 (d, *J* = 7.7 Hz, 1H), 8.21 (d, *J* = 7.7 Hz, 1H), 7.40 – 7.14 (m, 12H), 5.08 – 4.95 (m, 2H), 4.94 – 4.70 (m, 2H), 4.52 (q, *J* = 7.7 Hz, 1H), 4.25 – 4.18 (m, 1H), 3.90 – 3.80 (m, 1H), 3.56 (s, 3H), 2.97 (dd, *J* = 13.7, 6.9 Hz, 1H), 2.86 (dd, *J* = 13.7, 8.3 Hz, 1H), 2.27 – 2.15 (m, 2H), 2.03 – 1.94 (m, 1H), 1.88 (h, *J* = 6.8 Hz, 1H), 1.72 – 1.59 (m, 1H), 0.77 (d, *J* = 6.8 Hz, 6H). ¹³C NMR (201 MHz, DMSO) δ 203.32, 203.25, 173.10, 171.79, 171.53, 156.52, 137.66, 137.40, 129.57, 128.72, 128.63, 128.52, 128.17, 128.06, 127.47, 126.81, 84.35, 83.46, 65.81, 60.48, 54.64, 54.31, 51.69, 37.59, 30.74, 29.50, 24.55, 19.40, 18.44. ¹⁹F NMR (470 MHz, DMSO) δ -233.98, -234.08, -234.17; ESI-MS: *m/z* 558.3 [M+H]⁺; HPLC *t*_R = 7.844 min (Column A); HPLC Purity: 99.6%. Yield: 34 mg (34%).

Cbz-L-Val-L-Ser-L-Glu(OMe)-fluoromethylketone 23. ¹H NMR (800 MHz, DMSO-*d*₆) δ 8.37 (d, *J* = 7.6 Hz, 1H), 8.00 (d, *J* = 7.3 Hz, 1H), 7.41 – 7.25 (m, 6H), 5.29 – 4.94 (m, 5H), 4.38 – 4.17 (m, 2H), 3.91 (t, *J* = 7.7 Hz, 1H), 3.68 – 3.51 (m, 5H), 2.38 – 2.25 (m, 2H), 2.09 – 1.90 (m, 2H), 1.82 – 1.71 (m, 1H), 0.84 (dd, *J* = 28.6, 6.8 Hz, 7H). ¹³C NMR (201 MHz, DMSO) δ 203.64, 203.57, 173.16, 171.64, 171.20, 156.65, 137.39, 128.72, 128.16, 128.03, 120.03, 84.64, 83.75, 65.82, 61.80, 60.45, 55.39, 54.90, 51.71, 30.66, 29.55, 24.48, 19.50, 18.36. ¹⁹F NMR (470 MHz, DMSO) δ -234.55, -234.65, -234.75; ESI-MS: *m/z* 498.3 [M+H]⁺; HPLC *t*_R = 7.002 min (Column A); HPLC Purity: 95.7%. Yield: 9.6 mg (11%).

Cbz-L-Val-L-Thr-L-Glu(OMe)-fluoromethylketone 24. ¹H NMR (800 MHz, DMSO-*d*₆) δ 8.21 (d, *J* = 7.4 Hz, 1H), 7.72 (d, *J* = 8.1 Hz, 1H), 7.46 (d, *J* = 8.5 Hz, 1H), 7.41 – 7.28 (m, 5H), 5.26 – 5.08 (m, 2H), 5.04 (s, 2H), 4.35 – 4.27 (m, 2H), 4.23 – 4.15 (m, 2H), 4.02 – 3.92 (m, 2H), 3.56 (s, 3H), 2.40 – 2.25 (m, 2H), 2.08 – 1.94 (m, 2H), 1.81 – 1.68 (m, 1H), 1.05 (d, *J* = 6.3 Hz, 3H), 0.90 – 0.81 (m, 6H). ¹³C NMR (201 MHz, DMSO) δ 203.60, 173.14, 171.80, 171.04, 158.59, 158.42, 158.25, 156.73, 137.38, 128.72, 128.16, 128.02, 117.28, 115.82, 84.68, 83.79, 66.85, 65.83, 60.79, 58.55, 54.81, 51.72, 30.38, 29.63, 24.64, 20.28, 19.55, 18.45. ¹⁹F NMR (470 MHz, DMSO) δ -234.25, -234.35, -234.45; ESI-MS: *m/z* 512.3 [M+H]⁺; HPLC *t*_R = 7.154 min (Column A); HPLC Purity: 97.9%. Yield: 6.7 mg (7.3%).

Cbz-L-Val-L-Asn-L-Glu(OMe)-fluoromethylketone 25. ¹H NMR (800 MHz, DMSO-*d*₆) δ 8.24 (dd, *J* = 11.5, 7.8 Hz, 2H), 7.44 – 7.27 (m, 7H), 6.95 (s, 1H), 6.54 (s, 2H), 5.36 – 4.87 (m, 4H), 4.49 (q, *J* = 7.2 Hz, 1H), 4.24 (d, *J* = 10.6 Hz, 1H), 3.85 (t, *J* = 7.5 Hz, 1H), 3.56 (d, *J* = 1.9 Hz, 3H), 2.58

(dd, $J = 15.7, 7.4$ Hz, 1H), 2.45 (dd, $J = 15.7, 6.6$ Hz, 1H), 2.39 – 2.31 (m, 1H), 2.27 (dt, $J = 16.6, 8.1$ Hz, 1H), 2.01 (dq, $J = 13.2, 6.6, 5.9$ Hz, 1H), 1.94 (dt, $J = 13.9, 7.0$ Hz, 1H), 1.79 – 1.70 (m, 1H), 0.87 – 0.80 (m, 6H). ^{13}C NMR (201 MHz, DMSO) δ 203.64, 173.19, 171.83, 171.74, 171.49, 156.75, 137.33, 128.72, 128.18, 128.09, 84.72, 83.84, 65.88, 60.52, 54.95, 51.69, 50.07, 36.88, 30.61, 29.52, 24.47, 19.44, 18.47. ^{19}F NMR (470 MHz, DMSO) δ -234.67, -234.77, -234.87; ESI-MS: m/z 525.3 $[\text{M}+\text{H}]^+$; HPLC $t_R = 6.866$ min (Column A); HPLC Purity: 98.2%. Yield: 3.9 mg (4.1%).

Cbz-L-Val-L-Asp-L-Glu(OMe)-fluoromethylketone 26. ^1H NMR (800 MHz, DMSO- d_6) δ 8.37 – 8.21 (m, 2H), 7.46 – 7.23 (m, 6H), 5.29 – 4.90 (m, 4H), 4.53 (d, $J = 7.2$ Hz, 1H), 4.28 (dt, $J = 7.9, 4.0$ Hz, 1H), 3.85 (t, $J = 7.4$ Hz, 2H), 3.56 (s, 3H), 2.73 (dd, $J = 16.7, 6.5$ Hz, 1H), 2.57 (dd, $J = 16.7, 7.3$ Hz, 1H), 2.39 – 2.32 (m, 1H), 2.32 – 2.23 (m, 1H), 2.07 – 1.86 (m, 2H), 1.82 – 1.66 (m, 1H), 0.84 (dd, $J = 18.8, 6.7$ Hz, 6H). ^{13}C NMR (201 MHz, DMSO) δ 203.54, 203.48, 173.15, 172.16, 171.61, 171.40, 158.57, 158.40, 156.78, 137.30, 128.72, 128.19, 128.09, 127.63, 115.96, 84.66, 83.77, 65.90, 60.59, 54.92, 51.70, 49.86, 36.04, 30.61, 29.53, 24.49, 19.42, 18.42. ^{19}F NMR (470 MHz, DMSO) δ -234.48, -234.58, -234.68; ESI-MS: m/z 526.3 $[\text{M}+\text{H}]^+$; HPLC $t_R = 7.083$ min (Column B); HPLC Purity: 98.6%. Yield: 14 mg (15%).

Cbz-L-Val-L-Glu-L-Glu(OMe)-fluoromethylketone 27. ^1H NMR (800 MHz, DMSO- d_6) δ 8.36 (d, $J = 7.6$ Hz, 1H), 8.07 (d, $J = 7.5$ Hz, 1H), 7.41 – 7.26 (m, 6H), 6.54 (s, 1H), 5.16 (dq, $J = 47.2, 16.8$ Hz, 2H), 5.02 (q, $J = 12.7$ Hz, 2H), 4.37 – 4.29 (m, 1H), 4.29 – 4.20 (m, 1H), 3.87 (t, $J = 7.5$ Hz, 1H), 3.62 – 3.54 (m, 3H), 2.41 – 2.11 (m, 4H), 2.09 – 1.66 (m, 5H), 0.84 (dd, $J = 23.4, 6.7$ Hz, 6H). ^{13}C NMR (201 MHz, DMSO) δ 203.62, 203.55, 174.21, 173.07, 172.07, 171.70, 156.64, 137.38, 128.72, 128.17, 128.08, 84.76, 83.87, 65.82, 60.50, 54.58, 52.25, 51.74, 30.55, 30.38, 29.67, 27.24, 24.60, 19.50, 18.47. ^{19}F NMR (470 MHz, DMSO) δ -233.67, -233.77, -233.87; ESI-MS: m/z 540.3 $[\text{M}+\text{H}]^+$; HPLC $t_R = 7.074$ min (Column B); HPLC Purity: 95.3%. Yield: 7.0 mg (7.2%).

Cbz-D-Val-L-Ala-L-Glu(OMe)-fluoromethylketone 28. ^1H NMR (800 MHz, DMSO- d_6) δ 8.31 (d, $J = 7.1$ Hz, 1H), 8.12 (d, $J = 7.7$ Hz, 1H), 7.45 (d, $J = 7.7$ Hz, 1H), 7.38 – 7.29 (m, 5H), 5.19 – 5.03 (m, 2H), 5.04 – 4.92 (m, 2H), 4.36 – 4.30 (m, 1H), 4.24 (p, $J = 7.1$ Hz, 1H), 3.79 (t, $J = 7.6$ Hz, 1H), 3.57 (s, 3H), 2.43 – 2.28 (m, 2H), 2.10 – 2.02 (m, 1H), 1.91 (h, $J = 6.8$ Hz, 1H), 1.81 – 1.74 (m, 1H), 1.24 (d, $J = 7.2$ Hz, 3H), 0.86 (dd, $J = 13.2, 6.7$ Hz, 6H). ^{13}C NMR (201 MHz, DMSO) δ 203.61,

203.55, 173.17, 173.09, 171.87, 156.84, 137.23, 128.73, 128.24, 128.17, 128.07, 84.65, 83.77, 65.93, 60.98, 54.58, 51.75, 48.61, 30.26, 29.73, 24.53, 19.45, 18.98, 17.92. ^{19}F NMR (470 MHz, DMSO) δ -234.13, -234.23, -234.33; ESI-MS: m/z 482.3 $[\text{M}+\text{H}]^+$; HPLC t_{R} = 7.327 min (Column A); HPLC purity: 99.5%. Yield: 32 mg (37%).

Cbz-Gly-L-Ala-L-Glu(OMe)-fluoromethylketone 29. ^1H NMR (800 MHz, DMSO- d_6) δ 8.25 (d, J = 7.5 Hz, 1H), 8.13 (d, J = 6.9 Hz, 1H), 7.51 – 7.24 (m, 6H), 5.21 – 5.04 (m, 2H), 5.02 (s, 2H), 4.36 – 4.25 (m, 1H), 4.27 – 4.18 (m, 1H), 3.64 (d, J = 6.0 Hz, 2H), 3.58 (s, 3H), 2.41 – 2.25 (m, 2H), 2.12 – 1.98 (m, 1H), 1.80 – 1.70 (m, 1H), 1.23 (d, J = 7.2 Hz, 3H). ^{13}C NMR (201 MHz, DMSO) δ 203.67, 173.28, 173.12, 169.44, 156.94, 137.38, 128.73, 128.19, 128.10, 84.71, 83.83, 65.87, 54.65, 51.77, 48.69, 43.80, 29.75, 24.54, 18.13. ^{19}F NMR (470 MHz, DMSO) δ -233.95, -234.05, -234.15; ESI-MS: m/z 440.0 $[\text{M}+\text{H}]^+$; HPLC t_{R} = 10.598 min (Column B); HPLC Purity: 96.5%. Yield: 14 mg (18%).

Cbz-L-Ala-L-Ala-L-Glu(OMe)-fluoromethylketone 30. ^1H NMR (800 MHz, DMSO- d_6) δ 8.24 (d, J = 7.4 Hz, 1H), 8.06 (d, J = 6.9 Hz, 1H), 7.49 (d, J = 7.2 Hz, 1H), 7.39 – 7.33 (m, 4H), 7.31 (t, J = 7.0 Hz, 1H), 5.29 – 4.88 (m, 4H), 4.33 – 4.25 (m, 1H), 4.21 (p, J = 7.1 Hz, 1H), 4.04 (p, J = 7.2 Hz, 1H), 3.57 (s, 3H), 2.41 – 2.27 (m, 2H), 2.12 – 1.95 (m, 1H), 1.83 – 1.58 (m, 1H), 1.23 (d, J = 7.1 Hz, 3H), 1.19 (d, J = 7.2 Hz, 3H). ^{13}C NMR (201 MHz, DMSO) δ 173.28, 173.11, 156.20, 137.36, 128.72, 128.18, 128.10, 84.70, 83.82, 65.77, 54.67, 51.75, 50.38, 48.65, 29.68, 24.57, 18.32, 17.96. ^{19}F NMR (470 MHz, DMSO) δ -233.94, -234.04, -234.14; ESI-MS: m/z 454.0 $[\text{M}+\text{H}]^+$; HPLC t_{R} = 10.740 min (Column B); HPLC Purity: 95.3%. Yield: 24 mg (29%).

Cbz-L-Leu-L-Ala-L-Glu(OMe)-fluoromethylketone 31. ^1H NMR (800 MHz, DMSO- d_6) δ 8.27 (d, J = 7.4 Hz, 1H), 8.09 (d, J = 6.8 Hz, 1H), 7.44 (d, J = 8.1 Hz, 1H), 7.40 – 7.24 (m, 5H), 5.25 – 4.91 (m, 4H), 4.33 – 4.25 (m, 1H), 4.21 (p, J = 7.0 Hz, 1H), 4.08 – 3.97 (m, 1H), 3.58 (s, 3H), 2.39 – 2.25 (m, 2H), 2.07 – 2.00 (m, 1H), 1.82 – 1.71 (m, 1H), 1.71 – 1.53 (m, 1H), 1.48 – 1.38 (m, 2H), 1.23 (d, J = 7.1 Hz, 3H), 0.86 (dd, J = 12.9, 6.6 Hz, 6H). ^{13}C NMR (201 MHz, DMSO) δ 203.66, 203.60, 173.23, 173.11, 172.69, 156.40, 137.43, 128.71, 128.14, 128.01, 84.72, 83.84, 65.73, 54.66, 53.29, 51.75, 48.59, 40.90, 29.67, 24.58, 24.52, 23.47, 21.75, 17.93. ^{19}F NMR (470 MHz, DMSO) δ -

233.88, -233.98, -234.08; ESI-MS: m/z 496.1 $[M+H]^+$; HPLC t_R = 11.842 min (Column B); HPLC Purity: 99.4%. Yield: 32 mg (36%).

Cbz-L-Phe-L-Ala-L-Glu(OMe)-fluoromethylketone 32. 1H NMR (800 MHz, DMSO- d_6) δ 8.33 (d, J = 7.4 Hz, 1H), 8.27 (d, J = 6.8 Hz, 1H), 7.51 (d, J = 8.5 Hz, 1H), 7.35 – 7.14 (m, 11H), 5.25 – 5.07 (m, 2H), 4.93 (s, 2H), 4.40 – 4.15 (m, 3H), 3.57 (s, 3H), 3.01 (dd, J = 14.0, 3.7 Hz, 1H), 2.78 – 2.64 (m, 1H), 2.40 – 2.26 (m, 2H), 2.12 – 1.98 (m, 1H), 1.86 – 1.63 (m, 1H), 1.26 (d, J = 7.1 Hz, 3H). ^{13}C NMR (201 MHz, DMSO) δ 203.66, 203.59, 173.25, 173.11, 171.97, 156.30, 138.53, 137.37, 129.59, 128.66, 128.39, 128.06, 127.82, 126.59, 84.73, 83.85, 65.57, 56.34, 54.69, 51.76, 48.73, 37.66, 29.71, 24.57, 18.03. ^{19}F NMR (470 MHz, DMSO) δ -233.78, -233.88, -233.98; ESI-MS: m/z 530.0 $[M+H]^+$; HPLC t_R = 11.974 min (Column B); HPLC Purity: 98.2%. Yield: 33 mg (35%).

Cbz-L-Ser-L-Ala-L-Glu(OMe)-fluoromethylketone 33. 1H NMR (800 MHz, DMSO- d_6) δ 8.23 (d, J = 6.9 Hz, 1H), 8.18 (d, J = 7.7 Hz, 1H), 7.40 – 7.27 (m, 6H), 5.22 – 4.97 (m, 4H), 4.33 – 4.26 (m, 1H), 4.23 (p, J = 7.1 Hz, 1H), 4.10 (q, J = 6.6 Hz, 1H), 3.58 (s, 6H), 2.38 – 2.21 (m, 2H), 2.12 – 1.94 (m, 1H), 1.79 – 1.64 (m, 1H), 1.25 (d, J = 7.2 Hz, 3H). ^{13}C NMR (201 MHz, DMSO) δ 203.56, 173.26, 173.06, 170.72, 156.35, 137.30, 128.73, 128.19, 128.11, 84.64, 83.76, 65.90, 62.19, 57.17, 54.72, 51.76, 48.87, 29.68, 24.55, 17.86. ^{19}F NMR (470 MHz, $CDCl_3$) δ -234.08, -234.18, -234.27; ESI-MS: m/z 470.0 $[M+H]^+$; HPLC t_R = 10.354 min (Column B); HPLC Purity: 95.2%. Yield: 16 mg (19%).

Cbz-L-Thr-L-Ala-L-Glu(OMe)-fluoromethylketone 34. 1H NMR (800 MHz, DMSO- d_6) δ 8.24 (d, J = 7.4 Hz, 1H), 8.10 (d, J = 6.8 Hz, 1H), 7.39 – 7.28 (m, 5H), 7.02 (d, J = 8.4 Hz, 1H), 5.27 – 4.95 (m, 4H), 4.32 – 4.18 (m, 2H), 3.98 (dd, J = 8.5, 4.7 Hz, 1H), 3.94 (q, J = 5.9 Hz, 1H), 3.58 (s, 4H), 2.40 – 2.25 (m, 2H), 2.07 – 1.97 (m, 1H), 1.78 – 1.66 (m, 1H), 1.24 (d, J = 7.2 Hz, 3H), 1.06 (d, J = 6.4 Hz, 3H). ^{13}C NMR (201 MHz, DMSO) δ 203.60, 173.20, 173.09, 170.39, 156.52, 137.34, 128.73, 128.18, 128.04, 84.72, 83.83, 67.24, 65.93, 60.65, 54.68, 51.76, 48.69, 29.71, 24.55, 20.01, 18.01. ^{19}F NMR (470 MHz, DMSO) δ -233.88, -233.98, -234.08; ESI-MS: m/z 484.1 $[M+H]^+$; HPLC t_R = 10.583 min (Column B); HPLC Purity: 98.2%. Yield: 11 mg (12%).

Cbz-L-Asn-L-Ala-L-Glu(OMe)-fluoromethylketone 35. ^1H NMR (800 MHz, DMSO- d_6) δ 8.28 (d, $J = 7.0$ Hz, 2H), 7.49 (d, $J = 7.9$ Hz, 1H), 7.47 – 7.42 (m, 1H), 7.39 – 7.28 (m, 5H), 6.97 (s, 1H), 5.23 – 4.93 (m, 4H), 4.32 (q, $J = 7.3$ Hz, 1H), 4.30 – 4.23 (m, 1H), 4.15 (p, $J = 7.1$ Hz, 1H), 3.58 (s, 3H), 2.55 (dd, $J = 15.3, 6.7$ Hz, 1H), 2.45 – 2.39 (m, 1H), 2.39 – 2.26 (m, 2H), 2.11 – 1.94 (m, 1H), 1.84 – 1.70 (m, 1H), 1.24 (d, $J = 7.3$ Hz, 3H). ^{13}C NMR (201 MHz, DMSO) δ 173.35, 173.12, 172.18, 137.13, 128.72, 128.09, 84.65, 83.66, 65.86, 54.91, 51.75, 49.12, 37.71, 29.69, 24.47, 17.74. ^{19}F NMR (470 MHz, DMSO) δ -234.28, -234.38, -234.48; ESI-MS: m/z 496.9 $[\text{M}+\text{H}]^+$; HPLC $t_R = 10.042$ min (Column B); HPLC Purity: 95.3%. Yield: 8.6 mg (10%).

Cbz-L-Asp-L-Ala-L-Glu(OMe)-fluoromethylketone 36. ^1H NMR (800 MHz, DMSO- d_6) δ 8.21 (d, $J = 7.5$ Hz, 1H), 8.13 (d, $J = 6.9$ Hz, 1H), 7.61 (d, $J = 7.9$ Hz, 1H), 7.45 – 7.22 (m, 6H), 5.32 – 4.81 (m, 4H), 4.36 (td, $J = 8.5, 4.5$ Hz, 1H), 4.28 (ddd, $J = 9.7, 7.5, 4.6$ Hz, 1H), 4.18 (p, $J = 7.1$ Hz, 1H), 3.58 (s, 3H), 2.69 (dd, $J = 16.7, 4.6$ Hz, 1H), 2.41 – 2.22 (m, 2H), 2.12 – 1.96 (m, 1H), 1.82 – 1.66 (m, 1H), 1.23 (d, $J = 7.3$ Hz, 3H). ^{13}C NMR (201 MHz, DMSO) δ 203.67, 203.61, 173.22, 173.11, 172.20, 171.29, 156.27, 137.28, 128.72, 128.19, 128.08, 84.69, 83.80, 65.88, 54.75, 51.75, 51.60, 48.90, 36.53, 29.68, 25.88, 24.53, 17.90. ^{19}F NMR (470 MHz, DMSO) δ -233.94, -234.04, -234.14; ESI-MS: m/z 497.9 $[\text{M}+\text{H}]^+$; HPLC $t_R = 10.415$ min (Column B); HPLC Purity: 95.8%. Yield: 9.4 mg (10%).

p-ethynyl-Cbz-L-Val-Gly-L-Glu(OMe)-fluoromethylketone 37. ^1H NMR (500 MHz, Chloroform- d) δ 7.51 – 7.43 (m, 2H), 7.31 – 7.27 (m, 2H), 6.95 (t, $J = 5.6$ Hz, 1H), 5.55 (d, $J = 7.7$ Hz, 1H), 5.16 – 4.89 (m, 5H), 4.82 (q, 1H), 4.16 – 3.79 (m, 4H), 3.68 – 3.61 (m, 3H), 3.09 (s, 1H), 2.52 – 2.31 (m, 2H), 2.28 – 2.17 (m, 1H), 2.12 (q, $J = 6.7$ Hz, 1H), 1.92 (dq, $J = 14.8, 7.5$ Hz, 1H), 1.80 (s, 1H), 0.96 (dd, $J = 12.3, 6.8$ Hz, 6H). ^{13}C NMR (126 MHz, CDCl_3) δ 203.91, 203.76, 173.16, 171.94, 168.94, 156.46, 136.61, 132.18, 127.69, 121.91, 84.68, 83.21, 83.08, 77.56, 66.53, 60.88, 54.41, 51.83, 42.83, 30.50, 29.49, 25.14, 19.14, 18.87, 17.93. ^{19}F NMR (470 MHz, Chloroform- d) δ -232.73 (t, $J = 47.1$ Hz); ESI-MS: m/z 492.2 $[\text{M}+\text{H}]^+$; HPLC $t_R = 11.639$ min (Column B); HPLC Purity: 96.5%. Yield: 14 mg (23%).

p-ethynyl-Cbz-L-Val-L-Ala-L-Glu(OMe)-fluoromethylketone 38. ^1H NMR (800 MHz, DMSO- d_6) δ 8.33 (d, $J = 7.4$ Hz, 1H), 8.10 (d, $J = 6.7$ Hz, 1H), 7.47 (d, $J = 8.0$ Hz, 2H), 7.40 – 7.31 (m, 3H),

5.14 (dq, 2H), 5.04 (q, 2H), 4.31 – 4.25 (m, 1H), 4.23 (p, $J = 7.0$ Hz, 1H), 4.18 (s, 1H), 3.87 (dd, $J = 8.6, 6.6$ Hz, 1H), 3.57 (s, 3H), 2.39 – 2.27 (m, 2H), 2.07 – 1.99 (m, 1H), 1.99 – 1.91 (m, 1H), 1.79 – 1.70 (m, 1H), 1.22 (d, $J = 7.1$ Hz, 3H), 0.84 (dd, $J = 31.0, 6.8$ Hz, 6H). ^{13}C NMR (201 MHz, DMSO) δ 173.22, 173.11, 132.08, 128.06, 84.73, 83.85, 83.65, 81.31, 65.22, 60.28, 54.65, 51.74, 48.53, 40.39, 40.28, 30.68, 29.66, 24.55, 19.51, 18.43, 18.01. ^{19}F NMR (470 MHz, CDCl_3) δ -233.89, -233.99, -234.09; ESI-MS: m/z 506.2 $[\text{M}+\text{H}]^+$; HPLC $t_R = 11.704$ min (Column B); HPLC Purity: 97.9%. Yield: 39 mg (53%).

***p*-ethynyl-Cbz-*L*-Val-*L*-Ala-*L*-Glu(OMe)-chloromethylketone 39.** ^1H NMR (800 MHz, $\text{DMSO}-d_6$) δ 8.41 (d, $J = 7.4$ Hz, 1H), 8.12 (d, $J = 6.6$ Hz, 1H), 7.47 (d, $J = 8.0$ Hz, 2H), 7.39 – 7.30 (m, 3H), 5.06 – 5.00 (m, 2H), 4.54 (s, 2H), 4.33 – 4.27 (m, 1H), 4.26 – 4.20 (m, 1H), 4.18 (s, 1H), 3.89 – 3.84 (m, 1H), 3.57 (s, 3H), 2.38 – 2.25 (m, 2H), 2.08 – 2.02 (m, 1H), 1.98 – 1.92 (m, 1H), 1.79 – 1.68 (m, 1H), 1.22 (d, $J = 7.1$ Hz, 3H), 0.84 (dd, $J = 29.6, 6.8$ Hz, 6H). ^{13}C NMR (201 MHz, DMSO) δ 200.65, 173.23, 173.11, 171.40, 156.45, 138.43, 132.07, 128.06, 121.41, 83.65, 81.32, 65.22, 60.27, 56.06, 51.75, 48.57, 47.99, 40.39, 40.28, 30.68, 29.77, 24.87, 19.51, 18.45, 17.95. ESI-MS: m/z 522.2 $[\text{M}+\text{H}]^+$; HPLC $t_R = 12.054$ min (Column B), HPLC Purity: 95.2%. Yield: 25 mg (32%).

***p*-ethynyl-Cbz-*L*-Phe-*L*-Ala-*L*-Glu(OMe)-fluoromethylketone 40.** ^1H NMR (800 MHz, $\text{DMSO}-d_6$) δ 8.36 (d, $J = 7.5$ Hz, 1H), 8.30 (d, $J = 6.8$ Hz, 1H), 7.58 (d, $J = 8.6$ Hz, 1H), 7.43 (d, $J = 7.9$ Hz, 2H), 7.37 – 7.11 (m, 8H), 5.24 – 5.06 (m, 2H), 4.94 (s, 2H), 4.33 – 4.20 (m, 3H), 4.18 (s, 1H), 3.57 (s, 3H), 3.02 (dd, $J = 14.0, 3.6$ Hz, 1H), 2.71 (dd, $J = 13.9, 11.0$ Hz, 1H), 2.41 – 2.29 (m, 2H), 2.09 – 2.01 (m, 1H), 1.82 – 1.72 (m, 1H), 1.26 (d, $J = 7.1$ Hz, 3H). ^{13}C NMR (201 MHz, DMSO) δ 203.67, 203.60, 173.27, 173.12, 171.93, 156.17, 138.52, 138.39, 132.01, 131.90, 129.59, 128.40, 127.84, 127.30, 126.60, 121.33, 84.74, 83.85, 83.65, 81.29, 65.02, 56.36, 54.70, 51.76, 48.76, 29.70, 24.57, 18.02. ^{19}F NMR (470 MHz, DMSO) δ -233.80, -233.90, -234.00; ESI-MS: m/z 554.3 $[\text{M}+\text{H}]^+$; HPLC $t_R = 7.673$ min (Column A); HPLC Purity: 95.5%. Yield: 17 mg (5.7%).

***p*-ethynyl-Cbz-*L*-Phe-*D*-Ala-*L*-Glu(OMe)-fluoromethylketone 41.** ^1H NMR (800 MHz, $\text{DMSO}-d_6$) δ 8.33 (d, $J = 7.2$ Hz, 1H), 8.21 (d, $J = 7.7$ Hz, 1H), 7.66 (d, $J = 7.9$ Hz, 1H), 7.43 (d, $J = 7.9$ Hz, 2H), 7.31 – 7.16 (m, 7H), 5.30 – 5.06 (m, 2H), 5.02 – 4.89 (m, 2H), 4.38 – 4.29 (m, 1H), 4.28 – 4.14 (m, 3H), 3.56 (s, 3H), 2.94 (dd, $J = 13.6, 5.4$ Hz, 1H), 2.78 (dd, $J = 13.6, 9.8$ Hz, 1H), 2.38 – 2.26

(m, 2H), 2.07 – 2.00 (m, 1H), 1.81 – 1.72 (m, 1H), 1.15 (d, $J = 7.1$ Hz, 3H). ^{13}C NMR (201 MHz, DMSO) δ 203.86, 203.79, 173.14, 173.04, 171.71, 156.23, 138.28, 138.12, 132.03, 131.96, 129.63, 128.41, 127.92, 127.37, 126.67, 121.40, 84.65, 83.77, 83.64, 81.30, 65.13, 60.14, 56.65, 54.56, 51.75, 48.68, 37.81, 29.65, 24.68, 21.15, 17.99, 14.48. ^{19}F NMR (470 MHz, CDCl_3) δ -234.11, -234.21, -234.31; ESI-MS: m/z 554.3 $[\text{M}+\text{H}]^+$; HPLC $t_R = 7.700$ min (Column A); HPLC Purity: 96.1%. Yield: 29 mg (14%).

Fmoc-L-Val-L-Ala-L-Glu(OMe)-fluoromethylketone 42. ^1H NMR (500 MHz, $\text{DMSO}-d_6$) δ 8.34 (d, $J = 7.4$ Hz, 1H), 8.11 (d, $J = 6.7$ Hz, 1H), 7.86 (d, $J = 7.5$ Hz, 2H), 7.71 (dd, $J = 7.5, 4.9$ Hz, 2H), 7.48 – 7.34 (m, 3H), 7.34 – 7.23 (m, 2H), 5.12 (dq, $J = 46.5, 16.6$ Hz, 2H), 4.33 – 4.09 (m, 5H), 3.90 – 3.78 (m, 1H), 3.53 (s, 3H), 2.39 – 2.19 (m, 2H), 2.09 – 1.82 (m, 2H), 1.76 – 1.63 (m, 1H), 1.18 (d, $J = 7.1$ Hz, 3H), 0.82 (dd, $J = 11.5, 6.7$ Hz, 6H). ^{13}C NMR (126 MHz, CDCl_3) δ 173.17, 173.06, 171.41, 156.48, 144.11, 141.01, 127.97, 127.38, 125.73, 120.43, 66.00, 60.17, 54.57, 51.68, 48.49, 46.97, 30.67, 29.58, 24.46, 19.47, 18.57, 17.93. ^{19}F NMR (470 MHz, CDCl_3) δ -233.88, -233.89, -233.98, -234.07; ESI-MS: m/z 570.0 $[\text{M}+\text{H}]^+$; HPLC $t_R = 12.674$ (Column B); HPLC Purity: 96.6%. Yield: 45 mg (44%).

Fmoc-L-Val-L-Ala-L-Glu(OMe)-chloromethylketone 43. ^1H NMR (500 MHz, $\text{DMSO}-d_6$) δ 8.42 (d, $J = 7.4$ Hz, 1H), 8.13 (d, $J = 6.6$ Hz, 1H), 7.86 (d, $J = 7.6$ Hz, 2H), 7.75 – 7.66 (m, 2H), 7.47 – 7.33 (m, 3H), 7.33 – 7.23 (m, 2H), 4.52 (s, 2H), 4.30 – 4.10 (m, 5H), 3.89 – 3.78 (m, 1H), 3.53 (s, 3H), 2.35 – 2.19 (m, 2H), 2.08 – 1.97 (m, 1H), 1.95 – 1.85 (m, 1H), 1.79 – 1.64 (m, 1H), 1.19 (d, $J = 7.1$ Hz, 3H), 0.82 (dd, $J = 10.4, 6.7$ Hz, 6H). ^{13}C NMR (126 MHz, CDCl_3) δ 200.60, 173.06, 144.11, 141.01, 127.96, 127.37, 125.72, 120.42, 66.01, 55.98, 51.69, 48.52, 47.98, 46.97, 30.67, 29.69, 24.78, 19.47, 18.59, 17.88; ESI-MS: m/z 586.0 $[\text{M}+\text{H}]^+$; HPLC $t_R = 12.934$ min (Column B); HPLC purity: 95.7%. Yield: 25 mg (25%).

3.4.2 Biochemical and Cellular Assays

Fluorescence-based deubiquitinase activity assay

Reactions were performed in black 384 well plates (Fisher 12566624) in a final volume of 50 μL . DUBs were diluted in reaction buffer (50 mM Tris pH 7.6, 0.5 mM EDTA, 5 mM DTT, 0.1 %

(w/v) BSA) to a concentration of 2.5 nM or 0.025 nM for UCHL1 and UCHL3 respectively (Final concentration in well 1 nM or 0.01 nM for UCHL1 and UCHL3 respectively). To each well was added 20 μ L of DUB containing solution and 10 μ L of 5X inhibitor dissolved in reaction buffer and this was allowed to incubate, while sealed, for the 3 hours at room temperature. Reactions were initiated by the addition of 20 μ L of 125 nM (for UCHL1) or 250 nM (for UCHL3) Ub-Rho (Boston Biochem U-555, Final concentration 50 nM or 100 nM for UCHL1 and UCHL3, respectively). Reactions were incubated at room temperature and read immediately (λ ex = 485 nm, λ em = 535 nm) for 20 min. Readings were performed on a Synergy Neo2. Biochemical IC₅₀ were calculated using GraphPad Prism 8 (GraphPad Software, San Diego, CA (USA), www.graphpad.com). Error was reported as the 95% confidence interval calculated from experiments collected in technical triplicate.

Time-dependent activity assay

Reactions were performed in black 384 well plates (Fisher 12566624) in a final volume of 50 μ L. DUBs were diluted in reaction buffer (50 mM Tris pH 7.6, 0.5 mM EDTA, 5 mM DTT, 0.1 % (w/v) BSA) to a concentration of 2.5 nM or 0.025 nM for UCHL1 and UCHL3 respectively (Final concentration in well 1 nM or 0.01 nM for UCHL1 and UCHL3 respectively). To each well was added 20 μ L of DUB containing solution and 10 μ L of 5X inhibitor dissolved in reaction buffer and this was allowed to incubate, while sealed at room temperature. Reactions were initiated by the addition of 20 μ L of 125 nM (for UCHL1) or 250 nM (for UCHL3) Ub-Rho (Boston Biochem U-555, Final concentration 50 nM or 100 nM for UCHL1 and UCHL3, respectively) every 20 minutes for 2 hours. Reactions were incubated at room temperature and read immediately (λ ex = 485 nm, λ em = 535 nm) for 20 min. Readings were performed on a Synergy Neo2. Biochemical IC₅₀ were calculated using GraphPad Prism 8 (GraphPad Software, San Diego, CA (USA), www.graphpad.com). The first-order rate constant (k_{obs}) for each concentration was calculated and plotted as a function of inhibitor concentration. Curves were fit using the equation $Y = k_{inact}X/(K_I+X)$.

Probe labeling assays: KMS11 cells

12 hours prior to the addition of compounds to the cells, 1.2 million cells mL⁻¹ per well were seeded in a 12 well plate. Cells were incubated with inhibitor for 4 hours before washing the cells

three time with PBS to remove excess compound. Cells were harvested, pelleted, and lysed in 60 μ L of lysis buffer (0.5% NP-40 in 50 mM Tris pH 7.4). HA-Ub-VME was then added to a final concentration of 1 μ M and incubate for 1 hour at room temperature. An equal volume of 2X Laemmli sample buffer was added, and the samples were heated to 95 °C before separating by gel electrophoresis and analyzing by immunoblot.

Probe labeling assays: SW1271 cells

Cells were treated with 100 μ M inhibitor or DMSO for 4 h before being washed, scraped, and collected. Cell pellets were thawed on ice before resuspending in 200 μ L lysis buffer (50 mM Tris pH 7.6, 150 mM NaCl, 5 mM $MgCl_2$, 0.5 mM EDTA, 5 mM DTT, 2 mM ATP, 0.5% NP-40, 10% v/v glycerol) and incubating on ice for 30 minutes with vigorous vortexing every 10 minutes. Cell lysate was clarified by centrifugation (17,000 g for 10 minutes) and the supernatant was collected, and the concentration was determined by Bradford (performed according to manufacturer's protocol). Cells were normalized to 2 mg mL^{-1} . To each reaction mixture was added 36 μ L of lysate and 2 μ L of HA-Ub-VME or lysis buffer. This was incubated for 30 minutes at room temperature before quenching with 15 μ L of 4X Laemmli buffer and heating to 95 °C for 5 minutes. Samples were subjected to SDS-PAGE and immunoblot.

Probe labeling assays: SW1271 cell lysate

SW1271 cell pellets were thawed on ice before resuspending in 200 μ L lysis buffer (50 mM Tris pH 7.6, 150 mM NaCl, 5 mM $MgCl_2$, 0.5 mM EDTA, 5 mM DTT, 2 mM ATP, 0.5% NP-40, 10% v/v glycerol) and incubating on ice for 30 minutes with vigorous vortexing every 10 minutes. Cell lysate was clarified by centrifugation (17,000 g for 10 minutes) and the supernatant was collected, and the concentration was determined by Bradford (performed according to manufacturer's protocol). Cells were normalized to 2 mg mL^{-1} . To each reaction mixture was added 36 μ L of lysate and 2 μ L of DMSO or inhibitor. This was incubated for 3 hours at room temperature before adding 2 μ L of HA-Ub-VME. Samples were further incubated at room temperature for 30 minutes before quenching with 15 μ L of 4X Laemmli buffer and heating to 95 °C for 5 minutes. Samples were subjected to SDS-PAGE and immunoblot.

Cell viability assays

SW1271 cells were seeded in 96-well plates at 1,000 cells/well together with the compounds at desired concentration. The cells were cultured with the compounds for 6 days, and the cell viabilities were determined using CellTiter-Glo luminescent cell viability kit (Promega) following the manufacturer's protocol.

Cell proliferation assays

A 96 well plate was coated with 0.01% poly-L-Ornithine for one hour to prevent cell aggregation. KMS11 or KMS12 cells (1×10^6 cells/mL) were cultured for at least 72 hours prior to the proliferation assay. Cells were seeded at 30,000 cells per 100 μ L in each well. 100 μ L of media containing Incucyte Nuclight red reagent (1:2,000) was added to each well. Cells were incubated for 4 hours at 37 °C prior to scanning. The 96 well plate was then placed into the Incucyte analysis system using the phase contrast confluence metric and labelling efficiency on the red fluorescence channel to monitor cell proliferation. Cell were counted using red fluorescence using the Incucyte software to determine proliferation relative to DMSO control.

Scratch wound healing cell migration assay

SW1271 cells were seeded in 12-well plates at 1million cells/well. The cells were cultured overnight to grow as a confluent single layer. The cross-style wounds were created using pipet tips to scratch on the single layer of cells. The compounds were prepared in full growth media at the desired concentrations and added after the wounds were created. DMSO was used as the vehicle control. Photos of the wounds were captured immediately after adding treatments at 0 hours. Photos of the wounds were captured every 24 hours until the wounds heal. The areas of cross-style wounds were quantified using Image J 1.52a software. The migration rate (%) was defined as the percentage of area at each timepoint compared to the one at 0 hours.

CuAAC ligation and in-gel fluorescence: dose-response with recombinant protein

1 mg mL⁻¹ UCHL1 (from pgex 6p-1) (49 μ L) was incubated with various concentrations of inhibitor for 3 hours at room temperature in PBS starting block buffer (Thermo Scientific # 37538). After 3 hours, 6 μ L of a freshly prepared cocktail was added to each sample, consisting of: 3 μ L 1.7

mM THPTA in 1:4 DMSO/tBuOH (100 μ M final concentration), 1 μ L 50 mM CuSO₄ (1 mM final concentration), 1 μ L TCEP HCl (25 μ M final concentration), and 1 μ L Cy5-Azide (Click Chemistry Tools #AZ118) (25 μ M final concentration). The samples were allowed to react for 2 hours at room temperature protected from light before precipitating the sample by adding 600 μ L MeOH, 150 μ L Chloroform, and 400 μ L water, vortexing between each addition. The samples were pelleted by centrifuging at 17,000 x g for 5 minutes. The upper aqueous layer was removed without disturbing the precipitate, and 450 μ L MeOH was added again, followed by centrifuging at 17,000 x g for 5 minutes (2X) and decanting the solvent. The samples were allowed to air dry for 30 minutes before resuspending in 1X Laemmli buffer and boiling at 90 °C for 5 minutes. The samples were then analyzed by SDS-PAGE and imaged on a Licor Odyssey and subsequently Coomassie stained.

CuAAC ligation and in-gel fluorescence: UCHL1^{WT} and UCHL1^{C90A}

1 mg mL⁻¹ UCHL1^{WT} or UCHL1^{C90A} (from pgex 6p-1) (49 μ L) was incubated with 10 μ M inhibitor for 3 hours at room temperature in PBS starting block buffer (Thermo Scientific # 37538). After 3 hours, 6 μ L of a freshly prepared cocktail was added to each sample, consisting of: 3 μ L 1.7 mM THPTA in 1:4 DMSO/tBuOH (100 μ M final concentration), 1 μ L 50 mM CuSO₄ (1 mM final concentration), 1 μ L TCEP HCl (25 μ M final concentration), and 1 μ L Cy5-Azide (Click Chemistry Tools #AZ118) (25 μ M final concentration). The samples were allowed to react for 2 hours at room temperature protected from light before precipitating the sample by adding 600 μ L MeOH, 150 μ L Chloroform, and 400 μ L water, vortexing between each addition. The samples were pelleted by centrifuging at 17,000 x g for 5 minutes. The upper aqueous layer was removed without disturbing the precipitate, and 450 μ L MeOH was added again, followed by centrifuging at 17,000 x g for 5 minutes (2X) and decanting the solvent. The samples were allowed to air dry for 30 minutes before resuspending in 1X Laemmli buffer and boiling at 90 °C for 5 minutes. The samples were then analyzed by SDS-PAGE and imaged on a Licor Odyssey and subsequently Coomassie stained.

CuAAC ligation and in-gel fluorescence: treated cells

Cells were treated with 100 μ M inhibitor or DMSO for 4 h before being washed, scraped, and collected and frozen at -80 °C. Cells collected by Hao Chen on 12/16/19 were thawed on ice and lysed in 200 μ L of lysis buffer (1x PBS, 1% v/v Triton X-100, 0.1% w/v SDS, 1X HALT) for

30 minutes on ice with vigorous vortexing every 10 minutes. Samples were then pelleted at 17,000 x g for 10 minutes before collecting the supernatant and measuring concentration using BCA. Samples were normalized to 2 mg/mL and stored at -80 °C overnight. The following day, samples were thawed. While thawing, a click cocktail was prepared (for each sample, the cocktail consists of: 3 µL of 1.7 mM THPTA in 1:4 tBuOH/DMSO, 1 µL of 50 mM CuSO₄ in water, 1 µL of 1.25 mM Cy5-N3 in DMSO, and 1 µL of 50 mM TCEP in water freshly prepared). 50 µL of each sample was added to a new tube, and 6 µL of click cocktail was also added to these tubes. The samples were allowed to react for 2 hours at room temperature protected from light before precipitating the sample by adding 600 µL MeOH, 150 µL Chloroform, and 400 µL water, vortexing between each addition. The samples were pelleted by centrifuging at 17,000 x g for 5 minutes. The upper aqueous layer was removed without disturbing the precipitate, and 450 µL MeOH was added again, followed by centrifuging at 17,000 x g for 5 minutes (2X) and decanting the solvent. The samples were allowed to air dry for 30 minutes before resuspending in 1X Laemmli buffer and boiling at 90 °C for 5 minutes. The samples were then analyzed by SDS-PAGE and imaged on a Licor Odyssey and subsequently Coomassie stained.

K_d analysis of VAEFMK-treated UCHL1 by biolayer interferometry

Binding affinity measurements were performed according to protocols from Hewitt et. al.⁸¹ 5 µM His-UCHL1^{WT} was incubated with 2 mM VAEFMK **1** or DMSO overnight in reaction buffer (50 mM Tris pH 7.6, 0.5 mM EDTA, 5 mM DTT) at room temperature before buffer exchanging into water using Zeba spin desalting columns (ThermoScientific, catalog no. 89882). The concentration of UCHL1 was determined by A₂₈₀ on a NanoDrop system (ThermoScientific), after which His-UCHL1 was diluted into BLI buffer [1× PBS containing 0.05% (v/v) Tween 20 and 0.1% (w/v) bovine serum albumin (BSA)]. The concentration of Ub was determined by the BCA assay and diluted to top concentrations into BLI buffer, and 1:1 serial dilutions were completed. The top concentration of Ub was 2 µM. 40 µL of each solution was added to a 384-well tilted-bottom plate (Molecular Devices, part no. 185080). The Ni-NTA biosensor was dipped first into BLI buffer (initial baseline, 60 s), then into the His-UCH protein wells (loading step, 300 s), then into BLI buffer alone (baseline step, 60 s), then into the lowest concentration of UbV (association step, 120 s), and then into buffer alone (dissociation step, 100 s). A reference sensor loaded with protein was dipped into wells containing only buffer to adjust for protein-buffer signals. The association-

dissociation was repeated with increasing concentrations of UbV. All measurements were taken at 30 °C.

Biacore Data Analysis Software (version 8.2) was used to collect and analyze the raw data for the association and dissociation curves. After subtraction of a reference sensor (loaded sensors dipped into wells containing only buffer), averages of the association responses (in nanometer response signal from 110 to 115 s) were calculated and plotted as a function of UbV concentration in Prism 8. These data were fit to a nonlinear regression one-site specific binding model to determine a K_d .

Inhibitor half-life determination

A 10 μ l sample of the inhibitor (10 mM in DMSO) was diluted in Buffer A (100 mM Potassium Phosphate buffer pH 7.6, 10% v/v ACN, 1 mM GSH) or Buffer B (100 mM Potassium Phosphate buffer pH 7.6, 10% v/v ACN) (total volume = 1 ml). Reaction mixtures were kept under argon at 37 °C with gentle stirring. Every hour for 6 hours, 20 μ L was withdrawn from the reactions with Buffer A and Buffer B and mixed with 80 μ L water and injected into the HPLC. HPLC runs were performed using an Agilent 1200 system. HPLC separation used a C18 column (Hypersil Gold Part # 25003-25430) at ambient temperature. Mobile phase A was 0.1% TFA in Water, and mobile phase B was 0.1% TFA in ACN. The run flow was 1.0 mL/min. The gradient used was 5% A for 2 minutes, increasing linearly to 95% A for 10 minutes, and holding at 95% A for 3 minutes, decreasing to 5% and holding at 5% A for 6 minutes. Percent inhibitor remaining was calculated by dividing the area under curve for each molecule at each timepoint with GSH by the analogous sample at the same timepoint without GSH. The half-life of each molecule was calculated by fitting the data to a non-linear regression using GraphPad Prism 8.0.

CHAPTER 4. A MECHANISTIC UNDERSTANDING OF A NOVEL MACROMOLECULAR UCHL1 INHIBITOR

The following chapter was adapted with permission from Hewitt, C. S., Krabill A. D., Das C., and Flaherty D. P., *Biochemistry* 2020, 59, 37, 3447–3462, © 2020 American Chemical Society. DOI: 10.1021/acs.biochem.9b01076.

The post-translational addition of ubiquitin (Ub) to substrate proteins regulates signaling pathways including cell cycle and transcriptional regulation, as well as proteasomal degradation in eukaryotes. The attachment and removal of Ub to and from substrate proteins is controlled by E3 ligases and deubiquitinases (DUBs) respectively. Ubiquitin C-terminal hydrolase L1 (UCHL1) is a DUB that is endogenously expressed in the central nervous system, though exogenous UCHL1 expression is associated with a number of neurodegenerative diseases and cancer. Development of UCHL1 selective probes has been slow, thus the development of a UCHL1 selective Ub variant (UbV) may prove useful to probe the role of UCHL1 in relevant disease states. Herein, I describe efforts to elucidate the inhibitory mechanism of UCHL1 by Ub^{T9F} using molecular dynamics to understand the biochemical behavior of this Ub^{T9F}.

4.1 Introduction

The regulation of cellular homeostasis is the result of an intricate and concerted interplay between multiple proteins and pathways. Ubiquitin (Ub) is a highly conserved 76 amino acid protein that is integral to cellular homeostasis and plays a role in protein degradation, cell cycle regulation, and protein trafficking, among other roles.¹⁴⁵ The attachment of Ub to substrate proteins occurs by the formation of a covalent bond between the lysine residue of substrate proteins and the glycine 76 C-terminal carboxylic acid of Ub to form an isopeptide bond. This process is catalyzed by the cascading E1 activating, E2 conjugating, and E3 ligating enzymes. Ub can also be attached to other Ub monomers in both linear and branching chains of differing lengths and lysine linkages, adding layers of complexity and altering the phenotypic outcomes.¹⁴⁶ The removal of Ub is regulated by one of the hundred deubiquitinases (DUBs) that are expressed in the human genome. Considering the number of cellular processes affected by protein ubiquitination, it is no surprise that DUBs are key players in disease-relevant pathways.¹⁴⁷ As such, DUBs are considered promising emerging

therapeutic targets for a number of disease states including autoimmune¹⁴⁸ and neurodegenerative diseases¹⁴⁹ as well as cancers.^{13,150,151} DUBs are split into 7 families including: ubiquitin specific proteases (USPs), Machado Josephin domain proteases (MJDs), ovarian tumor proteases (OTUs), Jab1/MPN domain associated proteases (JAMMs), ubiquitin C-terminal hydrolases (UCHs), and the recently discovered MINDY and ZUFSP protease subfamilies.

Ubiquitin C-terminal hydrolase L1 (UCHL1) is a member of the UCH subfamily and is primarily expressed in the central nervous system where it comprises 1-5% of the total soluble brain tissue.^{20,152} UCHL1 has been linked to both familial and sporadic Parkinson's disease,^{53,60} as well as Alzheimer's disease.^{92,93,153} Ectopic expression of UCHL1 is observed in a number of cancers and overexpression is correlated with an increased metastatic behavior.^{38,97} The gold standard small molecule probe, LDN-57444,²⁹ has been used in over 200 studies to probe the role of UCHL1 in disease pathways. However, it suffers from poor solubility, chemical instability, and poor target engagement in cells.⁷² Our group, as well as others, have observed this yet the improper use of the molecule continues in both *in vitro* and *in vivo* experiments. A recently discovered cyanopyrrolidine UCHL1 inhibitor has been published by our lab and others, providing a substitute for LDN-57444.^{52,72,82} However, the majority of UCHL1 research continues to rely upon time-consuming and laborious genetic manipulation techniques to control UCHL1 expression levels.

DUB inhibitor discovery is still in its early stages and has been compared to the state of kinase inhibitor discovery 15 years prior. DUBs are considered to be a difficult drug target, and no DUB-targeting drugs have successfully progressed through clinical trials to become FDA approved. This is partially due to the conserved Ub-binding interfaces that are conserved within DUB subfamilies. As a result, there has been a high level of difficulty for designing small molecule inhibitors with selectivity within these subfamilies,^{126,154,155} though some progress has been made recently using covalent inhibitors.¹²⁶

Alternatively, the design of potent Ub variants with selectivity within the USP subfamily has been achieved using phage display and computational approaches.^{156,157} Many DUBs have been co-crystallized with Ub thanks to the availability of Ub activity-based probes (Ub-ABPs) that covalently modify the active site cysteine, providing structural information for a large number of DUBs. Additionally, the Ub-DUB binding interface represents a larger surface area, providing more opportunities for rational design compared to what would be available for small-molecule DUB inhibitors.

Our group hypothesized that the lack of reliable UCHL1 probes could be alleviated by the rational design of a UCHL1-selective UbV using computational techniques. Using both the ubiquitin-bound crystal structures of UCHL1⁷⁵ and UCHL3¹⁵⁸ in combination with predictive computational tools, our lab identified Ub^{T9F} as a UbV with increased selectivity for UCHL1 over UCHL3 in biochemical assays.¹⁰⁴ However, converting Ub^{T9F} into a Ub-ABP revealed a loss in cell lysate-based assays.¹⁵⁹ To gain insight into the macromolecular mechanism of inhibition and selectivity, I performed a series of molecular dynamic simulations. Herein, I present the results of these studies and provide a rationale for the selectivity observed in biochemical experiments as well as a putative reason for the loss of selectivity upon conversion of Ub^{T9F} into a Ub-ABP.

4.2 Results and Discussion

4.2.1 Computational Prediction and Biochemical Testing of UCHL1-Selective UbVs

Directed evolution via phage display and residue mutational scanning have both been successfully applied to the development of selective UbVs.^{156,157} Rather than using these approaches, our group sought to use computational methods to quickly reduce the number of UbVs that would need to be experimentally tested. Using FoldX^{160–162} and the RosettaDesign server,¹⁶³ our lab identified a series of mutants at the T9 residue of Ub that would both improve binding affinity towards UCHL1 and increase selectivity for UCHL1 over the nearest structural homolog UCHL3.

Two orthogonal assays were employed to assess the binding of UbVs against both UCHL1 and UCHL3. Biolayer interferometry (BLI) measurements of Ub^{WT} with UCHL1 ($K_d = 0.14 \pm 0.01$ μ M) and UCHL3 ($K_d = 0.43 \pm 0.04$ μ M) are similar to previously reported values.¹⁶⁴ The Ub^{T9F} mutant yielded displayed a high binding selectivity difference towards UCHL1 over UCHL3. Ub^{T9F} was 6-fold more selective for UCHL1, though the binding affinity towards both enzymes was decreased (Table 4.1).

The selectivity of Ub^{T9F} for UCHL1 was confirmed using an orthogonal assay to monitor the enzymatic cleavage of Ub-Rhodamine (Ub-Rho) by UCHL1 and UCHL3 in the presence of Ub^{T9F}. Here, Ub^{T9F} displayed a 35-fold inhibition selectivity for UCHL1 over UCHL3, though at the cost of reduced efficacy against UCHL1 compared to wild type Ub (Table 4.1).

Table 4.1 IC₅₀ and K_d values for UbVs with His-UCHL1 and His-UCHL3

UbV	L1 IC ₅₀ (μM) ^a	L3 IC ₅₀ (μM) ^a	Inhibition Selectivity	L1 K _d (μM) ^b	L3 K _d (μM) ^b	Binding Selectivity
WT	0.41 ± 0.03	0.82 ± 0.09	2.0	0.14 ± 0.01	0.43 ± 0.04	3.1
T9F	2.0 ± 0.3	70 ± 10	35.0	3.0 ± 0.9	18 ± 4	6
T9F/T66K	2.2 ± 0.1	> 25	> 11	1.3 ± 0.1	43 ± 6	26.9

^aExperiments were technical triplicate, and averages (and standard errors) are reported. ^bExperiments were performed in duplicate or triplicate, and averages (and standard errors) are reported. L1 = His-UCHL1, and L3 = His-UCHL3. Inhibition selectivity = L3 IC₅₀/L1 IC₅₀. Binding Selectivity = L3 K_d/L1 K_d.

To impart selectivity for UCHL1 over DUBs from the non-UCH subfamily, a previously reported T66 mutation was utilized.¹⁶⁵ T66 forms a hydrogen bond with a conserved lysine side chain in USP subfamily,^{166–169} though both computational prediction and visual inspection of the Ub-UCHL1 co-crystal structure suggested that a mutation to this residue would have little effect on interactions with UCHL1. We hypothesized that a lysine at this position would provide electrostatic repulsion with the positively charged side chains that are conserved in the USP subfamily, providing additional selectivity towards UCHL1. Thus, the double mutant Ub^{T9F/T66K} was generated (Figure 1). As expected, IC₅₀ and K_d values for the double mutant were similar to those from the Ub^{T9F} single point mutation (Table 4.1).

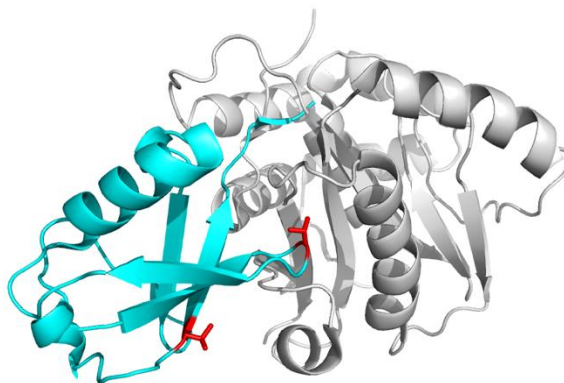


Figure 4.1 UCHL1 bound to ubiquitin. Residues for single point mutations (red sticks) at T9 and T66 on ubiquitin (cyan) in complex with UCHL1 (grey)

To assess the selectivity for Ub^{T9F/T66K} in cells, the activity-based probes (ABP) hemagglutinin-tagged (HA) Ub^{T9FT66K}-vinylmethylester (VME) and HA-Ub^{T9F/T66K}-propargyl (PRG) were generated. Both of these C-terminal modifications have been used to convert Ub^{WT} into Ub-ABPs.¹⁷⁰ It has also been shown that Ub-VME and Ub-PRG display differing selectivity towards DUBs based on their reactivities, with Ub-VME being more reactive and less selective while Ub-PRG is less reactive and more selective^{171,172}. Indeed, HA-Ub^{T9F/T66K}-VME reacted more quickly with UCHL1 than HA-Ub^{T9F/T66K}-PRG in SW1271 cell lysates (Figure 4.2). Both HA-UbV^{T9F/T66K}-ABPs did not react with non-UCH family DUBs (Figure 4.3). However, both ABPs reacted more quickly with UCHL3, indicating that the lower binding affinity towards UCHL3 may be overcome by its increased enzymatic activity.⁷⁴

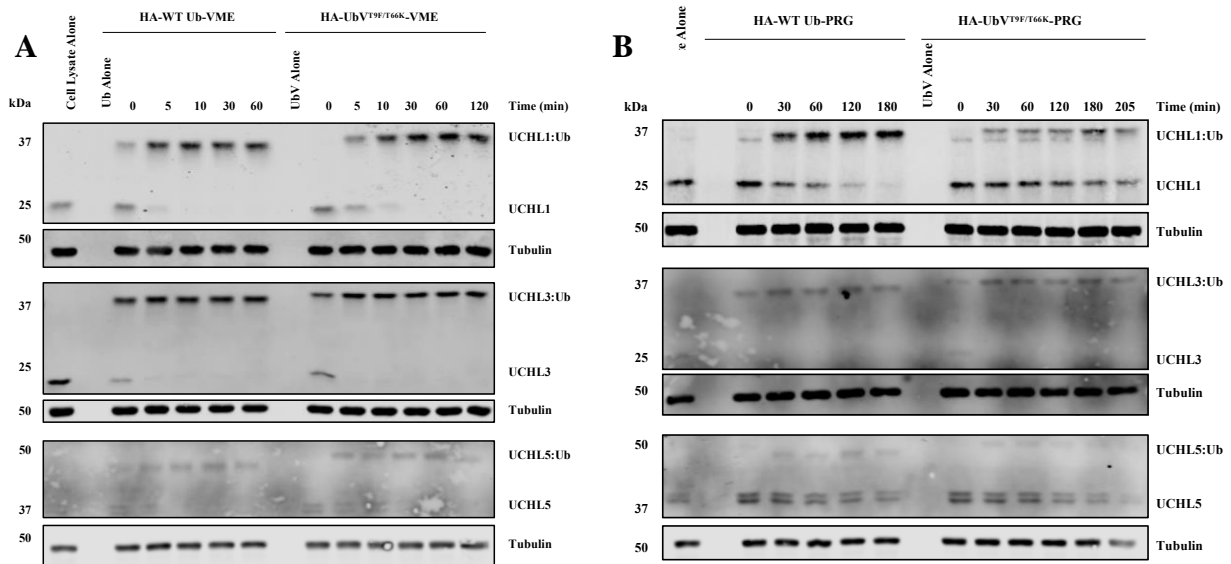


Figure 4.2 UbV^{T9FT66K}-ABP inhibits UCHs in a time-dependent manner. SW1271 Cell Lysate Time-Course Western Blots for HA-UbV^{T9F/T66K}-VME and HA-UbV^{T9F/T66K}-PRG with the UCH family. 0.5 μ M of HA-WT-Ub-VME/PRG and HA-UbV^{T9F/T66K}-VME/PRG was incubated with 0.5 mg/mL SW1271 cell lysate for the times stated above the lanes at 37 °C. **A)** UCHL1 (upper), UCHL3 (middle), and UCHL5 (lower) immunoblots and, **B)** UCHL1 (upper), UCHL3 (middle), and UCHL5 (lower) immunoblots.

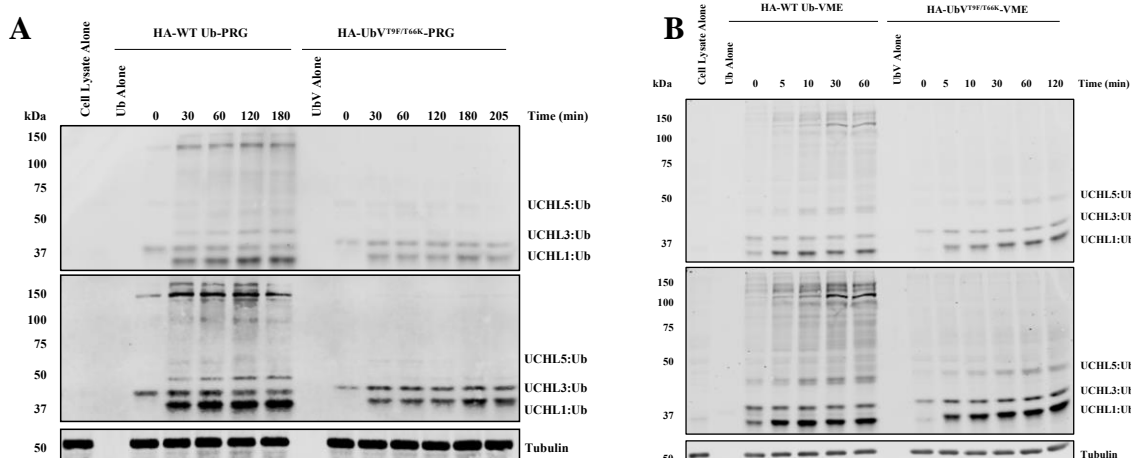


Figure 4.3 UbV^{T9FT66K}-ABP inhibits the UCH family selectively. SW1271 Cell Lysate Time-Course Western Blots Display UCH Selectivity of HA-UbV^{T9F/T66K}-PRG and HA-UbV^{T9F/T66K}-VME. 0.5 μ M of HA-WT-Ub-PRG/VME and HA-UbV^{T9F/T66K}-PRG/VME was incubated with 0.5 mg/mL SW1271 cell lysate for the times stated above the lanes at 37 °C. **A)** HA immunoblots with low brightness (upper) and high brightness (lower) with HA-UbV^{T9F/T66K}-PRG **B)** HA immunoblots with low brightness (upper) and high brightness (lower) with HA-UbV^{T9F/T66K}-VME.

Table 4.2 k_{inact}/K_I values for ABPs with UCHL1 and UCHL3.

Enzyme	ABP	k_{inact}/K_I ($\text{M}^{-1}\text{s}^{-1}$) ^a
UCHL1	WT-Ub-VME	6.70×10^3
	UbV ^{T9F/T66K} -VME	1.38×10^3
	WT-Ub-PRG	1.28×10^2
	UbV ^{T9F/T66K} -PRG	2.81×10^1
UCHL3	WT-Ub-VME	1.60×10^6
	UbV ^{T9F/T66K} -VME	1.33×10^7
	WT-Ub-PRG	4.79×10^6
	UbV ^{T9F/T66K} -PRG	6.44×10^3

^a k_{inact}/K_I data were extracted from linear regression slopes of graphs of [Ub-ABP] vs k_{obs} . k_{obs} values were extracted from the progress curve where various concentrations of Ub-ABP were incubated with His-UCHL1 or His-UCHL3. All Ub-ABPs contain a HA tag.

4.2.2 Modeling and Molecular Dynamics Simulations of the Ub^{T9F} mutant with UCHL1 and UCHL3

To investigate the roles of the T9F mutation in modulating the binding affinity and inactivation kinetics of UCHL1 and UCHL3, molecular dynamics (MD) simulations in Desmond (D.E. Shaw Research) and protein-protein interaction (PPI) analysis in BioLuminate (Schrödinger, LLC.) were performed. Several UCH and Ub complexes were simulated and analyzed to model the enzymes during the formation of the UCH-Ub complex, as well as the stability of the newly formed UCH-Ub complex. Apo-UCHL1 (PDB entry 2ETL) with Ub^{WT} (Ub:UCHL1^{Binding}) and UCHL1 from the Ub-bound crystal structure (PDB entry 3KW5) bound to Ub^{WT} (Ub:UCHL1^{Bound}) were both modeled, simulating the binding event as well as the bound complex for wild type Ub (providing a baseline for active UCHL1). Analogously, apo-UCHL1 (PDB entry 2ETL) with Ub^{T9F} (UbV^{T9F}:UCHL1^{Binding}) and UCHL1 from the Ub-bound crystal structure (PDB entry 3KW5) bound to Ub^{T9F} (UbV^{T9F}:UCHL1^{Bound}) were modeled, simulating the binding event as well as the bound complex for the UCH-selective Ub^{T9F} mutant. UCHL3 from the crystal structure of PDB entry 1XD3 with UbV^{T9F} (UbVT9F:UCHL3^{Binding}) was also simulated to model what may happen upon binding of UbV^{T9F} to UCHL3. Finally, apo-UCHL1 was modeled independently of Ub to determine a baseline for inactive UCHL1.

Loop dynamics of Ub^{T9F} result in selectivity for UCHL1 over UCHL3

The β 1– β 2 loop of WT-Ub (PDB entry 1UBQ) forms a bent conformation, resulting in a hydrogen bond interaction between the side chain hydroxyl groups of Thr7 and Thr9.¹⁷³ In both the Ub:UCHL1⁷⁵ and Ub:UCHL3¹⁵⁸ crystal structures (PDB entries 3KW5 and 1XD3, respectively), this bent conformation is maintained. The MD simulation of the Ub:UCHL1^{Binding} (PDB entry 2ETL) complex recapitulates this conformation, matching the experimentally determined loop configuration from the Ub:UCHL1 co-crystal structure (Figure 4.4A, cyan). However, upon Thr9Phe mutation on Ub, the Thr7 and Thr9 side chain hydrogen bond interaction is no longer possible. The UbV^{T9F}:UCHL1^{Binding} (PDB entry 2ETL) MD simulation suggests that in the absence of the Thr7 – Thr9 hydrogen bond interaction, the β 1– β 2 loop of Ub may initially assume an extended conformation (Figure 4.4A, gray).

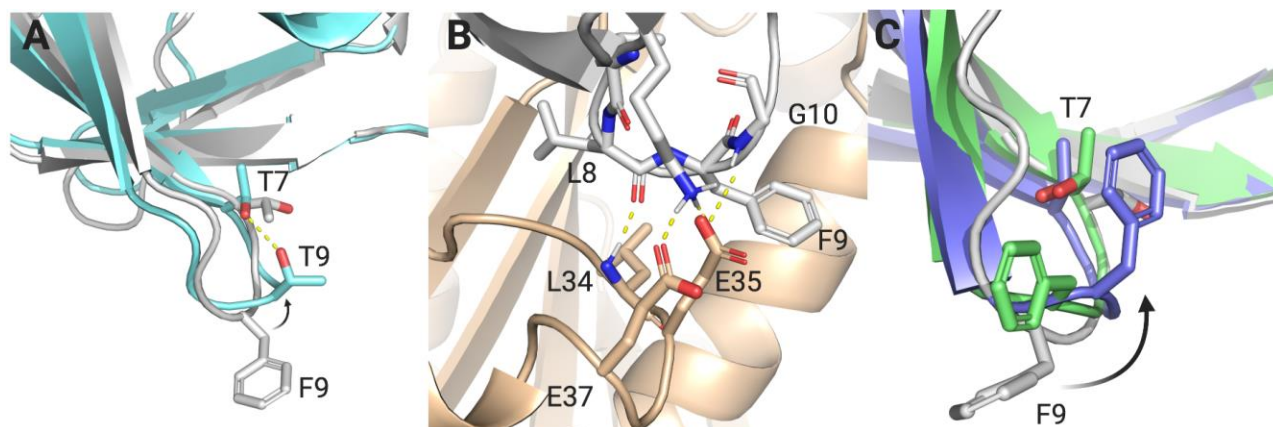


Figure 4.4 $\beta 1$ – $\beta 2$ loop dynamics and predicted interactions with UCHL1. **A)** Frames from MD simulation of Ub:UCHL1 (cyan) and UbV^{T9F}:UCHL1 (gray) complexes (PDB: 2ETL was used, not shown in **A** for clarity). Black arrow depicts change in loop position. Interactions between side chains of Thr7 and Thr9 on Ub shown with yellow dashed lines. **B)** Predicted binding interactions from UbV^{T9F}:UCHL1 complex (yellow dashed lines) with UbV^{T9F} (gray) with UCHL1 (gold) shown at the 9 ns timepoint of the MD simulation. **C)** Predicted UbV^{T9F} $\beta 1$ – $\beta 2$ loop conformational change of UbV^{T9F}:UCHL1 complex during binding at 9 ns (gray), 18 ns (green), 25 ns (purple). UCHL1 not shown for clarity to provide focus on loop. Black arrow depicts movement of loop as time progressed to a final state that resembles the $\beta 1$ – $\beta 2$ loop conformation in apo-Ub. Images were created in PyMol version 2.3.3. Figure created with Biorender.com.

Frames at 5 ns and 9 ns from the UbV^{T9F}:UCHL1^{Binding} (PDB entry 2ETL) MD simulation were isolated and evaluated using BioLuminate to analyze the protein-protein interactions that occur during the extended conformation of the $\beta 1$ – $\beta 2$ loop. Compared to the UbV:UCHL1^{Binding} (PDB entry 2ETL), the extended conformation of the UbV^{T9F}:UCHL1^{Binding} (PDB entry 2ETL) $\beta 1$ – $\beta 2$ loop in the MD simulation suggests that additional hydrogen bond interactions between UbV^{T9F} and UCHL1 are possible (Figure 4.4B). Additionally, these new interactions are not seen in the Ub-UCHL1 crystal structure (PDB entry 3KW5). In this extended $\beta 1$ – $\beta 2$ loop conformation, the backbone carbonyl of Leu8 and the backbone amide nitrogen of Gly10 on UbV^{T9F} have the potential to make hydrogen bonds with the backbone amide nitrogen of Leu34 and side chain carbonyl of Glu35 of UCHL1, respectively (Figure 4.4B). In addition, the sidechain nitrogen of Lys6 on UbV^{T9F} is in the proximity of the Glu35 and Glu37 side chains on UCHL1, providing the potential for additional hydrogen bond interactions with these two residues (Figure 4.4B). During the progression of the simulation, the $\beta 1$ – $\beta 2$ loop condenses and is no longer in an extended configuration, remaining in this conformation for the remainder of the simulation (Figure 4.4C). This places Phe9 of UbV^{T9F}

in the proximity of the hydroxyl group of Thr7 on UbV^{T9F}. This may be stabilized by a lone pair – pi interaction or may be the result of hydrophobic packing to reduce the entropy of this loop.¹⁷⁴ Two representative frames were selected from the UbV^{T9F}:UCHL1^{Binding} (PDB entry 2ETL) MD simulation (25 and 35 ns) and evaluated using BioLuminate to analyze the protein-protein interactions. In these frames, the β 1– β 2 loop is in a similarly bent conformation that is observed in the apo-Ub crystal structure (1UBQ). In this conformation, the previously observed interactions between the β 1– β 2 loop of UbV^{T9F} and UCHL1 are no longer present, consistent with the lack of interactions in the Ub:UCHL1^{Bound} (PDB entry 3KW5) co-crystallized complex. Therefore, the reduced affinity between UbV^{T9F} and UCHL1 compared to wild type Ub may be rationalized as a combination of new predicted hydrogen bonds from the extended β 1– β 2 loop, as well as a potential entropic penalty resulting from the β 1– β 2 loop rearrangement upon binding to UCHL1.

The same approach was employed to analyze the Ub:UCHL3 and UbV^{T9F}:UCHL3 interaction network. The Ub:UCHL3^{Bound} (PDB entry 1XD3) β 1– β 2 loop is in the same conformation as both the apo-Ub and Ub:UCHL1^{Bound} crystal structures. However, opposite of the predicted β 1– β 2 loop dynamics observed in the UbV^{T9F}:UCHL1^{Binding} (PDB entry 2ETL) MD simulation, the UbV^{T9F}:UCHL3 β 1– β 2 loop is predicted to extend during the binding event (Figure 4.5). Protein-protein interaction analysis of the Ub:UCHL3^{Bound} complex using BioLuminate suggests that a hydrogen bond between Lys6 of UbV^{T9F} and Asp38 of UCHL3 is able to form. Analysis of the Ub:UCHL3 co-crystal structure (PDB entry 1XD3) does not corroborate this interaction, suggesting that the mutation of Ub Thr9 to Phe9 may install a new hydrogen bond. Asp38 of UCHL3 corresponds to Glu37 of UCHL1, implying that the interaction between UbV^{T9F} Lys6 and an acidic residue of the UCH enzymes is conserved. An additional interaction is proposed to take place between UbV^{T9F} and the acidic residue Glu35 of UCHL1. The UbV^{T9F}:UCHL3^{Bound} structure does not recapitulate this interaction, as the corresponding amino acid on UCHL3 is Gly36. Beyond the UbV^{T9F} Lys6 UCHL3 Glu37 interaction, molecular modeling does not support the formation of any additional hydrogen bond interactions, throughout the duration of the MD simulation. Although additional studies, primarily structural analysis, are necessary to fully explain the effect of the T9F mutation on the binding of Ub to UCHL1 and UCHL3, the differences between the hydrogen bond interaction networks may provide an understanding of the experimentally observed difference in binding selectivity.

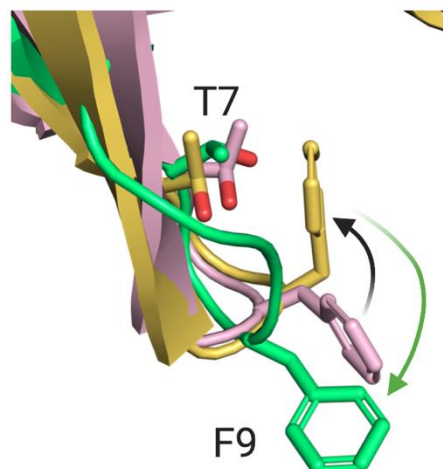


Figure 4.5 Molecular dynamics simulation of $\beta 1$ – $\beta 2$ loop of UbV^{T9F} upon binding to UCHL3. (PDB: 1XD3, not shown in figure). 19 ns (purple), 30 ns (yellow), and 92 ns (green) times point shown. Black arrow depicts movement of Phe9 from 19 – 30 ns during the binding event to UCHL3. Green arrow depicts movement of Phe9 from 30 – 92 ns during the binding event to UCHL3 as predicted by MD simulation. Images were created in PyMol version 2.3.3. Figure created with Biorender.com.

UCHL1 F214 MD simulations provide evidence for the mechanism of UbV^{T9F}-ABP inhibition

UbV^{T9F} binds selectively to UCHL1 over UCHL3, however reaction of the UbV^{T9F}-ABP favors UCHL3 over UCHL1. Although UCHL1 and UCHL3 share nearly 50% sequence homology, their structures differ in a key aspect. It is known that the catalytic triad of UCHL1 (D176, H161, and C90) are misaligned in the apo structure of UCHL1. Upon the binding of Ub, UCHL1 undergoes a conformational change that activates the catalytic cysteine via a rearrangement of the catalytic triad.⁷⁵ In comparison, the UCHL3 catalytic triad is in a constitutively active alignment.^{76,158} This difference likely accounts for the observed disparity between the catalytic activity of the two enzymes.⁷⁴ The misalignment of UCHL1's active site is easily visualized when overlaying the apo-UCHL1 and the Ub-bound crystal structures (Figure 4.6). The Ub $\beta 1$ – $\beta 2$ loop residues Leu 8 and Thr9 repel Phe214 of UCHL1, displacing it and causing it to flip inward. This causes a cascading event that subsequently forces Phe53 to swivel inward, pushing His161 in proximity to Cys90 to produce an active conformation. Therefore, it can be reasoned that the activation of UCHL1 relies on the rotation of Phe214. The covalent inhibition kinetic data for UbV^{T9F} and UCHL1 shows that the T9F mutation reduces the activity of UCHL1 relative to wild type Ub (Table 4.2), suggesting that Phe9 is not capable of activating UCHL1 as well as Thr9.

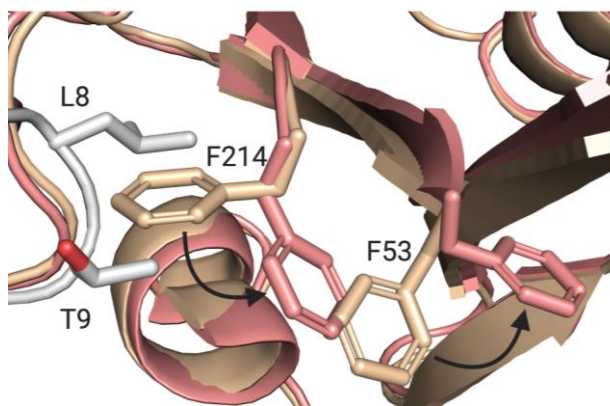


Figure 4.6 F214 activation cascade by the Ub β 1– β 2 loop. Overlaid crystal structures of UCHL1 (PDB: 2ETL; gold) and Ub-bound UCHL1. (PDB: 3KW5; salmon) zoomed in on Ub β 1– β 2 loop interaction with F214 and F53. Black arrows depict the conformational change of F214 upon Ub binding from the inactive (gold) to the active (salmon) state and subsequent cross-talk that flips F53. Images were created in PyMol version 2.3.3. Figure created with Biorender.com.

MD simulations were again used to investigate the role the T9F mutation has on the activation of UCHL1. To this end the radius of gyration (R_g), the root-mean-squared distance of the center of mass, of UCHL1s Phe214 was used as a metric to distinguish between activated (Ub-bound) and inactive (apo) UCHL1. The apo-UCHL1 crystal structure (PDB entry 2ETL) and the Ub-bound crystal structure (PDB entry 3KW5) were used to determine the benchmark R_g values for the active and inactive conformations of Phe214 (Figures 4.6 and 4.7). MD simulations were then performed with both apo-UCHL1 (PDB entry 2ETL) and Ub-bound UCHL1 (PDB entry 3KW5), and the R_g for Phe214 was plotted as function of time. As expected, Phe214 of apo-UCHL1 remained in an inactive conformation for the majority of the simulation, though a brief flip of Phe214 into an active conformation was observed at ~62 ns (Figure 4.7A). This suggests that UCHL1 may be able to become activated for short periods of time, even in the absence of Ub. These results may explain why relatively inert covalent inhibitors are able to modify the active site Cys90 when it is in the inactive state with no Ub present.^{33,52,72,82} The MD simulation for the Ub:UCHL1 complex (PDB entry 3KW5) displayed the expected results, with Phe214 remaining in the active conformation for the entirety of the simulation (Figure 4.8A). These two simulations provide the requisite controls to define the R_g values for active and inactive UCHL1.

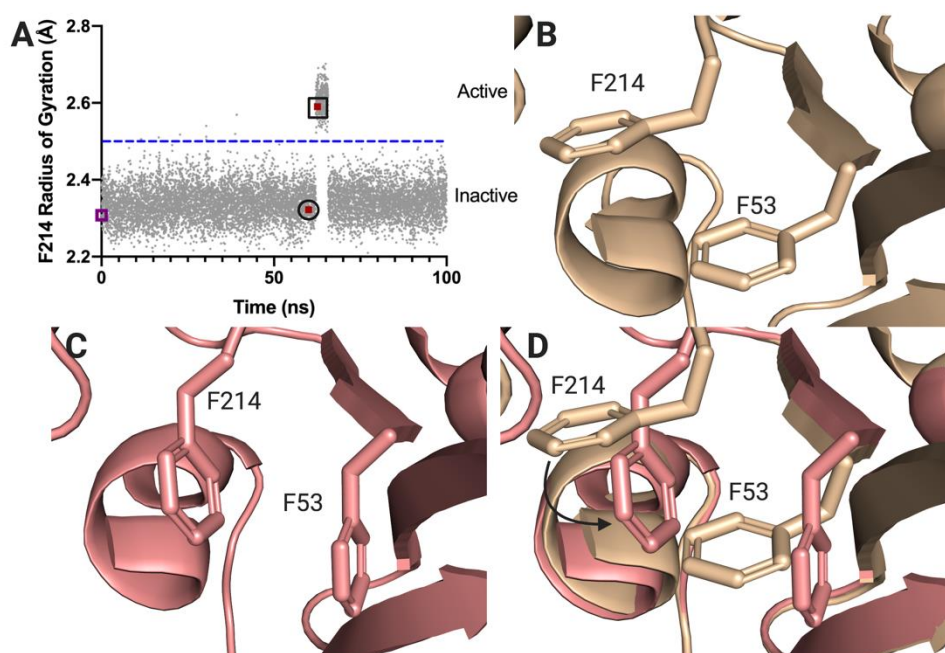


Figure 4.7 Molecular dynamics of Phe214 of apo-UCHL1 crystal structure (PDB: 2ETL) with no Ub present. **A)** Plot of R_g values for F214 versus time of the MD simulation for apo-UCHL1 in absence of Ub. Blue dashed line inserted as reference point between R_g values for inactive state and values for active state. R_g value at 60 ns shown in circle (inactive) and 63 ns shown in box (active). Initial R_g value for F214 from apo-UCHL1 crystal structure shown by purple box on Y-axis. **B)** Orientation of F214 of UCHL1 in the inactive conformation (gold) at 60 ns that corresponds to the R_g value at that time point. **C)** Orientation of F214 of UCHL1 in the active conformation (salmon) at 63 ns that corresponds to the R_g value at that time point. **D)** Overlay of MD simulation frames from 60 ns (gold) and 63 ns (salmon) that correspond to the values highlighted in the R_g versus time plot. The position of the F214 at 60 ns closely resembles that of the inactive conformation from apo-UCHL1 while the position of F214 at 63 ns resembles the active conformation. Black arrow depicts the change in position of F214. Residues 54 – 74 and 199 – 213 removed for clarity. Images were created in PyMol version 2.3.3. Figure created with Biorender.com.

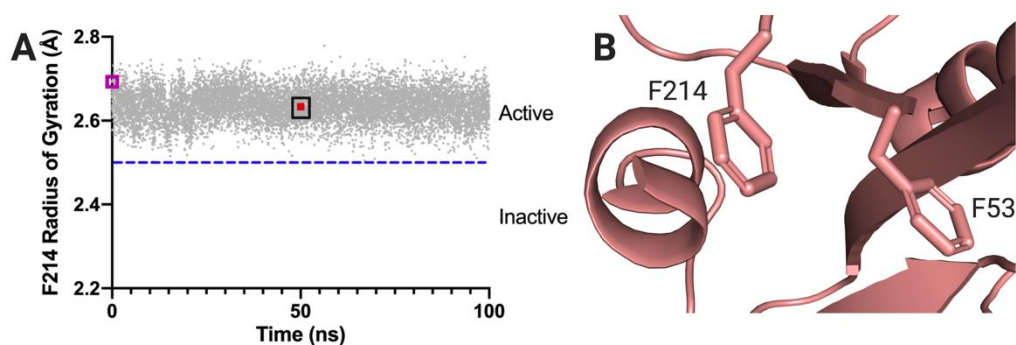


Figure 4.8 Molecular dynamics of Phe214 from Ub-bound UCHL1 crystal structure (PDB: 3KW5). **A)** Plot of R_g values for F214 versus time of the MD simulation for Ub-bound UCHL1. Blue dashed line inserted as reference point between R_g values for inactive state and values for active state. R_g value at 50 ns shown in circle (inactive). Initial R_g value for F214 from Ub-bound -UCHL1 crystal structure shown by purple box on Y-axis. **B)** Orientation of F214 of UCHL1 in the active conformation (salmon) at 50 ns that corresponds to the R_g value at that time point. Residues 54 – 74 and 199 – 213 removed for clarity. Images were created in PyMol version 2.3.3. Figure created with Biorender.com.

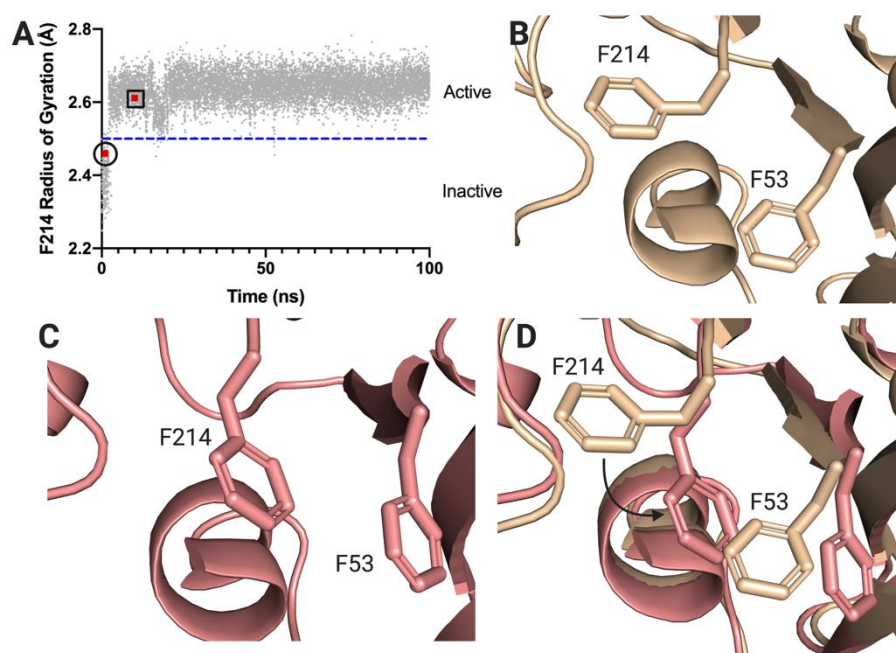


Figure 4.9 Molecular dynamics of Phe214 of apo-UCHL1 crystal structure (PDB: 2ETL) with Ub present. **A)** Plot of R_g values for F214 versus time of the MD simulation for apo-UCHL1 in presence of Ub. Blue dashed line inserted as reference point between R_g values for inactive state and values for active state. R_g value at 1 ns shown in circle (inactive) and 10 ns shown in box (active). **B)** Orientation of F214 of UCHL1 in the inactive conformation (gold sticks) at 1 ns that corresponds to the R_g value at that time point. **C)** Orientation of F214 of UCHL1 in the active conformation (salmon sticks) at 10 ns that corresponds to the R_g value at that time point. **D)** Overlay of MD simulation frames from 1 ns (gold sticks) and 10 ns (salmon sticks) that correspond to the values highlighted in the R_g versus time plot. The position of the F214 at 1 ns closely resembles that of the inactive conformation from apo-UCHL1 while the position of F214 at 10 ns resembles the active conformation. Black arrow depicts the change in position of F214. Residues 54 – 74 and 199 – 213 removed for clarity. Images were created in PyMol version 2.3.3. Figure created with Biorender.com.

Following these control simulations, the Ub:UCHL1^{Binding} simulation was performed using apo-UCHL1 (PDB entry 2ETL) and Ub to see if the MD simulations could accurately recapitulate *in silico* the observed activation of UCHL1 in the crystal structures. Indeed, upon binding of Ub to UCHL1 (PDB entry 2ETL) to form the Ub:UCHL1^{Binding} complex the Phe214 side chain of UCHL1 quickly rotated from inactive to active and remained so for the entirety of the simulation, successfully matching the experimentally observed results in crystallographic experiments (Figure 4.9). These results also provided a benchmark for expected *in silico* activation of UCHL1.

Next, the binding of UbV^{T9F} to UCHL1 (PDB entry 2ETL) was simulated to observe Phe214 in the UbV^{T9F}:UCHL1^{Binding} complex. The results from this MD simulation suggests that this

mutation causes Phe214 to oscillate between the active and inactive conformations of UCHL1, though UCHL1 remains in an inactive conformation for the majority of the simulation (Figure 4.10). These MD simulations provide evidence that although the T9F mutation is able to activate UCHL1 it is not able to keep UCHL1 in an active conformation as well as wild type Ub, reducing the catalytic activity of the enzyme.

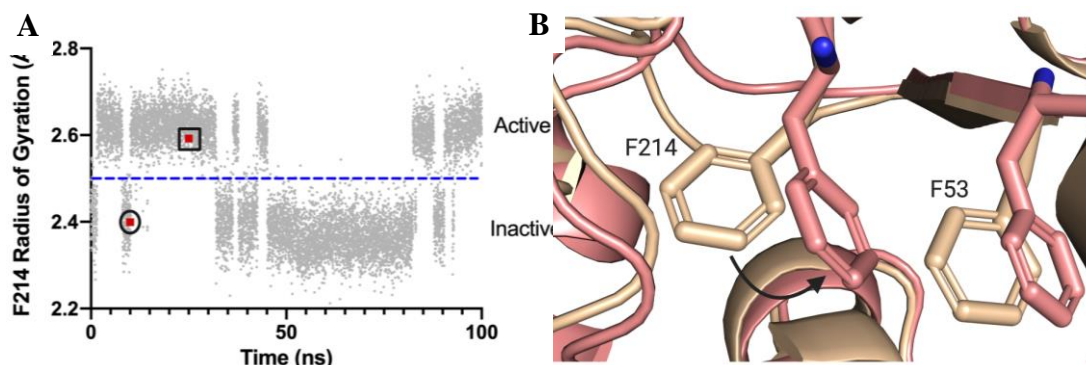


Figure 4.10 Dynamics of Phe214 upon binding of UbV^{T9F}. **A)** Plot of R_g values for F214 versus time of the MD simulation for UbV^{T9F}:UCHL1 (2ETL) complex. Blue dashed line inserted as point of reference between R_g values for inactive state and values for active state. R_g value at 10 ns shown in circle (inactive) and 25 ns shown in box (active). **B)** Overlay of MD simulation frames from 10 ns (gold) and 25 ns (salmon) that correspond to the values highlighted in the R_g versus time plot. The position of the F214 at 10 ns closely resembles that of the inactive conformation from apo-UCHL1 while the position of F214 at 25 ns resembles the active conformation. Black arrow depicts the change in position of F214. Residues 54 – 74 and 199 – 213 removed for clarity. Images were created in PyMol version 2.3.3. Figure created with Biorender.com.

Together, the results from these simulations provide insight into the modification of Ub-UCHL1 binding by the T9F mutation. Although the results from the MD simulations match what would be expected based on the experimental results, additional investigation (particularly structural studies) is required to confirm the new Ub-UCHL1 interactions. Regardless, the reduced affinity and reduced efficiency of UCHL1 to form a Ub-UCHL1 complex in the presence of the UbV^{T9F}-ABP compared to wild type Ub-ABPs can be rationalized from the MD simulation results. One contributing factor the reduced catalytic activation of UCHL1 by UbV^{T9F} is the 22-fold reduction in binding affinity relative to WT Ub. In addition to this, the T9F mutation may further reduce the enzymatic activity of UCHL1 by reducing the activation of the catalytic cysteine. The MD

simulations that support this hypothesis suggest that UCHL1 is never fully activated in the presence of UbV^{T9F}, but rather oscillates between active and inactive states during the binding of the substrate. This reduced activation likely contributes to the reduced efficacy of UCHL1 to form Ub-UCHL1 complexes with the Ub^{VT9F/T66K}-ABPs compared to the wild type Ub-ABPs. Combined with the already reduced catalytic activity of UCHL1 relative to UCHL3, it is likely that the reduced reactivity of UCHL1 caused by the T9F mutation is too much to overcome the high enzymatic activity of UCHL3 and provide a UCHL1 selective UbV. However, these experimental results provide valuable insight into the future development of UCHL1 selective UbVs. To avoid reducing the catalytic activity of UCHL1 even further and putting UCHL1 at a greater disadvantage compared to UCHL3, it would be best to leave the β 1– β 2 loop of Ub unaltered and focus on other locations to impart selectivity. Additionally, increasing the catalytic activity of UCHL1 by altering the β 1– β 2 loop may provide a feasible alternative to instilling selectivity towards UCHL1.

4.3 Conclusion

In conclusion, Ub mutations were identified that would provide binding selectivity towards UCHL1 over UCHL3. These mutations, particularly the T9F mutation, were validated experimentally using *in vitro* binding and activity assays. To provide further UCHL1 selectivity, an additional mutation at Thr66 to Lys was installed to reduce binding to USPs and other DUB families. Converting this double mutant to an ABP confirmed the reduction of non-UCH enzymes, though the Ub-ABP now appeared selective for UCHL3 of UCHL1. Kinetic analysis suggested that the intrinsic reactivity of UCHL3 was the cause of the inversion of selectivity in cellular assays compared to biochemical assays. MD simulations were then performed to probe the role of the T9F mutation in both UCHL1 binding and reactivity. The results from these simulations suggest that the T9F containing β 1– β 2 loop may provide new productive contacts between UbV^{T9F} and UCHL1 while also reducing the amount of time the enzyme remains in an active conformation while the bound to UbV^{T9F} compared to wildtype Ub. This hypothesis will serve as the basis for new studies to elucidate the role of mutations to the β 1– β 2 loop. Nonetheless, this study provides support for the feasibility of computationally designing UCHL1 selective UbV.

4.4 Experimental

4.4.1 Biochemical Assays

Plasmids, Mutagenesis, and Cloning.

All plasmids were ordered from GenScript (Piscataway, NJ) unless otherwise noted. The site-directed mutagenesis and validation of the pRSET-A monoubiquitin plasmid were outsourced to Gen- Script. Plasmids were transformed into competent BL21(DE3) E. coli cells (New England Biolabs, catalog no. C2527I) and plated on ampicillin agar plates. Single colonies were picked from the agar plates and grown overnight at 37 °C while being shaken at 250 rpm. Glycerol stocks were made from these cultures by mixing 20% glycerol and 80% bacterial culture and stored at –80 °C for future protein expressions.

Recombinant Expression of UCHL1 and UCHL3 Proteins.

A pET-15b plasmid construct was used for the expression of both six-histidine (His)-tagged UCHL1 and His- UCHL3 in bacterial culture. These plasmids were transformed into competent BL21(DE3) E. coli cells using the procedure previously described. Starter cultures were grown at 37 °C while being shaken at 250 rpm overnight. Ten milliliters of starter culture was inoculated into each liter of autoclaved LB medium containing 100 µg/mL ampicillin and grown at 37 °C while being shaken at 250 rpm to an OD of 0.4–0.8 before being induced with 300 µL of 1.0 M isopropyl β-D-1- thiogalactopyranoside. These induced cultures were grown for 18 h at 18 °C while being shaken at 250 rpm. Bacterial cell pellets were spun down at 4000g for 20 min and resuspended in lysis buffer (1× PBS containing 400 mM KCl). These resuspended bacterial cells were stored in a –80 °C freezer for lysis on a later date or taken directly to lysis by sonication. Lysed bacterial cells were pelleted by centrifugation at 14000g, and the supernatant was loaded onto a nickel-NTA column equilibrated with 1× PBS. After the flow-through was collected, the column was subjected to a 0 to 500 mM imidazole step gradient and fractions were collected. Both His- UCHL1 and His- UCHL3 eluted from the column at ~150 mM imidazole as evidenced by sodium dodecyl sulfate–polyacrylamide gel electrophoresis (SDS–PAGE) of fractions collected. Fractions that contained the desired protein were pooled together and dialyzed against 1× PBS containing 400 mM KCl with 1.0 mM DTT. This dialyzed protein sample was concentrated using Amicon Ultra Centrifugal Filters and purified by size-exclusion chromatography (SEC) on an S200 column using running buffer [50

mM Tris, 50 mM NaCl, and 1 mM DTT (pH 7.6)]. Fractions that contained the protein of interest were concentrated and held at -80°C for future experimental use.

Recombinant Expression of UbV Proteins.

Monoubiquitin (herein termed ubiquitin or Ub) variants were purified from a pRSET-A vector. The untagged WT-Ub pRSET-A vector construct was obtained from C. Das (Purdue University). This WT-Ub plasmid was sent to GenScript where site-directed mutagenesis was performed and validated. All UbVs were purified as described above with the following changes. The lysis buffer added to the bacterial cell pellets was 50 mM sodium acetate (pH 4.5). After lysis by sonication, the sample was boiled at 80°C for 5 min to precipitate out the undesired proteins. After centrifugation at 14000g, the pH of the supernatant was measured to be ~ 5 so it was adjusted to 4.5 with glacial acetic acid to further precipitate out undesired proteins. The precipitated proteins were centrifuged down at 4000g for 8 min. The supernatant was loaded onto a countertop SP Sepharose Fast Flow (Mono S) column (GE Healthcare, product no. 17-0729-10); the flow-through was collected, and the column was subjected to a 0 to 1.0 M NaCl step gradient to elute out the UbVs. The fractions that contained UbVs (determined through SDS-PAGE analysis) were concentrated and further purified by SEC on an S200 column as described above.

Ubiquitin Intein Chitin-Binding Domain Expressions.

Variations in the ubiquitin intein chitin-binding domain (Ub- intein-CBD) proteins were expressed in a pTXB1 vector (containing an Mxe intein/chitin-binding domain sequence). The process was performed for both WT-Ub and UbV. The WT-Ub-intein-CBD in a pTXB1 plasmid was provided by C. Das (Purdue University), and additions and mutations were made to this construct and validated by GenScript. The lysis buffer for these expressions was a 300 mM sodium acetate buffer containing 50 mM mercaptoethanesulfonic acid (MES) (pH 6.0) (herein termed equilibration buffer). After lysis by sonication, cell debris was pelleted as described above and the supernatant was run in a column containing chitin resin (New England Biolabs, catalog no. S6651S). Equilibration of the chitin column consisted of running 3 column volumes (CV) of equilibration buffer through the column prior to column loading. After a majority of the supernatant was flowed through the column a 30 min incubation step took place to allow for binding to the chitin resin. After

this step an additional 4 CV of equilibration buffer was washed through the column, after which equilibration buffer containing 50 mM MES sodium salt (MESNa) was added. This was incubated in the column for 18 h at 37 °C, after which the desired protein was eluted out using the same buffer. The eluted Ub-MESNa sample was concentrated to ~1.5 mL and stored at –80 °C until further use. Ub activity-based probes (Ub-ABPs) were constructed by reacting excess glycine-vinylmethylester (VME) or propargyl- amine (PRG) with Ub-MESNa overnight in 1.0 M sodium bicarbonate containing 150 mg of N-hydroxysuccinimide (NHS) in a total volume of 10 mL at pH 8.0 (to mitigate MESNa hydrolysis). This was dialyzed into 50 mM sodium acetate buffer (pH 4.5) and run on a Mono S column to separate out the reacted species. The fractions that contained ubiquitin species of interest were determined by reaction with UCHL1 for 30 min at 37 °C and a subsequent SDS–PAGE analysis.

Binding Affinity Measurements Using Biolayer Interferometry.

Ub and UbV binding affinity was measured according to a previously reported protocol³¹ with minor changes; mainly, our method utilized Ni-NTA-coated bio- sensors (Molecular Devices, part no. 18-5101) rather than streptavidin-coated sensors. Initial concentrations of the UCH proteins were determined by A280 on a NanoDrop system (ThermoScientific), after which His-UCHL1 and His-UCHL3 were diluted into BLI buffer [1× PBS containing 0.05% (v/v) Tween 20 and 0.1% (w/v) bovine serum albumin (BSA)] to concentrations of 25 and 100 µg/mL, respectively, to achieve a similar loading in BLI assays. UbVs were buffer exchanged into 1× PBS using 0.5 mL Zeba spin desalting columns (ThermoScientific, catalog no. 89882). The concentration of the UbVs was determined by the BCA assay and diluted to top concentrations into BLI buffer, and 1:1 serial dilutions were completed. Top concentrations differed in assay setups based on the expected K_d of UbV to UCH protein (for example, the WT-Ub top concentration was 2 µM for UCHL1 and 4 µM for UCHL3); 40 µL of each solution was added to a 384-well tilted-bottom plate (Molecular Devices, part no. 18- 5080). One Ni-NTA biosensor was used for each K_d measurement, dipping first into BLI buffer (initial baseline, 60 s), then into the His-UCH protein wells (loading step, 300 s), then into BLI buffer alone (baseline step, 60 s), then into the lowest concentration of UbV (association step, 120 s), and then into buffer alone (dissociation step, 100 s). A reference sensor loaded with protein was dipped into wells containing only buffer to adjust for protein-buffer signals. The

association- dissociation was repeated with increasing concentrations of UbV. All measurements were taken at 30 °C.

Biacore Data Analysis Software (version 8.2) was used to collect and analyze the raw data for the association and dissociation curves. After subtraction of a reference sensor (loaded sensors dipped into wells containing only buffer), averages of the association responses (in nanometer response signal from 110 to 115 s) were calculated and plotted as a function of UbV concentration in Prism 8. These data were fit to a nonlinear regression one-site specific binding model to determine a K_d. Nonspecific binding of the sensor to Ub (unloaded sensor tip dipped into Ub-containing wells) was checked with WT-Ub. The negligible nonspecific signal was observed at a WT-Ub concentration of 2 μM (not shown).

UCH Inhibition Assays.

UbVs were buffer exchanged into 50 mM Tris-HCl containing 0.5 mM EDTA (pH 7.6) using 0.5 mL Zeba spin desalting columns (ThermoScientific, catalog no. 89882). The concentrations of each UbV were determined by the BCA assay and diluted to 5× top assay concentrations in activity assay buffer [50 mM Tris, 0.5 mM EDTA, 0.1% bovine serum albumin, and 5 mM DTT (pH 7.6)]. For UCHL1, the 5× top assay concentrations were as follows: 62.5 μM for WT-Ub, 500 μM for UbV^{T9E}, 125 μM for UbV^{T9F}, 500 μM for UbV^{T9K}, 250 μM for UbV^{T9R}, 250 μM for UbV^{T9W}, 250 μM for UbV^{T9Y}, 250 μM for UbV^{K11I}, 500 μM for UbV^{K11Y}, 250 μM for UbV^{K11W}, 62.5 μM for UbV^{D39M}, 250 μM for UbV^{Q40Y}, 500 μM for UbV^{Q40W}, 500 μM for UbV^{V70F}, and 125 μM for UbV^{T9F/T66K}. For UCHL3, 5× top assay concentrations were as follows: 500 μM for WT-Ub, 250 μM for UbV^{T9E}, 500 μM for UbV^{T9F}, 500 μM for UbV^{T9K}, 250 μM for UbV^{T9R}, 250 μM for UbV^{T9W}, 250 μM for UbV^{T9Y}, 250 μM for UbV^{K11I}, 500 μM for UbV^{K11Y}, 250 μM for UbV^{K11W}, 62.5 μM for UbV^{D39M}, 250 μM for UbV^{Q40Y}, 500 μM for UbV^{Q40W}, 62.5 μM for UbV^{V70F}, and 125 μM for UbV^{T9F/T66K}. The 5 × top assay concentrations differed for each UbV on the basis of the expected IC₅₀. The 1:1 serial dilutions of 5× top assay concentrations for each UbVs were completed in activity assay buffer. His-UCHL1 and His-UCHL3 proteins were diluted into activity assay buffer, and 20 μL of 2.5 nM His-UCHL1 and 0.25 nM His-UCHL3 was added to wells of a black 384- well plate (Fisher Scientific, product no. 12566624) and incubated with 10 μL of a 5× concentration of UbV for 30 min. The difference in enzyme concentration was due to activity differences in the enzymes and necessary to obtain a readout in the linear range for analysis. A 450 nM stock of

ubiquitin rhodamine110 (Ub-Rho) was made, and 20 μ L of this stock was added to the assay wells directly before fluorescent measurements were recorded using a Synergy Neo2Multi-Mode Reader (Biotek) at excitation and emission wavelengths of 485 and 530 nm, respectively. Initial slopes were identified and plotted using Prism 8. The control (wells containing only activity assay buffer and no ubiquitin inhibitor) was normalized to 100% enzyme activity, and the sample wells were calculated as percent activity compared to the control.

DUB Engagement Assay in Cell Lysates.

DUB engagement assays were performed according to previously published protocols with minor changes.¹⁵⁹ Cell pellets were lysed in 50 mM Tris-HCl buffer (pH 7.4) containing 150 mM NaCl, 5 mM MgCl₂, 5 mM DTT, 2 mM ATP, 0.5% NP-40, and 10% glycerol (herein termed cell lysis buffer) for 30 min on ice. Every 10 min, the incubating cells were vortexed for 10 s to ensure homogeneous lysis. Cell lysates were clarified by centrifugation at 13000g for 10 min, and the supernatant was collected. Protein concentrations of clarified cell lysates were determined using a Bradford assay, and each sample was brought to a concentration of 0.5 mg/mL in cell lysis buffer. Initial hemagglutinin (HA)-tagged Ub activity-based probe (ABP of vinylmethylester or propargylamine) concentrations were determined by A280 on a NanoDrop system (Thermo-Scientific) and changed to 10 μ M in cell lysis buffer. Concentration determinations by A280 measurements were performed with all HA-containing Ub and UbVs because of the higher extinction coefficient provided by the HA sequence (leading to more accurate protein concentrations), relative to the monoubiquitins. One part of 10 μ M HA-Ub-ABP was added to 19 parts of 0.5 mg/mL cell lysate and incubated in a heat block at 37 °C for the times stated. The 4 \times Laemmli buffer was added to the samples to terminate the reaction at each time point. For the dose dependency blots, 1 part of a 20 \times concentration of HA-Ub-ABP was added to 19 parts of 0.5 mg/mL cell lysate and incubated in a heat block at 37 °C for the times stated. Ten microliters of each sample was loaded onto a 12% SDS-PAGE gel and run at a constant voltage of 190 V for ~75 min. For the USP7 Western blots, SDS-PAGE gels were run at a constant voltage of 190 V for 130 min to achieve band separation of USP7 and USP7:Ub-ABP. Gels were transferred to a nitrocellulose membrane and subjected to Western blot procedures. The following primary antibodies were used: HA-Tag-6e2 (Cell Signaling Technologies), C29F4 (Cell Signaling Technologies), Ab18181 (Abcam), UCHL1- 15C7 mouse hybridoma (University of Iowa Developmental Studies Hybridoma Bank),

UCHL3-Ab126621 (Abcam), UCHL5-Ab133508 (Abcam), α -tubulin-Ab7291 (Abcam) or Ab176560 (Abcam), and USP7-Ab4080 (Abcam). Fluorescent secondary antibodies (Licor IRDye 680RD goat anti-rabbit and Licor IRDye 800CW goat anti-mouse) were used. Images were collected on a Licor Odyssey system.

Ubiquitin Activity-Based Probe k_{inact}/K_I Assays.

k_{inact}/K_I is a metric that is relevant for irreversible inhibitors as the efficacy of the covalent bond formation is dependent on the rate of the bond-forming reaction as well as the ligand binding to the target. k_{inact}/K_I describes the potency of the first reversible binding event in terms of the inhibition constant (K_I) and the maximum rate of inactivation (k_{inact}). To obtain these data, His-UCHL1 and His-UCHL3 enzymes were diluted to 2.5 nM and 0.25 nM stock solutions, respectively, in 50 mM Tris-HCl (pH 7.6) buffer containing 0.5 mM EDTA, 5 mM DTT, and 0.1% (w/v) BSA. HA-WT-Ub-ABPs and HA-UbV-ABPs underwent 1:1 serial dilutions from a top concentration in the same buffer. The UCH enzyme concentrations were optimized to obtain a dynamic range of progress curves for k_{obs} determinations. Ub-Rho (Boston Biochem, catalog no. U-555) was diluted to 450 nM in the same buffer to make the Ub-Rho stock. Twenty microliters of a Ub-Rho stock solution was first added to each well in a 384- well plate followed by 10 μ L of HA-WT-Ub-ABP or HA-UbV- ABP. To initiate the reaction, 20 μ L of each respective enzyme stock solution was added and fluorescence measurements were immediately recorded on a Synergy Neo 2 Multi-Mode Reader (BioTek) at excitation and emission wavelengths of 489 and 530 nm, respectively. Progress curve raw data were input into Prism 8, and a baseline correction analysis was completed to obtain all of the time zero points at the origin for fitting purposes. Each progress curve underwent fitting to the equation $Y = V_0 * (1 - e^{-k_{\text{obs}} * t}) / k_{\text{obs}}$.¹⁴³ The k_{obs} values for each progress curve was graphed versus the concentration of HA-WT-Ub-ABP or HA-UbV-ABP. The slope of the linear fit was determined to be k_{inact}/K_I (the rate constant describing the UbV's inactivation efficiency) (covalent bond formation on the catalytic cysteine) on the UCH enzymes resulting from the potency (K_I) of binding and the maximum potential rate of inactivation (k_{inact}).

4.4.2 Computational Modeling and Analysis

Mutational Modeling and Molecular Dynamics.

An initial structural alignment was performed to align the apo-UCHL1 X-ray crystal structure (PDB entry 2ETL) to the Ub- bound UCHL1 X-ray crystal structure (PDB entry 3KW5) in Maestro using Protein Prep Wizard (Schrödinger, LLC). The thioester bond between UCHL1 and Ub was broken; UCHL1 from the 3KW5 structure was removed, being replaced by UCHL1 from 2ETL, and the glycine vinylmethyl ester moiety was built back into Ub. Preprocessing was completed by generating heteroatom states using Epik42 (Schrödinger, LLC) for the pH range of 7.4 ± 0.2 . Hydrogen bond assignments were optimized using PROPKA (Schrödinger, LLC) at a pH of 7.4. Removal of waters 3.0 Å beyond heteroatoms with fewer than three H-bonds to non-waters was completed. Initial energy minimization was completed using the OPLS3e force field to yield the minimized Ub:UCHL1 (2ETL) structure. The T9F mutation was generated by selecting Thr9 and mutating it to a Phe and repeating the protein preparation process as described above yielding a minimized UbVT9F:UCHL1 (2ETL) structure. Four more structures were generated in a similar manner, excluding the first alignment step. For these structures, the 3KW5 crystal structure was used to generate the Ub:UCHL1 (3KW5) and T9F UbV :UCHL1 (3KW5) minimized structures. In an identical manner, the 1XD3 crystal structure was used to generate the Ub:UCHL1 (1XD3) and UbVT9F:UCHL3 (1XD3) minimized structures. Finally, an apo-UCHL1 structure was prepared from 2ETL following the process described above, excluding the alignment step.

Each minimized structure was further prepared for molecular dynamics simulation using Desmond (D. E. Shaw Research, release 2020-1) in System Builder (Schrödinger, LLC). The solvent model was set to TIP3P, and orthorhombic was set as the box shape. The box size calculation used was according to buffer, and the volume was minimized. The system was neutralized by adding sodium ions (the number of ions was automatically calculated by System Builder), and salt ions (Na^+ and Cl^-) were added at a concentration of 0.15 M. The system was then minimized using the OPLS3e force field.

The molecular dynamics simulation was performed using the Molecular Dynamics application (D. E. Shaw Research) within Maestro (Schrödinger, LLC). The simulation time was set to 100 ns with 10 ps recording intervals. All other settings were left as default. Phe214 was selected, and the radius of gyration (R_g) was calculated at each recording interval. The R_g was plotted versus time in GraphPad Prism version 8.3.1.

Interaction Analysis in BioLuminate.

Molecular dynamics files were used to extract modified .pdb files (waters and ions deleted) at representative time points for UCHL1- and UCHL3-Ub interactions. Preprocessing was completed by generating heteroatom states using Epik (Schrödinger, LLC) for the pH range of 7.4 \pm 2.0. Hydrogen bond assignments were optimized using PROPKA (Schrödinger, LLC) at a pH of 7.4. Removal of waters 3.0 Å beyond heteroatoms with fewer than three H-bonds to non-waters was completed. Energy minimization was completed using the OPLS3e force field to yield the minimized structures for interaction analysis using BioLuminate^{43,44} (Schrödinger, LLC).

CHAPTER 5. FUTURE DIRECTIONS

5.1 Further Optimization of VAEFMK

To the best of our knowledge, a structure-based drug design (SBDD) campaign has not been carried out for ubiquitin C-terminal hydrolase L1 (UCHL1). Compared to ligand-based drug design (LBDD), SBDD represents a powerful way to optimize protein-ligand interactions, using observations from a ligand-bound structure to quickly improve the molecular scaffold.¹⁷⁵ It is our hypothesis that SAR for VAEFMK can be applied to the UCHL1-VAEFMK co-crystal structure to further improve its efficacy, with a focus on reducing the peptidic nature of the inhibitor.

A good example of protease inhibitor development that originated from a covalent peptide is Pralnacasan (VX-740) (Figure 5.1). A covalent peptide inhibitor of caspase-1, acetylated-YVAD-aldehyde (Ac-YVAD-CHO) (Figure 5.1), was converted into a peptidomimetic using knowledge from previous LBDD studies.¹⁴¹ By using a number of medicinal chemistry techniques including molecular rigidification, masking a carboxylic acid to generate a pro-drug, and inclusion of non-natural amino acids, peptidomimetics VRT-043198 and VX-765 were synthesized (Figure 5.1).¹⁷⁶ VX-765 is an orally bioavailable caspase inhibitor with a good pharmacokinetic profile, and VRT-043198 is the bioactive metabolite of XV-765.¹⁷⁶ A more flexible analog was later designed to improve potency and further reduce the peptidic nature of the molecule (VX-740 /Pralnacasan) (Figure 5.1).¹⁷⁷ Pralnacasan progressed into clinical trials for rheumatoid arthritis, though it eventually failed due to liver toxicity issues.¹⁷⁸ Regardless, this story exemplifies the potential of peptides as starting points for the development of potent small-molecule inhibitors, and techniques used to develop Pralnacasan may be applied VAEFMK.

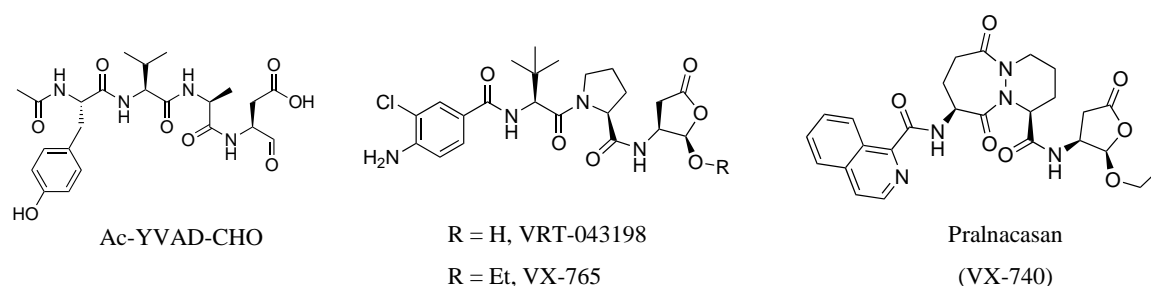


Figure 5.1 Chemical structures of caspase-1 inhibitors. Ac-YVAD-CHO was converted to peptidomimetic VX-765 (active metabolite is VRT-043198). Further optimization yielded Pralnacasan (VX-740).

The structure-activity relationship (SAR) described in chapter 3 as well as the ligand-bound co-crystal structure provide valuable information that may be used to progress VAEFMK (Figure 5.2) into more drug-like space. As described in chapter 3, maintaining the crystallographically observed protein-ligand interactions may confer selectivity towards UCHL1. SAR for VAEFMK suggests that replacing the alanine of VAEFMK with a proline may be tolerated, producing VPEFMK (Figure 5.2B and C), reducing the flexibility of the molecule. Docking of VAEFMK and VPEFMK suggest that this modification would be well tolerated, with the proline overlapping the space normally consumed by the alanine while allowing for the same protein-ligand interactions to occur (Figure 5.2A). This would likely reduce the entropic penalty upon binding to UCHL1 and improve the efficacy of the molecule. However, the slow reactivity of the fluoromethylketone would likely still need to be rectified to further improve the inhibitor.

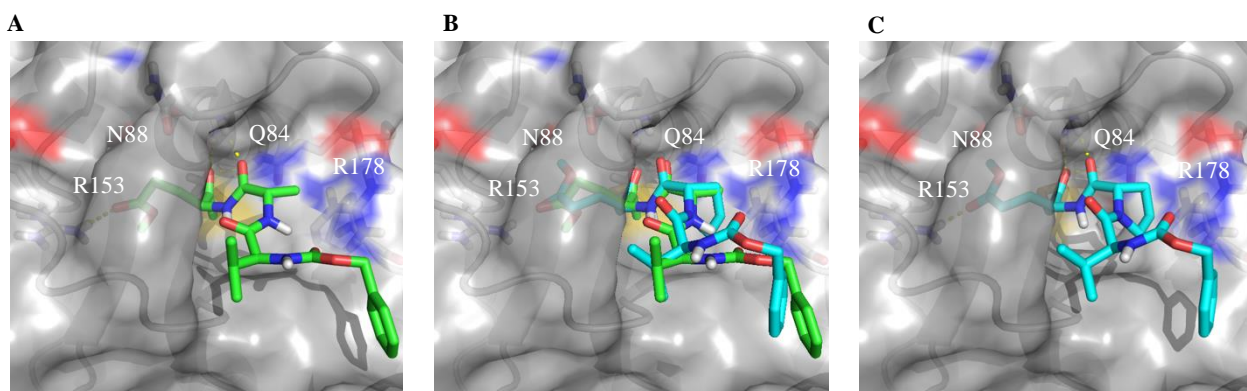


Figure 5.2 Molecular modeling of VAEFMK analogs with UCHL1. **A)** VAEFMK (green sticks) docked with UCHL1 (grey) has hydrogen bond interactions (yellow dashes) with R153, N88, and Q84. **B)** VPEFMK (cyan sticks) maintains a similar pose as VAEFMK (green sticks). **C)** VPEFMK (cyan sticks) has hydrogen bond interactions with R153, N88, and Q84.

As stated in chapter 3, the efficacy of covalent inhibitors can be altered by modifying the reversible interactions between the protein and ligand as well as tuning the reactivity of the covalent “warhead”.¹³² VAEFMK was previously converted into the matched molecular pair analog VAECMK, though it was unable to inhibit UCHL1. This was not due to a loss of chemical reactivity, but instead possible due to occlusion from the active site because of unfavorable sterics. Removing the glutamic acid side chain of VPEFMK and replacing the fluorine for a chlorine results in VPGCMK (Figure 5.3), which is predicted to maintain a similar pose to VPEFMK (Figure 5.3A). The carbonyl oxygen between glycine and proline of VPEFMK is predicted to maintain the hydrogen bonds with the N88 backbone nitrogen and Q84 side chain amide nitrogen (Figure 5.3B), though the interaction with R153 is no longer predicted to occur. While this modification does remove one hydrogen bond to UCHL1 (Figure 5.3B), molecular modeling of UCHL1 with MT-19 (Chapter 2, Figure 2.8) suggests that this interaction between UCHL1 and an inhibitor is not required for binding or selectivity. VPGFMK (not shown) docks in an identical manner to VPGCMK and may be used to determine the contribution of the R153 hydrogen bond interactions. In addition, VAGFMK could also be synthesized and tested to determine the contributions of the R153 hydrogen bond interaction. However, the efficacy of this series of analogs would need to be validated experimentally.

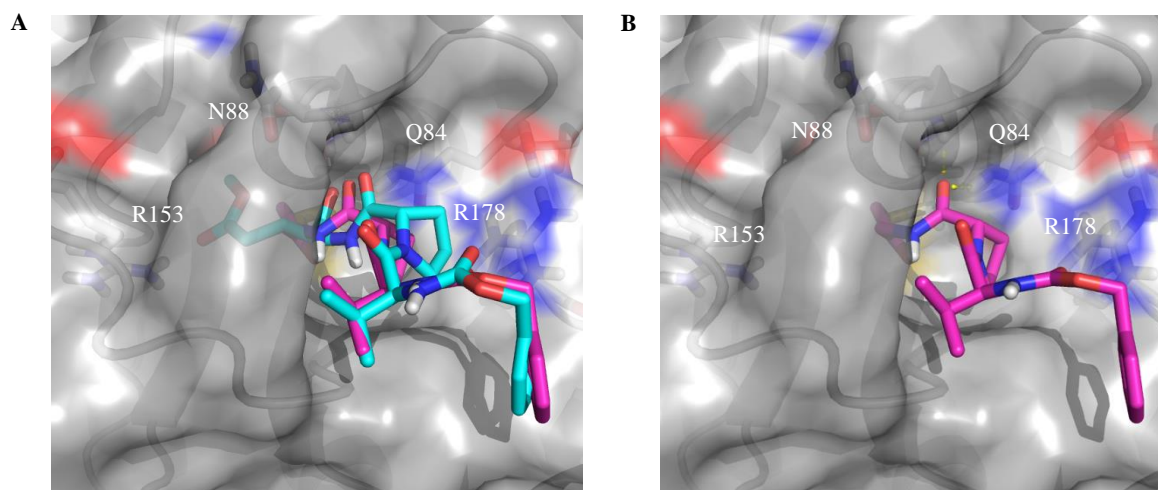


Figure 5.3 Predicted pose and interactions between VPGCMK and UCHL1. **A)** VPEGMK (cyan sticks) and VPGCMK (magenta sticks) are predicted to bind to UCHL1 with similar poses. **B)** VPGCMK is predicted to have hydrogen bonds (yellow dashes) with N88 and Q84.

Further modifications may be explored by computational chemistry. The Cbz-protected valine of VPECMK does not form any enthalpic interactions with UCHL1. Furthermore, the R178

guanidine group provides the opportunity to form additional hydrogen bonds. Removing the Cbz-Val group may provide a vector for targeting R178 in addition to other nearby amino acids.

Finally, with this SAR information in hand, it is possible to explore untested chemical space by docking covalent inhibitor libraries into UCHL1 ensuring that the key interactions are formed. Libraries that contain varying electrophiles may be prepared and docked into the grid defined by VAEFMK in the UCHL1-VAEFMK crystal structure (PDB entry 4DM9). Adding hydrogen bond constraints with ASN88 and GLN84 ensures that the experimentally observed key interactions are prioritized. Post processing the docked poses using the molecular mechanics-generalized Born surface area (MM-GBSA) ΔG bind values to estimate the free energy of binding provides a way to narrow down the molecules of interest.^{179,180} Further analysis using MD simulations may provide additional information regarding the strength of interactions between the molecules and UCHL1.

5.2 Covalent Fragments as UCHL1 Inhibitors

Fragment-based drug discovery (FBDD) continues to mature and has been proven to be an invaluable technique for hit identification against difficult targets.¹⁸¹ Lately, covalent fragments have gained traction to identify hits for proteases.¹⁴³ A recent example of this is the discovery of covalent fragments that target the SARS-CoV-2 main protease (M^{Pro}) that is essential for the viral replication of the cause of COVID-19, SARS-CoV-2.¹⁸² A library of covalent fragments was screened using intact protein mass spectrometry and crystallography yielding over 70 hits that bind to SARS-CoV-2 M^{Pro} , either covalently or non-covalently, in less than 2 months. These hits represent a large chemical space that covers a number of binding locations on the protein and will no doubt be useful in the development of novel inhibitors of SARS-CoV-2.

Our lab was inspired to pursue a similar approach in an effort to identify new chemical matter for the development of UCHL1-selective covalent inhibitors. A diverse 1,700-member covalent fragment library was procured containing four cysteine-reactive electrophiles: activated nitriles, chloroacetamides, acrylamides, and epoxides. These fragments were incubated with UCHL1 for 1 hour before determining the remaining enzymatic activity of UCHL1 using a Ub-Rhodamine (Ub-Rho) enzyme activity assay (Figure 5.4A).¹⁰⁴ Hits were validated in triplicate and counter screened against UCHL3 (Figure 5.4A). The hit with the best balance of potency and selectivity towards UCHL1 was fragment **1** (Figure 5.4B). Engagement of UCHL1 by fragment **1** was also validated in intact protein mass spectrometry experiments (data not shown). Finally, addition of an alkyne to hit

fragment **1** allowed for Copper-catalyzed azide-alkyne cycloaddition (CuAAC) “click” chemistry experiments providing fragment **2** (Figure 5.4B).^{115,118} SW1271 lung cancer cells were treated with fragment **2** for 1 hour at X μ M, followed by washing and pelleting. Cell pellets were lysed, clarified, and normalized prior to CuAAC ligation of a fluorophore. Samples were separated by gel electrophoresis and visualized by fluorescent imaging to determine engagement in cells by fragment **2**. Preliminary data suggests that Fragment **2** selectively engages a protein that matches the molecular weight of UCHL1 (Figure 5.4C), though the identity of this protein must be validated in future experiments. Interestingly, preliminary crystal structures suggest that this fragment may be binding to UCHL1 in a manner that fulfills the key pharmacophore features of VAEFMK (data not shown). Although much work remains to explore the validity of this fragment as a UCHL1 inhibitor, this data validates covalent fragment screening as an approach to identify novel chemical matter for the development of UCHL1-selective inhibitors.

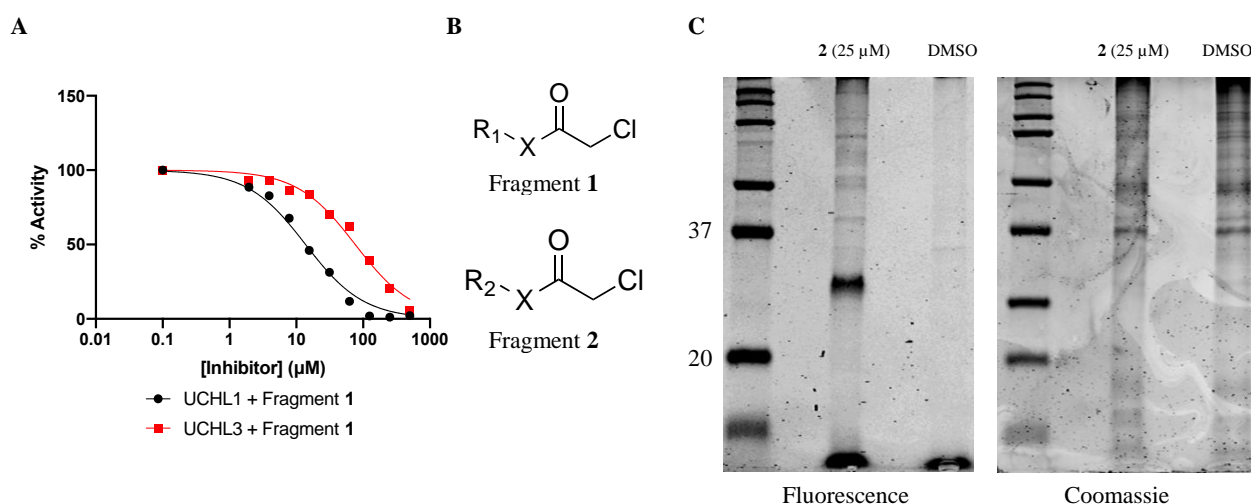


Figure 5.4 Biochemical and cellular engagement of UCHL1 by fragment **1** and **2**. **A**) Dose-response curves for Fragment **1** versus UCHL1 (IC_{50} = 13.75 μ M, 95% CI = 12.35 μ M to 15.30 μ M) and UCHL3 (IC_{50} = 76.14 μ M, 95% CI = 67.23 μ M to 86.23 μ M). **B**) General chemical structures for hit fragment **1** and alkyne containing analog **2**. **C**) Fluorescent labeling of a protein at 25 kDa by fragment **2** in intact SW1271 cells. Coomassie staining shows equal protein loading. Data collected by Ryan Imhoff.

5.3 A Novel Caged-Luciferin Ubiquitin Variant for Tracking UCH Activity in Cells

Tracking the activity of deubiquinating (DUB) enzymes in intact cells, and *in vivo*, remains a challenge despite the recent progress made in the DUB activity-based probe (ABP) field.^{81,82,116,183} Ubiquitin (Ub) activity-based probes (ABPs) are currently used extensively to determine DUB activity.^{170,184} However, these Ub-ABPs are generally non-selective, non-cell permeable, and require immunoblotting to quantify DUB activity. Thus, a Ub-ABP that could be used to monitor DUB activity in cells in real time would prove invaluable to the DUB research field. We hypothesize that combining the UCH-selective Ub-ABPs with cell-permeating strategies^{183,185} and a split-luciferin chemiluminescence approach^{186,187} will provide a UCH selective Ub-ABP that may be used in cells and *in vivo*.

5.4 Conclusion

A growing body of literature points to UCHL1 as a potential therapeutic or diagnostic target for a number of disease states, yet little has been done to advance our understanding of both UCHL1 inhibitor design and the pool of available small molecule probes. This dissertation highlights the mechanisms of inhibition for existing UCHL1 inhibitors, as well as the design and characterization of novel small molecule and macromolecular UCHL1 inhibitors.

In chapter 2, we focused on the characterization and utility of a novel cyanopyrrolidine scaffold of UCHL1 inhibitors introduced above. This inhibitor was characterized using a combination of biochemical assays and experiments and demonstrated, for the first time, the utility of covalent inhibitors as ABPs for UCHL1. However, the utility of this probe in determining the role of UCHL1 in various disease states was limited because of off-target engagement and non-specific toxicity.

Chapter 3 characterized the selectivity and utility of a previously published covalent inhibitor of UCHL1, VAEFMK, as well SAR studies. Although few improvements were made to the efficacy of the parent compound, analysis of the SAR provides the rationale for future optimization away from peptides and towards a more drug-like space. Furthermore, an in-depth biochemical and cellular characterization of the fluoromethylketone analogs generated during the SAR studies shows the impressive selectivity of this molecular scaffold towards UCHL1. While the potency of this inhibitor limits its utility as a potential therapeutic agent, its selectivity makes it an invaluable probe

for determining the role of UCHL1 in various disease states, with pharmacological inhibition directly matching phenotypic results from the genetic depletion of intracellular UCHL1.

Chapter 4 explored the dynamics and mechanism of action for a new set of macromolecular Ub-based UCHL1 inhibitors, supported by biochemical and molecular dynamics (MD) simulations. Here, MD simulations suggested that loop dynamics of Ub played a role in conveying selectivity of the Ub variant (UbV) T9F towards UCHL1 in biochemical assays. In addition, these MD simulations provide evidence that the T9F mutation inhibits UCHL1 by reducing the amount of time UCHL1 is able to spend in its active conformation, even when bound to Ub^{T9F}.

Finally, chapter 5 introduced future directions for the identification and development of novel tool compounds to monitoring UCH activity *in vivo*. Using SAR information from chapter 3 and taking inspiration from the development of potent caspase inhibitors, a route was laid out to progress VAEFMK into more drug-like space. In parallel, this SAR information may be used in a virtual screening approach to identify new chemical matter that fulfills the pharmacophore provided by VAEFMK. Novel chemical scaffolds that inhibit UCHL1 have also been identified by our lab by screening covalent fragment libraries. Although this study is still in its early stages, it represents a promising starting point for the development of a more potent UCHL1-selective small molecule inhibitor. Finally, a route to develop a novel chemiluminescent UCH-selective Ub-ABP for *in vivo* use is described, an advancement that is much needed in the DUB research field.

Taken together, these chapters described in detail the design of new tools to elucidate the role of UCHL1 in disease pathology. The results will be relevant for optimization and design of future UCHL1 covalent inhibitors and improve their potential as selective probes that should replace LDN-57444 and be used to elucidate UCHL1's role in disease state pathogenesis. Finally, these studies confirmed the validity of covalent inhibition as the leading approach to target UCHL1.

REFERENCES

1. Glickman, M. H. & Ciechanover, A. The ubiquitin-proteasome proteolytic pathway: Destruction for the sake of construction. *Physiol. Rev.* **82**, 373–428 (2002).
2. Schulman, B. A. & Wade Harper, J. Ubiquitin-like protein activation by E1 enzymes: The apex for downstream signalling pathways. *Nat. Rev. Mol. Cell Biol.* **10**, 319–331 (2009).
3. Ye, Y. & Rape, M. Building ubiquitin chains: E2 enzymes at work. *Nat. Rev. Mol. Cell Biol.* **10**, 755–764 (2009).
4. Deshaies, R. J. & Joazeiro, C. A. P. RING Domain E3 Ubiquitin Ligases. *Annu. Rev. Biochem.* **78**, 399–434 (2009).
5. Xu, P. *et al.* Quantitative Proteomics Reveals the Function of Unconventional Ubiquitin Chains in Proteasomal Degradation. *Cell* **137**, 133–145 (2009).
6. Peng, J. *et al.* A proteomics approach to understanding protein ubiquitination. *Nat. Biotechnol.* **21**, 921–926 (2003).
7. Komander, D. & Rape, M. The ubiquitin code. *Annu. Rev. Biochem.* **81**, 203–229 (2012).
8. Komander, D., Clague, M. J. & Urbé, S. Breaking the chains: Structure and function of the deubiquitinases. *Nat. Rev. Mol. Cell Biol.* **10**, 550–563 (2009).
9. Harrigan, J. A., Jacq, X., Martin, N. M. & Jackson, S. P. Deubiquitylating enzymes and drug discovery : emerging opportunities. *Nat. Publ. Gr.* **17**, 57–77 (2017).
10. Hewings, D. S. *et al.* Reactive-site-centric chemoproteomics identifies a distinct class of deubiquitinase enzymes. *Nat. Commun.* **9**, 1162 (2018).
11. Abdul Rehman, S. A. *et al.* MINDY-1 Is a Member of an Evolutionarily Conserved and Structurally Distinct New Family of Deubiquitinating Enzymes. *Mol. Cell* **63**, 146–155 (2016).
12. Komander, D. The emerging complexity of protein ubiquitination. *Biochem. Soc. Trans.* **37**, 937–53 (2009).
13. Hussain, S., Zhang, Y. & Galaray, P. J. DUBs and cancer: The role of deubiquitinating enzymes as oncogenes, non-oncogenes and tumor suppressors. *Cell Cycle* **8**, 1688–1697 (2009).
14. Lu, D. *et al.* Mutations of deubiquitinase OTUD1 are associated with autoimmune disorders. *J. Autoimmun.* **94**, 156–165 (2018).

15. Sun, S. C., Chang, J. H. & Jin, J. Regulation of nuclear factor- κ B in autoimmunity. *Trends Immunol.* **34**, 282–289 (2013).
16. Shembade, N. & Harhaj, E. W. Regulation of NF- κ B signaling by the A20 deubiquitinase. *Cell. Mol. Immunol.* **9**, 123–130 (2012).
17. Ardley, H. C., Hung, C. C. & Robinson, P. A. The aggravating role of the ubiquitin-proteasome system in neurodegeneration. *FEBS Lett.* **579**, 571–576 (2005).
18. Todi, S. V. & Paulson, H. L. Balancing act: Deubiquitinating enzymes in the nervous system. *Trends Neurosci.* **34**, 370–382 (2011).
19. Jara, J. H., Frank, D. D. & Özdinler, P. H. Could Dysregulation of UPS be a Common Underlying Mechanism for Cancer and Neurodegeneration? Lessons from UCHL1. *Cell Biochem. Biophys.* **67**, 45–53 (2013).
20. Wilkinson, K. D. *et al.* The neuron-specific protein PGP 9.5 is a ubiquitin carboxyl-terminal hydrolase. *Science* (80-.). **246**, 670–673 (1989).
21. Hibi, K. *et al.* PGP9.5 As a candidate tumor marker for non-small-cell lung cancer. *Am. J. Pathol.* **155**, 711–715 (1999).
22. Tezel, E., Hibi, K., Nagasaka, T. & Nakao, A. PGP9.5 as a prognostic factor in pancreatic cancer. *Clin. Cancer Res.* **6**, 4764–4767 (2000).
23. Kim, H. J. *et al.* Ubiquitin C-terminal hydrolase-L1 increases cancer cell invasion by modulating hydrogen peroxide generated via NADPH oxidase 4. *Oncotarget* **6**, 16287–16303 (2015).
24. Goto, Y. *et al.* UCHL1 provides diagnostic and antimetastatic strategies due to its deubiquitinating effect on HIF-1 α . *Nat. Commun.* **6**, 6153 (2015).
25. Miyoshi, Y. *et al.* High expression of ubiquitin caboxy-terminal hydrolase-L1 and -L3 mRNA predicts early recurrence in patients with invasive breast cancer. *Cancer Sci.* **97**, 523–529 (2006).
26. Seliger, B. *et al.* Ubiquitin COOH-terminal hydrolase 1: A biomarker of renal cell carcinoma associated with enhanced tumor cell proliferation and migration. *Clin. Cancer Res.* **13**, 27–37 (2007).
27. Ma, Y. *et al.* Proteomic profiling of proteins associated with lymph node metastasis in colorectal cancer. *J. Cell. Biochem.* **110**, 1512–1519 (2010).

28. Bedekovics, T., Hussain, S., Feldman, A. L. & Galardy, P. J. UCH-L1 is induced in germinal center B-cells and identifies patients with aggressive germinal center diffuse large B-cell lymphoma. *Blood* **127**, 1564–1575 (2015).
29. Liu, Y. *et al.* Discovery of Inhibitors that Elucidate the Role of UCH-L1 Activity in the H1299 Lung Cancer Cell Line. *Chem. Biol.* **10**, 837–846 (2003).
30. Mermerian, A. H., Case, A., Stein, R. L. & Cuny, G. D. Structure-activity relationship, kinetic mechanism, and selectivity for a new class of ubiquitin C-terminal hydrolase-L1 (UCH-L1) inhibitors. *Bioorganic Med. Chem. Lett.* **17**, 3729–3732 (2007).
31. Jones, A. *et al.* Patent Number WO 2016/046530 A1. (2016).
32. Kemp, M., Stockley, M. & Jones, A. Preparation of cyanopyrrolidines as DUB inhibitors for the treatment of cancer. (2017).
33. Davies, C. W. *et al.* The co-crystal structure of ubiquitin carboxy-terminal hydrolase L1 (UCHL1) with a tripeptide fluoromethyl ketone (Z-VAE(OMe)-FMK). *Bioorganic Med. Chem. Lett.* **22**, 3900–3904 (2012).
34. Hussain, S. *et al.* The de-ubiquitinase UCH-L1 is an oncogene that drives the development of lymphoma in vivo by deregulating PHLPP1 and Akt signaling. *Leukemia* **24**, 1641–1655 (2010).
35. Ubiquitination, A. D. *et al.* Ubiquitin Hydrolase UCH-L1 Destabilizes mTOR Complex 1 by Antagonizing DDB1-CUL4-Mediated Ubiquitination of Raptor. *Mol. Cell. Biol.* **33**, 1188–1197 (2013).
36. Otsuki, T. *et al.* Expression of protein gene product 9.5 (PGP9.5)/ubiquitin-C-terminal hydrolase 1 (UCHL-1) in human myeloma cells. *Br. J. Haematol.* **127**, 292–298 (2004).
37. Hibi, K. *et al.* PGP9.5 as a candidate tumor marker for non-small-cell lung cancer. *Am. J. Pathol.* **155**, 711–5 (1999).
38. Kim, H.-J. J. *et al.* Ubiquitin C-terminal hydrolase-L1 is a key regulator of tumor cell invasion and metastasis. *Oncogene* **28**, 117–127 (2009).
39. Chen, G. *et al.* Proteomic analysis of lung adenocarcinoma: Identification of a highly expressed set of proteins in tumors. *Clin. Cancer Res.* **8**, 2298–2305 (2002).
40. Carolan, B. J. *et al.* Up-regulation of expression of the ubiquitin carboxyl-terminal hydrolase L1 gene in human airway epithelium of cigarette smokers. *Cancer Res.* **66**, 10729–10740 (2006).

41. Yoo, H. J. *et al.* Genetic and expression alterations in association with the sarcomatous change of cholangiocarcinoma cells. *Exp. Mol. Med.* **41**, 102–115 (2009).
42. Sanchez-Diaz, P. C. *et al.* Ubiquitin carboxyl-Terminal esterase L1 (UCHL1) is associated with stem-like cancer cell functions in pediatric high-grade glioma. *PLoS One* **12**, 1–19 (2017).
43. Hurst-Kennedy, J., Chin, L. S. & Li, L. Ubiquitin C-terminal hydrolase L1 in tumorigenesis. *Biochem. Res. Int.* **2012**, (2012).
44. Bedekovics, T., Hussain, S. & Galardy, P. J. Walking the tightrope: UCH-L1 as an mTOR inhibitor and B-cell oncogene. *Oncotarget* **10**, 5124–5125 (2019).
45. Hussain, S. *et al.* The de-ubiquitinase UCH-L1 is an oncogene that drives the development of lymphoma in vivo by deregulating PHLPP1 and Akt signaling. *Leukemia* **24**, 1641–1655 (2010).
46. Weichhart, T. MTOR as Regulator of Lifespan, Aging, and Cellular Senescence: A Mini-Review. *Gerontology* **64**, 127–134 (2018).
47. Hussain, S. *et al.* UCH-L1 bypasses mTOR to promote protein biosynthesis and is required for MYC driven lymphomagenesis in mice. *Blood* **132**, blood-2018-05-848515 (2018).
48. Shimada, Y. *et al.* Ubiquitin C-terminal hydrolase-L1 has prognostic relevance and is a therapeutic target for high-grade neuroendocrine lung cancers. *Cancer Sci.* **111**, 610–620 (2020).
49. Semenza, G. L. Targeting HIF-1 for cancer therapy. *Nat. Rev. Cancer* **3**, 721–732 (2003).
50. Li, X. *et al.* Ubiquitin carboxyl-terminal hydrolase L1 promotes hypoxia-inducible factor 1-dependent tumor cell malignancy in spheroid models. *Cancer Sci.* **111**, 239–252 (2020).
51. Lien, H. C. *et al.* Differential expression of ubiquitin carboxy-terminal hydrolase L1 in breast carcinoma and its biological significance. *Hum. Pathol.* **44**, 1838–1848 (2013).
52. Liu, S. *et al.* Deubiquitinase activity profiling identifies UCHL1 as a candidate oncoprotein that promotes TGF β -induced breast cancer metastasis. *Clin. Cancer Res.* **26**, 1460–1473 (2020).
53. Choi, J. *et al.* Oxidative Modifications and Down-regulation of Ubiquitin Carboxyl-terminal Hydrolase L1 Associated with Idiopathic Parkinson's and Alzheimer's Diseases. *J. Biol. Chem.* **279**, 13256–13264 (2004).

54. Healy, D. G., Abou-Sleiman, P. M. & Wood, N. W. Genetic causes of Parkinson's disease: UCHL-1. *Cell Tissue Res.* **318**, 189–194 (2004).
55. Facheris, M. *et al.* UCHL1 is associated with Parkinson's disease: A case-unaffected sibling and case-unrelated control study. *Neurosci. Lett.* **381**, 131–134 (2005).
56. Setsuie, R. *et al.* Dopaminergic neuronal loss in transgenic mice expressing the Parkinson's disease-associated UCH-L1 I93M mutant. *Neurochem. Int.* **50**, 119–129 (2007).
57. Bilguvar, K. *et al.* Recessive loss of function of the neuronal ubiquitin hydrolase UCHL1 leads to early-onset progressive neurodegeneration. *Proc. Natl. Acad. Sci.* **110**, 3489–3494 (2013).
58. Rydning, S. L. *et al.* Novel UCHL1 mutations reveal new insights into ubiquitin processing. *Hum. Mol. Genet.* **26**, 1031–1040 (2017).
59. Nishikawa, K. *et al.* Alterations of structure and hydrolase activity of parkinsonism-associated human ubiquitin carboxyl-terminal hydrolase L1 variants. *Biochem. Biophys. Res. Commun.* **304**, 176–183 (2003).
60. Kabuta, T. *et al.* Aberrant molecular properties shared by familial Parkinson's disease-associated mutant UCH-L1 and carbonyl-modified UCH-L1. *Hum. Mol. Genet.* **17**, 1482–1496 (2008).
61. Pukab, K. & Richter-Landsberg, C. Inhibition of UCH-L1 in oligodendroglial cells results in microtubule stabilization and prevents α -synuclein aggregate formation by activating the autophagic pathway: implications for multiple system atrophy. *Front. Cell. Neurosci.* **9**, 163 (2015).
62. Costes, S., Gurlo, T., Rivera, J. F. & Butler, P. C. UCHL1 deficiency exacerbates human islet amyloid polypeptide toxicity in β -cells: Evidence of interplay between the ubiquitin/proteasome system and autophagy. *Autophagy* **10**, 1004–1014 (2014).
63. Bugliani, M. *et al.* Microarray analysis of isolated human islet transcriptome in type 2 diabetes and the role of the ubiquitin-proteasome system in pancreatic beta cell dysfunction. *Mol. Cell. Endocrinol.* **367**, 1–10 (2013).
64. Costes, S. *et al.* Beta-Cell Dysfunctional ERAD/Ubiquitin/Proteasome System in Type 2 Diabetes Mediated by Islet Amyloid Polypeptide-Induced UCH-L1 Deficiency. *Diabetes* **60**, 227–238 (2011).

65. Hausmann, R., Kaiser, A., Lang, C., Bohnert, M. & Betz, P. A quantitative immunohistochemical study on the time-dependent course of acute inflammatory cellular response to human brain injury. *Int. J. Legal Med.* **112**, 227–232 (1999).
66. Mondello, S. *et al.* CLINICAL UTILITY OF SERUM LEVELS OF UBIQUITIN C-TERMINAL HYDROLASE AS A BIOMARKER FOR SEVERE TRAUMATIC BRAIN INJURY. *Neurosurgery* **70**, 846 (2012).
67. Bi, H. L. *et al.* Inhibition of UCHL1 by LDN-57444 attenuates Ang II–Induced atrial fibrillation in mice. *Hypertens. Res.* **43**, 168–177 (2020).
68. Wilson, C. L. *et al.* Ubiquitin C-terminal hydrolase 1: A novel functional marker for liver myofibroblasts and a therapeutic target in chronic liver disease. *J. Hepatol.* **63**, 1421–1428 (2015).
69. McCarthy, J. M. *et al.* Idiopathic sclerosing inflammation of the orbit: immunohistologic analysis and comparison with retroperitoneal fibrosis. *Mod. Pathol.* **6**, 581–587 (1993).
70. Lewis, S. B. *et al.* Identification and preliminary characterization of ubiquitin C terminal hydrolase 1 (UCHL1) as a biomarker of neuronal loss in aneurysmal subarachnoid hemorrhage. *J. Neurosci. Res.* **88**, 1475–1484 (2010).
71. Rossi, M. A. Fibrosis and inflammatory cells in human chronic chagasic myocarditis: Scanning electron microscopy and immunohistochemical observations. *Int. J. Cardiol.* **66**, 183–194 (1998).
72. Panyain, N. *et al.* Discovery of a potent and selective covalent inhibitor and activity-based probe for the deubiquitylating enzyme UCHL1, with anti-fibrotic activity. *J. Am. Chem. Soc.* **142**, 12020–12026 (2020).
73. Chittaranjan Das*†‡, Quyen Q. Hoang*†‡, Cheryl A. Kreinbring*, Sarah J. Luchansky†, Robin K. Meray†, Soumya S. Ray†, Peter T. Lansbury†, Dagmar Ringe*†, and G. A. P. Structural basis for conformational plasticity of the Parkinson’s disease-associated ubiquitin hydrolase UCH-L1. **103**, (2006).
74. Larsen, C. N., Krantz, B. A. & Wilkinson, K. D. Substrate specificity of deubiquitinating enzymes: Ubiquitin C-terminal hydrolases. *Biochemistry* **37**, 3358–3368 (1998).
75. Boudreaux, D. A., Maiti, T. K., Davies, C. W. & Das, C. Ubiquitin vinyl methyl ester binding orients the misaligned active site of the ubiquitin hydrolase UCHL1 into productive conformation. *Proc. Natl. Acad. Sci. U. S. A.* **107**, 9117–9122 (2010).

76. Johnston, S. C., Larsen, C. N., Cook, W. J., Wilkinson, K. D. & Hill, C. P. Crystal structure of a deubiquitinating enzyme (human UCH-L3) at 1.8 Å resolution. *EMBO J.* **16**, 3787–3796 (1997).
77. Bi, H. L. *et al.* The deubiquitinase UCHL1 regulates cardiac hypertrophy by stabilizing epidermal growth factor receptor. *Sci. Adv.* **6**, (2020).
78. Kobayashi, E. *et al.* Inhibition of UCH-L1 deubiquitinating activity with two forms of LDN-57444 has anti-invasive effects in metastatic carcinoma cells. *Int. J. Mol. Sci.* **20**, (2019).
79. Turnbull, A. P. *et al.* Molecular basis of USP7 inhibition by selective small-molecule inhibitors. *Nature* **550**, 481–486 (2017).
80. Kategaya, L. *et al.* USP7 small-molecule inhibitors interfere with ubiquitin binding. *Nature* **550**, (Nature Publishing Group, 2017).
81. Hewitt, C. S., Krabill, A. D., Das, C. & Flaherty, D. P. Development of Ubiquitin Variants with Selectivity for Ubiquitin C-Terminal Hydrolase Deubiquitinases. *Biochemistry* **59**, 3447–3462 (2020).
82. Krabill, A. D. A. D. *et al.* Ubiquitin C-Terminal Hydrolase L1: Biochemical and Cellular Characterization of a Covalent Cyanopyrrolidine-Based Inhibitor. *ChemBioChem* **21**, 712–722 (2020).
83. Geurink, P. P., Kooij, R., Sapmaz, A., Liu, S. & Xin, B. A Small-Molecule Activity-Based Probe for Monitoring Ubiquitin C-terminal Hydrolase L1 (UCHL1) Activity in Live Cells and Zebrafish Embryos. *bioRxiv* (2019).
84. Harrigan, J. A., Jacq, X., Martin, N. M. & Jackson, S. P. Deubiquitylating enzymes and drug discovery: Emerging opportunities. *Nat. Rev. Drug Discov.* **17**, 57–77 (2018).
85. Kwasna, D. *et al.* Discovery and Characterization of ZUFSP/ZUP1, a Distinct Deubiquitinase Class Important for Genome Stability. *Mol. Cell* **70**, 150-164.e6 (2018).
86. Jang, M. J., Baek, S. H. & Kim, J. H. UCH-L1 promotes cancer metastasis in prostate cancer cells through EMT induction. *Cancer Lett.* **302**, 128–135 (2011).
87. Setsuie, R. & Wada, K. The functions of UCH-L1 and its relation to neurodegenerative diseases. *Neurochem. Int.* **51**, 105–111 (2007).
88. Graham, S. H., Ph, M. D. D. & Liu, H. Life and death in the trash heap: The ubiquitin proteasome pathway and UCHL1 in brain aging, neurodegenerative disease and cerebral Ischemia. *Ageing Res. Rev.* **34**, 30–38 (2017).

89. Lowe, J., McDermott, H., Landon, M., Mayer, R. J. & Wilkinson, K. D. Ubiquitin carboxyl-terminal hydrolase (PGP 9.5) is selectively present in ubiquitinated inclusion bodies characteristic of human neurodegenerative diseases. *J. Pathol.* **161**, 153–160 (1990).
90. Atkin, G. & Paulson, H. Ubiquitin pathways in neurodegenerative disease. *Front. Mol. Neurosci.* **7**, 63 (2014).
91. Lim, K.-H. & Baek, K.-H. Deubiquitinating Enzymes as Therapeutic Targets in Cancer. *Curr. Pharm. Des.* **19**, 4039–4052 (2013).
92. Xue, S. & Jia, J. Genetic association between Ubiquitin Carboxy-terminal Hydrolase-L1 gene S18Y polymorphism and sporadic Alzheimer's disease in a Chinese Han population. *Brain Res.* **1087**, 28–32 (2006).
93. Öhrfelt, A. *et al.* Increased Cerebrospinal Fluid Levels of Ubiquitin Carboxyl-Terminal Hydrolase L1 in Patients with Alzheimer's Disease. *Dement. Geriatr. Cogn. Dis. Extra* **6**, 283–294 (2016).
94. Gong, B., Radulovic, M., Figueiredo-Pereira, M. E. & Cardozo, C. The Ubiquitin-Proteasome System: Potential Therapeutic Targets for Alzheimer's Disease and Spinal Cord Injury. *Front. Mol. Neurosci.* **9**, 4 (2016).
95. Kabuta, T. *et al.* Aberrant interaction between Parkinson disease-associated mutant UCH-L1 and the lysosomal receptor for chaperone-mediated autophagy. *J. Biol. Chem.* **283**, 23731–23738 (2008).
96. Andersson, F. I. *et al.* The effect of Parkinson's-disease-associated mutations on the deubiquitinating enzyme UCH-L1. *J. Mol. Biol.* **407**, 261–272 (2011).
97. Hussain, S. *et al.* UCH-L1 bypasses mTOR to promote protein biosynthesis and is required for MYC-driven lymphomagenesis in mice. *Blood* **132**, 2564–2574 (2018).
98. Hussain, S. *et al.* The de-ubiquitinase UCH-L1 is an oncogene that drives the development of lymphoma in vivo by deregulating PHLPP1 and Akt signaling. *Leukemia* **24**, 1641–1655 (2010).
99. Bedekovics, T., Hussain, S., Feldman, A. L. & Galaray, P. J. UCH-L1 is induced in germinal center B cells and identifies patients with aggressive germinal center diffuse large B-cell lymphoma. *Blood* **127**, 1564–1574 (2016).

100. Hussain, S., Bedekovics, T., Chesi, M., Bergsagel, L. P. & Galaray, P. J. UCHL1 is a biomarker of aggressive multiple myeloma required for disease progression. *Oncotarget* **5**, (2015).
101. KEMP, M. I., STOCKLEY, M. L. & JONES, A. Patent Number WO 2017/009650 A1. (2017).
102. Deaton, D. N. *et al.* Novel and potent cyclic cyanamide-based cathepsin K inhibitors. *Bioorganic Med. Chem. Lett.* **15**, 1815–1819 (2005).
103. Yadav, M., Shinde, A., Chouhan, B., Giridhar, R. & Menard, R. Peptidomimetic 2-cyanopyrrolidines as potent selective cathepsin L inhibitors. *J. Enzyme Inhib. Med. Chem.* **23**, 190–197 (2008).
104. Hassiepen, U. *et al.* A sensitive fluorescence intensity assay for deubiquitinating proteases using ubiquitin-rhodamine110-glycine as substrate. *Anal. Biochem.* **371**, 201–207 (2007).
105. De Cesco, S., Kurian, J., Dufresne, C., Mittermaier, A. K. & Moitessier, N. Covalent inhibitors design and discovery. *Eur. J. Med. Chem.* **138**, 96–114 (2017).
106. Mons, E. *et al.* The Alkyne Moiety as a Latent Electrophile in Irreversible Covalent Small Molecule Inhibitors of Cathepsin K. *J. Am. Chem. Soc.* **141**, 3507–3514 (2019).
107. Strelow, J. *et al.* Mechanism of Action Assays for Enzymes *. 1–27 (2012).
108. Strelow, J. M. A perspective on the kinetics of covalent and irreversible inhibition. *SLAS Discov.* **22**, 3–20 (2017).
109. Ekkebus, R., Flierman, D., Geurink, P. P. & Ovaas, H. Catching a DUB in the act: Novel ubiquitin-based active site directed probes. *Curr. Opin. Chem. Biol.* **23**, 63–70 (2014).
110. Breeze, A. L. Isotope-filtered NMR methods for the study of biomolecular structure and interactions. *Prog. Nucl. Magn. Reson. Spectrosc.* **36**, 323–372 (2000).
111. Zwahlen, C. *et al.* Methods for measurement of intermolecular NOEs by multinuclear NMR spectroscopy: Application to a bacteriophage λ N-peptide/boxB RNA complex. *J. Am. Chem. Soc.* **119**, 6711–6721 (1997).
112. Ogura, K., Terasawa, H. & Inagaki, F. An improved double-tuned and isotope-filtered pulse scheme based on a pulsed field gradient and a wide-band inversion shaped pulse. *J. Biomol. NMR* **8**, 492–498 (1996).
113. Iwahara, J., Wojciak, J. M. & Clubb, R. T. Improved NMR spectra of a protein-DNA complex through rational mutagenesis and the application of a sensitivity optimized isotope-filtered NOESY experiment. *J. Biomol. NMR* **19**, 231–241 (2001).

114. Cowley, G. S. *et al.* Parallel genome-scale loss of function screens in 216 cancer cell lines for the identification of context-specific genetic dependencies. *Sci. Data* **1**, 1–12 (2014).
115. Kolb, H. C., Finn, M. G. & Sharpless, K. B. Click Chemistry: Diverse Chemical Function from a Few Good Reactions. *Angew. Chem. Int. Ed. Engl.* **40**, 2004–2021 (2001).
116. Ward, J. A. *et al.* Quantitative Chemical Proteomic Profiling of Ubiquitin Specific Proteases in Intact Cancer Cells. *ACS Chem. Biol.* **11**, 4268–3272 (2016).
117. Arrowsmith, C. H. *et al.* The promise and peril of chemical probes. *Nat. Chem. Biol.* **11**, 536–541 (2015).
118. Kolb, H. C. & Sharpless, K. B. The growing impact of click chemistry on drug discovery. *Drug Discov. Today* **8**, (2003).
119. Feng, C., Roy, A. & Post, C. B. Entropic allostery dominates the phosphorylation-dependent regulation of Syk tyrosine kinase release from immunoreceptor tyrosine-based activation motifs. *Protein Sci.* **27**, 1780–1796 (2018).
120. Acconcia, F., Sigismund, S. & Polo, S. Ubiquitin in trafficking: The network at work. *Exp. Cell Res.* **315**, 1610–1618 (2009).
121. Jackson, S. P. & Durocher, D. Regulation of DNA Damage Responses by Ubiquitin and SUMO. *Mol. Cell* **49**, 795–807 (2013).
122. Myung, J., Kim, K. B. & Crews, C. M. The ubiquitin-proteasome pathway and proteasome inhibitors. *Med. Res. Rev.* **21**, 245–273 (2001).
123. Rahighi, S. *et al.* Specific Recognition of Linear Ubiquitin Chains by NEMO Is Important for NF- κ B Activation. *Cell* **136**, 1098–1109 (2009).
124. Haakonsen, D. L. & Rape, M. Branching Out: Improved Signaling by Heterotypic Ubiquitin Chains. *Trends Cell Biol.* **29**, 704–716 (2019).
125. Kemp, M. *Recent Advances in the Discovery of Deubiquitinating Enzyme Inhibitors. Progress in Medicinal Chemistry* **55**, (Elsevier B.V., 2016).
126. Schauer, N. J., Magin, R. S., Liu, X., Doherty, L. M. & Buhrlage, S. J. Advances in Discovering Deubiquitinating Enzyme (DUB) Inhibitors. *J. Med. Chem.* **63**, acs.jmedchem.9b01138 (2019).
127. Fang, Y., Fu, D. & Shen, X. Z. The potential role of ubiquitin c-terminal hydrolases in oncogenesis. *Biochim. Biophys. Acta - Rev. Cancer* **1806**, 1–6 (2010).

128. Day, I. N. M. & Thompson, R. J. UCHL1 (PGP 9.5): Neuronal biomarker and ubiquitin system protein. *Prog. Neurobiol.* **90**, 327–362 (2010).
129. Bedekovics, T., Hussain, S. & Galardy, P. J. Catalytically Active UCH-L1 Is Required for MYC Driven B-Cell Lymphomagenesis. *Blood* **130**, 644 LP – 644 (2017).
130. Gu, Y. yu *et al.* The de-ubiquitinase UCHL1 promotes gastric cancer metastasis via the Akt and Erk1/2 pathways. *Tumor Biol.* **36**, 8379–8387 (2015).
131. Panyain, N. *et al.* *Discovery of a Potent and Selective Covalent Inhibitor and Activity-Based Probe for the Deubiquitylating Enzyme UCHL1 , with Anti-Fibrotic Activity.* (2019). doi:10.26434/chemrxiv.10058429.v1
132. Powers, J. C., Asgian, J. L. & James, K. E. Irreversible Inhibitors of Serine , Cysteine , and Threonine Proteases. (2002).
133. Curran, M. P. & McKeage, K. Bortezomib: A review of its use in patients with multiple myeloma. *Drugs* **69**, 859–888 (2009).
134. Chen, D., Frezza, M., Schmitt, S., Kanwar, J. & Dou, Q. P. Bortezomib as the First Proteasome Inhibitor Anticancer Drug: Current Status and Future Perspectives. *Curr. Cander Drug Targets* **11**, 239–253 (2011).
135. Palmer, J. Process for Forming a Fluoromethyl Ketone. *U.S. Pat. No. 5,210,272.* (1993).
136. Witte, M. D. *et al.* Bodipy-VAD-Fmk, a useful tool to study yeast peptide N-glycanase activity. *Org. Biomol. Chem.* **5**, 3690–3697 (2007).
137. Morris, T. S. *et al.* In Vitro and Ex Vivo Inhibition of Hepatitis A Virus 3C Proteinase by a Peptidyl Monofluoromethyl Ketone t. **5**, 797–807 (1997).
138. Misaghi, S., Pacold, M. E., Blom, D., Ploegh, H. L. & Korbel, G. A. Using a small molecule inhibitor of peptide: N-glycanaseto probe its role in glycoprotein turnover. *Chem. Biol.* **11**, 1677–1687 (2004).
139. Seki, H., Kawaguchi, T. & Higuchi, T. Specificity of esterases and structure of prodrug esters: Reactivity of various acylated acetaminophen compounds and acetylaminobenzoated compounds. *J. Pharm. Sci.* **77**, 855–860 (1988).
140. Adessi C & Soto C. Converting a Peptide into a Drug: Strategies to Improve Stability and Bioavailability. *Curr. Med. Chem.* **9**, 16 (2002).

141. Dolle, R. E. *et al.* Aspartyl α -((1-Phenyl-3-(trifluoromethyl)-pyrazol-5-yl)oxy)methyl Ketones as Interleukin-1 β Converting Enzyme Inhibitors. Significance of the P1 and P3 Amido Nitrogens for Enzyme–Peptide Inhibitor Binding. *J. Med. Chem.* **37**, 3863–3866 (1994).
142. Kathman, S. G., Xu, Z. & Statsyuk, A. V. A Fragment-Based Method to Discover Irreversible Covalent Inhibitors of Cysteine Proteases. 4–9 (2014).
143. Resnick, E. *et al.* Rapid Covalent-Probe Discovery by Electrophile-Fragment Screening. *J. Am. Chem. Soc.* **141**, 8951–8968 (2019).
144. Ekkebus, R., Flierman, D., Geurink, P. P. & Ovaas, H. Catching a DUB in the act : novel ubiquitin-based active site directed probes Reggy Ekkebus , Dennis Flierman , Paul P Geurink and. 63–70 (2014).
145. Gilberto, S. & Peter, M. Dynamic ubiquitin signaling in cell cycle regulation. *J. Cell Biol.* **216**, 2259–2271 (2017).
146. Akutsu, M., Dikic, I. & Bremm, A. Ubiquitin chain diversity at a glance. *J. Cell Sci.* **129**, 875–880 (2016).
147. Heideker, J. & Wertz, I. E. DUBs, the regulation of cell identity and disease. *Biochem. J.* **465**, 1–26 (2015).
148. Frias-Staheli, N. *et al.* Ovarian Tumor Domain-Containing Viral Proteases Evade Ubiquitin- and ISG15-Dependent Innate Immune Responses. *Cell Host Microbe* **2**, 404–416 (2007).
149. Edelmann, M. J., Nicholson, B. & Kessler, B. M. Pharmacological targets in the ubiquitin system offer new ways of treating cancer, neurodegenerative disorders and infectious diseases. *Expert Rev. Mol. Med.* **13**, 1–17 (2011).
150. Sheng, Y. *et al.* Molecular recognition of p53 and MDM2 by USP7/HAUSP. *Nat. Struct. Mol. Biol.* **13**, 285–291 (2006).
151. Fraile, J. M. *et al.* Deubiquitinases in cancer : new functions and therapeutic options. *Oncogene* **31**, 2373–2388 (2012).
152. Bishop, P., Rocca, D. & Henley, J. M. Ubiquitin C-Terminal hydrolase L1 (UCH-L1): Structure, distribution and roles in brain function and dysfunction. *Biochem. J.* **473**, 2453–2462 (2016).

153. Zhang, M., Cai, F., Zhang, S., Zhang, S. & Song, W. Overexpression of ubiquitin carboxyl-terminal hydrolase L1 (UCHL1) delays Alzheimer's progression in vivo. *Sci. Rep.* **4**, 1–6 (2014).
154. Ndubaku, C. & Tsui, V. Inhibiting the deubiquitinating enzymes (DUBs). *J. Med. Chem.* **58**, 1581–1595 (2015).
155. Reyes-Turcu, F. E., Ventii, K. H. & Wilkinson, K. D. Regulation and Cellular Roles of Ubiquitin-Specific Deubiquitinating Enzymes. *Annu. Rev. Biochem.* **78**, 363–397 (2009).
156. Leung, I., Jarvik, N. & Sidhu, S. S. A Highly Diverse and Functional Naïve Ubiquitin Variant Library for Generation of Intracellular Affinity Reagents. *J. Mol. Biol.* **429**, 115–127 (2017).
157. Zhang, W. *et al.* Generation and Validation of Intracellular Ubiquitin Variant Inhibitors for USP7 and USP10. *J. Mol. Biol.* **429**, 3546–3560 (2017).
158. Misaghi, S. *et al.* Structure of the ubiquitin hydrolase UCH-L3 complexed with a suicide substrate. *J. Biol. Chem.* **280**, 1512–1520 (2005).
159. Griffin, P. *et al.* Method for measuring the activity of deubiquitinating enzymes in cell lines and tissue samples. *J. Vis. Exp.* 1–7 (2015). doi:10.3791/52784
160. van Durme, J. *et al.* A graphical interface for the FoldX forcefield. *Bioinformatics* **27**, 1711–1712 (2011).
161. Buß, O., Rudat, J. & Ochsenreither, K. FoldX as Protein Engineering Tool: Better Than Random Based Approaches? *Comput. Struct. Biotechnol. J.* **16**, 25–33 (2018).
162. Schymkowitz, J. *et al.* The FoldX web server: An online force field. *Nucleic Acids Res.* **33**, 382–388 (2005).
163. Liu, Y. & Kuhlman, B. RosettaDesign server for protein design. *Nucleic Acids Res.* **34**, 235–238 (2006).
164. Zhang, Y. *et al.* Conformational stabilization of ubiquitin yields potent and selective inhibitors of USP7. *Nat. Chem. Biol.* **9**, 51–58 (2013).
165. Tencer, A. H., Liang, Q. & Zhuang, Z. Divergence in Ubiquitin Interaction and Catalysis among the Ubiquitin-Specific Protease Family Deubiquitinating Enzymes. *Biochemistry* **55**, 4708–4719 (2016).
166. Hu, M. *et al.* Crystal structure of a UBP-family deubiquitinating enzyme in isolation and in complex with ubiquitin aldehyde. *Cell* **111**, 1041–1054 (2002).

167. Renatus, M. *et al.* Structural Basis of Ubiquitin Recognition by the Deubiquitinating Protease USP2. *Structure* **14**, 1293–1302 (2006).
168. Hu, M. *et al.* Structure and mechanisms of the proteasome-associated deubiquitinating enzyme USP14. *EMBO J.* **24**, 3747–3756 (2005).
169. Ernst, A. *et al.* A Strategy for Modulation of Enzymes in the Ubiquitin System. *Science* (80-.). **209**, 590–595 (2013).
170. Galardy, P. J. *et al.* Activity-based ubiquitin-specific protease (USP) profiling of virus-infected and malignant human cells. *Proc. Natl. Acad. Sci.* **101**, 2253–2258 (2004).
171. Love, K. R., Pandya, R. K., Spooner, E. & Ploegh, H. L. Ubiquitin C-terminal electrophiles are activity-based probes for identification and mechanistic study of ubiquitin conjugating machinery. *ACS Chem. Biol.* **4**, 275–287 (2009).
172. Ekkebus, R. *et al.* On Terminal Alkynes That Can React with Active-Site Cysteine Nucleophiles in Proteases. *J. Am. Chem. Soc.* **135**, 2867–2870 (2013).
173. Vijay-Kuman, S., Bugg, C. E. & Cook, W. J. Structure of Ubiquitin Refined at 1.8 Å Resolution. *J. Mol. Biol.* **194**, 531–544 (1987).
174. Egli, M. & Sarkhel, S. Lone pair-aromatic interactions: To stabilize or not to stabilize. *Acc. Chem. Res.* **40**, 197–205 (2007).
175. Anderson, A. C. The Process of Structure-Based Drug Design. *Chem. Biol.* **10**, 787–797 (2003).
176. Wannamaker, W. *et al.* (S)-1-((S)-2-[[1-(4-amino-3-chloro-phenyl)-methanoyl]-amino]-3,3-dimethyl-butanoyl)-pyrrolidine-2-carboxylic acid ((2R,3S)-2-ethoxy-5-oxo- tetrahydro-furan-3-yl)-amide (VX-765), an orally available selective interleukin (IL)-converting enzyme/caspase-1 i. *J. Pharmacol. Exp. Ther.* **321**, 509–516 (2007).
177. Dolle, R. E. *et al.* Pyridazinodiazepines as a high-affinity, P2-P3 peptidomimetic class of interleukin-1 β -converting enzyme inhibitor. *J. Med. Chem.* **40**, 1941–1946 (1997).
178. Poręba, M., Strózyk, A., Salvesen, G. S. & Drąg, M. Caspase substrates and inhibitors. *Cold Spring Harb. Perspect. Biol.* **5**, 1–20 (2013).
179. Beard, H., Cholleti, A., Pearlman, D., Sherman, W. & Loving, K. A. Applying physics-based scoring to calculate free energies of binding for single amino acid mutations in protein-protein complexes. *PLoS One* **8**, 1–11 (2013).

180. Genheden, S. & Ryde, U. The MM/PBSA and MM/GBSA methods to estimate ligand-binding affinities. *Expert Opin. Drug Discov.* **10**, 449–461 (2015).
181. Erlanson, D. A., Davis, B. J., Jahnke, W. & Box, G. Perspective Fragment-Based Drug Discovery : Advancing Fragments in the Absence of Crystal Structures. *Cell Chem. Biol.* 1–7 (2019). doi:10.1016/j.chembiol.2018.10.001
182. Douangamath, A. *et al.* Crystallographic and electrophilic fragment screening of the SARS-CoV-2 main protease. *Nat. Commun.* **11**, 1–11 (2020).
183. Gui, W. *et al.* Cell-Permeable Activity-Based Ubiquitin Probes Enable Intracellular Profiling of Human Deubiquitinases. *J. Am. Chem. Soc.* **140**, 12424–12433 (2018).
184. Hewings, D. S., Flygare, J. A., Bogoy, M. & Wertz, I. E. Activity-based probes for the ubiquitin conjugation–deconjugation machinery: new chemistries, new tools, and new insights. *FEBS J.* **284**, 1555–1576 (2017).
185. Lindgren, M., Hällbrink, M., Prochiantz, A. & Langel, Ü. Cell-penetrating peptides. *Trends Pharmacol. Sci.* **21**, 99–103 (2000).
186. Godinat, A. *et al.* A biocompatible in vivo ligation reaction and its application for noninvasive bioluminescent imaging of protease activity in living mice. *ACS Chem. Biol.* **8**, 987–999 (2013).
187. Godinat, A. *et al.* A biocompatible ‘split luciferin’ reaction and its application for non-invasive bioluminescent imaging of protease activity in living animals. *Curr. Protoc. Chem. Biol.* **6**, 169–189 (2014).

VITA

Aaron David Krabill, son of David and Beverly Krabill, was born April 9, 1993 in Goshen Indiana. He was raised in Goshen, IN where he graduated from Goshen High School in 2011. Aaron went on to DePauw University where he earned his Bachelor of Arts degree majoring in Biochemistry in 2015. Following completion of his degree, he joined the Medicinal Chemistry and Molecular Pharmacology department at Purdue University's College of Pharmacy. In December of 2015, he joined Dr. Daniel Flaherty's lab as the first of two graduate students. Aaron's work in the Flaherty lab focused on the development and characterization of covalent UCHL1-selective chemical probes. During his PhD studies, Aaron earned the Purdue Graduate School Ross Fellowship, the Kienly Award for outstanding graduate teaching, the Purdue Research Foundation Fellowship, and the Gibbs Travel Award. In addition to his time in lab, Aaron was actively involved in the MCMP graduate student organization as the treasurer and was a member of College of Pharmacy Graduate Student Council as the MCMP representative. Additionally, Aaron assisted and led the organization of the Hitchhiker's Guide to the Biomolecular Galaxy mini-symposium for two years in 2016 – 2018.

PUBLICATIONS

Hewitt, C. S.; **Krabill A. D.**; Das, C.; Flaherty, D.P. Development of Ubiquitin Variants with Selectivity for Ubiquitin C-Terminal Hydrolase Deubiquitinases. *ACS Biochemistry*. 2020. 10.1021/acs.biochem.9b01076.

Kaur, J.; Cao, X.; Abutaleb, N. S.; Elakashif, A.; Graboski, A.; **Krabill, A.**; Abdel K., Ahmed; An, W.; Bhardwaj, A.; Seleem, M.; Flaherty, D. Optimization of acetazolamide-based scaffold as potent inhibitors of vancomycin- resistant Enterococcus. *Journal of Medicinal Chemistry*. 2020. 10.1021/acs.jmedchem.0c00734.

Krabill, A. D.; Chen, H.; Hussain, S.; Feng, C.; Abdullah, A., Das, C.; Aryal, U. K.; Post, C. B.; Wendt, M. K.; Galardy, P. J.; Flaherty, D. P. Ubiquitin C-Terminal Hydrolase L1: Biochemical and Cellular Characterization of a Covalent Cyanopyrrolidine-Based Inhibitor. *ChemBioChem*. 2019, 20. DOI: 10.1002/cbic.201900434